NUMERICAL SIMULATIONS OF STRONGLY CORRELATED ELECTRON AND SPIN SYSTEMS

A Dissertation

Presented to the Faculty of the Graduate School

of Cornell University

in Partial Fulfillment of the Requirements for the Degree of

Doctor of Philosophy

by

Hitesh Jaiprakash Changlani

May 2013

NUMERICAL SIMULATIONS OF STRONGLY CORRELATED ELECTRON AND SPIN SYSTEMS

Hitesh Jaiprakash Changlani, Ph.D.

Cornell University 2013

Developing analytical and numerical tools for strongly correlated systems is a central challenge for the condensed matter physics community. In the absence of exact solutions and controlled analytical approximations, numerical techniques have often contributed to our understanding of these systems. Exact Diagonalization (ED) requires the storage of at least two vectors the size of the Hilbert space under consideration (which grows exponentially with system size) which makes it affordable only for small systems. The Density Matrix Renormalization Group (DMRG) uses an intelligent Hilbert space truncation procedure to significantly reduce this cost, but in its present formulation is limited to quasi-1D systems. Quantum Monte Carlo (QMC) maps the Schrödinger equation to the diffusion equation (in imaginary time) and only samples the eigenvector over time, thereby avoiding the memory limitation. However, the stochasticity involved in the method gives rise to the the "sign problem" characteristic of fermion and frustrated spin systems.

The first part of this thesis is an effort to make progress in the development of a numerical technique which overcomes the above mentioned problems. We consider novel variational wavefunctions, christened "Correlator Product States" (CPS), that have a general functional form which hopes to capture essential correlations in the ground states of spin and fermion systems in any dimension. We also consider a recent proposal to modify projector (Green's Function) Quantum Monte Carlo to ameliorate the sign problem for realistic and model Hamiltonians (such as the Hubbard model). This exploration led to our own set

of improvements, primarily a semistochastic formulation of projector Quantum Monte Carlo.

Despite their limitations, existing numerical techniques can yield physical insights into a wide variety of problems. The second part of this thesis considers one such numerical technique - DMRG - and adapts it to study the Heisenberg antiferromagnet on a generic tree graph. Our attention turns to a systematic numerical and semi-analytical study of the effect of local even/odd sublattice imbalance on the low energy spectrum of antiferromagnets on regular Cayley trees. Finally, motivated by previous experiments and theories of randomly diluted antiferromagnets (where an even/odd sublattice imbalance naturally occurs), we present our study of the Heisenberg antiferromagnet on the Cayley tree at the percolation threshold. Our work shows how to detect "emergent" low energy degrees of freedom and compute the effective interactions between them by using data from DMRG calculations.

BIOGRAPHICAL SKETCH

Hitesh J. Changlani was born on December $29, 1985$ in Mumbai (then Bombay), India to Shri Jaiprakash Changlani and Shrimati Vinita Changlani. From a very young age, he was excited about mathematics and science. His family recognized his talent and made sure he was guided well in his academic endeavors.

After a brief phase of wanting to be a mathematician, Hitesh attended the Indian Institute of Technology Bombay from 2003 to 2007 and chose to study Engineering Physics (not being sure whether he wanted to be an engineer or a physicist!). Even midway during his undergraduate studies, Hitesh was not fully sure of pursuing physics as a career. This changed when he was exposed to the wonderful world of quantum mechanics, whose abstractness and non-intuitive results greatly appealed to him.

Hitesh started his Ph.D. program at Cornell University in the fall of 2007. He has been fortunate enough to collaborate with three advisors during his time there - Prof. Chris Henley, Prof. Cyrus Umrigar and Prof. Garnet Chan, all of whom have left an indelible impression on him. He hopes to incorporate their perspectives in his own research in the coming years. In April 2013, he will join the Physics Department at the University of Illinois at Urbana-Champaign as a postdoctoral researcher.

Hitesh met Suravi through some common friends at Cornell in November 2009. They were married on June 2, 2012.

I dedicate this thesis to my loving family.

ACKNOWLEDGMENTS

First of all, I would like to thank my advisor Professor Christopher Henley for his excellent guidance and support during my Ph.D. His dedication and commitment to scientific research are exemplary and have influenced me greatly. His vast breadth of knowledge, tremendous physical insights and unique way of looking at things have been a guiding force and have complemented my 'numerical way' of approaching problems. I am quite grateful to him for convincing me to look for simple explanations even when the problem looked quite complex. The end results were certainly more satisfying this way than they would have been otherwise.

I sincerely thank Prof. Umrigar and Prof. Garnet Chan from whom I have inherited almost all my knowledge of the numerical machinery which was instrumental in 'getting things to work' in this thesis. I am indebted to Prof. Garnet Chan for training me when I was still a young graduate student and for helping me overcome my fear of programming (and initial reluctance to toil with computer codes for long hours). I am happy to acknowledge that most of my knowledge of the workings of the DMRG algorithm and literature on tensor networks was gained by being a reasonably attentive observer of his group meetings. Prof. Cyrus Umrigar has been an excellent guide and has helped me explore the rather challenging problem of numerically simulating fermion systems with Quantum Monte Carlo. I am grateful to him for teaching me about the various areas of Quantum Monte Carlo and for patiently listening to all my ideas. I also thank him for the excellent tomatoes and eggs I received from his farm as it saved me quite a few trips to the grocery shops!

I would also like to thank Prof. Daniel Ralph for serving on my thesis committee and for encouraging me to look out for experimental connections to my

work. I thank Prof. Piet Brouwer, Prof. Rob Thorne and Prof. Erich Mueller for serving on my first-year committee and whose friendly attitudes eased the transition into academic life at Cornell.

A word of thanks to my external collaborators: Prof. Anders Sandvik, for hosting me at Boston University during my visit in September 2009 and for all the discussions at APS March Meetings and over email; Prof. Andreas Läuchli for his hospitality at the University of Innsbruck, Austria and for pushing me in a research direction which became quite fruitful. I am also thankful to Prof. Läuchli for offering me the opportunity to visit him for a few months to explore new research directions.

I acknowledge the funding agencies that supported my research. My work has been was supported by the National Science Foundation through CHE-0645380 and DMR-1005466, the DOE-CMSN program, the David and Lucile Packard Foundation, the Alfred P. Sloan Foundation, and the Camille and Henry Dreyfus Foundation. My work also made use of the Cornell Center for Materials Research computer facilities which are supported through the NSF MRSEC program (DMR-1120296).

I also wish to thank Deb Hatfield, John Miner and Kacey Bray of the Cornell Physics Department Administrative Staff who always made sure I had a Teaching Assistantship when I needed it. I thank Connie Wright, Doug Milton and Judy Wilson of the Laboratory of Atomic and Solid State Physics for their help with my Graduate Research Assistant appointments.

I have had the pleasure of working with multiple student and postdoctoral collaborators during my time at Cornell. It is a pleasure to thank Prof. Henley's group members Shivam Ghosh, Sumiran Pujari, Zach Lamberty and Matt Lapa for all the scientific discussions and critical readings of my manuscripts

during group meetings. I am indebted to Shivam and Sumiran for tremendous inputs on my projects and for being my sounding board for all my crazy (and some not-so-crazy) suggestions and ideas. I thank Prof. Garnet Chan's group members: Jesse Kinder, Eric Neuscamman, Jon Dorando, Debashree Ghosh, Dominika Zgid, Claire Ralph, Johannes Hachmann, Sandeep Sharma, Jun Yang and Weifeng Hu for all the discussions on DMRG and Tensor networks, the C++ programming tips and for the wonderful times in and out of Baker laboratory. It is safe to say I have learnt nearly all my Fortran90 and Ubuntu Installation tips from Frank Petruzielo of the Umrigar group. It has been a pleasure to interact with him and Adam Holmes and I appreciate all the brainstorming sessions we had to battle our common enemy (also known as the 'sign problem'!).

Cornell has been a wonderful place to forge friendships which I will cherish for years to come. To all my fellow residents of 536 Thurston Ave (integrated over a span of 5 years) Ravishankar Sundararaman, Benjamin Kreis, Stephen Poprocki, Shivam Ghosh, Kshitij Auluck, Srivatsan Ravi, Leif Ristroph, James Leadoux, Stefan Baur, Mark Buckley, Robert Rodriguez: a big thanks for making Ithaca a home away from home. To all my Physics friends: Ben Kreis, Turan Birol, Ravishankar Sundararaman, YJ Chen, Stephen Poprocki, Kendra Weaver, Colwyn Guilford, Yao Weng, Kartik Ayyer, Mihir Khadilkar: thank you for all the wonderful first year homework sessions, pot-lucks and dinners that eliminated the loneliness of a graduate student's life. To my friends in the Cricket Club and Cornell India Association: I am thankful for all the efforts you put in to make all the experiences memorable and enjoyable.

I am sure I have not been able to thank everyone who contributed to my wonderful experience at Cornell, they must accept my sincerest apologies.

Any acknowledgement would be incomplete without a warm thanks to my family and friends back home in India. My parents have been very supportive of my decision to pursue my ambitions and I can only hope that I do justice to their tremendous belief in me. My sister's presence in New York City has also given me a sense that I'm not too far from family after all.

And finally a big thanks to my wife Suravi who has made many sacrifices for me along the way, and who has always completely supported me in all my endeavors. Her immense confidence in my abilities has been a constant driving force. *Ami tomake bhalobashi*!

TABLE OF CONTENTS

LIST OF TABLES

LIST OF FIGURES

CHAPTER 1

INTRODUCTION TO STRONGLY CORRELATED SYSTEMS

1.1 Introduction

The advent of quantum mechanics has been perhaps the most celebrated event in physics in the 20^{th} century (along with special and general relativity of course!). It has revolutionized how physicists view the physical world. Even after almost a century of research, its laws never fail to surprise us. Its impact has been far reaching for humanity because it has affected our daily lives. Right from the semiconductor transistor (and hence the computer I am using to write this thesis) to the laser (which is now an indispensable tool in medicine and biology), quantum mechanics is all around us. The two main phenomena that motivate this thesis, superconductivity and magnetism, are not possible without quantum mechanics.

Right at the inception of quantum mechanics, one of its key founders, Paul Dirac, remarked in his paper on "Quantum Mechanics of Many-Electron Systems" [1],

> The underlying physical laws necessary for the mathematical theory of a large part of physics and the whole of chemistry are thus completely known, and the difficulty is only that the exact application of these laws leads to equations much too complicated to be soluble. It therefore becomes desirable that approximate practical methods of applying quantum mechanics should be developed, which can lead to an explanation of the main features of complex atomic

systems without too much computation.

Thus, even though quantum mechanics accurately describes electrons and atoms, a direct application of these laws is probably futile without intelligent approximations. This also brings us to a line of thought pioneered by Anderson in his article "More is Different" [2],

> The ability to reduce everything to simple fundamental laws does not imply the ability to start from those laws and reconstruct the universe... At each stage (of the hierarchy of size scales) entirely new laws, concepts and generalizations are necessary, requiring inspiration and creativity to just as great a degree as in the previous one. Psychology is not applied biology and biology is not applied chemistry.

Present research in solid state physics (and the line of thinking presented in this thesis) borrows from the viewpoint endorsed by Anderson. The laws are well known, but how do we study complicated materials composed of a variety of atoms? How do we even start?

To be precise, one of the main objectives of this thesis is to solve the Schrödinger equation

$$H\Psi = E\Psi \tag{1.1}$$

where H is the Hamiltonian of interactions between the constituent particles, $\Psi(\mathbf{r_1}, \mathbf{r_2}, ...\mathbf{r_N})$ is the wavefunction (eigenstate) for the entire system (composed of N particles with coordinates denoted by $\mathbf{r_i}$ [1]) and E is the energy of that state.

[1] The coordinates $\mathbf{r_i}$ correspond to space or spin degrees of freedom (or a combination of both), or could also refer to other quantum numbers.

For all the systems we have considered in this thesis, the Hilbert space is finite dimensional, obtained by discretizing the space over which the constituent particles can move. Throughout this thesis we have worked at absolute zero temperature and thus are interested in determining only the properties of the ground and some low energy excited states of these systems.

To get a sense of the computational complexity hindering us from achieving the above mentioned objectives, let us consider a system of 100 interacting quantum mechanical spins. Let us also consider the seemingly straightforward task of storing the quantum mechanical superposition of the basis states describing the entire state of the system. Up to a factor of unity the number of basis states of these 100 spins (each spin having two possibilities $\uparrow$ and $\downarrow$) is approximately 10^{30} which corresponds to roughly 10^{16} petabytes (PB) of data. To put things in perspective, IBM has the largest storage array ever, with a capacity of 120 petabytes [3]. Even if we construct one IBM storage array every day over the next century, we'll find we are still way too short - all we can get is about 10^8 PB of storage.

As you may have already appreciated, we are *not* going to solve the problem of storing the state of 100 spins in this manner; at least not within the lifetime of this author. Maybe we will never solve this problem. Even if we do, how are we to say anything meaningful about the thermodynamic limit (large size, Avogadro number of particles) which involves sizes orders of magnitude larger than what we considered above?

Even though the situation does not appear too bright, we have some respite that for most physical systems in Nature (and those that we study and simulate), the Hamiltonian involves local interactions (by which we mean that interaction

strengths fall off rapidly with distance). Moreover, physical interactions generally involve a maximum of two-body interactions making the Hamiltonian extremely sparse. These ingredients are often enough to provide an approximate structure to the low energy eigenfunctions, which drastically reduce the amount of information necessary to describe the system. The only problem is: what is this structure?

There is another advantage that comes along with a physically motivated Hamiltonian. Since the interactions are local, it is reasonable to expect that studying small systems will lead to *meaningful* insights into what happens for larger systems. Note that as solid state physicists, we are mostly interested in physics at large scales (or low energies) and ways to extrapolate to this limit are not always clear. Nevertheless, this is a very fruitful direction and has been adopted in this thesis.

Despite all this, solving a "many body problem" is a big challenge. The limit in which the problem *does* becomes tractable is when the many body system is made up of completely *non-interacting bodies*. Another tractable case is when each body can be said to be experiencing the "mean field" provided by interactions with the other bodies. In either case, the many body problem is converted into a one particle problem, one which is relatively easy to solve. By this we mean that the wavefunction $\Psi(\mathbf{r_1}, \mathbf{r_2}, ...\mathbf{r_N})$, we are seeking factorizes in terms of one particle wavefunctions (Φ_i), i.e.,

$$\Psi(\mathbf{r_1}, \mathbf{r_2}, ...\mathbf{r_N}) = \Phi_1(\mathbf{r_1})\Phi_2(\mathbf{r_2})...\Phi_N(\mathbf{r_N}) \tag{1.2}$$

Since we are primarily dealing with fermions (a similar generalization holds for bosons as well), we have the antisymmetric form, which can be expressed as a

determinant,

$$\Psi\left(\mathbf{r_1}, \mathbf{r_2}, ...\mathbf{r_N}\right) = \begin{vmatrix} \Phi_1(\mathbf{r_1}) & \Phi_2(\mathbf{r_1}) & .. & .. & \Phi_N(\mathbf{r_1}) \\ \Phi_1(\mathbf{r_2}) & \Phi_2(\mathbf{r_2}) & .. & .. & \Phi_N(\mathbf{r_2}) \\ \Phi_1(\mathbf{r_3}) & \Phi_2(\mathbf{r_3}) & .. & .. & .. \\ & & .. & .. & .. \\ \Phi_1(\mathbf{r_N}) & \Phi_2(\mathbf{r_N}) & .. & .. & \Phi_N(\mathbf{r_N}) \end{vmatrix} \tag{1.3}$$

The fact that the one particle problem is relatively "easy" does not make it physically uninteresting. After all, non interacting fermions are the basis for theories of metals and non interacting bosons are responsible for the phenomenon of Bose Einstein Condensation! In addition, using the single particle viewpoint is very useful in study of systems where the particles are *weakly interacting*, with the use of many body perturbation theory.

Some caution needs to be exercised in our mention of *ignoring* electron-electron interactions in the band theory of metals (see the book by Ashcroft and Mermin [4]) considering that the interactions are known to be *strong*. The resolution to this apparent paradox is the following. One finds (almost magically) that it is reasonable to assume that the *role of interactions* is solely to change the parameters (such as the mass) of the bare electrons. The effective low energy theory of these materials is then well described in terms of the "dressed electrons" which *do not* strongly interact with one another. This is the basis of Landau's Fermi liquid picture (for example see the book of Pines and Noziéres [5]) which justifies an adiabatic connection between the Hamiltonian of a real metal (involving "itinerant" electrons) and that of a nearly free electron gas [2].

To summarize the point being made here, systems that are effectively de-

[2]For a rigorous justification of the Fermi liquid picture we refer the reader to the article by Shankar [6].

scribed by one-body Hamiltonians can be understood very well with existing theories and techniques and from a "computational complexity" viewpoint can be considered to be in the "solved" category.

However, not all problems fit into this category. In particular, there exist a wide class of materials involving the transition metals whose valence electrons are in atomic d or f orbitals. Since these orbitals are fairly localized in space, the Coulomb interaction between electrons (on the same ion) is effectively greatly enhanced (compared to the itinerant case where the electrons are in s or p orbitals) and cannot be ignored in comparison to their kinetic energy. In this regime, the assumptions that justify the use of Fermi Liquid theory break down and there does not appear to be an alternate description that involves an effective one particle picture. Rather, the many-body nature of the problem is *essential* in describing physical phenomena (such as the Mott metal-insulator transition and antiferromagnetism) seen in this class of materials.

1.2 Strongly correlated systems

In this section, I will discuss some examples from the class of problems where the many body nature of the problem is essential in understanding the physics at play. Such systems have been given the umbrella name of "strongly correlated systems". This list is by no means exhaustive, but will provide the outline for understanding the work in later Chapters.

1.2 .1 High T_c superconductors

The widely successful BCS mean field theory [7](for a historical review of how this theory developed see [8]) provides an understanding for the class of superconductors whose normal state (the state at high temperature) is a Landau Fermi liquid.

In 1986, J.G. Bednorz and K.A. Müller [9] discovered superconductivity in a lanthanum based cuprate perovskite material (Ba-La-Cu-O system or LBCO) with a T_c (superconducting transition temperature) of 35 K, higher than had previously been recorded for any compound. This finding and subsequent discovery of other cuprates, all with "high" values of T_c, could not be understood within the BCS framework because these materials are 'bad metals' in their normal state [3].

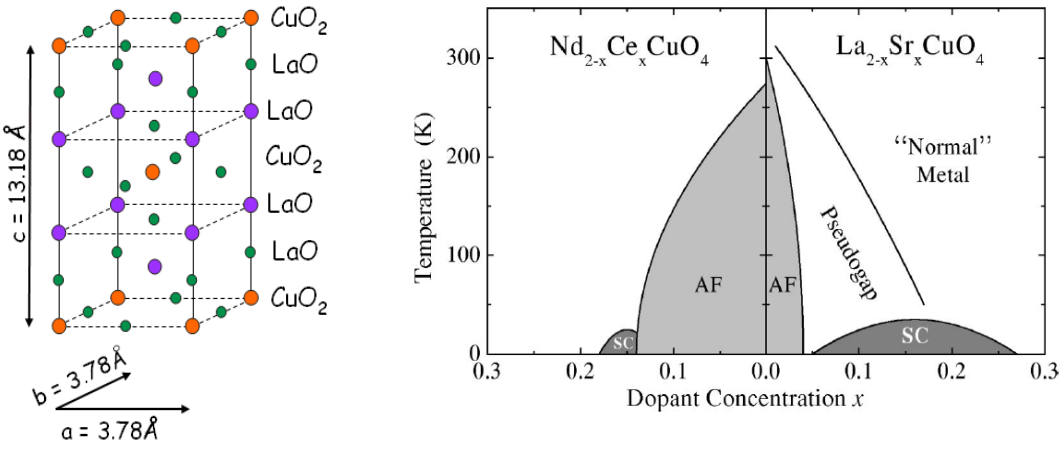

Figure 1.1: The structure of lanthanum cuprate showing the CuO_2 planes believed to be instrumental in unconventional superconductivity (figure taken from [10]). The phase diagram of this material, when doped with strontium is also shown (figure taken from the work of Damascelli et al. [11]).

[3] In addition to posing an academically exciting and unsolved challenge, a very important objective of the research in the field of high T_c superconductivity is to investigate the possibility of a room temperature superconductor. Such a discovery would be remarkable as it may revolutionize many technologies (and possibly solve the energy crisis!)

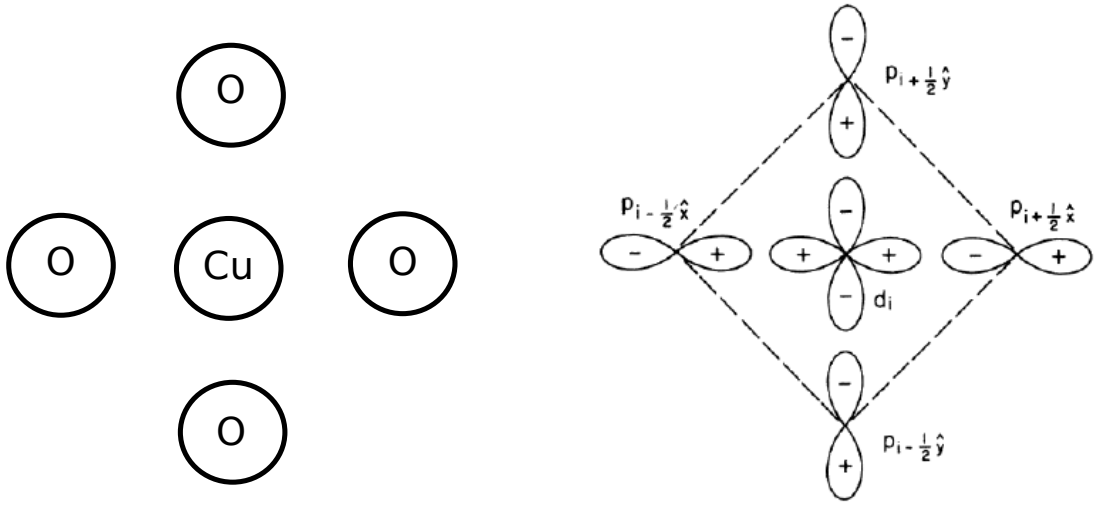

Figure 1.2: Unit cell of the copper-oxygen planes. The $d_{x^2-y^2}$ orbital of copper (Cu) and the appropriate p orbitals of oxygen (O) are also shown.

Based on the generic phase diagram of the cuprates (see Figure 1.1), it is believed that the CuO_2 planes (call a given copper-oxygen plane as the X-Y plane) are primarily responsible for superconductivity. These planes may be modelled (see Figure 1.2) using the "three band model" involving the $d_{x^2-y^2}$ orbital of copper and the p_x orbitals for the oxygens along the X-axis and the p_y orbitals for the oxygens along the Y-axis. Zaanen, Sawatzky and Allen [12], Anderson [13] and Zhang and Rice [14] have argued that there are good reasons for considering an effective low energy description involving *only* the copper atoms.

The model that is pertinent to this research is the one band Hubbard model on a square lattice, which will be discussed in section 1.3 .1.

1.2 .2 Magnetism

Magnetic moments of atoms arise from electric currents (orbital angular momentum of electrons) and/or the "spin" angular momentum. The typical energy

scale of the magnetostatic interaction between two such moments is generally much smaller (by two to three orders of magnitude) than the temperature below which they tend to align or anti align with one another. In fact, it is quantum mechanical "exchange" [15, 16] (having its origin in the Pauli exclusion principle, Coulomb repulsion and electron hopping) that is primarily responsible for an effective ferro- or antiferromagnetic interaction between magnetic moments.

Magnetism in materials, arising due to itinerant or localized electrons, is ubiquitous in nature and the laboratory. Thus, magnets are widely studied and researched. From our point of view (for this thesis), the essential thing to appreciate is that the parent (undoped) materials of the cuprates are *antiferromagnetic* insulators (see the phase diagram in Figure 1.1) and can be modelled by a nearest neighbor Heisenberg model, whose Hamiltonian will be discussed in section 1.3 .3. The Heisenberg Hamiltonian and its variants (on various geometries) are believed to be applicable in other situations as well, such as in the study of molecular magnets [17] or the recently discovered Herbertsmithite crystal (having the kagome structure) [18].

1.2 .3 Quantum Hall effect

Another strongly correlated system is the two dimensional electron gas (realized in gallium arsenide heterostructures), subjected to a strong magnetic field perpendicular to the plane. When an electric field is applied transverse to the magnetic field, von Klitzing [19] found the Hall conductance to occur in integer multiples thereby indicating it was "quantized" (this discovery resulting in a Nobel Prize in 1985).

Following the "integer quantum Hall effect", a fractional version of the same effect was discovered by Tsui and Störmer [20] and theoretically explained by Laughlin [21], leading to their Nobel Prize in 1998. The theoretical explanations suggest that this phenomenon is a collective phenomenon of all the electrons which leads to emergent "quasi-particles" with fractional statistics. In fact, Laughlin [21] showed explicitly that the approximate ground state wavefunction for this system is,

$$\Psi(z_1, z_2, ...z_N) = \prod_{i>j}(z_i - z_j)^n \prod_k \exp(-|z_k|^2) \tag{1.4}$$

where $z_k \equiv x_k + iy_k$ and x_i and y_i refer to the two dimensional coordinates of the i th electron. Since the wavefunction is antisymmetric (under exchange of electron labels), n is odd.

The Laughlin wavefunction lies in the class of Jastrow wavefunctions widely used to study many electron systems. The work presented in Chapter 3 is inspired (in part) by the idea of the Laughlin wavefunction, in search of a generic ansatz (functional form) for ground state wavefunctions of a wide class of strongly correlated systems.

1.3 Lattice models for strongly correlated systems

Even though we would like to simulate the full Schrödinger equation, we accept that an ab-initio (first principles) simulation is computationally infeasible. Moreover such an exercise probably does not illuminate the low energy physics of these systems in a manner which is easy to digest.

Rather, we make a leap of faith and adhere to the philosophy of Anderson.

Instead of studying the actual (full) Hamiltonian in play, we study an effective Hamiltonian defined on a discrete lattice, that (we believe) is closely related to the former. Note that there is no rigorous justification for such a procedure. One can hope that the essential low energy physics will be captured to an extent that is sufficient to explain experimental observations. Even if we are wrong, there is some merit in performing this exercise: we can *systematically* understand which terms in the Hamiltonian are important and which terms are not.

In this thesis we will not discuss why a certain model is right or wrong for describing the physical phenomena in play. Rather we will try to numerically simulate the model for its own sake, which in itself is quite a challenging task!

1.3 .1 Hubbard Model

As mentioned earlier, one of the simplest (in looks only!) models that drives theoretical research in the area of high T_c superconductivity is the Hubbard model, named after its originator John Hubbard [22].

The Hubbard model on a square lattice in two dimensions with nearest neighbor hopping t and onsite Coulomb repulsion U, is given by,

$$H_{\text{Hubbard}} = -t \sum_{\langle i,j \rangle, \sigma} c^{\dagger}_{i,\sigma} c_{j,\sigma} + U \sum_{i} n_{i,\uparrow} n_{i,\downarrow} \tag{1.5}$$

where σ refers to the spin index of the electrons and $\langle i, j \rangle$ refer to nearest neighbor sites i and j. $c^{\dagger}_{i,\sigma}$ and $c_{i,\sigma}$ refer to electron creation and annihilation operators respectively and $n_{i,\sigma}$ refers to the electron number operator (at site i and having spin σ). Each site on the lattice can have one of the four possiblities for its electronic occupation: no electron, one $\uparrow$ electron, one $\downarrow$ electron or a double

occupation indicated by ↑↓.

In addition to the hopping and Coulomb parameters, one can also vary the filling (number of ↑ and ↓ electrons). The general definition of "filling", n, used in the literature is,

$$\langle n \rangle = \frac{N_\uparrow + N_\downarrow}{N} \tag{1.6}$$

where $N_\uparrow$ ($N_\downarrow$) is the number of electrons with spin ↑ (↓), and N is the total number of sites.

The 2D Hubbard model has been studied by various analytical methods (some examples include the Gutzwiller Approximation [23, 24] and slave boson mean field theory [25]) and numerical approaches (for Exact Diagonalization studies see the summary of results in the review by Dagotto [26], for Quantum Monte Carlo studies see for example [27, 28, 29, 30, 31, 32, 33], for Density Matrix Renormalization Group (inclusive of quasi-2D systems) approaches see [34, 35] and for Dynamical Mean Field theory see the reviews by Tremblay et al. [36] and by Maier et al. [37]), but it appears that no consensus has been reached on what its phase diagram really is[4].

Chapter 4 showcases our efforts towards developing a numerical technique for studying strongly correlated systems, and we demonstrate this by simulating the Hubbard model at $U/t \sim 4$ at and below quarter filling.

[4]For a review on the 2D Hubbard model from a numerical viewpoint refer to the article by Scalapino [38].

1.3 .2 Spinless Fermion model

Even though the Hubbard model is supposed to be a minimalist model for the cuprates, it is extremely difficult to simulate by exact methods owing to the unfavorable scaling of the size of its Hilbert space (4^N, where N is the number of sites). Owing to this complexity, Uhrig and Vlaming [39], and later N. G. Zhang and C. L. Henley [40, 41, 42] proposed investigations of a model where fermions of only one type were present (hence the name 'spinless fermion'). Their idea was to consider a simplified model that possibly shows similar qualitative phenomena (such as stripes) as the spinfull Hubbard model.

The spinless fermion model has a nearest neighbor hopping (kinetic) term denoted by strength t and nearest neighbor repulsion strength V,

$$H_{t-V} = -t \sum_{\langle i,j \rangle} c_i^\dagger c_j + V \sum_{\langle i,j \rangle} n_i n_j \tag{1.7}$$

The spinless fermion Hamiltonian had also been previously explored (with Quantum Monte Carlo) in the context of two dimensional spin-polarized fermion gases [43].

The relatively favorable scaling of the size of the Hilbert space of this model (2^N in general, 1.54^N for $V/t \to \infty$), led Zhang and Henley to study lattices larger than possible with the Hubbard model, with Exact Diagonalization (see section 2.1). This allowed them to explore a large part of the phase diagram of this model [5].

In this thesis, the spinless fermion model will be used to benchmark the accuracy of the generic class of variational wavefunctions we introduce in Chapter 3.

[5] For a detailed study of this model, I refer the reader to the thesis of N.G. Zhang [44]

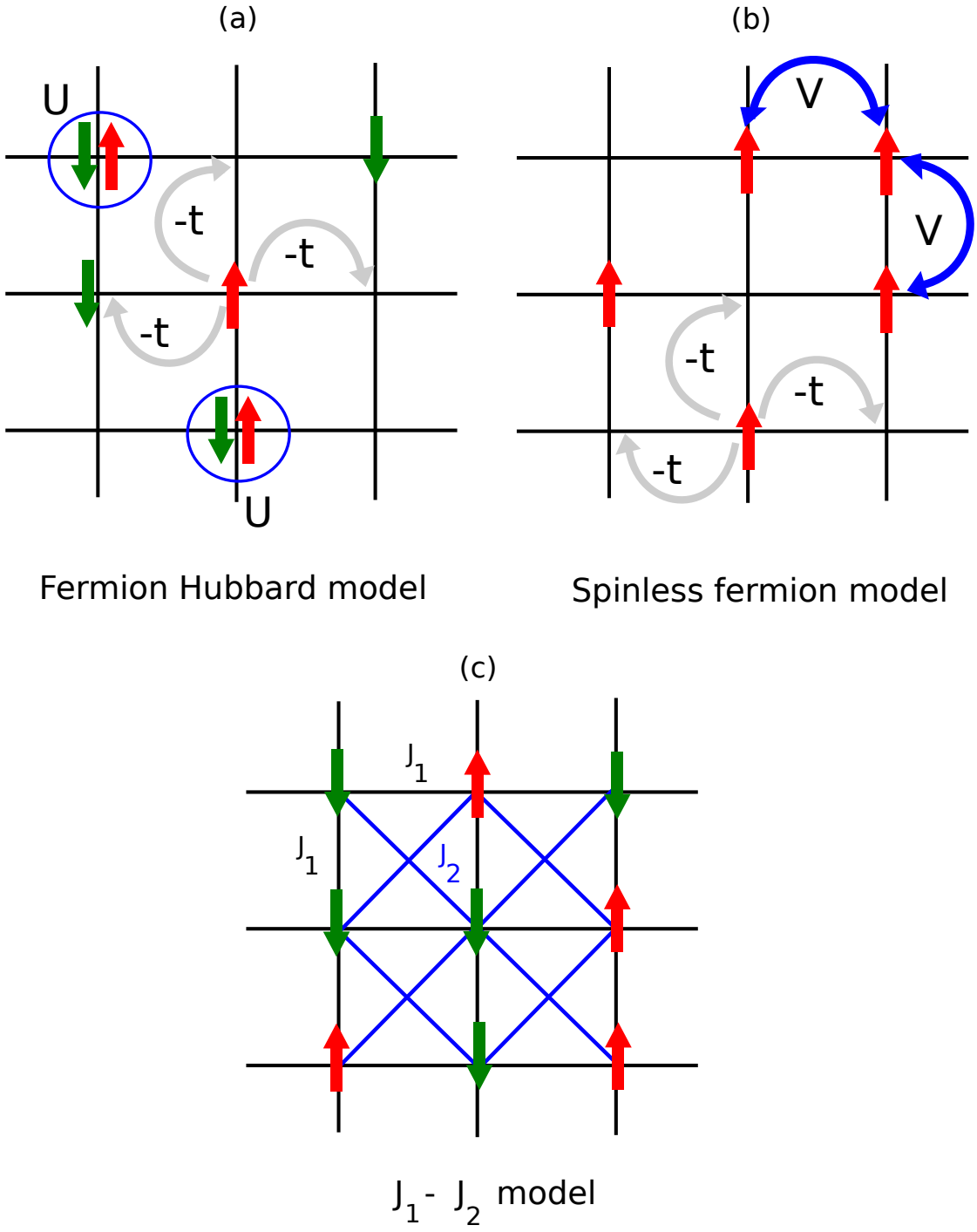

Figure 1.3: Models simulated in this thesis (a) Fermion Hubbard model with nearest neighbor hopping t and onsite Coulomb repulsion U (pertinent to Chapters 3 and 4) and (b) Spinless fermion model with nearest neighbor hopping t and nearest neighbor repulsion V (pertinent to Chapter 3) (c) J_1-J_2 model on the square lattice (pertinent to Chapter 3).

1.3 .3 Heisenberg model

At exactly half filling (one electron per site) and in the limit of large U/t of the Hubbard model, electrons find any hopping to be unfavorable as it leads to double occupancies which cost energy U. Thus the kinetic energy of the electrons is suppressed. The resultant low energy effective model (derived within second order perturbation theory) has exactly one electron per site, with only its spin degree of freedom which is variable, and is known as the (nearest neighbor) Heisenberg model

$$H_{\text{Heisenberg}} = J \sum_{\langle ij \rangle} \mathbf{S}_i \cdot \mathbf{S}_j, \tag{1.8}$$

where $\mathbf{S_i}$ are Pauli spin $1/2$ operators and the sum runs over nearest-neighbor occupied sites. The effective interaction (J) turns out to be antiferromagnetic and is given in terms of the Hubbard parameters t and U as,

$$J \equiv \frac{4t^2}{U} \tag{1.9}$$

This simplification of dealing with 'spins' instead of electrons reduces the size of the Hilbert space from 4^N to 2^N.

The 2D Heisenberg model has been studied analytically (using spin wave [45, 46, 47], Schwinger Bosons [48, 49, 50, 51, 52], Renormalization group approaches) and numerically [53, 54] (for a review of the importance of this model and usefulness to study the cuprates refer to the review article by Manousakis [55]).

From a computational physicist's point of view, the nearest neighbor Heisenberg model, on a bipartite lattice such as the square lattice, is extremely useful as it is amenable to large scale Quantum Monte Carlo simulations [56, 57]. Thus it is a model that is often used to benchmark new techniques and methods (as is the case in Chapter 3).

One can also consider Heisenberg models with next-to nearest neighbor interactions: for the square lattice these interactions lead to the *frustrated* $J_1 - J_2$ model [6] (see Figure 1.3). For the purpose of this thesis, the $J_1 - J_2$ model will only be used for the purpose of benchmarking our proposed technique in Chapter 3.

The nearest neighbor Heisenberg model finds its way again in Part II of this thesis: it is the main subject in Chapters 8 and 9 where it is studied on the Bethe lattice without and with dilution (at the percolation threshold) respectively.

1.4 Organization of the Thesis

In this Chapter we have showcased "strongly correlated systems": a class of systems where the "single particle picture" breaks down. Numerically simulating these systems is an enormous challenge because we are dealing with a problem (exponential scaling of the Hilbert space) where putting in more computer time or memory will not necessarily lead to a solution. This entails the search for approximate numerical methods which utilize the fact that we are dealing with physical Hamiltonians. The first part of this thesis thus attempts to develop numerical techniques to simulate the models introduced in this Chapter.

In this Chapter, we introduced models for the cuprates whose undoped parent materials have (long range) antiferromagnetic order. In order to study how this order is affected on diluting the system, Vajk et al. [63] performed an ex-

[6] The $J_1 - J_2$ model is not amenable to large scale simulations (except in the limits $J_2/J_1 = 0$ and $J_2/J_1 \to \infty$). For further reading of analytical and numerical calculations of this model and to get a sense of the issues that remain with understand the phase diagram (as a function of J_2/J_1) one may refer to the papers [58, 59, 60, 61, 62] and references therein.

periment to replace the magnetic copper (Cu) atoms in the CuO_2 planes with non magnetic zinc (Zn) or magnesium (Mg). This experiment and subsequent theoretical and numerical studies motivate the second part of this thesis. Our contribution is to provide an understanding of the low energy physics of a randomly diluted antiferromagnet at the percolation threshold, by using an existing numerical technique and adapting it suitably to study our problem.

BIBLIOGRAPHY

[1] P. A. M. Dirac, Proceedings of the Royal Society of London. Series A, Containing Papers of a Mathematical and Physical Character **123**, pp. 714 (1929).

[2] P. W. Anderson, Science **177**, 393 (1972).

[3] Simonite, T., "IBM Builds Biggest Data Drive Ever", *MIT Technology Review* (25 th August 2011).

[4] N. W. Ashcroft, N. D. Mermin, *Solid State Physics*, Holt, Rinehart and Winston (1976).

[5] D. Pines, P. Noziéres, The Theory of Quantum Liquids. New York: Benjamin; 1966.

[6] R. Shankar, Rev. Mod. Phys. **66**, 129 (1994).

[7] J. Bardeen, L. N. Cooper, and J. R. Schrieffer, Phys. Rev. **108**, 1175 (1957).

[8] BCS: 50 Years, eds. L.N. Cooper, D. Feldman, World Scientific; 2010.

[9] J. G. Bednorz and K. A. Müller, Zeitschrift für Physik B Condensed Matter **64**, 189 (1986).

[10] J. Hoffman, Harvard group website, http://hoffman.physics.harvard.edu/.

[11] A. Damascelli, Z. Hussain, and Z.-X. Shen, Rev. Mod. Phys. **75**, 473 (2003).

[12] J. Zaanen, G. A. Sawatzky, and J. W. Allen, Phys. Rev. Lett. **55**, 418 (1985).

[13] P. W. Anderson, Science **235**, pp. 1196 (1987).

[14] F. C. Zhang and T. M. Rice, Phys. Rev. B **37**, 3759 (1988).

[15] H. Kramers, Physica **1**, 182 (1934).

[16] P. W. Anderson, Phys. Rev. **79**, 350 (1950).

[17] O. Kahn, *Molecular Magnetism*, Wiley-VCH (1993).

[18] J. S. Helton *et al.*, Phys. Rev. Lett. **98**, 107204 (2007).

[19] K. v. Klitzing, G. Dorda, and M. Pepper, Phys. Rev. Lett. **45**, 494 (1980).

[20] D. C. Tsui, H. L. Stormer, and A. C. Gossard, Phys. Rev. Lett. **48**, 1559 (1982).

[21] R. Laughlin, Phys. Rev. Lett. **50**, 1395 (1983).

[22] J. Hubbard, Proceedings of the Royal Society of London. Series A. Mathematical and Physical Sciences **276**, 238 (1963).

[23] M. C. Gutzwiller, Phys. Rev. **137**, A1726 (1965).

[24] W. F. Brinkman and T. M. Rice, Phys. Rev. B **2**, 4302 (1970).

[25] G. Kotliar and A. E. Ruckenstein, Phys. Rev. Lett. **57**, 1362 (1986).

[26] E. Dagotto, Rev. Mod. Phys. **66**, 763 (1994).

[27] J. E. Hirsch, Phys. Rev. B **31**, 4403 (1985).

[28] H. Yokoyama and H. Shiba, Journal of the Physical Society of Japan **56**, 1490 (1987).

[29] S. N. Coppersmith and C. C. Yu, Phys. Rev. B **39**, 11464 (1989).

[30] S. R. White *et al.*, Phys. Rev. B **40**, 506 (1989).

[31] N. Furukawa and M. Imada, Journal of the Physical Society of Japan **61**, 3331 (1992).

[32] S. Zhang, J. Carlson, and J. E. Gubernatis, Phys. Rev. Lett. **74**, 3652 (1995).

[33] C. N. Varney *et al.*, Phys. Rev. B **80**, 075116 (2009).

[34] T. Xiang, Phys. Rev. B **53**, R10445 (1996).

[35] E. Jeckelmann, D. J. Scalapino, and S. R. White, Phys. Rev. B **58**, 9492 (1998).

[36] A.-M. S. Tremblay, B. Kyung, and D. Senechal, Low Temperature Physics **32**, 424 (2006).

[37] T. Maier, M. Jarrell, T. Pruschke, and M. H. Hettler, Rev. Mod. Phys. **77**, 1027 (2005).

[38] D. Scalapino, Chapter 13 in *Handbook of High-Temperature Superconductivity*, eds. J. R. Schrieffer, J.S. Brooks, Springer 2007. This Chapter is also available online at http://arxiv.org/abs/cond-mat/0610710.

[39] G. S. Uhrig and R. Vlaming, Phys. Rev. Lett. **71**, 271 (1993).

[40] C. L. Henley and N.-G. Zhang, Phys. Rev. B **63**, 233107 (2001).

[41] N. G. Zhang and C. L. Henley, Phys. Rev. B **68**, 014506 (2003).

[42] N. G. Zhang and C. L. Henley, The European Physical Journal B - Condensed Matter and Complex Systems **38**, 409 (2004).

[43] J. E. Gubernatis, D. J. Scalapino, R. L. Sugar, and W. D. Toussaint, Phys. Rev. B **32**, 103 (1985).

[44] N.G. Zhang, Ph.D. thesis, Cornell University (2002); http://people.ccmr.cornell.edu/ clh/Theses/zhangthesis.pdf.

[45] M. Takahashi, Phys. Rev. Lett. **58**, 168 (1987).

[46] J. E. Hirsch and S. Tang, Phys. Rev. B **39**, 2887 (1989).

[47] D. A. Huse, Phys. Rev. B **37**, 2380 (1988).

[48] A. Chubukov, Phys. Rev. B **44**, 12318 (1991).

[49] A. V. Chubukov, S. Sachdev, and J. Ye, Phys. Rev. B **49**, 11919 (1994).

[50] S. Sarker, C. Jayaprakash, H. R. Krishnamurthy, and M. Ma, Phys. Rev. B **40**, 5028 (1989).

[51] A. Auerbach and D. P. Arovas, Phys. Rev. Lett. **61**, 617 (1988).

[52] A.Auerbach, D.P.Arovas, arXiv:0809.4836v2 (unpublished).

[53] N. Trivedi and D. M. Ceperley, Phys. Rev. B **40**, 2737 (1989); N. Trivedi and D. M. Ceperley, Phys. Rev. B **41**, 4552 (1990).

[54] D. A. Huse and V. Elser, Phys. Rev. Lett. **60**, 2531 (1988).

[55] E. Manousakis, Rev. Mod. Phys. **63**, 1 (1991).

[56] A. W. Sandvik, Phys. Rev. B **56**, 11678 (1997).

[57] M. Calandra Buonaura and S. Sorella, Phys. Rev. B **57**, 11446 (1998).

[58] P. Chandra and B. Doucot, Phys. Rev. B **38**, 9335 (1988).

[59] R. F. Bishop, D. J. J. Farnell, and J. B. Parkinson, Phys. Rev. B **58**, 6394 (1998).

[60] L. Capriotti, F. Becca, A. Parola, and S. Sorella, Phys. Rev. Lett. **87**, 097201 (2001).

[61] J. Richter *et al.*, Phys. Rev. B **81**, 174429 (2010).

[62] H.-C. Jiang, H. Yao, and L. Balents, Phys. Rev. B **86**, 024424 (2012).

[63] O. P. Vajk *et al.*, Science **295**, 1691 (2002).

Part I

Quest for a Numerical Technique

CHAPTER 2

NUMERICAL METHODS FOR STRONGLY CORRELATED SYSTEMS

In the previous Chapter, we established that the many-body problem is in general quite hard to solve. From the point of view of this thesis "strongly correlated systems", systems where electron-electron interactions are strong, are of particular interest.

We have indicated that we would (ideally) like to compute the desired wavefunctions (in particular the ground state) of the many body system. However, obtaining the wavefunction *does not* necessarily underlie the purpose of computation. We will see, as this thesis develops, that it will suffice to have methods that directly compute "integrated quantities" which are physically relevant, such as the energy, magnetization, susceptibility and spin-spin correlation functions. As long as we can get the expectation (average) values of these observables, we can consider ourselves fairly successful.

In this Chapter, we briefly survey some of the numerical methods that have been used to simulate and understand model Hamiltonians for strongly correlated systems. We will briefly explain the basic concepts used in the methods (without getting into all the technical details!) and will attempt to point out their relative strengths and weaknesses. This exercise aims to lay down the foundations for understanding the research presented in Chapters 3 and 4.

Before we proceed, the reader must note that numerical methods are not the only ways of studying strongly correlated systems. Exact analytic solutions do exist for systems such as the 1D Heisenberg model (solved with the Bethe Ansatz [1]) and 1D Hubbard model (solved by Lieb and Wu [2]), and analytic

approximations (such as mean field theories and the renormalization group) have been immensely valuable in developing our understanding. However, a discussion of these topics is beyond the scope of this thesis.

2.1 Exact Diagonalization

As mentioned before, there is a clear victor in the battle between an exponentially growing Hilbert space and the amount of computer memory and time we can devote to process it. Despite this limitation, one can numerically study systems with significantly large spaces (running into millions of states or more).

Naively one would imagine that solving the Schrödinger equation (1.1) in a discrete basis of size N_H demands storage of a $N_H \times N_H$ matrix and the ability to completely diagonalize it on a computer. There are a few drawbacks with this viewpoint. As mentioned previously, physical Hamiltonians are local and sufficiently sparse requiring (often) only order N_H storage. Secondly, it is not even crucial to store the Hamiltonian: all one needs to know is the *action* of the Hamiltonian on a vector in the Hilbert space. And finally, we are not necessarily interested in *all* the eigenvalues and eigenvectors of the system; the lowest energy ones would suffice for most of our purposes.

The set of algorithms that solve for a few eigenvectors and eigenvalues (nearly) exactly, are given the name "exact diagonalization" (ED). At the heart of all these algorithms is the power method, which is based on the fact that the largest (by magnitude) eigenvalue of a matrix can be obtained by repeated application of that matrix onto a random vector $|v\rangle$. To see why this is so, express the random vector $|v\rangle$ in terms of the (unknown) eigenbasis (denoted by $\{|i\rangle\}$) of the matrix

as,

$$|v\rangle = \sum_i c_i |i\rangle \tag{2.1}$$

where $c_i \equiv \langle i|v\rangle$ is the coefficient expansion of the vector $|v\rangle$ in the eigenbasis. Without loss of generality, let us also arrange the eigenbasis such that the corresponding (unknown) eigenvalues satisfy $|E_0| > |E_1| .... > |E_{N-1}|$. Often, it is E_0 and $|0\rangle$ that we seek.

Applying the Hamiltonian matrix [1] m times to this vector gives,

$$H^m|v\rangle = \sum_i E_i^m c_i |i\rangle \tag{2.2}$$

Note that the component $|0\rangle$, with the dominant eigenvalue, grows relative to the other components with each application of the matrix (unless c_0 is exactly zero). Thus for sufficiently large m, we may take the desired approximate ground state (unnormalized) wavefunction to be $\psi \equiv H^{m-1}|v\rangle$. We can calculate the energy of this state,

$$\begin{aligned} E &= \frac{\langle\psi|H|\psi\rangle}{\langle\psi|\psi\rangle} && \text{(2.3a)} \\ &= E_0 + \left(\frac{c_1}{c_0}\right)\left(\frac{E_1}{E_0}\right)^m + ... && \text{(2.3b)} \\ &\approx E_0 && \text{(2.3c)} \end{aligned}$$

where the approximation in equation (2.3c) becomes exact in the limit of m going to infinity. Observe that the error (to leading order) in the energy goes as $((E_1/E_0)^m)$. The ratio of E_1/E_0 thus decides the rate of convergence with m. In practice m is taken to be 'large enough' (its value depending on the details of the Hamiltonian), such that the ground state energy and eigenvector have

[1] The matrix being applied may be the Hamiltonian or a suitably defined projector such as $1+\tau(E-H)$. Note that the ground state is not necessarily the state with the largest (by magnitude) eigenvalue and so direct application of the Hamiltonian does not generally work. However, one could always add a constant shift to the energy spectrum to make the ground state the state with the most dominant eigenvalue.

converged to a desired accuracy. Note that all the power method demands is the ability to store two vectors ($H^n|v\rangle$ and $H^{n+1}|v\rangle$) whose dimensions equal the size of the Hilbert space.

Despite its simplicity, the power method is quite inefficient since a lot of information (from powers 0 to m-2 of the Hamiltonian matrix) is discarded. Instead, one could construct an approximation for the full Hamiltonian in the "Krylov" space

$$\mathcal{K} = \{v, Hv, H^2v, ...H^{m-1}v\}, \tag{2.4}$$

The Hamiltonian in this space is a $m \times m$ matrix (where $m << N_H$), which is easy to diagonalize numerically. One such member of the exact diagonalization family is the Lanczos [3] technique, which I discuss in Appendix 2.A . The principle behind this idea is that the Krylov space provides a compact description for expressing the ground state (and possibly other low energy excited states) wavefunction(s). Said another way, the expansion of the full wavefunction in terms of the Krylov basis is a rapidly convergent series and requires reasonably small m, compared to its expansion in the occupation number (or S_z) basis in terms of which the Hamiltonian is originally written down.

One can reduce the computational cost of exact diagonalization (ED) by utilizing the matrix-block diagonal structure of the Hamiltonian (owing to good quantum numbers), and work with only the matrix-block of interest [2]. Spatial and/or time symmetries may be used to reduce the size of the Hilbert space, at the cost of making the Hamiltonian less sparse and more time consuming to compute. Thus the choice to use symmetries depends on the size of the problem

[2]This does not mean that we can necessarily *use all* the good quantum numbers. For example, the total z component of the spin (S_z quantum number) of a state is easy to use, but total spin S (in general) is not.

and the type of computing resources available.

To get a sense of the size of the spaces that can be dealt with using the exact diagonalization method, we mention that typical workstations (with 4 - 8 GB RAM) can handle of the order of 100 million states. With state-of-the-art implementations, the largest reported Hilbert space sizes correspond to the order of 100 billion basis states (for example, the 48 site spin 1/2 Kagome lattice antiferromagnet corresponds to 80 billion basis states [4]).

2.2 Quantum Monte Carlo

Though a numerically exact result is extremely desirable, it is not always possible. Moreover, the entire wavefunction is not what we seek, rather we wish to estimate certain quantum mechanical averages.

For a wide variety of systems, it is enough to *sample* the Hilbert space over a reasonably long "time" rather than have the complete information about it in memory. Notice the mention of "time", even though what we are interested in is the time independent Schrödinger equation. This "time" does not refer to the real time; rather it refers to the fact that the wavefunction is used to define a probability distribution [3], whose statistics we collect over time.

Sampling this distribution comes at the cost of a statistical error in the estimation of measured observables. Said differently, the idea is to express the expectation value of an observable as a sum (or integrand) and use Monte Carlo to perform the summation (or integration). The central limit theorem guaran-

[3] The exact relation between the wavefunction and the probability distribution being sampled is method specific.

tees that this error goes down as $1/\sqrt{\#\,\text{samples}}$ (if the second moment of the integrand is finite), with a prefactor that depends on the specifics of the system under consideration and the efficiency with which the space is sampled.

The collective name given to stochastic methods which involve sampling of the Hilbert space (i.e. when applied to a quantum system) is "Quantum Monte Carlo". The interested reader may refer to the review article by Foulkes et al. [5] and the book edited by Nightingale and Umrigar [6].

The simplest "flavor" of Quantum Monte Carlo is Variational Monte Carlo (VMC) [7, 8]. In VMC, one computes the variational energy E of the Hamiltonian H using a trial wavefunction Ψ_T,

$$E = \frac{\langle \Psi_T | H | \Psi_T \rangle}{\langle \Psi_T | \Psi_T \rangle} \tag{2.5}$$

using Monte Carlo sampling. The variational principle guarantees that $E \geq E_0$ where E_0 is the ground state energy, the equality holds only [4] when $\Psi_0 = \Psi_T$. It is assumed that the trial wavefunction $\Psi_T(\mathbf{R})$ can be computed efficiently (i.e. in a reasonable amount of time) for a given configuration ($\mathbf{R}$) of particles, for this method to be of practical use.

We label the states in configuration space (say the occupation number kets in real space) as $|R\rangle$. In order to compute the variational energy E, we introduce the identity operator $1 = |R\rangle\langle R|$ in equation (2.5), to get,

$$E = \sum_R \frac{\langle \Psi_T | R \rangle \langle R | H | \Psi_T \rangle}{\langle \Psi_T | \Psi_T \rangle} \tag{2.6a}$$

$$= \sum_R \frac{|\langle \Psi_T | R \rangle|^2}{\langle \Psi_T | \Psi_T \rangle} \frac{\langle R | H | \Psi_T \rangle}{\langle R | \Psi_T \rangle} \tag{2.6b}$$

[4] assuming the ground state is non degenerate.

Observe that $|\langle\Psi_T|R\rangle|^2 / \langle\Psi_T|\Psi_T\rangle$ is a probability distribution function and

$$E_L(\mathbf{R}) \equiv \frac{\langle R\,|H|\,\Psi_T\rangle}{\langle R|\Psi_T\rangle} \tag{2.7}$$

is defined to be the "local energy". $E_L(\mathbf{R})$ can be computed efficiently since the Hamiltonian is sparse. To see why this is so, we introduce an identity operator $1 = |R'\rangle\langle R'|$ in equation (2.7), to get,

$$E_L(\mathbf{R}) \equiv \frac{\langle R\,|H|\,\Psi_T\rangle}{\langle R|\Psi_T\rangle} = \sum_{R'} \langle R\,|H|\,R'\rangle\,\frac{\langle R'|\Psi_T\rangle}{\langle R|\Psi_T\rangle} \tag{2.8}$$

Notice that the summation runs over only those terms which have $\langle R|H|R'\rangle \neq 0$ which involves a computation of terms whose number only polynomially increasing with system size. For example, in the case of the Hubbard model in real space this number is a maximum of $4N_e + 1$ where N_e is the total number of electrons.

VMC requires a very "good" many-body trial wavefunction Ψ_T: by which we mean that the wavefunction should capture the essential physics of the problem. Arriving at a choice for Ψ_T is (in general) quite a challenge itself and may require tremendous physical insight. Even after this step, there may be significant effort involved in optimizing the parameters that define Ψ_T to obtain the lowest energy (or variance [9]) possible. Recent progress [10, 11, 12, 13] in algorithms for optimization of parameters has been helpful in this regard.

The limited flexibility in the parametrization of the trial wavefunction is the single most important problem with VMC, as the method may not reveal any physics that is not already built into the wavefunction. Thus VMC is a *biased* method and of limited use in situations where several competing (and distinct) phases of matter have very similar variational energies.

In Chapter 3, our effort is focused on defining a class of variational wave-

functions which have a *flexible* form, and whose parameters can be *efficiently optimized* to provide a good description for a wide variety of strongly correlated systems.

The second flavor of Quantum Monte Carlo is Projector Monte Carlo which is an umbrella term for methods (such as Diffusion Monte Carlo [14, 15], Green's Function Monte Carlo [16, 17], Path Integral QMC [18], World Line MC, Auxiliary Field QMC [19, 20] and its modification Constrained Path Monte Carlo [21, 22] etc.) that apply a projector (P) stochastically onto a trial state Ψ_T (not orthogonal to the ground state) to filter out the ground state wavefunction Ψ_0 (just like the power method)

$$\lim_{m\to\infty} P^m|\Psi_T\rangle \propto |\Psi_0\rangle \tag{2.9}$$

To be a little more concrete in our discussion we consider the projector $\exp(-\beta H)$ which is motivated by mapping the Schrödinger equation to a diffusion equation (in imaginary time)[5]. In the diffusion problem, the particles perform a random walk and at any instant their number in a given volume is not very relevant. However, looking at a given volume for a long enough time period and averaging over the number of particles over the entire time, does tell us the *equilibrium* probability *distribution* of the particles. Note that the probability distribution in every region of space is always positive (or zero), as the number of particles cannot be negative!

In Projector Monte Carlo, the role of real space is now played by the Hilbert space of electron configurations, the role of the diffusing particles is now played

[5]We emphasize, that one does not necessarily have to use the imaginary time evolution operator $\exp(-\beta H)$ to project to the ground state. When the Hilbert space is finite dimensional as is the case for discrete finite lattice models, one can use $1 + \tau(E_T - H)$ where E_T is a constant close to the yet (unknown) ground state energy. However, for pedagogical purposes, the analogy with the diffusion equation is fruitful.

by 'walkers' (entities which carry the labels of *all* electron coordinates) and the role of the equilibrium probability distribution being sampled over time is taken over by the quantum mechanical wavefunction (*not* its absolute value squared). Since the wavefunction can be positive or negative, the 'walkers' also carry 'signs'.

Over time, these walkers can (in general) contribute large positive and large negative values to the measured observables. Since this is done stochastically, it can lead to large uncertainties in the estimation of their averages (expectation values). This uncertainty is known to grow exponentially with system size, rendering a naive implementation of the Projector Monte Carlo method totally ineffective. This generic problem with Projector Monte Carlo Methods is referred to as the "sign problem" and is rather characteristic of systems involving fermions or frustrated spin interactions.

We emphasize, that the "sign problem" is a pure consequence of stochasticity involved in a Monte Carlo calculation. Chapter 4 motivates a way in which the sign problem could be reduced, by advocating a hybrid of deterministic and stochastic projection.

The sign problem is not always present [6]. One can still use Projector Quantum Monte Carlo methods in situations where the distribution being sampled has the same sign over all space as is the case for many bosonic systems. Other important examples of 'sign problem free' cases include the Hubbard model on a bipartite lattice at exactly half filling (when treated with the 'Auxiliary Field

[6] An important point to note is that the sign problem is basis dependent (a trivial basis where there is no sign problem is the eigenbasis, but to transform to that basis requires an exponential amount of effort anyway). A paper by Troyer and Wiese [23] has shown that such a basis cannot be determined in polynomial time for a general Hamiltonian. It is not clear if there is some intelligent method to find a 'sign problem free' basis for physically realistic Hamiltonians in polynomial time.

Quantum Monte Carlo' approach [20]) and the Heisenberg model [17]. The sign problem can also be solved if one knows apriori the regions of space where the wavefunction is positive and negative [7].

Where it works, that is there is no "sign problem", Projector Quantum Monte Carlo is a highly desirable method because of its scalability i.e. the largest system sizes it can go to. Even the statistical error, which was presented as a drawback of the method, can be significantly reduced by collecting samples on parallel machines, a feature well suited to modern day machines.

2.3 Density Matrix Renormalization Group

The renormalization group (developed by several authors in various contexts, see for example the work of Wilson [28] and Kadanoff [29]) has provided a way to generate great insight into the understanding of the low energy physics of model Hamiltonians of classical and quantum systems.

One example of the renormalization group approach is the "Real Space Renormalization Group" (RSRG). A central idea of the approach is to divide a very big system into "blocks of sites" and replace their combined degrees of freedom by fewer effective degrees of freedom. There is no established way of "thinning out" these degrees of freedom; "renormalization" is an umbrella name given to any transformation that involves truncations of the Hilbert space.

[7] This idea has been applied to problems in the continuum [24, 25, 26]. In case the nodes (zeros of the wavefunction) are known only approximately, the Fixed Node method yields a result with a *systematic* error which cannot be eliminated.
For discrete spaces, the term 'Fixed Node Green's Function Monte Carlo' is used for the concept introduced by van Bemmel et al. [27].

One of the earliest and most notable applications of the theory was a study of the Kondo Hamiltonian[8]. By applying a very clever coarse graining procedure, Wilson [28] was able to perform a "Numerical Renormalization Group" [9] study of this model, which eventually won him the Nobel prize in 1982.

However, the success of the Kondo calculation was never quite repeated. It was understood that RSRG was limited in its approach because it only perturbatively treats the interblock couplings, which does not seem to be a reasonable thing to do for a wide class of physical systems of interest [10]. In fact, as pointed out by Wilson in a talk at Cornell and later by White and Noack [32], the simple problem of a single particle in a 1D box failed with real space renormalization group approaches.

The idea that the environment surrounding a block has an instrumental role in the "optimal" truncation of its local Hilbert space led to the birth of the Density Matrix Renormalization Group algorithm [33]. The foundational principle is that it is best to retain those states on a block of sites (denoted by B) which have "dominant weights" in its reduced density matrix ρ_B, calculated in the quantum many body state $|\Psi\rangle$,

$$\hat{\rho}_B = \mathrm{Tr}_{\mathrm{Env}} |\Psi\rangle \langle\Psi| \tag{2.10}$$

For the purpose of the remainder of this Chapter, it will also be useful to define the coefficients of the wavefunction $\psi^{s_1\ s_2\ \cdots\ s_N}$

$$|\Psi\rangle = \sum_{s_1 s_2 \ldots s_N} \psi^{s_1\ s_2 \ldots\ s_N} |s_1\ s_2\ \ldots\ s_N\rangle \tag{2.11}$$

[8]The Kondo Hamiltonian is a model Hamiltonian that describes a sea of free electrons ("Fermi sea") interacting with a localized electron

[9]This calculation scheme called the "Numerical Renormalization Group" (NRG) is a renormalization scheme in a basis that is neither real nor momentum space.

[10]One effort to increase correlations between the blocks is Contractor Renormalization Group [30] (which is also known as RSRG with Effective Interaction [31]).

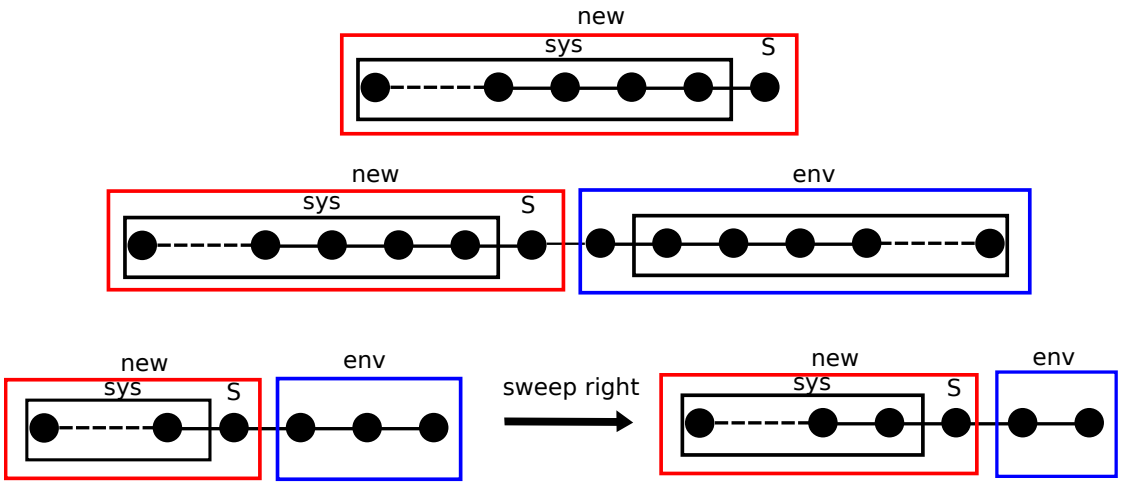

Figure 2.1: (a) In Wilson's way of thinking of Renormalization Group, a site is added to an existing system and their combined Hilbert space is truncated. (b) In DMRG (for simulating an *infinite system*), one can create a mirror image of the system plus site (which is the environment) and solve for the ground state for the 'universe' or 'superblock'. The environment is traced out and a density matrix based truncation is performed on the Hilbert space of the system+site. (c) In the "sweep algorithm" on a *finite* system, one grows the "system" at the cost of "shrinking" the environment or vice versa. Each iteration of the sweep represents a division of the 'universe' into system + site + environment. Details of the implementation will be discussed in Chapter 7.

where $s_1, s_2..$ etc. refer to "physical indices" which, for example, could be spins or occupation numbers.

The Density Matrix Renormalization Group (DMRG) algorithm (summarized briefly in Figure 2.1 and to be discussed in detail in Chapter 7) has been very successful in describing the low energy physics of 1D systems. For a detailed review refer to the articles by Schollwöck [34] and Hallberg [35]. For an (unpublished) introduction to DMRG, I also refer the reader to the article by Chan et al. [36].

Algorithmic developments have been able to push the frontiers of DMRG to deal with reasonably wide (about 12 sites) strip geometries in two dimensions [37] (primarily for spin systems [38, 39]). DMRG has also been used for

fermions on ladder geometries (see for example [40]).

A few years after the DMRG was formulated, Ostlund and Rommer [41] understood that the wavefunction generated with the DMRG algorithm is a Matrix Product State (MPS) (I discuss this connection in Appendix 2.C),

$$\psi_{MPS}^{s_1 s_2 .....s_N} = \sum_{i_1 ... i_{N-1}} A_{i_1}^{s_1} A_{i_1 i_2}^{s_2} A_{i_2 i_3}^{s_3} .....A_{i_{N-1}}^{s_N} \tag{2.12}$$

where $i_1, i_2, ..$ etc. refer to the "auxiliary indices" (indices associated with a matrix) which are summed over. Incidentally, the Matrix Product State is known to be the exact solution of the Affleck-Kennedy-Lieb-Tasaki (AKLT) model for the spin-1 chain [42].

DMRG has no sign problem (unlike QMC), but is limited in its applicability to systems in high dimensions. The framework in terms of which this limitation of MPS/DMRG may be understood requires us to define the concept of "entanglement entropy" of a block,

$$\mathcal{S}_E = -\sum_i \lambda_i \ln(\lambda_i) \tag{2.13}$$

where λ_i refer to the eigenvalues of the reduced density matrix of a block ρ_B (see equation (2.10)).

The so called "boundary (area) law", states that the ground state entanglement entropy $\mathcal{S}_E$ of a real space block is proportional to its boundary (area) [11]. Hastings [43] has shown that the entanglement entropy captured by the MPS wavefunction is $O(\text{constant})$ and does not scale with the size of the block. In 1D this is not an issue: the boundary ("area") of a 1D block is just two points, but in higher dimensions that is not the case.

[11] In 2D "area" would refer to the perimeter of a block.

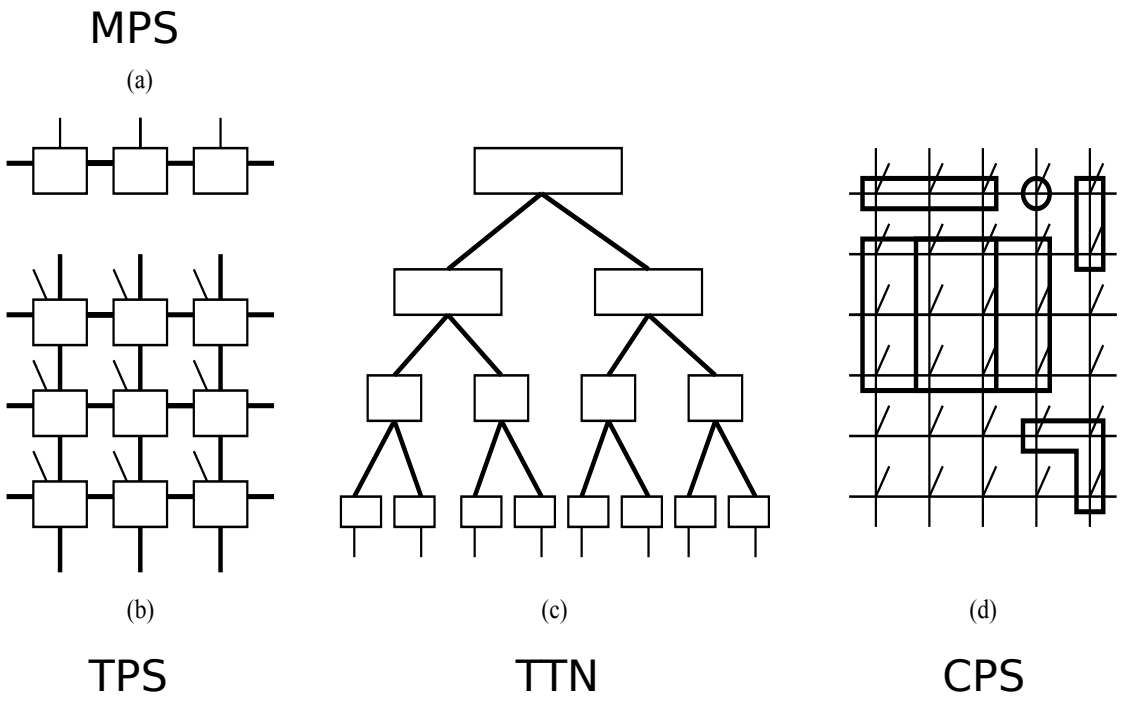

Figure 2.2: Some candidate variational wavefunctions. (a) Matrix Product state (b) Tensor Product state/ PEPS (c) Tree Tensor Network for a 1D system (d) Correlator Product state. For (a),(b),(c) the boxes represent variational tensors, which have a physical index (indicated by a line coming out of tensor) and auxiliary indices (thicker lines connecting tensors). In the case of (d), the lines coming out of the sites again represent a physical index whereas the boxes represent correlators (or variational Jastrow factors). Correlators could be of any shape and can overlap.

2.4 Tensor Network approaches

The idea that MPS is a good variational ansatz for a large class of 1D physical systems, brings up the natural question: what are the equivalents of the MPS wavefunction in high dimensions?

There has thus been a great surge of interest in exploring different ansätze for *higher* dimensional systems. These include the direct extensions of MPS to higher dimensions, namely the Projected Entanglement Pair states (PEPS) or tensor product states (TPS) proposed by Gendiar and Nishino [44] and inde-

pendently by Verstraete and Cirac [45] and Tree Tensor Networks (TTN) (for a review of these ansätze see the review by Cirac and Verstraete [46]), which may be best understood by the network of tensors illustrated in Figure 2.2 (b) and (c). One must note that the *tensors* are contracted (i.e. auxiliary indices are summed over) to obtain a *scalar* wavefunction coefficient.

Our own effort [47, 48] (see Chapter 3), along with other investigators [49, 50] has been in the application of extended Jastrow wavefunctions (on the lines of Marshall-Huse-Elser wavefunctions [51, 52]) to models of interacting spins and electrons on a lattice. These have been christened Correlator Product states (CPS), Entangled Product states (EPS) or Complete Graph Tensor network states (CGTN).

To illustrate the CPS ansatz, we give an example,

$$\begin{aligned} \psi_{CPS}^{s_1 s_2 \ldots\ldots s_N} &= \prod_{\{s\}} C^{\{s\}} \\ &= C^{s_1 s_2} C^{s_2 s_3} C^{s_1 s_3 s_4} \ldots\ldots \end{aligned} \tag{2.14}$$

where $C^{s_1 s_2}$ and $C^{s_2 s_3}$ are "pair correlators" and $C^{s_1 s_3 s_4}$ refers to a "triple correlator". Correlators could be of any "shape" i.e. correlate any sites of choice.

Note in particular that the CPS involves a product of scalars and has no auxiliary indices to sum over (i.e. no tensor network to contract), making its computation (for a given configuration) efficient.

In Figure 2.2, we have diagrammatically represented the MPS, TPS, TTN and CPS wavefunctions. We must appreciate that all these candidate wavefunctions ultimately reduce the exponential number of parameters describing the full wavefunction $\psi^{s_1 s_2 \ldots\ldots s_N}$, to a polynomial number.

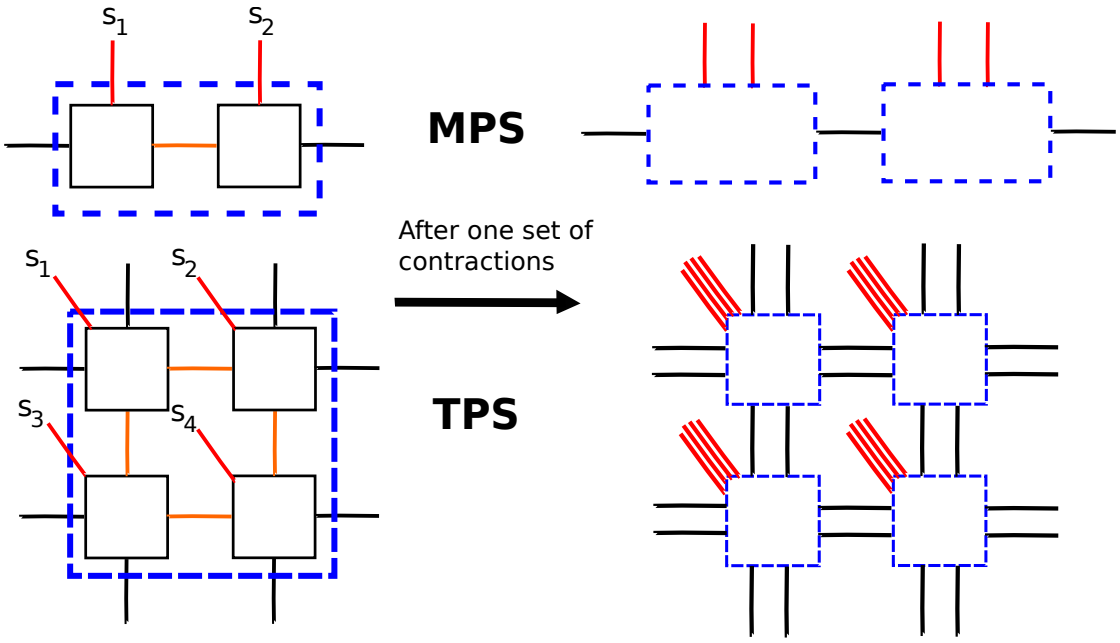

Figure 2.3: Contraction of MPS is efficient because the number of auxiliary indices does not increase on contracting two or more matrices. On the other hand, in the case of TPS, the number of auxiliary indices to sum over grows exponentially with the number of tensors involved in the contraction.

Another variational ansatz is a hierarchical tensor network (whose inherent structure is based on renormalization group ideas) known as the Multi-scale Entanglement Renormalization Ansatz (MERA) proposed by Vidal [53].

There are some clear challenges to be met for researchers in the field of tensor networks. On the algorithmic front, the main challenge is to find efficient approximations to contract tensors in polynomial time (see for example the problem with contracting a TPS exactly in Figure 2.3) to compute observables such as the energy. On the conceptual front, a big limitation seems to be that such wavefunctions cannot capture the free fermion limit very well because the entanglement entropy of the ground state does not satisfy the right "area law" [12].

[12]For free fermions, the entanglement entropy scales as $\mathcal{S}_E \sim L \log L$ versus $\mathcal{S}_E \sim L$ for the TPS, where L refers to the "area" (or perimeter for two dimensional systems) of the real space block of sites.

2.5 Dynamical Mean Field Theory

Up to this point, we have primarily seen methods which are based on computing or sampling wavefunctions. These methods have their merits, but they are ultimately restricted to ground (and some excited) states of finite systems. In addition, we have approached strongly correlated systems from the "atomic limit"; taking into account the fact that electrons are relatively localized in these cases. We would like to have a method that can *also* capture the limit where the electrons are delocalized. In fact, Density Functional Theory (DFT), which has been the workhorse for weakly correlated solids (such as band metals), works well in this limit. [13]

The Dynamical Mean Field Theory, developed by many researchers over the years (for a review see Kotliar et al. [54]), addresses these issues. It is capable of churning out the spectral information of the system in the thermodynamic limit and is formulated in a way that bridges the gap between the "atomic limit" and the "nearly free electron gas limit". The approach has been very successful for studying metal-insulator transitions in model and ab-initio Hamiltonians.

The idea is to consider a single site (or cluster of sites) - the so called "impurity", which is immersed in an effective medium or "bath" provided by the other sites. The main ingredient of DMFT then is to set up a *self-consistency* condition ensuring that the impurity Green's function and bath Green's function match up. In order to solve the self-consistency equations, one has to make an approximation that the lattice self energy is momentum *independent*. The main problem associated with this approximation is that it washes out all the spatial

[13] Although DFT is formally exact, the absence of good approximations to functionals for strongly correlated systems limits its use. Hence it has not been reviewed in this Chapter.

information about the system beyond the size of the cluster of sites chosen.

The author does not fully understand why application of DMFT to spin systems is limited (one DMFT study for a spin system is for Resonating Valence Bond Antiferromagnets by Georges et al. [55]): it would be interesting to see if there are avenues to be explored in this direction.

2.6 Outline of Part I of this thesis

In this Chapter, we have surveyed the numerical methods available in the literature and tried to highlight their strengths and weaknesses. This understanding will be instrumental in our appreciation of the remaining two chapters in Part I of this thesis.

In Chapter 3, I will present a published paper [47] on a class of Variational wavefunctions whose form extends the well known Jastrow wavefunctions. I will also outline some details of this work, not included in the published version, in the Appendices. Some results from the published paper [48] and some unpublished results have also been used in the main text of this Chapter.

In Chapter 4, I will discuss some of my published results [56] and unpublished work on a new projector Quantum Monte Carlo method christened "Semistochastic Quantum Monte Carlo" (or SQMC for short). The theory is a hybrid between stochastic (QMC) and deterministic projection (power method). Many of the the ideas and concepts used borrow from previous Monte Carlo approaches. The approach that is most relevant to this Chapter is called Full Configuration Interaction Quantum Monte Carlo (or FCIQMC for short) recently proposed by

Alavi and coworkers [57, 58].

2.A Lanczos algorithm

In the main text of this Chapter (section 2.1), we discussed the foundation of the exact diagonalization algorithm. Here we elaborate on one such method, the Lanczos algorithm [3]. Results obtained from this technique were useful for benchmarking numerical techniques discussed in this thesis (Chapter 3 and Chapter 4). The algorithm also forms a crucial part of the DMRG technique (see Chapter 7).

We remind the reader that the way this method works is by generating a basis of orthogonal vectors $\{v_i\}$ which span the 'Krylov' space,

$$\mathcal{K} = \{v_1, Hv_1, H^2v_1, ...H^{m-1}v_1\}, \tag{2.15}$$

and expressing the Hamiltonian H as a $m \times m$ matrix in this basis. This matrix is easier to diagonalize as m is much smaller than the size of the full Hilbert space.

We now give a brief outline of the workings of the Lanczos algorithm below, noting that the central steps are valid for Hermitian matrices only.

1. To begin with, we list out the complete set of 'configurations' i.e. all the basis elements of the full Hilbert space. This step involves generating only those states which have the right particle number or total S_z symmetry (this depends on the problem one is trying to solve).
2. Develop an efficient indexing scheme to determine where the configuration is located in the data structure being used to store the Hilbert space

vector.

For example, let us say that entry i of a C++ vector (representing the Hilbert space vector) corresponds to configuration $|\uparrow\downarrow\ 0\ \uparrow\rangle$. If one is given the configuration $|\uparrow\downarrow\ 0\ \uparrow\rangle$, determining its location i is an 'inverse problem', which in general is not easy to solve. Solutions to this problem include using an inverse map (for converting the integer representation of a configuration to an index), binary searching a sorted list and hashing functions (see for example Lin [59]).

3. Choose a random vector v_1 in the Hilbert space and normalize it. If a better guess is available (for example from a variational wavefunction), use it.

4. Consider the action of H on v_1 and project out the v_1 component from the resulting vector, and then normalize it, to get vector v_2 i.e.,

$$\alpha_1 \equiv \langle v_1|H|v_1\rangle \tag{2.16a}$$

$$w_1 = Hv_1 - \alpha_1 v_1 \tag{2.16b}$$

$$\beta_2 = \|w_1\| \tag{2.16c}$$

$$v_2 = \frac{w_1}{\beta_2} \tag{2.16d}$$

Observe that $\beta_2 = \langle v_2\,|w_1\,\rangle = \langle v_2|H|v_1\rangle - \langle v_2\,|v_1\,\rangle\,\langle v_1|H|v_1\rangle = \langle v_2|H|v_1\rangle$ where we have used the orthogonality of $|v_1\rangle$ and $|v_2\rangle$.

5. We will now show, by mathematical induction, that the Hamiltonian is tridiagonal in the Krylov basis.

Let us assume that n orthogonal Krylov basis vectors $\{v_i\}$ have been generated and that the Hamiltonian is tridiagonal in this basis. To expand the size of the basis by one vector, i.e. to obtain v_{n+1}, consider the action of H on v_n and project out successively the v_{n-1} and v_n components from

it. This idea is expressed by the Lanczos iteration step summarized in the equations below,

$$
\begin{aligned}
w_n &= H v_n - \beta_n v_{n-1} && \text{(2.17a)} \\
\alpha_n &\equiv \langle v_n \, | w_n \rangle = \langle v_n \, | H | v_n \rangle && \text{(2.17b)} \\
w_n &\rightarrow w_n - \alpha_n v_n \\
&= H v_n - \langle v_n | H | v_n \rangle v_n - \langle v_n | H | v_{n-1} \rangle v_{n-1} && \text{(2.17c)} \\
\beta_{n+1} &= \| w_n \| && \text{(2.17d)} \\
v_{n+1} &= \frac{w_n}{\beta_{n+1}} && \text{(2.17e)}
\end{aligned}
$$

As the above equations indicate, v_{n+1} is orthogonal to both v_{n-1} and v_n by construction. However, v_{n+1} is also orthogonal to all v_i, for $1 \leq i < n-1$. To see why this is so, consider equation (2.17c) and project it against v_i for i between 0 and n. After this action, equation (2.17c) reads as,

$$
\begin{aligned}
\langle v_i | v_{n+1} \rangle &\propto \langle v_i | w_n \rangle \\
&= \langle v_i | H | v_n \rangle - \langle v_n | H | v_n \rangle \langle v_i | v_n \rangle - \langle v_n | H | v_{n-1} \rangle \langle v_i | v_{n-1} \rangle && \text{(2.18)}
\end{aligned}
$$

Using the orthogonality of the basis i.e. $\langle v_i | v_{n-1} \rangle = 0$ and $\langle v_i | v_n \rangle = 0$ and the tridiagonal nature of H i.e. $\langle v_i | H | v_n \rangle = 0$ for $1 \leq i < n-1$, we conclude that the newly constructed vector v_{n+1} is orthogonal to all previous v_i.

We will now see that the Hamiltonian H remains tridiagonal on expanding the size of the basis. Since the $n \times n$ Hamiltonian is already assumed to be tridiagonal (as part of the induction process), it suffices to show that $\langle v_{n+1} | H | v_i \rangle = \langle v_i | H | v_{n+1} \rangle = 0$ for all i such that $1 \leq i \leq n-1$.

The proof is straightforward. Appreciate that (by construction) the Lanczos step ensures that $H v_i$ lies in the span of $\{v_j\}$ for $1 \leq j \leq i+1$. Thus $H v_i$ (for i from 1 to $n-1$) is orthogonal to v_{n+1} i.e. $\langle v_{n+1} | H | v_i \rangle = 0$. From the Hermiticity of the Hamiltonian it follows that $\langle v_i | H | v_{n+1} \rangle = 0$ as well.

(To formally complete the proof by induction, we need to verify that the first two Krylov vectors are orthogonal to each other and the Hamiltonian in the 2x2 basis is tridiagonal. The former has already been shown to be the case in the preceding point and the latter is true for any 2x2 matrix.)

6. It is a well understood problem in the literature, that owing to round off errors (due to finite machine precision), the Krylov vectors lose their orthogonality. Thus an additional check for orthogonality is needed. If this check fails, we explicitly reorthogonalize the new Krylov vector with respect to all previously obtained vectors by projecting out their components i.e.

$$w_j \rightarrow w_j - \sum_{i=1}^{j} \langle v_i | w_j \rangle \, v_i \tag{2.19a}$$

$$v_{j+1} = \frac{w_j}{\beta_{j+1}} \tag{2.19b}$$

7. If the above procedure does not yield a vector w_j with sufficiently large norm, it means we have generated a number of vectors as large as the size of the space or some closed subspace of it. In that case, we start with another random vector that is orthogonal to all others previously generated.

8. At the end of m iterations, we obtain the tridiagonal matrix T, representing the Hamiltonian in the basis of $v_1, v_2, ...v_m$ (spanning the Krylov space)

$$T = \begin{pmatrix} \alpha_1 & \beta_2 & & & & \\ \beta_2 & \alpha_2 & \beta_3 & & & \\ & \beta_3 & \ldots & & & \\ & & & \ldots & & \\ & & & & \alpha_{m-1} & \beta_m \\ & & & & \beta_m & \alpha_m \end{pmatrix} \tag{2.20}$$

and diagonalize it directly (using LAPACK routine) to obtain the eigenvalues and eigenvectors.

9. If needed, compute the eigenvectors of H, from the eigenvectors of T and the Krylov vectors $V = (v_0\ v_1\ v_2....v_{m-1})$ by using,

$$y = Vu \tag{2.21}$$

where y are the eigenvectors of H and u are the eigenvectors of T.

10. The Lanczos method cannot resolve degeneracies. In order to overcome this limitation, one could use the Band Lanczos or Block Lanczos algorithms or the Jacobi-Davidson algorithm (for an overview of the methods mentioned here refer to the book [3]).

    However, we do something much simpler. Once we have obtained an eigenstate e to a desired accuracy, we restart the Lanczos with a new random vector and make sure that the new Krylov space generated from it is orthogonal to e. To do so, we simply project out e from each Krylov space vector.

2.B Metropolis algorithm

Since Variational Monte Carlo is crucial to the understanding of Chapter 3, I will give an introduction to the algorithm and the principle of *detailed balance* which is central to the method [14].

Consider all the states of the classical or quantum system under consideration. We label them as $a_0, a_1....a_n$. Let us also label the probability of the system

[14] I first learnt how detailed balance works from the pedagogical review of Krauth [60].

being in state a_i to be $\pi(a_i)$: for a quantum system $\pi(a_i) = |\psi(a_i)|^2$.

Imagine a dynamics associated with sampling the states of this system that takes the system from one state to the other. There are no restrictions on what this dynamics is, as long as it ensures that each state a_i is visited a fraction of the time proportional to its probability $\pi(a_i)$. This condition subsumes the requirement that the system must be able to make a transition from one state to any other in a finite number of steps i.e. the dynamics must be *ergodic*.

The transition probability for going from state a_i to state a_j will be labelled as $p(a_i \to a_j)$ and our objective is to derive a mathematical condition for $p(a_i \to a_j)$ in terms of $\pi(a_i)$ and $\pi(a_j)$.

We will also attach a time label t to the probability $\pi(a_i)$ i.e.

$$\pi(a_i) \to \pi(a_i, t) \tag{2.22}$$

to make our interpretation of the dynamical process concrete. Eventually, we will drop the time label all together.

To derive this condition, we first write an expression for $\pi(a_i)$. To be in state a_i at time t,

1. The system can either be in state a_i at time t-1 and remain there;
2. or make a transition from some other state a_j ($a_j \neq a_i$) to state a_i.

Thus we have,

$$\pi(a_i, t) = \pi(a_i, t-1)p(a_i \to a_i) + \sum_j \pi(a_j, t-1)p(a_j \to a_i) \tag{2.23}$$

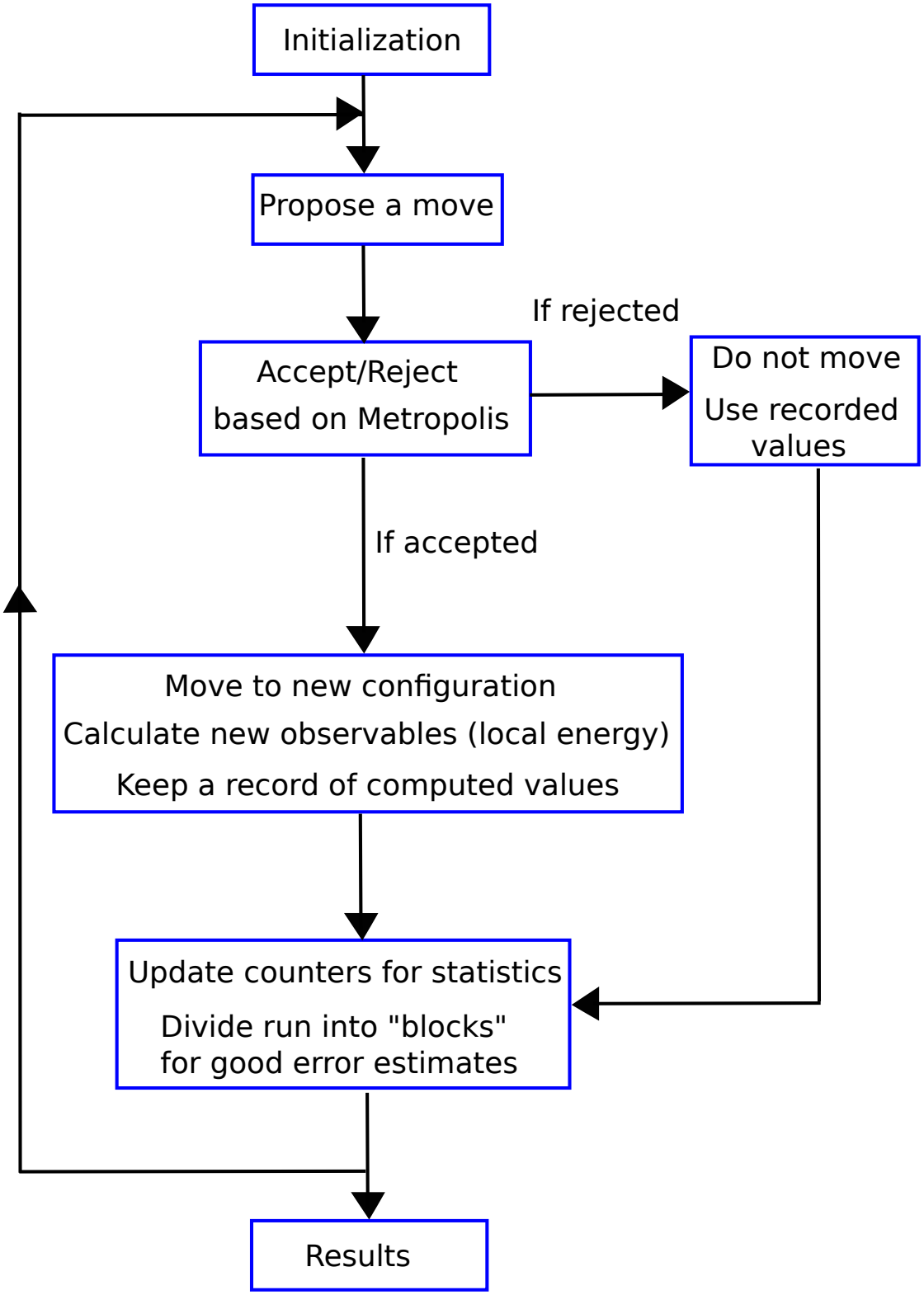

Figure 2.4: A flow chart for Variational Monte Carlo

Dropping the time dependence from equation (2.23) and rearranging terms we get,

$$\pi(a_i)(1 - p(a_i \to a_i)) = \sum_j \pi(a_j)p(a_j \to a_i) \tag{2.24}$$

Noting that the sum of transition probabilities out of state a_i must equal 1 i.e. $\sum_j p(a_j \to a_i) = 1$, we recast equation (2.24) as,

$$\pi(a_i) \sum_{j \neq i} p(a_i \to a_j) = \sum_j \pi(a_j)p(a_j \to a_i) \tag{2.25}$$

Equation (2.25) is called the *stationarity condition*. However, we may demand a more stringent condition by forcing each term on the left to equal the ones on the right, i.e.

$$\pi(a_i)p(a_i \to a_j) = \pi(a_j)p(a_j \to a_i) \tag{2.26}$$

This equation (2.26) is known as the condition of *detailed balance*. It tells us that if the probability of being at a_i is larger than the probability of being at a_j then the transition probability $p(a_i \to a_j)$ must be smaller than $p(a_j \to a_i)$.

We may now choose a form for $p(a_i \to a_j)$ which explicitly satisfies equation (2.26). One such choice is used in the Metropolis algorithm [61] [15],

$$p(a_i \to a_j) = \min\left(1, \frac{\pi(a_j)}{\pi(a_i)}\right) \tag{2.27}$$

2.C Relationship of Matrix Product States to DMRG

In this Chapter (section 2.4), I asked the reader to take a leap of faith when I said that the one dimensional Matrix product state is a variational wavefunction whose (optimal) parameters are effectively obtained by the DMRG procedure.

[15] This choice of $p(a_i \to a_j)$ is one of the simplest forms of the Metropolis algorithm.

This connection is not *apriori* obvious and was the subject of a paper by Ostlund and Rommer [41].

To understand the connection, we need to develop the concept of basis transformations involved in the DMRG (and more generally in any sort of real space RG) procedure. (The reader should also note that the *details* of the DMRG are not crucial here. These details will be formally discussed in Chapter 7 of this thesis where the one dimensional DMRG has been generalized to tree graphs.)

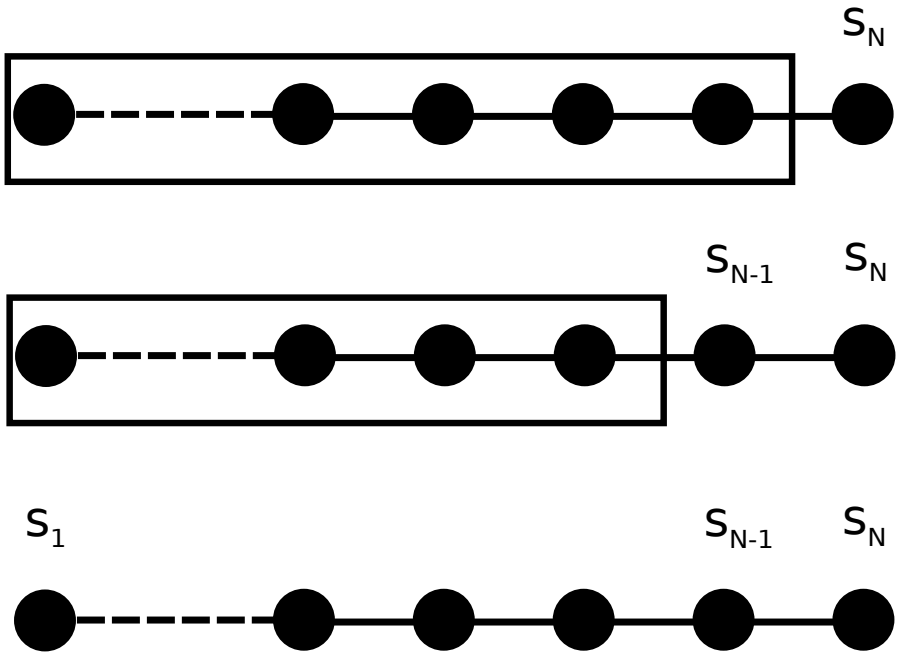

Figure 2.5: Basis transformations recursively carried out to illuminate the connection between the Matrix Product State and the Renormalization Group. For details refer to the text.

Assume we have a set of basis states (not necessarily a complete set) on a block of $n-1$ sites, which we label as $|\alpha_{n-1}\rangle$. Consider the addition of one extra site to this system with a local Hilbert space having d degrees of freedom and labelled by $|s_n\rangle$. The wavefunctions for the n site system (labelled by $|\alpha_n\rangle$) are

expressed by performing a transformation,

$$|\alpha_n\rangle = \sum_{\alpha_{n-1},s_n} A^{\alpha_n}_{\alpha_{n-1},s_n}|\alpha_{n-1}\rangle|s_n\rangle \tag{2.28}$$

We can think of the object $A^{\alpha_n}_{\alpha_{n-1},s_n}$ as a matrix with one index $\{\alpha_n\}$ and the other index to be the compound index $\{\alpha_{n-1}, s_n\}$. If the transformation from $|\alpha_{n-1}\rangle|s_n\rangle \rightarrow |\alpha_n\rangle$ is a 'rotation of the basis', A is a unitary matrix. If the transformation is a 'renormalization' i.e. there is a loss of information, A is a map from $d \times D$ states (corresponding to the number of possibilities for $\{\alpha_{n-1}, s_n\}$) to (say) D states (corresponding to the number of possibilities for $|\alpha_n\rangle$). In this case A is a $D \times (dD)$ matrix.

Note that without any loss of generality, the elements of $A^{\alpha_n}_{\alpha_{n-1},s_n}$ can be rearranged to give it the form,

$$A^{\alpha_n}_{\alpha_{n-1},s_n} \rightarrow A^{s_n}_{\alpha_n,\alpha_{n-1}} \tag{2.29}$$

$A^{s_n}_{\alpha,\alpha_{n-1}}$ has now taken the form of a $d \times (D^2)$ matrix. The motivation for performing this rearrangement of indices will soon become apparent.

Now we consider the basis states $|\alpha_{n-1}\rangle$ and rewrite them in terms of $|\alpha_{n-2}\rangle|s_{n-1}\rangle$. This transformation may be written just like equation (2.28), and the indices of the transformation matrix can be rearranged (as in (2.29)),

$$|\alpha_{n-1}\rangle = \sum_{\alpha_{n-2},s_{n-1}} A^{s_{n-1}}_{\alpha_{n-1},\alpha_{n-2}}|\alpha_{n-1}\rangle|s_n\rangle \tag{2.30}$$

Performing a sequence of basis transformations (such as those in equations (2.28) and (2.30)), we get,

$$|\Psi\rangle = \sum_{s_1,s_2,....s_n} \left(\sum_{\alpha_{n-1},\alpha_{n-2}...} A^{s_{n-1}}_{\Psi,\alpha_{n-1}} A^{s_{n-1}}_{\alpha_{n-1},\alpha_{n-2}} ....A^{s_1}_{\alpha_1,\alpha_0} \right) |s_1\rangle|s_2\rangle....|s_n\rangle \tag{2.31}$$

which corresponds to a Matrix Product State.

BIBLIOGRAPHY

[1] H. Bethe, Zeitschrift für Physik A Hadrons and Nuclei **71**, 205 (1931).

[2] E. H. Lieb and F. Y. Wu, Phys. Rev. Lett. **20**, 1445 (1968).

[3] *Templates for the Solution of Algebraic Eigenvalue Problems: a Practical Guide* Z.Bai, J. Demmel, J. Dongarra, A. Ruhe, and H. van der Vorst, Society for Industrial and Applied Mathematics (2000).

[4] A. Laüchli, APS March Meeting, Boston, MA, USA (2012). This work is unpublished.

[5] W. M. C. Foulkes, L. Mitas, R. J. Needs, and G. Rajagopal, Rev. Mod. Phys. **73**, 33 (2001).

[6] *Quantum Monte Carlo Methods in Physics and Chemistry*, *NATO ASI Ser. C 525*, edited by M. P. Nightingale and C. J. Umrigar (Kluwer, Dordrecht, 1999).

[7] W. L. McMillan, Phys. Rev. **138**, A442 (1965).

[8] D. Ceperley, G. V. Chester, and M. H. Kalos, Phys. Rev. B **16**, 3081 (1977).

[9] C. J. Umrigar, K. G. Wilson, and J. W. Wilkins, Phys. Rev. Lett. **60**, 1719 (1988).

[10] J. Toulouse and C. J. Umrigar, J. Chem. Phys. **126**, 084102 (2007).

[11] J. Toulouse and C. J. Umrigar, J. Chem. Phys. **128**, 174101 (2008).

[12] C. J. Umrigar *et al.*, Phys. Rev. Lett. **98**, 110201 (2007).

[13] E. Neuscamman, C. J. Umrigar, and G. K.-L. Chan, Phys. Rev. B **85**, 045103 (2012).

[14] M. H. Kalos, Phys. Rev. **128**, 1791 (1962).

[15] J. B. Anderson, The Journal of Chemical Physics **63**, 1499 (1975).

[16] R. Blankenbecler and R. L. Sugar, Phys. Rev. D **27**, 1304 (1983).

[17] N. Trivedi and D. M. Ceperley, Phys. Rev. B **40**, 2737 (1989); N. Trivedi and D. M. Ceperley, Phys. Rev. B **41**, 4552 (1990).

[18] D. M. Ceperley, Rev. Mod. Phys. **67**, 279 (1995).

[19] R. Blankenbecler, D. J. Scalapino, and R. L. Sugar, Phys. Rev. D **24**, 2278 (1981).

[20] J. E. Hirsch, Phys. Rev. B **28**, 4059 (1983).

[21] S. Zhang, J. Carlson, and J. E. Gubernatis, Phys. Rev. Lett. **74**, 3652 (1995).

[22] S. Zhang, J. Carlson, and J. E. Gubernatis, Phys. Rev. B **55**, 7464 (1997).

[23] M. Troyer and U.-J. Wiese, Phys. Rev. Lett. **94**, 170201 (2005).

[24] J. B. Anderson, The Journal of Chemical Physics **65**, 4121 (1976).

[25] D. M. Ceperley and B. J. Alder, Phys. Rev. Lett. **45**, 566 (1980).

[26] C. J. Umrigar, M. P. Nightingale, and K. J. Runge, J. Chem. Phys. **99**, 2865 (1993).

[27] H. J. M. van Bemmel *et al.*, Phys. Rev. Lett. **72**, 2442 (1994).

[28] K. G. Wilson, Rev. Mod. Phys. **47**, 773 (1975).

[29] L.P. Kadanoff, Physics, 2, 263 (1966).

[30] M. Indergand et al., Phys. Rev. B74, 064429 (2006).; E. Rico, cond-mat/0601254; P. Li and S.Q. Shen, Phys. Rev. B71, 212401 (2005); M.A. Hajj and J.P. Malrieu, Phys. Rev. B72, 094436 (2005); M.A. Hajj et al., Phys. Rev. B70 094415 (2004); R. Budnik and A. Auerbach, Phys. Rev. Lett. 93, 187205 (2004); D. Poilblanc et al., Phys. Rev. B69, 220406 (2004); D. Poilblanc, D. J. Scalapino and S. Capponi, Phys. Rev. Lett. 91, 137203 (2003); H. Mueller, J. Piekarewicz and J.R. Shepard, Phys. Rev. C66, 024324 (2002).

[31] J.-P. Malrieu and N. Guihéry, Phys. Rev. B **63**, 085110 (2001).

[32] S. R. White and R. M. Noack, Phys. Rev. Lett. **68**, 3487 (1992).

[33] S. R. White, Phys. Rev. Lett. **69**, 2863 (1992).

[34] U. Schollwöck, Rev. Mod. Phys. **77**, 259 (2005).

[35] K. A. Hallberg, Advances in Physics **55**, 477 (2006).

[36] G. K-L Chan, J. J. Dorando, D. Ghosh, J. Hachmann, E. Neuscamman, H. Wang, T. Yanai, arXiv:0711.1398 (2007).

[37] E. Stoudenmire and S. R. White, Annual Review of Condensed Matter Physics **3**, 111 (2012).

[38] S. Yan, D. A. Huse, and S. R. White, Science **332**, 1173 (2011).

[39] H.-C. Jiang, H. Yao, and L. Balents, Phys. Rev. B **86**, 024424 (2012).

[40] E. Jeckelmann, D. J. Scalapino, and S. R. White, Phys. Rev. B **58**, 9492 (1998).

[41] S. Östlund and S. Rommer, Phys. Rev. Lett. **75**, 3537 (1995).

[42] I. Affleck, T. Kennedy, E. H. Lieb, and H. Tasaki, Phys. Rev. Lett. **59**, 799 (1987).

[43] M. B. Hastings, Phys. Rev. B **76**, 035114 (2007).

[44] A. Gendiar and T. Nishino, Phys. Rev. E **65**, 046702 (2002).

[45] F. Verstraete, J. I. Cirac, arXiv:cond-mat/0407066.

[46] J. I. Cirac and F. Verstraete, Journal of Physics A: Mathematical and Theoretical **42**, 504004 (2009).

[47] H. J. Changlani, J. M. Kinder, C. J. Umrigar, and G. K.-L. Chan, Phys. Rev. B **80**, 245116 (2009).

[48] E. Neuscamman, H. Changlani, J. Kinder, and G. K.-L. Chan, Phys. Rev. B **84**, 205132 (2011).

[49] F. Mezzacapo, N. Schuch, M. Boninsegni, and J. I. Cirac, New J. Phys. **11**, 083026 (2009), the ansatz considered here has the same form as the CPS.

[50] K. H. Marti *et al.*, New Journal of Physics **12**, 103008 (2010).

[51] D. A. Huse and V. Elser, Phys. Rev. Lett. **60**, 2531 (1988).

[52] C. L. Henley and B. E. Larson, J. Appl. Phys. **67**, 5752 (1990).

[53] G. Vidal, Phys. Rev. Lett. **101**, 110501 (2008).

[54] G. Kotliar *et al.*, Rev. Mod. Phys. **78**, 865 (2006).

[55] A. Georges, R. Siddharthan, and S. Florens, Phys. Rev. Lett. **87**, 277203 (2001).

[56] F. R. Petruzielo, A. A. Holmes, H. J. Changlani, M. P. Nightingale, C. J. Umrigar, arXiv:1207.6138, accepted for publication in *Physical Review Letters* (2012).

[57] G. H. Booth, A. J. W. Thom, and A. Alavi, J. Chem. Phys. **131**, 054106 (2009).

[58] D. Cleland, G. H. Booth, and A. Alavi, J. Chem. Phys. **132**, 041103 (2010).

[59] H. Q. Lin, Phys. Rev. B **42**, 6561 (1990).

[60] W. Krauth, Statistical Mechanics: Algorithms and Computations, Oxford University Press (US),2006. Parts of this book were earlier available as a set of pedagogical notes.

[61] N. Metropolis *et al.*, The Journal of Chemical Physics **21**, 1087 (1953).

CHAPTER 3

CORRELATOR PRODUCT STATES (CPS)

The text in this Chapter has been adapted from the paper by H. J. Changlani, J. M. Kinder, C. J. Umrigar and G. K. -L. Chan published in Physical Review B [1]. Some perspectives (section 3.3 .6 and all the Appendices) and unpublished results (Table 3.2 and Table 3.4) have been added after publication. In addition, some published results (Table 3.5) from the paper by E. Neuscamman, H. Changlani, J. Kinder and G. K.-L. Chan [2] have been added to this Chapter. I am grateful to J. Richter for sharing his Exact Diagonalization results for the 6x6 $J_1 - J_2$ model.

3.1 Introduction

How can one efficiently approximate an eigenstate of a strongly correlated quantum system? In one-dimensional systems, the density matrix renormalization group (DMRG) provides a powerful and systematic numerical approach [3, 4]. However, the accuracy of the DMRG in two or more dimensions is limited by the one-dimensional encoding of correlations in the matrix product states (MPS) that form the variational basis of the DMRG [4]. Generalizations of MPS to higher dimensions — tensor network or tensor product states (TPS) [5, 6, 7, 8, 9, 10] — have been introduced recently, but these engender considerable computational complexity (which does *not* arise with MPS). This has made it difficult to practically extend the success and accuracy of the DMRG to higher dimensions.

In this Chapter we examine a different class of quantum states: *correlator*

product states (CPS). Unlike MPS and TPS, which introduce auxiliary degrees of freedom to generate correlations between physical degrees of freedom, CPS correlate the physical degrees of freedom explicitly. The CPS form has been rediscovered many times [11, 12, 13] but the potential of CPS as an alternative to MPS/TPS for systematically approximating strongly correlated problems remains largely unexplored. Here we take up this possibility. CPS share many of the local properties of MPS/TPS but appear more suitable for practical calculations in more than one dimension as well as for fermion systems.

To establish the potential of CPS, we analyze the relation between CPS and common families of analytic and numerical trial wave functions. We then discuss the most important properties of CPS: they permit efficient evaluation of observables and efficient optimization. Finally, we present variational Monte Carlo calculations for both spin and fermion systems. Our CPS results compare favorably with calculations using other variational wave functions that contain a similar number of variational parameters.

Note: As the original manuscript was completed we were informed of recent work by Isaev *et al.* on hierarchical mean-field theory [14] and by Mezzacapo *et al.* on entangled plaquette states [15] as well as earlier work on string-bond states [16]. All these studies consider wave functions similar to CPS and share many of our own objectives. However, while our current efforts are related, especially to Ref. [15], we focus on aspects of CPS not addressed in these other works, such as the relationship with well-known analytical and numerical wave functions, and we consider different physical problems, such as fermion simulations. Thus we regard our work as complementary rather than overlapping.

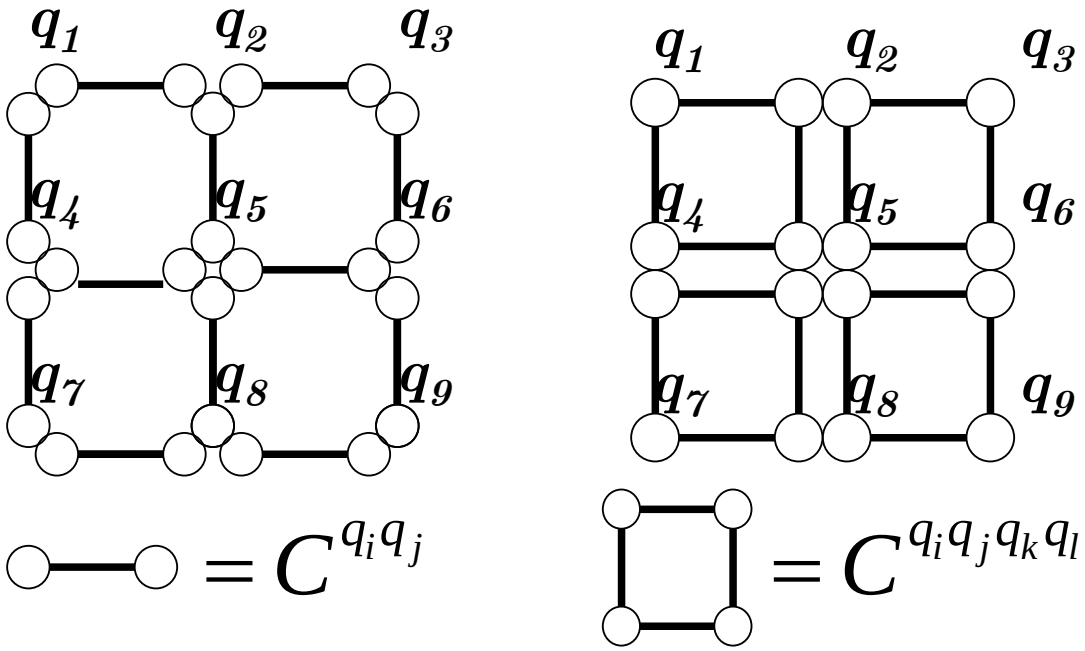

Figure 3.1: Nearest-neighbor 2-site and 2×2 plaquette CPS on a 2D lattice. The CPS weight for a given quantum configuration $|q_1 q_2 \dots q_L\rangle$ is obtained by multiplying correlator coefficients together as in Eq. (3.2)

.

3.2 Correlator Product States

Consider a set of quantum degrees of freedom $Q \equiv \{q_1, q_2 \dots q_L\}$ on a lattice with L sites in one or more dimensions. Each q_i might represent a spin $S = 1/2$ degree of freedom, where $q \in \{\uparrow, \downarrow\}$, or a fermion degree of freedom, in which case $q \in \{0, 1\}$. An arbitrary quantum state can be expanded over all configurations as

$$|\Psi\rangle = \sum_{\{q\}} \Psi^{q_1 q_2 \dots q_L} |q_1 q_2 \dots q_L\rangle. \tag{3.1}$$

A general quantum wave function requires an exponential number of parameters — one for each configuration. One way to reduce the complexity of the problem is to impose some structure on the coefficients $\Psi(Q)$. Correlator product states (CPS) are one example of this approach.

CPS are obtained by associating variational degrees of freedom directly with correlations between groups of sites. For example, in the nearest-neighbor 2-site CPS, a correlator is associated with each neighboring pair of sites:

$$|\Psi\rangle = \sum_{\{q\}} \prod_{\langle ij \rangle} C^{q_i q_j} |q_1 \dots q_L\rangle, \tag{3.2}$$

where $\langle ij \rangle$ denotes nearest neighbors. The coefficients in Eq. (3.1) are given by products of correlator coefficients. For example, in a one-dimensional lattice, the amplitude of a configuration is

$$\Psi(Q) = C^{q_1 q_2} C^{q_2 q_3} C^{q_3 q_4} \dots C^{q_{L-1} q_L}. \tag{3.3}$$

Eq. (3.2) can be extended to higher dimensions simply by associating correlators with (overlapping) bonds on the lattice (Fig. 3.1). The nearest-neighbor 2-site CPS is an extremely simple CPS. Longer range correlations can be introduced by removing the nearest neighbor restriction on pair correlations or by including explicit correlations among more sites with correlators such as $C^{q_1 q_2 q_3}$. It is clear that CPS in principle are capable of providing a complete basis to express any wavefunction: in the limit of L-site correlators, the CPS amplitudes are precisely the coefficients of Eq. (3.1). (Since this regime is clearly not achievable one hopes that the convergence with the size of the correlator is rapid.)

When there is a global constraint on the total spin S or particle number N we can use projected CPS wave functions. For example, for fixed particle number, the N-projected nearest-neighbor 2-site CPS is

$$|\Psi\rangle = \sum_{\{q\}} \prod_{\langle ij \rangle} C^{q_i q_j} \hat{P}_N |q_1 \dots q_L\rangle, \tag{3.4}$$

where $\hat{P}_N$ ensures that $\sum_i q_i = N$. Such projections do not introduce any complications in working with CPS and may be included in both deterministic and stochastic calculations without difficulty.

It is sometimes useful to write the CPS in a different form. Each correlator element $C^{q_i q_j}$ can be viewed as the matrix element of a correlator operator $\hat{C}^{ij}$ that is diagonal in the quantum basis $\{|q_i q_j\rangle\}$:

$$\langle q_i q_j | \hat{C}^{ij} | q_i' q_j' \rangle = \delta_{q_i q_i'} \delta_{q_j q_j'} C^{q_i q_j}. \tag{3.5}$$

The CPS wave function is obtained by acting a string of commuting correlator operators on a reference state $|\Phi\rangle$. For example, a 2-site CPS may be written as

$$|\Psi\rangle = \prod_{i>j} \hat{C}^{ij} |\Phi\rangle. \tag{3.6}$$

When there are no constraints, the reference state is taken to be an equally weighted sum over all quantum configurations:

$$|\Phi\rangle = \sum_{\{q\}} |q_1 q_2 \dots q_L\rangle \tag{3.7}$$

otherwise, $|\Phi\rangle$ is projected to satisfy the constraint. For example, if particle number is fixed, $|\Phi_N\rangle$ is an equally weighted sum over all quantum configurations with particle number N,

$$|\Phi_N\rangle = \sum_{\{q\}} \hat{P}_N |q_1 q_2 \dots q_L\rangle. \tag{3.8}$$

Note that both projectors and correlators are diagonal operators in the Hilbert space and commute with one another: this means that the projection can be applied directly to the reference state and this simplifies numerical algorithms using CPS. The operator representation is also useful when considering extensions to the CPS form such as alternative reference states.

3.3 Connection to Other Wave Functions

Many strongly correlated quantum states can be represented exactly as correlator product states. CPS also have much in common with several classes of widely used variational wave functions: matrix product states, tensor product states, and resonating valence bond states. In this section, we discuss the connections between these wave functions.

3.3 .1 Huse-Elser wave functions

In their study of frustrated spin systems, Huse and Elser constructed states in which the quantum amplitudes $\Psi(Q)$ correspond to classical Boltzmann weights $\exp(-\beta E[Q]/2)$ multiplied by a complex phase [12]. The weights are derived from an effective classical Hamiltonian $\hat{H}^{cl}$. For example, in the case of pairwise correlations, $\hat{H}^{cl} = \sum_{ij} \hat{h}^{cl}_{ij}$ with $\hat{h}^{cl}_{ij} = K_{ij}\hat{S}^i_z\hat{S}^j_z$. The corresponding wave function can be represented as a 2-site CPS with $\hat{C}^{ij} = \exp(-\beta\hat{h}^{cl}_{ij}/2 + i\hat{\phi}_{ij})$ where $\hat{\phi}_{ij}$ assigns a complex phase to the pair ij.

For the square and triangular Heisenberg lattices, Huse and Elser demonstrated that a very compact variational ground-state could be obtained with a semi-analytic three-parameter model for $\hat{H}^{cl}$ (containing up to 3-site interactions) and an analytically determined phase. Although CPS can represent such highly constrained wave functions for symmetric systems, it can also serve as the foundation of a more general numerical method. By allowing correlators to vary freely and by considering hierarchies of larger correlated clusters, we can hope to construct rapidly converging approximations to *arbitrary* strongly

correlated quantum states, as the DMRG does for one-dimensional quantum problems.

3.3 .2 Laughlin wave function

In 1983, Laughlin proposed a variational wave function to explain the fractional quantum Hall effect [17]. The Laughlin wave function describes a strongly interacting system with topological order. Like the Huse and Elser wave functions, Laughlin's wave function can be associated with the Boltzmann weights of an effective classical Hamiltonian and can be represented exactly as a correlator product state.

The Laughlin quantum Hall state at filling fraction $1/m$ can be written in first quantization as

$$\Psi(\mathbf{r}_1, \ldots \mathbf{r}_N) = \prod_{\lambda<\mu}^{N} (z_\lambda - z_\mu)^m e^{-\alpha \sum_\kappa |z_\kappa|^2} \tag{3.9}$$

where z_λ is the (complex) coordinate of particle λ. (A Greek subscript indicates the coordinate of a particular electron. A Roman subscript indicates the coordinate of a lattice site.) Alternatively, the system can be mapped onto a *discrete* set of coordinates $z_1, \ldots, z_L$ with an associated set of occupation numbers $q_1, \ldots, q_L$. Then Eq. (3.9) can be exactly expressed as a 2-site CPS in the occupation number

representation

$$|\Psi\rangle = \sum_{\{q\}} \prod_i C_1^{q_i} \prod_{i<j} C_2^{q_i q_j} \hat{P}_N |q_1 \dots q_L\rangle \tag{3.10}$$

$$\mathbf{C_1} = \begin{pmatrix} 1 \\ e^{-\alpha|z_i|^2} \end{pmatrix} \tag{3.11}$$

$$\mathbf{C_2} = \begin{pmatrix} 1 & 1 \\ 1 & (z_i - z_j)^m \end{pmatrix} \tag{3.12}$$

The CPS wave function exactly reproduces the Laughlin wave function. It is, in some ways, more general than Eq. (3.9). The CPS form could be used to extend the Laughlin state beyond 2-site correlators while maintaining antisymmetry of the state, or to find a better variational energy in open or disordered systems.

3.3 .3 Toric code

Kitaev's toric code is another interesting quantum state with an exact CPS representation. Kitaev proposed the toric code as a model for topological quantum computing. The Hamiltonian is a sum of site and plaquette projectors on a square lattice with spins placed on the bonds. On a torus, the ground state of this Hamiltonian is 4-fold degenerate with a gap to all other excitations [18]. It is an example of a quantum system with topological order.

The ground state can be obtained from the zero-temperature Boltzmann weights of a classical Hamiltonian $\hat{H}^{cl}_{\text{toric}} = \sum_{\square_i} \hat{h}_{\square_i}$. The sum is over all plaquettes $\square_i$, and $\hat{h}_{\square_i}$ is a product of $\hat{S}_z$ operators associated with the spins on the edges of the plaquette [6]. The amplitudes of the toric code wave function can be generated

by a CPS with plaquette correlators:

$$C_{\square}^{ijkl} = \begin{cases} 1 & \text{if } S_z^i S_z^j S_z^k S_z^l > 0, \\ 0 & \text{if } S_z^i S_z^j S_z^k S_z^l < 0. \end{cases} \tag{3.13}$$

The exact representation of the toric code and Laughlin's wave function demonstrate the ability of CPS to describe systems with topological order.

3.3 .4 MPS and TPS

Correlator product states are conceptually related to matrix and tensor product states. All of these wave functions can easily express entanglement between local degrees of freedom. Nonetheless, CPS and MPS/TPS form different classes of quantum states and one is not a proper subset of the other.

A matrix product state (MPS) is obtained by approximating the quantum amplitudes $\Psi(Q)$ in Eq. (3.1) as a product of matrices, one for each site on the lattice:

$$\Psi(Q) = \sum_{\{i\}} A_{i_1 i_2}^{q_1} A_{i_2 i_3}^{q_2} \dots A_{i_L i_1}^{q_L} \tag{3.14}$$

The "auxiliary" indices $\{i\}$ are contracted in a one-dimensional pattern — a matrix product — and this gives rise to the low computational cost of working with MPS. However, the one-dimensional structure prevents MPS from efficiently describing correlations in higher dimensions. Tensor product states (TPS) extend MPS by approximating the amplitudes $\Psi(Q)$ by more general tensor contractions. Because of the more complicated contraction pattern, TPS can in principle describe higher dimensional correlations [6, 8, 9]. Unlike MPS, the

TPS contraction *cannot* be evaluated efficiently in general. This leads to the high computational cost of working with TPS.

To demonstrate the relationship between CPS and MPS/TPS, we consider a simple example of a nearest-neighbor 2-site CPS, for a chain of length 3 with periodic boundary conditions. The full wavefunction for this three-site system may be written in terms of the CPS amplitudes,

$$\Psi^{q_1 q_2 q_3} = C^{q_1 q_2} C^{q_2 q_3} C^{q_3 q_1} \tag{3.15}$$

Applying singular value decomposition to one of the correlators gives

$$C^{qq'} = \sum_i U_i^q \sigma_i V_i^{q'} = \sum_i U_i^q W_i^{q'}, \tag{3.16}$$

where we have absorbed the diagonal matrix σ_i into $W_i^{q'}$. With this decomposition, $|\Psi\rangle$ can be mapped to a MPS of auxiliary dimension 2:

$$\Psi^{q_1 q_2 q_3} = \sum_{\{i\}} U_{i_1}^{q_1} \left(W_{i_1}^{q_2} U_{i_2}^{q_2}\right) \left(W_{i_2}^{q_3} U_{i_3}^{q_3}\right) W_{i_3}^{q_1}. \tag{3.17}$$

This is equivalent to Eq. (3.14) with $A_{ij}^q = W_i^q U_j^q$. The matrices of the resulting MPS (of dimension 2) have a restricted form. More complicated CPS (e.g., with 3-site correlators) map to MPS with larger auxiliary dimension and more flexible forms for the matrices. (The dimension of the matrices grows exponentially with the range or number of sites in the correlator.) An *arbitrary* MPS cannot be mapped onto a CPS with less than the complete basis of L-site correlators. Conversely, a one-dimensional CPS with *long-range* correlators (such as the general 2-site CPS used in the Laughlin state) can only be represented by a MPS with an auxiliary dimension that spans the full Hilbert space. These arguments can be extended to higher dimensions and similar conclusions hold for the mappings between CPS and TPS. For a given number of variational degrees of freedom, only a subset of CPS can be exactly written as MPS/TPS and vice versa.

While the correlators in the CPS have no auxiliary indices, they could be augmented by additional auxiliary indices. For example, string-bond states may be considered one-site correlators with a pair of auxiliary indices [16]. n-site correlators can be generalized in an analogous way.

The concept of an area (boundary) law is sometimes used in the analysis of many-body wave functions. If the amount of entanglement (refer to Chapter 2) between a system and its environment scales with the "area" of the boundary between the two, the system is said to obey an area (boundary) law.

Arguments from quantum information theory suggest that wave functions that satisfy a boundary law can accurately describe systems (in any dimension) with a finite correlation length [19] (Some critical systems with long-range correlations also satisfy a boundary law, but others may violate the boundary law at zero temperature.)

MPS wave functions satisfy a one-dimensional boundary law and have a finite correlation length. (Long-range correlations can be reproduced over a finite range, but for large enough sizes, one will begin to see exponential decays because of the limited form of the wavefunction.) TPS satisfy boundary laws in two or more dimensions. CPS with local correlators like nearest neighbor pairs or plaquettes also satisfy an area (boundary) law, making them promising candidates for systems with a finite correlation length. CPS with long-range correlators, such as those used in the Laughlin wave function, are not constrained by an area (boundary) law and can describe even more entanglement between system and environment, obeying a volume law instead.

3.3 .5 RVB states

Resonating valence bond (RVB) states are widely used in strongly correlated quantum problems [20, 21]. A fermion RVB state can be written as a product of a Jastrow factor and a projected BCS wave function

$$|\Psi_{\text{RVB}}\rangle = e^{\sum_{ij} J_{ij}\hat{n}_i\hat{n}_j}\ \hat{P}_N\ e^{\sum_{ij}\lambda_{ij}a_i^\dagger a_j^\dagger}|\text{vac}\rangle \tag{3.18}$$

where J_{ij} and λ_{ij} are commonly taken to be real.

There is a close relationship between CPS and RVB states. At half-filling, the N-projected 2-site CPS can be expressed in the form of Eq. (3.18). Consider a dimer covering of the lattice. Let $\lambda_{ij} = 1$ for each pair ij that is connected by a dimer and $\lambda_{ij} = 0$ otherwise. The corresponding projected BCS state is the CPS reference (uniform reference) $|\Phi_N\rangle$ defined earlier:

$$\hat{P}_N\ e^{\sum_{i<j} a_i^\dagger a_j^\dagger}|\text{vac}\rangle = \hat{P}_N \sum_{\{q\}} |q_1 q_2 \ldots q_L\rangle = |\Phi_N\rangle. \tag{3.19}$$

If the Jastrow factor is allowed to become *complex*, then the 2-site correlator $\hat{C}^{ij}$ is fully parameterized as

$$\hat{C}^{ij} = \exp(J_0 + J_1^i\hat{n}_i + J_1^j\hat{n}_j + J_2^{ij}\hat{n}_i\hat{n}_j), \tag{3.20}$$

where the J's are complex numbers. Thus the CPS and RVB wave functions are identical.

Despite the existence of a mapping between the two wave functions, the emphasis of the CPS parameterization is quite different from that of commonly studied RVB states. For fermion RVB wave functions where J_{ij} is real, the Jastrow factor is positive and the nodes of the fermion wave function are those of the projected BCS state. In general, such a wave function cannot be exact. In contrast, the CPS wave function can modify the nodes of the reference

wave function $|\Phi_N\rangle$ through the complex Jastrow factor. By using higher order correlators, the CPS state can therefore become exact. While the most flexible RVB/CPS form would combine a complex Jastrow factor with an arbitrary projected BCS reference, there are computational advantages to the simpler CPS reference (uniform reference), including the possibility to efficiently evaluate observables without the use of a stochastic algorithm [2].

3.3 .6 Slater-Jastrow wavefunctions

After the publication of our manuscript, we realized some potential shortcomings of the CPS wavefunction for fermions in two dimensions. This forms the subject of Appendix 3.D .

The resolution to this is to generalize the Slater-Jastrow theory to use CPS. The CPS serves to include additional correlations beyond just the usual pairwise Jastrows (or onsite Gutzwiller [22] factors) used in previous studies of the fermionic Hubbard model (see the earliest studies on VMC on the Hubbard model [23, 24]). [1]

To obtain the Slater determinant part of the wavefunction, we use the (mean field) Hartree Fock approximation to the Hubbard Hamiltonian i.e. we simply diagonalize,

$$H_{HF} = -t \sum_{\langle i,j\rangle,\sigma} a^{\dagger}_{i\sigma} a_{j,\sigma} + \frac{U}{2}\left(\sum_i n_{i\uparrow} \langle n_{i\downarrow}\rangle + \sum_i n_{i\downarrow} \langle n_{i\uparrow}\rangle\right) \tag{3.21}$$

and then self consistently solve for $\langle n_{i\uparrow}\rangle$ and $\langle n_{i\downarrow}\rangle$ [2].

[1] This is perhaps a bit more restrictive than CPS would have liked to be, because one cannot change the nodes of the Slater determinant part of the many body wavefunction.

[2] For a translationally invariant system we can skip over the self consistency step since the

We then introduce correlations between electrons in real space by multiplying the determinant with the CPS wavefunction Ψ_{CPS} (Note, for example, a Gutzwiller factor g^{n_d} suppresses the weight of configurations which have double occupancies, is a one-site CPS). The many body wavefunction thus has the form,

$$\Psi\left(\mathbf{R}_{\uparrow},\mathbf{R}_{\downarrow}\right)=\Psi_{CPS}\begin{vmatrix} \phi_{1\uparrow}(r_{1\uparrow}) & \phi_2(r_{1\uparrow}) & .. & .. & \phi_{n_u\uparrow}(r_{1\uparrow}) \\ \phi_{1\uparrow}(r_{2\uparrow}) & & .. & .. & \phi_{n_u\uparrow}(r_{2\uparrow}) \\ \phi_{1\uparrow}(r_{3\uparrow}) & & .. & .. & .. \\ & & .. & .. & .. \\ \phi_{1\uparrow}(r_{n\uparrow}) & & .. & .. & \phi_{n_u\uparrow}(r_{n_u\uparrow}) \end{vmatrix} \begin{vmatrix} \phi_{1\downarrow}(r_{1\downarrow}) & \phi_{2\downarrow}(r_{1\downarrow}) & .. & .. & \phi_{n_d\downarrow}(r_{1\downarrow}) \\ \phi_{1\downarrow}(r_{2\downarrow}) & & .. & .. & \phi_{n_d\downarrow}(r_{2\downarrow}) \\ \phi_{1\downarrow}(r_{3\downarrow}) & & .. & .. & .. \\ & & .. & .. & .. \\ \phi_{1\downarrow}(r_{n\downarrow}) & & .. & .. & \phi_{n_d\downarrow}(r_{n_d\downarrow}) \end{vmatrix} \tag{3.22}$$

where ϕ represent the one particle orbitals (eigenvectors of H_{HF}) obtained from the HF procedure.

3.4 Computational Cost of CPS

To be useful in practical calculations, a variational wave function must allow *efficient* evaluation of expectation values and optimization of its parameters.

This combination of properties in matrix product states is responsible for the success of the density matrix renormalization group. The expectation value of typical observables can be evaluated exactly in a time which is polynomial in the size of the system. Likewise, the amplitude of a given configuration can also be evaluated exactly in polynomial time. As shown in Eq. (3.14), the amplitude of a configuration is the trace of the product of L independent $m\times m$ matrices, where m is the dimension of the auxiliary indices $\{i\}$ and L is the number of lattice sites. The cost for evaluating the amplitude is $\mathcal{O}(m^3L)$.

eigenvectors we are looking for are simply the eigenvectors of $-t\sum_{\langle i,j\rangle,\sigma}a^{\dagger}_{i\sigma}a_{j,\sigma}$ (since the diagonal is constant); which are plane waves for uniform Bravais lattices.

Tensor product states generalize the structure of MPS to higher dimensions, but numerical efficiency is lost. In general, TPS amplitudes cannot be evaluated exactly in polynomial time. Additional renormalization procedures must be used while performing the contractions, which introduces an error that depends on the system size. For fermions, such errors can result in amplitudes or expectation values incompatible with a fermion wave function as well as a variational energy below the fermion ground state, a so-called N-representability problem. As a result, only certain classes of TPS are capable of efficient polynomial simulation.

Like MPS, correlator product states allow efficient, exact evaluation of wave function amplitudes and expectation values. For example, the amplitudes of a pair CPS are $\Psi(Q) = \prod_{i<j} C^{q_i q_j}$. The amplitude is a *simple product of numbers.* This is true for any CPS, and thus the complexity is proportional only to the number of correlators in the ansatz. This is manifestly polynomial in the system size. In general, evaluation of the amplitude with n-site correlators will require $\mathcal{O}(L)$ multiplications if the correlators act *locally* — e.g, nearest neighbors, plaquettes, etc. — and $\mathcal{O}(L^n)$ if there are no restrictions.

This property allows efficient Monte Carlo sampling of expectation values. (Deterministic algorithms can also be used but are presented elsewhere [2].) Moreover, constraints such as fixed particle number or total spin are easily handled within the Monte Carlo algorithm by limiting the Metropolis walk to states that satisfy these constraints. The expectation value of an operator is given by $\langle A \rangle = \sum_Q P(Q) A(Q)$, where $P(Q) = |\Psi(Q)|^2$ and

$$A(Q) = \sum_{Q'} \langle Q|\hat{A}|Q'\rangle \, \frac{\Psi(Q')}{\Psi(Q)}. \tag{3.23}$$

The sum over Q' extends over only those Q' for which $\langle Q|\hat{A}|Q'\rangle \neq 0$. As long as

$\hat{A}$ is sparse in the chosen basis, its expectation value can be evaluated efficiently. If $|\Psi\rangle$ is local (e.g., nearest-neighbor pair CPS), a further simplification occurs for operators such as $a_i^\dagger a_j$, $a_i^\dagger a_j^\dagger a_k a_l$, or $\mathbf{S}_i \cdot \mathbf{S}_j$. For these operators, most of the factors in $\Psi(Q)$ and $\Psi(Q')$ are identical and cancel from the ratio so that the time required to evaluate the expectation value is independent of the system size and depends only on the number of Monte Carlo samples.

As with MPS and TPS, we can take advantage of the product structure of CPS when minimizing the variational energy and use an efficient local optimization or "sweep" algorithm. The energy is minimized with respect to one of the correlators while the others are held fixed, then repeated for each of the correlators in turn until the energy has converged. This algorithm is described in more detail in the next section.

3.5 Spin and Fermion Simulations

We have implemented a pilot variational Monte Carlo code to optimize general CPS wavefunctions (for an overview of our computer implementation see Appendix 3.A). Below, we present our results for certain models of interacting spins and fermions.

In Table 3.1 we show our results for (i) the 2D square Heisenberg model defined by the Hamiltonian

$$H = J \sum_{\langle ij \rangle} \mathbf{S}_i \cdot \mathbf{S}_j, \tag{3.24}$$

Note: After publication of our manuscript, we also simulated (ii) the $J_1 - J_2$ model on the square lattice to check how well CPS performs for a frustrated

spin system (see Chapter 1, section 1.3 .3). The Hamiltonian for this model is,

$$H_{J_1-J_2} = J_1 \sum_{\langle ij \rangle} \mathbf{S}_i \cdot \mathbf{S}_j + J_2 \sum_{\langle\langle ij \rangle\rangle} \mathbf{S}_i \cdot \mathbf{S}_j \tag{3.25}$$

where $\langle i, j \rangle$ and $\langle\langle i, j \rangle\rangle$ refers to nearest and next to nearest neighbor pairs of sites i, j respectively. The results of our simulations are shown in Table 3.2.

To test how well CPS does for fermions, we simulated the (iii) 1D and 2D spinless fermion model. (The 2D version was simulated after publication.) This model is defined by the Hamiltonian

$$H = \sum_{\langle ij \rangle} -t(c_i^\dagger c_j + c_j^\dagger c_i) + V n_i n_j. \tag{3.26}$$

Each site can only be occupied or unoccupied, and the energy V is the cost of placing two fermions on neighboring sites. Results for this model are discussed in Tables 3.3 and 3.4.

Finally, after publication, we also simulated (iv) the spinfull fermion Hubbard model in 1D and 2D,

$$H = \sum_{\langle ij \rangle, \sigma} -t(c_{i,\sigma}^\dagger c_{j,\sigma} + c_{j,\sigma}^\dagger c_{i,\sigma}) + U \sum_i n_{i\uparrow} n_{i\downarrow}. \tag{3.27}$$

where U denotes the onsite Coulomb repulsion between electrons having opposite spins. Results for this model are shown in Table 3.5.

We studied periodic and open boundary conditions for the Heisenberg and 1D spinless fermion models. For the 2D spinless fermion and all Hubbard models we used only open boundary conditions.

Table 3.1: Variational Monte Carlo energies (in units of J) using CPS for the 2D $S = 1/2$ Heisenberg model, including percent errors (ΔE). CPS[2] denotes nearest-neighbor 2-site correlators and CPS[$n \times n$] denotes plaquette correlators. The "exact" 6×6 and 8×8 energies are obtained from a stochastic series expansion MC calculation using ALPS [25]. Unlike matrix product states, correlator product states maintain good accuracy as the width is increased.

Lattice	CPS[2]	ΔE	CPS[2×2]	ΔE	CPS[3×3]	ΔE	Exact
Periodic Boundary Conditions							
4×4	-11.057(1)	1.5%	-11.109(1)	1.1%	-11.2202(2)	0.1%	-11.2285
6×6	-23.816(3)	2.6%	-24.052(2)	1.6%	-24.313(2)	0.5%	-24.441(2)
8×8	-41.780(5)	3.1%	-42.338(4)	1.8%	-42.711(3)	0.9%	-43.105(3)
Open Boundary Conditions							
4×4	-8.8960(5)	3.2%	-9.0574(4)	1.4%	-9.1481(2)	0.5%	-9.1892
6×6	-20.811(1)	4.2%	-21.176(1)	2.5%	-21.510(1)	1.0%	-21.727(2)
8×8	-37.846(3)	4.5%	-38.511(2)	2.8%	-39.109(2)	1.3%	-39.616(2)

Table 3.2: Variational Monte Carlo energies (in units of J_1) and some correlation functions (measured with respect to the origin (0,0)) compared with Exact Diagonalization data for the $J_1 - J_2$ model on a 6x6 square lattice with periodic boundaries. 3x3 plaquettes and all-pair correlators were used. We have defined the notation $G_E(\mathbf{r}) = \langle \mathbf{S}((0,0)) \cdot \mathbf{S}(\mathbf{r}) \rangle_{\text{Exact}}$ and $G_C(\mathbf{r}) = \langle \mathbf{S}((0,0)) \cdot \mathbf{S}(\mathbf{r}) \rangle_{\text{CPS}}$.

J_2/J_1	$-E_C$	$-E_E$	$G_C(0,1)$	$G_E(0,1)$	$G_C(0,2)$	$G_E(0,2)$	$G_C(2,2)$	$G_E(2,2)$
0.1	22.893(1)	22.971	−0.337	−0.339	0.180	0.177	0.158	0.147
0.2	21.467(1)	21.566	−0.338	−0.338	0.167	0.165	0.136	0.129
0.3	20.113(2)	20.249	−0.337	−0.334	0.154	0.148	0.122	0.104
0.4	18.849(1)	19.071	−0.333	−0.325	0.136	0.124	0.095	0.066
0.5	17.704(2)	18.137	−0.315	−0.304	0.115	0.094	0.072	0.0134
0.6	17.412(1)	17.757	+0.132	−0.219	0.075	0.0968	0.074	0.0012

Table 3.3: Variational Monte Carlo energies (in units of t) for the L-site 1D spinless fermion model with repulsion U using periodic and open boundary conditions, including percent errors (ΔE). CPS[n] denotes n-site correlators; DMRG[m] denotes a DMRG calculation with m renormalized states. Since CPS and DMRG calculations are not directly comparable in terms of complexity, the approximate number of degrees of freedom per site (d.o.f.) is listed in the bottom row. (The numbers are exact in the limit of an infinite lattice.) Encouragingly, CPS are competitive with MPS for a comparable number of variational parameters. Exact energies are from m=500 DMRG calculations.

L	U	CPS[3]	ΔE	DMRG[3]	ΔE	CPS[4]	ΔE	DMRG[4]	ΔE	Exact
Periodic Boundary Conditions										
12	0	-7.052(1)	5.5%	-7.165	4.0%	-7.213(1)	3.4%	-7.313	2.0%	-7.464
12	4	-2.692(2)	4.1%	-2.577	8.2%	-2.756(1)	1.8%	-2.725	2.9%	-2.807
12	8	-1.461(1)	1.1%	-1.430	3.1%	-1.474(1)	0.2%	-1.462	1.0%	-1.477
24	0	-14.432(2)	5.0%	-14.608	3.8%	-14.714(2)	3.2%	-14.832	2.4%	-15.192
24	4	-5.34(1)	5.1%	-5.340	5.1%	-5.482(1)	2.6%	-5.403	4.0%	-5.626
24	8	-2.929(2)	0.8%	-2.860	3.2%	-2.931(1)	0.7%	-2.900	1.8%	-2.953
36	0	-21.82(1)	4.6%	-22.035	3.6%	-22.21(1)	2.8%	-22.421	1.9%	-22.860
36	4	-7.93(3)	6.0%	-8.127	3.7%	-8.17(1)	3.2%	-8.173	3.2%	-8.440
36	8	-4.390(2)	0.9%	-4.302	2.9%	-4.400(1)	0.7%	-4.355	1.7%	-4.430
Open Boundary Conditions										
12	0	-7.204(1)	1.3%	-7.185	1.5%	-7.274(1)	0.3%	-7.265	0.4%	-7.296
12	4	-3.748(1)	4.0%	-3.787	3.0%	-3.887(1)	0.5%	-3.894	0.3%	-3.905
12	8	-2.847(2)	4.6%	-2.920	2.2%	-2.971(1)	0.4%	-2.981	0.1%	-2.984
24	0	-14.593(1)	2.2%	-14.609	2.1%	-14.767(1)	1.1%	-14.838	0.6%	-14.926
24	4	-6.32(1)	7.8%	-6.543	4.5%	-6.687(1)	2.4%	-6.803	0.7%	-6.851
24	8	-4.287(2)	6.6%	-4.414	3.8%	-4.498(2)	2.0%	-4.576	0.3%	-4.590
36	0	-21.978(2)	2.6%	-22.035	2.3%	-22.260(2)	1.3%	-22.421	0.6%	-22.562
36	4	-8.83(3)	9.1%	-9.323	4.0%	-9.36(1)	3.6%	-9.625	0.9%	-9.713
36	8	-5.660(2)	7.3%	-5.873	3.8%	-5.934(3)	2.8%	-6.078	0.4%	-6.104
	d.o.f	8		18		16		32		

Table 3.4: Variational Monte Carlo energies (in units of t) using the CPS-HF wavefunction compared with Exact Diagonalization data for the 4×5 2D (open boundaries) spinless fermion model with 9 and 10 particles

V/t	HF	CPS[pairs]	CPS[2x2]	Exact
		$N = 9$		
0.1	-13.852220	-13.8552(1)	-13.8554(1)	-13.855847
0.2	-13.421361	-13.4335(2)	-13.4339(1)	-13.435887
0.4	-12.568451	-12.6172(1)	-12.6194(4)	-12.626805
0.6	-11.726227	-11.8364(4)	-11.8411(2)	-11.858284
0.8	-10.894018	-11.090(1)	-11.0985(3)	-11.130324
1.0	-10.071844	-10.380(1)	-10.3921(3)	-10.443427
1.2	-9.297130	-9.641(3)	-9.6579(4)	-9.798339
1.4	-8.641101	-8.931(2)	-8.9483(4)	-9.195805
2.0	-7.197420	-7.424(1)	-7.4486(3)	-7.647270
4.0	-4.770708	-4.884(1)	-4.9105(3)	-4.995879
6.0	-3.737447	-3.806(2)	-3.8238(2)	-3.879309
		$N = 10$		
0.1	-13.811734	-13.8155(1)	-13.8158(1)	-13.816619
0.2	-13.227552	-13.2429(1)	-13.2438(2)	-13.247490
0.4	-12.070914	-12.1329(7)	-12.1368(4)	-12.154428
0.6	-10.953859	-11.0574(2)	-11.0611(2)	-11.126673
0.8	-9.959797	-10.084(1)	-10.0884(2)	-10.173728
1.0	-9.091679	-9.222(1)	-9.2273(2)	-9.306636
1.2	-8.338197	-8.465(1)	-8.4712(2)	-8.532610
1.4	-7.682727	-7.800(2)	-7.8072(2)	-7.850684
2.0	-6.162227	-6.248(1)	-6.2529(2)	-6.265810
4.0	-3.588544	-3.610(1)	-3.6141(1)	-3.615113
6.0	-2.489502	-2.495(1)	-2.4988(1)	-2.499139

Optimization method

We optimize the correlators by minimizing the variational energy with a sweep algorithm. At each step of each sweep, a target correlator is updated while the other correlators are fixed. Because the wave function $|\Psi\rangle$ is linear in the target correlator coefficients, the derivatives of $|\Psi\rangle$ with respect to these coefficients define a vector space for the optimization. For instance, if the target

Table 3.5: Ground state energies for the Hubbard model at half filling with open boundary conditions. The DMRG results used m=1600 renormalized states. The correlator sizes used were 3-site (indicated by VMC CPS), and 5-site (indicated by VMC CPS[5]) for the 1D lattices and 4-site (2×2) for the 4×5 lattice. Energies are in units of t, with the uncertainty in the final digit placed in parentheses.

$U/t = 1$

Lattice Size	DMRG	RHF	VMC	VMC CPS[5]
1x14	-13.916691	-13.6335	-13.908(1)	-13.9121(1)
1x18	-18.071822	-17.7191	-18.059(1)	-18.0655(5)
1x22	-22.229341	-21.8073	-22.212(1)	-22.2204(7)

$U/t = 2$

Lattice Size	DMRG	RHF	VMC CPS	VMC CPS[5]
1x14	-11.279897	-10.133544	-11.240(1)	-11.250(1)
1x18	-14.653987	-13.219131	-14.591(1)	-14.621(1)
1x22	-18.029379	-16.307287	-17.947(2)	-17.981(2)
4x5	-20.127521	-18.800678	-19.917(1)	-.-

$U/t = 4$

Lattice Size	DMRG	RHF	VMC CPS	VMC CPS[5]
1x14	-7.672349	-3.133544	-7.556(1)	-7.606(2)
1x18	-9.965398	-4.219131	-9.770(3)	-9.875(2)
1x22	-12.259082	-5.307287	-11.982(3)	-12.116(3)
4x5	-14.404488	-8.800678	-13.350(1)	-.-

correlator has elements C^μ, then the vector space is generated by the basis $|\tilde{\Psi}_\mu\rangle$ where

$$|\tilde{\Psi}_\mu\rangle = \frac{\partial|\Psi\rangle}{\partial C^\mu}. \tag{3.28}$$

Any vector in this space defines a CPS wave function: $\mathbf{x}$ corresponds to the wave function $|\Psi(\mathbf{x})\rangle = \sum_\mu x^\mu |\tilde{\Psi}_\mu\rangle$.

It is convenient to work in a slightly different basis in which one vector $\mathbf{x}_0$ corresponds to the current value of the target correlator and the other vectors $\mathbf{x}_i$ are orthogonal to $\mathbf{x}_0$ (but not necessarily to each other). The updated target

correlator will be a linear combination of the $\mathbf{x}_\alpha$ where $\alpha \in \{0, i\}$.

We construct the Hamiltonian $\mathcal{H}_{\alpha\beta}$ and the overlap matrix $\mathcal{S}_{\alpha\beta}$ in this space:

$$\mathcal{H}_{\alpha\beta} = \langle \Psi(\mathbf{x}_\alpha) | \hat{H} | \Psi(\mathbf{x}_\beta) \rangle \tag{3.29}$$

$$\mathcal{S}_{\alpha\beta} = \langle \Psi(\mathbf{x}_\alpha) | \Psi(\mathbf{x}_\beta) \rangle, \tag{3.30}$$

where $\hat{H}$ is the model Hamiltonian being studied. We then solve the generalized eigenvalue problem

$$\mathcal{H} \cdot \mathbf{C} = \lambda \mathcal{S} \cdot \mathbf{C}, \tag{3.31}$$

where $\mathbf{C}$ is a linear combination of the $\mathbf{x}_\alpha$. The eigenvector with the lowest eigenvalue defines the optimal target correlator coefficients $\tilde{C}^\mu$ that give the lowest energy when all other correlators are fixed. We sweep over all of the correlators one at a time until the energy stops decreasing.

This defines a general sweep algorithm for optimizing CPS. However to converge the sweeps when the Hamiltonian and overlap matrix are constructed via Monte Carlo sampling it is very important to minimize the stochastic error. Nightingale and Melik-Alaverdian [26], and Toulouse and Umrigar [27, 28] defined efficient estimators for variational Monte Carlo optimization (see details of these estimators in Appendix 3.C), and we have used these to construct $\mathcal{H}$ and $\mathcal{S}$. For numerical stability, it is important to monitor the change in the variational parameters and reject extremely large changes during a single iteration [27, 28]. For CPS, this can be achieved by adding a dynamically adjusted diagonal shift to $\mathcal{H}$ that penalizes large changes away from C^μ: $\delta\mathcal{H}_{00} = 0$, $\delta\mathcal{H}_{ii} > 0$. Using this sweep algorithm, we find that the variational energy of the CPS converges (within statistical error) in less than 5 sweeps.

To obtain the numbers in the Tables, we ran the linear optimization routine

for each system through 3 or 4 sweeps, after which the energy stopped decreasing and instead fluctuated within a small range of values. We chose one wavefunction (set of correlators) from the final sweep and calculated the energy and variance reported in the tables using a larger number of Monte Carlo samples than we used during the optimization procedure.

Results

Table 3.1 shows the optimized energies obtained for the 2D square Heisenberg model. This model tests the ability of CPS to describe two-dimensional correlations. When open boundary conditions are used, the system is not translation invariant and requires the kind of general parameterization of the CPS emphasized here rather than the more restricted forms used by Huse and Elser [12].

The nearest-neighbor 2-site CPS (CPS[2]) has only four variational parameters per site and gives errors in the range of 3–5% for open boundary conditions and 1–3% for periodic boundary conditions. The error is rapidly reduced by increasing the correlator size. For example, for the 8×8 periodic model, going from pair to 2×2 to 3×3 plaquettes, the error goes from 3.1% to 1.8% to 0.9%. The rapid convergence of the error with the correlator size is consistent with the results of Mezzacapo *et al.* for hardcore boson systems with periodic boundary conditions [15].

As discussed earlier, CPS with local correlators like those used in Table 3.1 satisfy an area (boundary) law, which allows them to accurately simulate systems with a finite correlation length. However, the 2D Heisenberg model is gapless with long-range correlations, so we expect the error to increase as the

size of the lattice increases. Nonetheless, the energetic error of the CPS wave function with a fixed correlator size grows quite slowly as the lattice size is increased. This is not true of MPS, in which the number of variational parameters per site required to achieve a given accuracy grows rapidly with the width of a 2D system.

We performed a series of DMRG calculations for the Heisenberg model on the lattices in Table 3.1 with a range of values of m using ALPS [25]. The variational objects in the DMRG are $m \times m$ matrices. For periodic boundary conditions, $m \approx 35$, 250, and 750 are required for 1 percent accuracy on the 4×4, 6×6, and 8×8 lattices respectively. The latter calculation, which utilizes about 1.1 million variational parameters per site (neglecting symmetry and conservation of quantum numbers), is to be contrasted with the much more compact description using the CPS with 3×3 correlators, which corresponds to just 512 parameters per site.

To test how well CPS performs for a frustrated Heisenberg model, we simulated the $J_1 - J_2$ model using 3×3 plaquette correlators and correlators connecting all pairs of sites. We present data for J_2/J_1 in the range from 0.0 to 0.6. As Table 3.2 shows, the relative energy error is quite small for small J_2/J_1 but increases to about 2% around $J_2/J_1 \sim 0.5$. In addition, the error in the correlation functions (especially at long distances) seem to increase with increasing frustration. Though, not shown in the tables, we also saw a reduction of the energy error as a function of J_2/J_1 from 0.6 to 1.0.

Another point to be noted is that for $J_2/J_1 = 0.6$, our simulation indicates that the CPS solution can break the symmetries of the lattice (based on observation of nearest neighbor ferromagnetic correlations only along one axis) as

it shows the formation of columnar order. Such solutions are to be expected because of the presence of many local minima in the energy landscape.

The spinless 1D fermion model with periodic boundary conditions has non-trivial fermion correlations and cannot be mapped onto a local spin model. Consequently, this model tests the ability of the CPS to capture fermion correlations. In Table 3.3 we compare 3-site and 4-site nearest-neighbor CPS energies (CPS[3] and CPS[4]) with DMRG calculations for $m = 3$ and $m = 4$ renormalized states. DMRG calculations were carried out using ALPS [25]. For open boundary conditions, the error in the CPS energy is smallest in the noninteracting system and largest for an intermediate interaction strength ($U/t = 4$). For periodic boundary conditions, the CPS[4] errors range from less than 1% for the U=8 case to approximately 3% for the free fermion system — a difficult limit for a locally entangled state. The DMRG energies follow the same trends.

To make a meaningful comparison with the DMRG results, we also show the approximate number of variational degrees of freedom per site in each ansatz. A DMRG[m] wave function has $\mathcal{O}(2m^2L)$ degrees of freedom (2 $m\times m$ matrices at each site) whereas the CPS[n] wave function has $\mathcal{O}(2^nL)$ degrees of freedom (an n-site correlator at each site) [3]. As a result, the CPS[4] wave function has a similar complexity to the DMRG[3] state. Depending on the boundary conditions and the length of the lattice, the exact number of degrees of freedom may be less than this estimate. For instance, when $L = 12$ for an open chain, the DMRG[3] wave function has about 14.7 parameters per site and the CPS[4] wave function has 12. Comparing the CPS and DMRG calculations with similar

[3]The factor of 2 in 2^nL is for models in which there are 2 degrees of freedom per site. For the spinfull fermion Hubbard model this number would be 4. The other assumption here is that correlators of only one kind are used, one correlator being associated with each site. An example of this is a square plaquette for a square lattice. If one were to use pair-correlators, correlating all pairs of sites, one would have order L^2 number of variational parameters

numbers of variational parameters, we see that the CPS energies are indeed very competitive, especially for periodic boundary conditions, where a CPS includes direct correlations between the ends of the chain.

To further test CPS for fermions, we simulated the spinless fermion model in two dimensions. We observed that the CPS ansatz alone did not provide an accurate description of this system. Instead, we optimized a CPS-Hartree Fock wavefunction for a 4×5 square lattice at half filling (10 particles) and with one hole at half filling (9 particles). The results in Table 3.4 show that the pair and plaquette correlators reduce the energy of the Hartree Fock wavefunction in the entire range of V/t from 0.1 to 6.0, the energy error with respect to exact diagonalization being largest in the range of $V/t \sim 1 - 2$. In this parameter regime, it is harder to capture the correct energy of the 9 particle problem than the 10 particle one. This is because the former is more strongly correlated (i.e. its wavefunction involves many more important states).

We also test the CPS-Hartree Fock (CPS-HF) wavefunction for the 1D and 2D spinfull fermion Hubbard model at half filling. As Table 3.5 shows, for 1D systems we can progressively reduce the energy by increasing the size of the correlators (and/or their range) as is shown by the CPS[3] (three site correlators) and CPS[5] (five site correlators) results. For 2D, for the CPS-HF ansatz is more limited, and the error in the energy is at the 7-8$\%$ level.

Minimizing the CPS energy is a nonlinear optimization problem and the sweep algorithm may not converge to the global minimum of the variational energy. We have repeated the optimization for different initial wave functions to avoid local minima (but there are no guarantees that we achieve the lowest state possible). The DMRG algorithm can also converge to a local minimum

for $m = 3$ or 4. We repeated each of these DMRG calculation 100 times with the same input and reported the lowest energy obtained in Table 3.3. Although convergence to local minima is possible in both CPS and DMRG calculations, we believe the results reported in Tables 3.1 and 3.3 indicate the competitive accuracy of CPS as a general variational method.

3.6 Conclusion

In this Chapter, we evaluated correlator product states as a route to describing strongly correlated wave functions in any dimension. Our preliminary numerical studies indicate that CPS can capture both nontrivial fermion correlations and two-dimensional correlations. Together with the analysis showing the connections between CPS and many interesting quantum states, this supports the intriguing possibility that CPS are sufficiently flexible to systematically approximate general strongly correlated spin and fermion problems in two or more dimensions.

Nonetheless, many questions remain to be answered. For example, how well do CPS reproduce correlation functions? While properties are harder to obtain accurately than energies in variational calculations, our view is that so long as successive CPS[n] calculations form a sufficiently rapidly convergent approximation to the quantum state of interest, then accurate approximations to correlation functions can be constructed, as in the case of DMRG calculations. Detailed investigations of such questions and the analysis of more complex systems like the full Hubbard model or the *t-J* model will require more sophisticated numerical treatments and alternative numerical techniques such as deterministic

evaluation methods. We are currently exploring these areas.

3.A Structure of the CPS code

Here, I describe briefly the structure of the CPS code. We have programmed in C++ and extensively used object oriented programming and polymorphism of class objects. The advantage of doing so is the ease of building new wavefunctions and new Hamiltonians in the code without changing any of its core setup. The main data structures and modules have also been shown in Figure 3.2.

1. **Configuration :** As mentioned in the main text of this Chapter, we work in the occupation number representation. The "Configuration" (call it **R**) is a C++ vector of 1's and 0's with length equalling the size of the system (or twice the size of the system for spinfull fermions). For a spin 1/2 spin system, "1" is interpreted as "spin-up" and "0" as "spin-down". For a spinfull fermion system, two vector elements per site are reserved for denoting the occupation of up and down electrons.
2. **Lattice/Adjacency List :** The underlying graph or lattice on which the spin or electron model is defined can be stored as a list of "pairs" denoting the connection between sites. Again a C++ vector is used for this purpose.
3. **Hamiltonian :** The Hamiltonian is a C++ class, with multiple functions associated with it. In particular, we are interested in the action of the Hamiltonian on a Configuration (**R**). This action gives us a set of all "new Configurations" (**R'**) which have a non zero matrix element with the input Configuration. It also calculates the value of the non zero matrix elements $\langle R'|H|R\rangle$.

4. **Wavefunction :** Like the Hamiltonian, the Wavefunction is a C++ class. It consists of routines that can compute the value of the wavefunction for a given configuration ($\Psi(\mathbf{R})$) and efficiently compute wavefunction ratios for two configurations (see Appendix 3.B) related by an electron hop (or spin exchange).

5. **Statistics of observables :** The use of the Hamiltonian and the wavefunction can tell us the "local energy" ($H\Psi(\mathbf{R})/\mathbf{\Psi}(\mathbf{R})$) for a configuration, which when averaged over the VMC run, gives us the total energy of the trial wavefunction. In addition to the energy, the derivatives of the energy with respect to wavefunction parameters can also be calculated using Monte Carlo.

6. **Wavefunction Optimization**: It is crucial to have a very robust optimization algorithm when dealing with a large number of parameters. We have experimented with the linear optimization method (when the number of parameters is a few thousand or less, as construction of $\mathcal{H}$ and $\mathcal{S}$ can get expensive, see also Appendix 3.C) and steepest descent algorithms (for larger number of parameters). There is no theoretical foundation for ensuring that we get to the global minimum. However, we try out multiple optimizations starting from various random wavefunctions in order to achieve this objective.

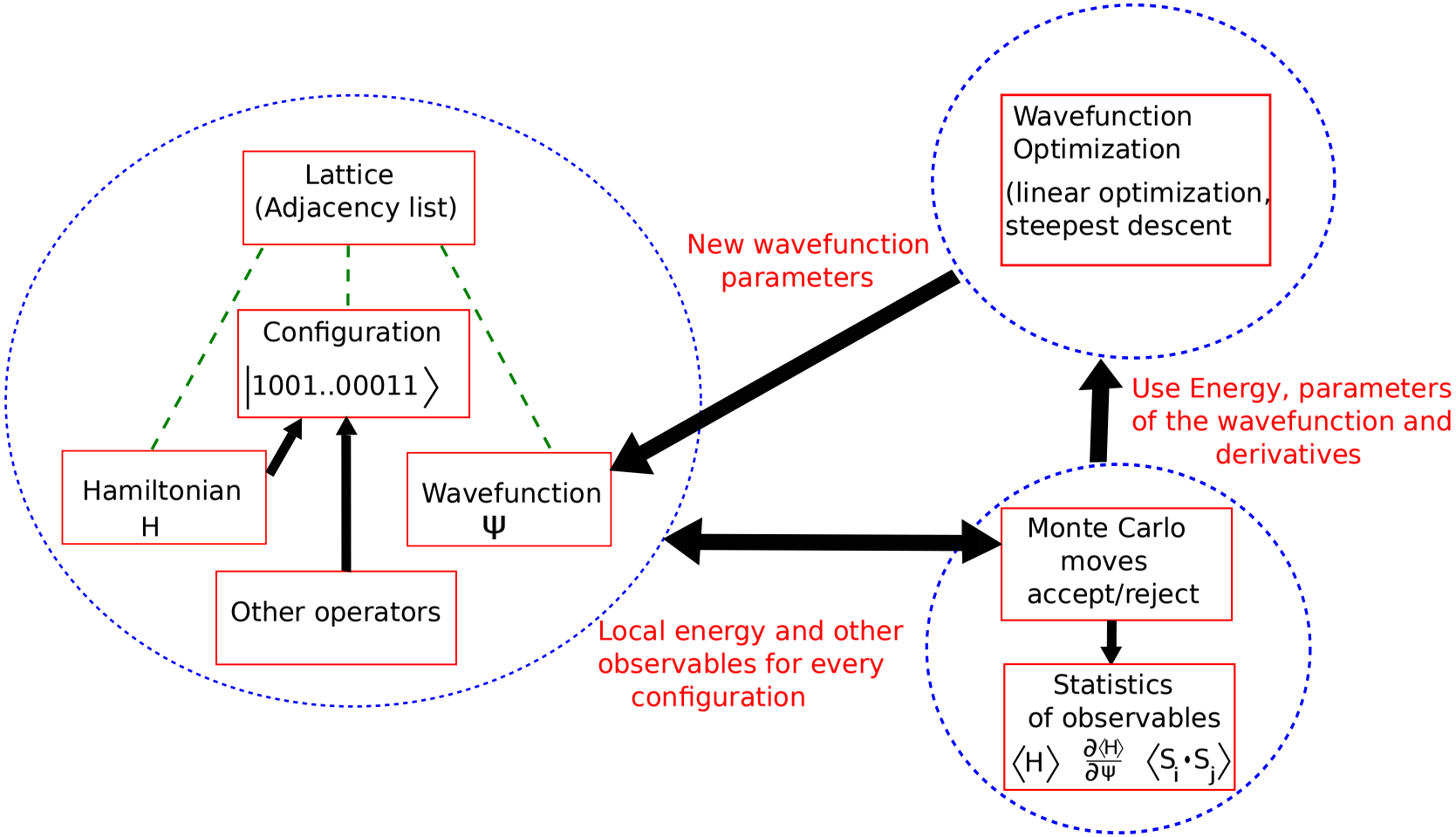

Figure 3.2: Structure of the CPS code.

3.B Computing determinant ratios efficiently

Consider the Slater determinant composed by filling n electrons located at spatial locations $\mathbf{R} = \mathbf{r_1}, \mathbf{r_2}, ...\mathbf{r_n}$ (spanning the rows of the determinant) into the lowest n one particle orbitals. In our VMC calculations, at the Metropolis step, we propose a "one electron move" [4], giving us a new configuration of electrons $\bar{\mathbf{R}}' = \mathbf{r_1}, \mathbf{r_2}, .\mathbf{r_i'}..\mathbf{r_n}$

Thus, the determinant corresponding to $\mathbf{R}'$ differs from the determinant corresponding to $\mathbf{R}$ in exactly one row. In order to know the transition probability $p(\mathbf{R} \to \mathbf{R}')$ in the Metropolis algorithm, one needs to know the ratio of the wavefunction amplitudes (and hence ratio of determinants) corresponding to $\mathbf{R}$ and $\mathbf{R}'$. Naively, one would calculate both determinants *independently* and then take their ratio, leading to an order n^3 computational cost for the evaluation. In this Appendix we will show that for matrices differing in one row,

Result 1 : Computing the ratio of their determinants is only an order n operation, if the inverse of one of the matrices is available.

Result 2 : Obtaining the inverse of one matrix from the (given) inverse of the other is an order n^2 operation.

Consider the given "old matrix" to be $\mathbf{A}$ and the "new matrix" (differing in one row from $\mathbf{A}$) to be $\mathbf{B}$. Their i, j matrix elements are denoted by A_{ij} and B_{ij}. To prove **Result 1** let us first recall a formula for the inverse,

$$\mathbf{A}^{-1} = \frac{1}{\mathrm{det}\mathbf{A}} \mathrm{adj}\mathbf{A} \tag{3.32}$$

[4]Note that the Hubbard Hamiltonian in real space makes allows for an electron hop to its nearest neighbor

where det $\mathbf{A}$ is the determinant of matrix $\mathbf{A}$ and adj $\mathbf{A}$ is the 'adjugate' of $\mathbf{A}$ which is defined in terms of the matrix of cofactors as,

$$\text{adj}(\mathbf{A}_{ij}) = C_{ij} \tag{3.33}$$

where C_{ij} is the cofactor of element $\mathbf{A}_{ij}$.

Thus a formula for the determinant of matrix $\mathbf{A}$ may be written as,

$$\det \mathbf{A} = A_{11}C_{11} + A_{12}C_{12}...A_{1n}C_{1n} \tag{3.34}$$

Now imagine replacing the first row [5] of the matrix $\mathbf{A}$ to get matrix $\mathbf{B}$. Since only a row of $\mathbf{A}$ has changed but the corresponding cofactors of the elements of that row have not, we get,

$$\text{det}\mathbf{B} = B_{11}C_{11} + B_{12}C_{12}...B_{1n}C_{1n} \tag{3.35}$$

and thus the ratio det$\mathbf{B}$/det$\mathbf{A}$ is given by,

$$\frac{\text{det}\mathbf{B}}{\text{det}\mathbf{A}} = B_{11}A_{11}^{-1} + B_{12}A_{12}^{-1}...B_{1n}A_{1n}^{-1} \tag{3.36}$$

where we have used $\mathbf{A}_{ij}^{-1} = C_{ij}/\text{det}\mathbf{A}$. Note that the ratio can thus be calculated in order n time as it is requires a element-wise multiplication (a dot product) of two vectors $\bar{b} \equiv \{B_{11}, B_{12}, ...B_{1n}\}$ and $\bar{a} \equiv \{A_{11}^{-1}, A_{12}^{-1}...A_{1n}^{-1}\}$. This completes the proof of **Result 1**.

We now go on to derive **Result 2** for obtaining $\mathbf{B}^{-1}$ from $\mathbf{A}^{-1}$. For this purpose, we use the Sherman Morrison formula [29, 30],

$$(\mathbf{A} + uv^T)^{-1} = \mathbf{A}^{-1} - \frac{\mathbf{A}^{-1}uv^T\mathbf{A}^{-1}}{1 + v^T\mathbf{A}^{-1}u} \tag{3.37}$$

[5] The proof also applies if a row other than the first one was replaced instead. Note a determinant of a matrix is affected by a overall sign change when its rows are re-ordered.

If $\mathbf{A}$ and $\mathbf{B}$ differ in the first row, set $v^T = [B_{11} - A_{11}, B_{12} - A_{12}, ...B_{1n} - A_{1n}]$ and $u^T = [1, 0, 0, ...0]$ and apply the Sherman Morrison formula (3.37) to directly get $\mathbf{B}^{-1}$.

Note that the term $\mathbf{A}^{-1}uv^T\mathbf{A}^{-1}$ involves a matrix multiplication of a column vector $(\mathbf{A}^{-1}u)$ and a row vector $(v^T\mathbf{A}^{-1})$ which involves at the most is order n^2 operations (Given the form of u and v, obtaining $\mathbf{A}^{-1}u$ and $v^T\mathbf{A}^{-1}$ involves order n and order n^2 operations respectively). The term $1 + v^T\mathbf{A}^{-1}u$ involves a dot product of a row vector with a column vector and thus needs only order n operations. Hence, based on equation (3.37), finding the inverse $\mathbf{B}^{-1}$ scales as order n^2. This proves **Result 2**.

3.C Linear Optimization: Estimators for $\mathcal{H}$ and $\mathcal{S}$

In the main text of this Chapter, we discussed briefly our use of the linear method (see also Toulouse and Umrigar [27, 28] for a description). In this Appendix, I fill in the mathematical details that were omitted in the published paper [1].

To begin with, Ψ_i refers to the usual partial derivative of the wavefunction with respect to a parameter x_i,

$$\Psi_i \equiv \frac{\partial \Psi(\mathbf{x})}{\partial x_i} \tag{3.38}$$

and $\tilde{\Psi}_i$ refer to the 'orthogonal derivatives': we take the usual partial derivative of the wavefunction with respect to a parameter and project out the wavefunction $|\Psi_0\rangle$ from it, i.e.

$$|\tilde{\Psi}_i\rangle \equiv |\Psi_i\rangle - \langle\Psi_i|\Psi_0\rangle|\Psi_0\rangle \tag{3.39}$$

We will use the notation $S_{0i} \equiv \langle \Psi_i | \Psi_0 \rangle$.

The 'new wavefunction' (yet unknown) $\Psi(\mathbf{x})$ can be written in terms of the 'old wavefunction' Ψ_0, which is normalized, (both being parameterized by $N = N_{opt} + 1$ parameters) as,

$$|\Psi(\mathbf{x})\rangle = |\Psi_0\rangle + \sum_{i=1}^{N_{opt}} \Delta \mathbf{x_i} |\tilde{\Psi}_i\rangle \tag{3.40a}$$

$$= \sum_{i=0}^{N_{opt}} \Delta \mathbf{x_i} |\bar{\Psi}_i\rangle \tag{3.40b}$$

where in equation (3.40b), we have written equation (3.40a) more compactly with the understanding that,

$$|\tilde{\Psi}_0\rangle \equiv |\Psi_0\rangle \tag{3.41a}$$

$$\Delta \mathbf{x_0} = 1 \tag{3.41b}$$

and $|\Psi_0\rangle$ is normalized to 1.

It is straightforward to derive that energy minimization (more rigorously, it is only the stationarity) with respect to all parameters $\mathbf{x_i}$

$$\min_{\mathbf{x}} \frac{\langle \Psi(\mathbf{x}) | H | \Psi(\mathbf{x}) \rangle}{\langle \Psi(\mathbf{x}) | \Psi(\mathbf{x}) \rangle} \tag{3.42}$$

reduces to solution of the generalized eigenproblem

$$\sum_j \mathcal{H}_{ij} \Delta \mathbf{x_j} = \lambda \sum_{\mathbf{j}} \mathcal{S}_{\mathbf{ij}} \boldsymbol{\Delta} \mathbf{x_j} \tag{3.43}$$

where $\mathcal{H}$ and $\mathcal{S}$ are the "Hamiltonian" and "overlap" matrices (respectively) in the $N_{opt} + 1$ basis spanned by $|\Psi_0\rangle$ and its $N_{opt} = N - 1$ orthogonal derivatives $|\tilde{\Psi}_i\rangle$ ($i = 1$ to N_{opt}). These matrices are defined to be,

$$\mathcal{H}_{ij} = \langle \tilde{\Psi}_i | H | \tilde{\Psi}_j \rangle \tag{3.44}$$

$$\mathcal{S}_{ij} = \langle \tilde{\Psi}_i | \tilde{\Psi}_j \rangle \tag{3.45}$$

By plugging in expressions for $\tilde{\Psi}_i$ from equation (3.39) in equations (3.44) and (3.45), and introducing appropriate normalization factors ($\langle\Psi_0|\Psi_0\rangle$) we arrive at the formulae,

$$\begin{aligned}
\mathcal{H}_{ij} &= \frac{\langle\Psi_i|H|\Psi_j\rangle}{\langle\Psi_0|\Psi_0\rangle} + \frac{\langle\Psi_i|\Psi_0\rangle}{\langle\Psi_0|\Psi_0\rangle}\frac{\langle\Psi_j|\Psi_0\rangle}{\langle\Psi_0|\Psi_0\rangle}\frac{\langle\Psi_0|H|\Psi_0\rangle}{\langle\Psi_0|\Psi_0\rangle} - \frac{\langle\Psi_j|H|\Psi_0\rangle}{\langle\Psi_0|\Psi_0\rangle}\frac{\langle\Psi_0|\Psi_i\rangle}{\langle\Psi_0|\Psi_0\rangle} - \frac{\langle\Psi_0|H|\Psi_i\rangle}{\langle\Psi_0|\Psi_0\rangle}\frac{\langle\Psi_j|\Psi_0\rangle}{\langle\Psi_0|\Psi_0\rangle} \\
\mathcal{S}_{ij} &= \frac{\langle\Psi_i|\Psi_j\rangle}{\langle\Psi_0|\Psi_0\rangle} + \frac{\langle\Psi_i|\Psi_0\rangle}{\langle\Psi_0|\Psi_0\rangle}\frac{\langle\Psi_j|\Psi_0\rangle}{\langle\Psi_0|\Psi_0\rangle} - \frac{\langle\Psi_j|\Psi_0\rangle}{\langle\Psi_0|\Psi_0\rangle}\frac{\langle\Psi_0|\Psi_i\rangle}{\langle\Psi_0|\Psi_0\rangle} - \frac{\langle\Psi_0|\Psi_i\rangle\langle\Psi_j|\Psi_0\rangle}{\langle\Psi_0|\Psi_0\rangle}
\end{aligned} \tag{3.46}$$

Consider for example, the term

$$\frac{\langle\Psi_i|H|\Psi_j\rangle}{\langle\Psi_0|\Psi_0\rangle} \tag{3.47}$$

Introducing a complete set of states $|R\rangle\langle R|$ we can recast the term in (3.47) in the form

$$\sum_R \frac{\langle\Psi_i|R\rangle\langle R|H|\Psi_j\rangle}{\langle\Psi_0|\Psi_0\rangle} \tag{3.48}$$

Now multiplying and dividing the numerator by $|\langle R|\Psi_0\rangle|^2$ we can re-express (3.49) as a VMC average,

$$\sum_R \left(\frac{|\langle R|\Psi_0\rangle|^2}{\langle\Psi_0|\Psi_0\rangle}\right)\frac{\langle\Psi_i|R\rangle}{\langle\Psi_0|R\rangle}\frac{\langle R|H|\Psi_j\rangle}{\langle R|\Psi_0\rangle} \tag{3.49}$$

which may be written as

$$\left\langle \frac{\Psi_i(\mathbf{R})}{\Psi_0(\mathbf{R})}\frac{H\Psi_j(\mathbf{R})}{\Psi_0(\mathbf{R})} \right\rangle \tag{3.50}$$

For all terms in equation (3.46), one can use the 'trick' of introducing a complete set of states $|R\rangle\langle R|$ and express them in the form of estimators that can be sampled with VMC. Thus we get,

$$\begin{aligned}
\mathcal{H}_{ij} &= \left\langle \frac{\Psi_i(\mathbf{R})}{\Psi_0(\mathbf{R})}\frac{H\Psi_j(\mathbf{R})}{\Psi_0(\mathbf{R})} \right\rangle + \left\langle \frac{\Psi_i(\mathbf{R})}{\Psi_0(\mathbf{R})} \right\rangle \left\langle \frac{\Psi_j(\mathbf{R})}{\Psi_0(\mathbf{R})} \right\rangle \langle E_L(\mathbf{R})\rangle \\
&\quad - \left\langle \frac{\Psi_i(\mathbf{R})}{\Psi_0(\mathbf{R})} \right\rangle \left\langle \frac{\Psi_j(\mathbf{R})}{\Psi_0(\mathbf{R})} E_L(\mathbf{R}) \right\rangle - \left\langle \frac{\Psi_j(\mathbf{R})}{\Psi_0(\mathbf{R})} \right\rangle \left\langle \frac{\Psi_i(\mathbf{R})}{\Psi_0(\mathbf{R})} E_L(\mathbf{R}) \right\rangle \qquad (3.51a) \\
\mathcal{S}_{ij} &= \left\langle \frac{\Psi_i(\mathbf{R})}{\Psi_0(\mathbf{R})}\frac{\Psi_j(\mathbf{R})}{\Psi_0(\mathbf{R})} \right\rangle - \left\langle \frac{\Psi_i(\mathbf{R})}{\Psi_0(\mathbf{R})} \right\rangle \left\langle \frac{\Psi_j(\mathbf{R})}{\Psi_0(\mathbf{R})} \right\rangle \qquad (3.51b)
\end{aligned}$$

where $E_L(\mathbf{R})$ is defined to be,

$$E_L(\mathbf{R}) \equiv \frac{\langle R|H|\Psi_0\rangle}{\langle R|\Psi_0\rangle} \tag{3.52}$$

Observe that $\mathcal{H}_{ij}$ is not a symmetric (Hermitian) matrix, even though the quantum mechanical Hamiltonian H is. We do not symmetrize $\mathcal{H}$: it has been argued [26, 27, 28] that working with the non-symmetric form leads to smaller statistical errors when the averages occurring in $\mathcal{H}$ are computed over a finite number of samples [6].

The linear method has also been used for nonlinear parameters, a case that does not occur for the CPS wavefunction. Hence we do not discuss this extension here. The interested reader may refer to [27, 28].

3.D The problem with fermions

In the main text of this Chapter, I mentioned briefly that the CPS is used with an antisymmetric wavefunction when dealing with fermions. Part of the reason for doing so, is that our optimizations using the CPS alone did not yield accurate results even when dealing with big correlators. In comparison, the spin systems had no such problem. This led me to a (somewhat pedagogical) example which may highlight the missing ingredient.

Let us consider two non interacting fermionic systems (shown in Figure 3.3) with a hopping Hamiltonian,

$$H = -tc_1^\dagger c_2 - tc_3^\dagger c_4 + \text{h.c.} \tag{3.53}$$

Also let us impose the constraint that there is one electron on 1-2 and one electron on 3-4. Then working out the exact ground state of the system I get the

[6] In the limit of an infinite number of samples $\mathcal{H}$ is symmetric

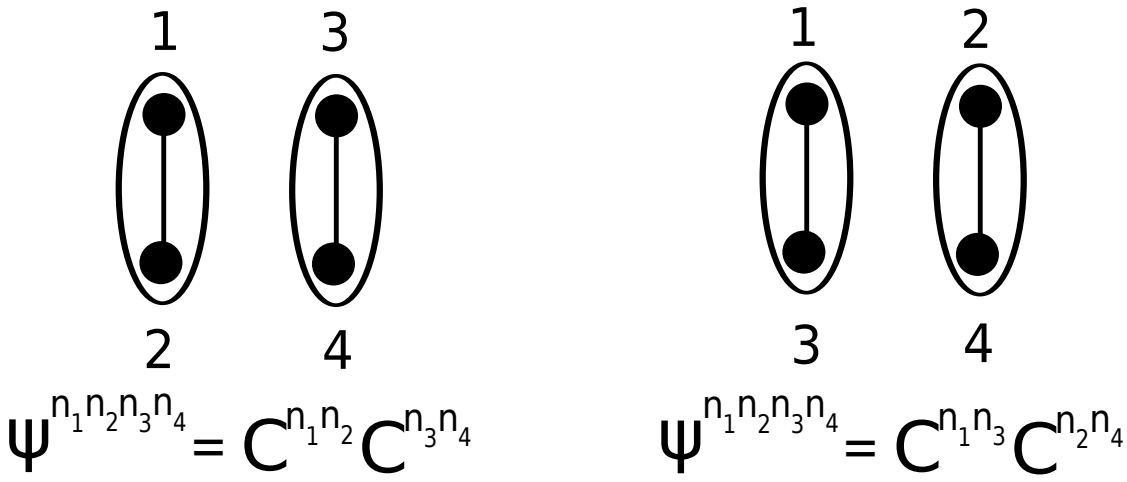

Figure 3.3: Toy system to understand a potential problem in simulating fermions. Two non interacting systems are considered with the constraint of one fermion per system. The same set of systems is renumbered keeping the correlators the same. Refer to the text for details.

ground state wavefunction to be,

$$|\psi\rangle = \left(c_1^\dagger + c_2^\dagger\right)\left(c_3^\dagger + c_4^\dagger\right)|vac\rangle_{1-2} \otimes |vac\rangle_{3-4} \tag{3.54a}$$

$$= c_1^\dagger c_3^\dagger + c_2^\dagger c_3^\dagger + c_1^\dagger c_4^\dagger + c_2^\dagger c_4^\dagger |vac\rangle \tag{3.54b}$$

Consider the pair correlators: one pair connecting sites 1 and 2 and the other pair connecting sites 3 and 4. It is easy to see that the correlators $C^{n_1=0,n_2=1} = 1$,$C^{n_1=1,n_2=0} = 1$ and $C^{n_3=0,n_4=1} = 1$,$C^{n_3=1,n_4=0} = 1$ describe the ground state of this system.

Now, let us renumber the lattice sites, switching 2 and 3, but keep the same physical Hamiltonian and the same correlator connections (1 with 3, 2 with 4). One can easily see that the ground state of this system is,

$$|\psi\rangle = c_1^\dagger c_2^\dagger + c_1^\dagger c_4^\dagger - c_2^\dagger c_3^\dagger + c_3^\dagger c_4^\dagger |vac\rangle \tag{3.55}$$

In order to describe the ground state I need,

$$C^{n_1=1,n_3=0}C^{n_2=1,n_4=0} = +1 \tag{3.56a}$$

$$C^{n_1=1,n_3=0}C^{n_2=0,n_4=1} = +1 \tag{3.56b}$$

$$C^{n_1=0,n_3=1}C^{n_2=1,n_4=0} = -1 \tag{3.56c}$$

$$C^{n_1=0,n_3=1}C^{n_2=0,n_4=1} = +1 \tag{3.56d}$$

Equations (3.56a) and (3.56b) give us,

$$C^{n_2=1,n_4=0} = C^{n_2=0,n_4=1} \tag{3.57}$$

and equations (3.56c) and (3.56d) give us,

$$C^{n_2=1,n_4=0} = -C^{n_2=0,n_4=1} \tag{3.58}$$

Since equations (3.57) and (3.58) are inconsistent, I find that there is no self consistent set of correlators that can now describe the ground state in this new numbering.

This simple exercise shows that the CPS written "as-is" is not *manifestly invariant* for fermion problems. However, by making correlator connections between *all pairs* of sites (as has been done in the work of Marti et al. [31]), one can insure that if the CPS is a good approximation of the ground state wavefunction for a certain numbering of the lattice, then it will remain a good wavefunction for any other numbering. (The effect of the pair correlators is to compensate for the phases that arise due to fermionic anticommutation relations.)

BIBLIOGRAPHY

[1] H. J. Changlani, J. M. Kinder, C. J. Umrigar, and G. K.-L. Chan, Phys. Rev. B **80**, 245116 (2009).

[2] E. Neuscamman, H. Changlani, J. Kinder, and G. K.-L. Chan, Phys. Rev. B **84**, 205132 (2011).

[3] S. R. White, Phys. Rev. Lett. **69**, 2863 (1992).

[4] U. Schollwöck, Rev. Mod. Phys. **77**, 259 (2005).

[5] A. Gendiar, N. Maeshima, and T. Nishino, Prog. Theor. Phys. **110**, 691 (2003).

[6] F. Verstraete, M. M. Wolf, D. Perez-Garcia, and J. I. Cirac, Phys. Rev. Lett. **96**, 220601 (2006).

[7] G. Evenbly and G. Vidal, Phys. Rev. Lett. **102**, 180406 (2009).

[8] A. W. Sandvik and G. Vidal, Phys. Rev. Lett. **99**, 220602 (2007).

[9] H. C. Jiang, Z. Y. Weng, and T. Xiang, Phys. Rev. Lett. **101**, 090603 (2008).

[10] Z. C. Gu, M. Levin, B. Swingle, and X. G. Wen, Phys. Rev. B **79**, 085118 (2009).

[11] M. P. Nightingale and H. W. J. Bloete, Phys. Rev. B **33**, 659 (1986).

[12] D. A. Huse and V. Elser, Phys. Rev. Lett. **60**, 2531 (1988).

[13] A. Gendiar and T. Nishino, Phys. Rev. E **65**, 046702 (2002).

[14] L. Isaev, G. Ortiz, and J. Dukelsky, Phys. Rev. B **79**, 024409 (2009), this study uses correlators which do not overlap and which are treated in a mean-field way.

[15] F. Mezzacapo, N. Schuch, M. Boninsegni, and J. I. Cirac, New J. Phys. **11**, 083026 (2009), the ansatz considered here has the same form as the CPS.

[16] N. Schuch, M. Wolf, F. Verstraete, and I. Cirac, Phys. Rev. Lett. **100**, 040501 (2008).

[17] R. Laughlin, Phys. Rev. Lett. **50**, 1395 (1983).

[18] A. Kitaev, Ann. Phys. **303**, 2 (2003).

[19] M. Wolf, F. Verstraete, M. Hastings, and J. Cirac, Phys. Rev. Lett. **100**, 70502 (2008).

[20] S. Liang, B. Doucot, and P. W. Anderson, Phys. Rev. Lett. **61**, 365 (1988).

[21] A. Parola, F. Becca, L. Capriotti, and S. Sorella, J. Magnetism and Magnetic Materials **272**, 138 (2004).

[22] M. C. Gutzwiller, Phys. Rev. **137**, A1726 (1965).

[23] H. Yokoyama and H. Shiba, Journal of the Physical Society of Japan **56**, 1490 (1987).

[24] H. Yokoyama and H. Shiba, Journal of the Physical Society of Japan **56**, 3582 (1987).

[25] A. Albuquerque *et al.*, Journal of Magnetism and Magnetic Materials **310**, 1187 (2007).

[26] M. Nightingale and V. Melik-Alaverdian, Phys. Rev. Lett. **87**, 43401 (2001).

[27] J. Toulouse and C. J. Umrigar, J. Chem. Phys. **126**, 084102 (2007).

[28] J. Toulouse and C. J. Umrigar, J. Chem. Phys. **128**, 174101 (2008).

[29] J. Sherman and W. J. Morrison, Ann. Math. Stat. **21**, 124 (1950).

[30] M. Bartlett, Ann. Math. Stat. **22**, 107 (1951).

[31] K. H. Marti *et al.*, New Journal of Physics **12**, 103008 (2010).

CHAPTER 4

SEMISTOCHASTIC QUANTUM MONTE CARLO (SQMC)

4.1 Introduction

As we have already seen, one of our main objectives is to be able to compute the eigenvalue (and other observables) associated with the ground state of a physical Hamiltonian. The Hilbert space is so large that the matrix cannot be stored (even sparsely). If we managed to save a few vectors, one could proceed with exact diagonalization methods. But we easily exceed this limit even for a system of modest size.

Quantum Monte Carlo methods (see the references in Chapter 2, the review by Foulkes [1] and the book by Nightingale and Umrigar [2]) can be used to perform the task that (the exact) power method is designed for, at the cost of introducing stochasticity (and an associated statistical error in the observables). The reason this idea works is as follows: since the ground state eigenvector is not needed in its entirety, it is sufficient to "sample" it over time to obtain averages of relevant physical observables. This is achieved by applying the projector *stochastically* to evolve the representation of the eigenvector in time.

One does not have to *necessarily* choose exact diagonalization (ED) over Monte Carlo and maybe one can have the best of both worlds. This attitude led to our efforts in developing a hybrid method consisting of a numerically exact representation and projection in a small *deterministic* subspace, complemented by *stochastic* treatment of the rest of the space. The success of this *semistochastic* approach hinges crucially on the assumption that such a division of the space is

"profitable", which depends on the fraction of the total weight of the dominant eigenstate that is carried by the deterministic subspace.

In this Chapter, we develop and apply the semistochastic Quantum Monte Carlo method (henceforth abbreviated as SQMC) to compute the ground state energies of quantum mechanical Hamiltonians represented in a discrete basis. We also borrow new ideas from the Full Configuration Interaction Quantum Monte Carlo (FCIQMC) method which has been recently proposed by Alavi and coworkers [3, 4, 5, 6, 7] [1] and concurrently by Ohtsuka and Nagase [9, 10, 11]. The benefit of SQMC over the corresponding FCIQMC method is large for the systems presented here since the Hartree Fock determinant, augmented by a small set of additional determinants, indeed represents a significant fraction of the total spectral weight of the ground state wave function. In fact, many quantum chemical Hamiltonians have this nice property as well; however, these Hamiltonians will not be discussed in this Chapter.

This Chapter borrows from and extends the results presented in the paper by F. R. Petruzielo, A. A. Holmes, Hitesh J. Changlani (the author), M.P. Nightingale and C. J. Umrigar which has been accepted for publication in *Physical Review Letters* [12]. I acknowledge that the results were generated as part of a combined effort by me and fellow students: Adam Holmes and Frank Petruzielo.

4.2 Projector Monte Carlo and the 'Sign Problem'

In Chapter 2, we discussed Monte Carlo methods (see section 2.2) and gave a brief overview of the basic idea of the projector Monte Carlo method and what

[1] For a very detailed account see the thesis of Booth [8].

the "sign problem" was. Here, we will be a bit more rigorous in our definitions and mathematically formulate the problem.

To begin with, the matrix element of the projector P_{ij} (or Green's function) is defined as,

$$P_{ij} = \delta_{ij} - \tau \left(H_{ij} - E_T \delta_{ij} \right) \tag{4.1}$$

where δ_{ij} refers to the Kronecker delta function, τ is the time step, H_{ij} refers to the Hamiltonian matrix element between many body basis states labelled by i and j. E_T is the "trial energy", a constant that may be updated during the projection process, based on the knowledge of the best estimate of the ground state energy. At the start of the run, E_T may be set to the Hartree Fock energy.

Let us look at the projector (4.1) a bit more carefully. The diagonal element (for state i) of the projector defined in equation (4.1) is,

$$P_{ii} = 1 + \tau(E_T - H_{ii}). \tag{4.2}$$

We note that even if H_{ii} is large and positive, τ (a positive quantity) and/or E_T can always be suitably adjusted to make P_{ii} *always* positive for all i.

Consider now the off diagonal element $i \neq j$ of the projector defined in equation (4.1)

$$P_{ij} = -\tau H_{ij} \tag{4.3}$$

In this case, no adjustments of τ or E_T can be made to render P_{ij} to be positive if H_{ij} is positive.

For the projector (4.1) to be treated as a stochastic (or Markov) matrix one needs the following two conditions to hold,

1. Each and every element of P_{ij} must be strictly nonnegative and real.

2. The sum of all elements in a row (individually for each row) must equal 1, i.e.

$$\sum_j P_{ij} = 1 \tag{4.4}$$

The violation of second criterion (4.4) is *not* a problem when performing Monte Carlo simulations. One can always "normalize" a row on the fly (and separately account for the total weight of the row) to give the projector matrix its stochastic (Markov chain) interpretation [2].

What is serious and ultimately the cause of the "sign problem" is that all the off diagonal elements of the projector are not positive, nor are there sign changes of basis states that can be found that bring it into this desired form [3].

Projector QMC has thus been used most successfully for systems that *do not* have a sign problem [13, 14]. Projector QMC has also been used in conjunction with a fixed-node approximation [15] which maps the projector with a sign problem to one without a sign problem. This method is variational, but has a "fixed node error" that cannot be eliminated and depends heavily on the quality of the nodal structure provided by the trial wavefunction.

As mentioned previously, recent progress by Alavi and coworkers with their Full Configuration Interaction-Quantum Monte Carlo Method (FCIQMC) method [3] and its "initiator extension" [4] (a term we will explain later in the Chapter) has

[2]For Monte Carlo methods to be of "practical" use, the inherent assumption here is that the number of non zero elements of the projector (in each of its rows) does not scale exponentially with system size.

[3]This is perhaps best explained with an example. The nearest neighbor Heisenberg model on a square lattice might naively appear to have a "sign problem" because all the off diagonal matrix elements of the Hamiltonian are nonnegative (and that of the projector non positive). However, by considering a *unitary* transformation of the spin operator on site m, $S_m \rightarrow -S_m$, for all m that belong to (say) the odd sublattice, one ensures that *all* the off diagonal matrix elements of the Hamiltonian are necessarily non positive and the projector is necessarily non negative.

enabled the treatment of systems with a sign problem (albeit at the cost of introducing a systematic error, which can be controlled by increasing the walker population).

4.3 General ingredients for Projector Quantum Monte Carlo

In this section, I will describe the general ingredients of a Projector Monte Carlo code which predate the FCIQMC and SQMC developments. The idea is to get acquainted with the concepts and terminology that are commonly used in the Quantum Monte Carlo literature.

4.3 .1 "Walkers" and their dynamics

To understand the projection process, we need to first realize how the wavefunction is represented. Surely, we *cannot* save the full wavefunction: if we can, then we are in a regime where we should be performing exact diagonalization instead.

The important idea introduced by Quantum Monte Carlo methods is that a wavefunction[4] has a 'stochastic representation'. By this we mean that the wavefunction can be represented by 'walkers', entities that carry 'weights' and are associated with 'configurations' or states in the Hilbert space. The weight of the walker is a real number [5] and its value at one time instant is not of particular

[4]Since QMC involves a projection process, the wavefunction we obtain is the ground state consistent with the symmetry conditions imposed on the starting state (such as total S_z or total momentum $\mathbf{k}$)

[5]Generalization to complex valued wavefunctions is also possible, but has not been implemented.

physical relevance. It is only when the weights are averaged over a long time (for a given state of the Hilbert space) over many "generations" do they represent (within statistical errors) the true ground state wavefunction amplitudes $C_i(\infty)$ [6]. This idea is mathematically written as,

$$C_i(\infty) \propto \sum_{n=0}^{\infty} w_i(n\tau) \tag{4.5}$$

where $w_i(n\tau)$ is the weight of a walker on state i at "time" $n\tau$.

One might interchangeably use the jargon (for example) "there are 3 walkers with weight 1.1 on configuration $\mathbf{R}$" versus saying "there is 1 walker with weight 3.3 on configuration $\mathbf{R}$". The former jargon is preferable when a large weight needs to split into smaller ones to reduce the statistical fluctuation associated with the dynamics of the walkers. The latter jargon is probably a bit more preferable when talking about real valued weights and in the context of cancelling or adding walker weights after the "walker moves" have been performed.

In our QMC program each walker is represented by two integers $I_{R_\uparrow}$,$I_{R_\downarrow}$ that denote the occupation of up and down electrons (on a lattice or in the space of orbitals) R, and a real valued weight. The list of walkers at a given generation is an array in our program and is always kept sorted based on the integer representation $I_{R_\uparrow}$,$I_{R_\downarrow}$ of the walker's configuration.

The *projector* imparts dynamics to the walkers i.e. governs the evolution in time of the walkers. To understand the walker dynamics let us explicitly write down the equation for the evolution of wavefunction amplitudes $C_i(t)$ for

[6]Note we are only interested in the "long time limit" of the evolving wavefunction amplitudes

configuration i with time [7],

$$C_i(t+\tau) = \sum_j P_{ij} C_j(t) \tag{4.6}$$

$$= (1+\tau(E_T - H_{ii}))C_i(t) + \sum_{i \neq j} -\tau H_{ij} C_j(t) \tag{4.7}$$

Now consider the first term in equation (4.7). This term corresponds to a "diagonal" move: take the weight of the walker at configuration i having weight w_i at time t and scale it by $(1+\tau(E_T - H_{ii}))$. If the walker weight is reduced, it is equivalent to saying "some walkers have died" and if the weight grows, we say the walker has created "clones".

The second term in equation (4.7) represents an "off diagonal move". The walker at i may be thought of as a "parent" which can "spawn progeny" (or "create children walkers") on other configurations j according to the action of $-\tau H_{ij}$) at time $t+\tau$. There are various ways in which the children can be spawned: two such ways implemented in our code will be discussed later in the section.

The combined set of walkers that were created from the previous set (by stochastic application of the projector) i.e. the "progeny" along with the surviving "parents" are said to form a "new generation". Any history of where the child came from previously is erased.

Thus, the idea involved in QMC methods is to store *only* one generation of walkers at a time, but to maintain a *running average* of the desired observables (such as the energy) over many such generations. To see how this ex-

[7] The equation (4.7) we present here is exact if we wish to project out the ground state. One may also obtain the same equation by linearizing the imaginary time Schrödinger equation (see Booth et al. [3]), in which case it gives the *false* impression that equation (4.7) is only an approximation to a true projection equation. This point is important to note because there is no "time step error" in Projector Monte Carlo when working in a finite Hilbert space (owing to the bounded energy spectrum).

plicitly works out, we will presently discuss how the energy measurement is performed.

4.3 .2 Mixed energy estimator

The energy of a wavefunction Ψ, can be estimated in projector Monte Carlo methods using the mixed estimator E_{mix},

$$E_{\text{mix}} = \frac{\langle \Psi \left| H \right| \Psi_T \rangle}{\langle \Psi | \Psi_T \rangle} \tag{4.8}$$

Note that the mixed energy estimator is exactly equal to the ground state energy E_0 only when Ψ or Ψ_T or both are exact. In all other cases, the "mixed energy" can be above or below the exact energy. In short, there is no (variational) principle that exists for the mixed estimator.

Before we proceed further, we find it convenient to define the amplitudes of the trial wavefunction t_i (i refers to a state in the Hilbert space),

$$|\Psi_T\rangle \equiv \sum_i t_i |i\rangle \tag{4.9}$$

Now, one does not have an explicit representation for Ψ, rather we know its stochastic representation over N_g generations. Thus we have,

$$\Psi = \lim_{N_g \to \infty} \Psi_{N_g} \tag{4.10a}$$

$$\Psi_{N_g} \equiv \sum_{n=1}^{N_g} \sum_i w_i(n\tau) |i\rangle \tag{4.10b}$$

Plugging equations (4.10a) and (4.10b) in the expression for the mixed energy estimator, we get,

$$E_{\text{mix}} = \lim_{N_g \to \infty} \frac{\left\langle \Psi_{N_g} \left| H \right| \Psi_T \right\rangle}{\left\langle \Psi_{N_g} | \Psi_T \right\rangle} \tag{4.11a}$$

$$= \lim_{N_g \to \infty} \frac{\sum_n \sum_i w_i(n\tau) \sum_j H_{ij} t_j}{\sum_n \sum_i w_i(n\tau) t_i} \tag{4.11b}$$

Based on the expression for E_{mix}, one may also define the "energy of the n^{th} generation of walkers" to be,

$$E_{\text{gen}} = \frac{\sum_i w_i(n\tau) \sum_j H_{ij} t_j}{\sum_i w_i(n\tau) t_i} \tag{4.12}$$

4.3 .3 Estimation of errors

Any quantity (number) measured using the Monte Carlo procedure can be considered *incomplete* without a knowledge of the magnitude of the statistical error. Thus it is important to have a reliable way of estimating errors.

We would be naive in using the recorded energy of every generation of walkers to estimate the error in the energy. This is because the walkers from one generation to the next are very *correlated* with one another; we would be underestimating the error if we did not take this into account.

The way around this is to divide the full "time" of the simulation into "time-blocks". Another way of saying this is that several walker generations are grouped together and the the energy is computed for that group. These energies can then be thought of as (nearly) independent "data samples" and whose standard deviation gives us an estimate of the statistical error.

An underlying assumption here is that the time of a "time-block" is chosen to be much greater than the *autocorrelation time* of the walkers. To make sure that the autocorrelation time (τ_{corr}) is indeed smaller than the time (T) of a time-block, we estimate it via,

$$\langle E^{(b)}(t+T) E^{(b)}(t) \rangle - \langle E^{(b)}(t+T) \rangle \langle E^{(b)}(t) \rangle \sim \exp(-t/\tau_{\text{corr}}) \tag{4.13}$$

where $E^{(b)}$ is the energy recorded over every time-block.

The systematic errors, because of approximations in the projection process, are (in general) hard to estimate. Since we adjust E_T to keep the population of walkers roughly constant, we introduce a "population control error" (see a way of estimating the population control error in the work by Umrigar et al. [16]). In the case of FCIQMC/SQMC, we will see that an additional systematic error exists owing to the finite population, but much larger than population-control, and which has its origin in the "initiator" approximation (see section 4.4 .2). Thus, the hope is to work with "large enough" populations such that the systematic error is smaller than the statistical error thereby not affecting the results of the calculation.

This expectation is quite idealistic. In practice, there were systems (such as the Hubbard model at large fillings and large U/t) we simulated [8] that had a significant "initiator bias" that could not be reduced (to a value lower than the statistical error) for walker populations we could afford in our calculations (on a single core).

4.3 .4 Time step

Up to this point our discussion assumes that the projector necessarily projects out the ground state wavefunction when applied sufficiently many times (ideally infinite) to a starting state.

To ensure that this is the case, we need to set τ (to a value below some upper bound) to make the ground state wavefunction (with lowest eigenvalue of H) correspond to the eigenvalue of the projector which has the largest magnitude

[8] This bias did not seem to be a problem for the quantum chemical systems we simulated.

(the reader may refer to the discussion of the power method in section 2.1).

The eigenvalue of the projector corresponding to the lowest eigenvalue of H (the ground state energy E_0) is $1 + \tau(E_T - E_0)$ and the largest eigenvalue of H (the highest excited state energy is E_H) is $1 + \tau(E_T - E_H)$. We demand that,

$$|1 + \tau(E_T - E_0)| > |1 + \tau(E_T - E_H)| \tag{4.14}$$

In the limit that we are sampling the ground state, E_T is equal to E_0 and thus condition (4.14) becomes,

$$1 > |1 + \tau(E_0 - E_H)| \tag{4.15}$$

Now use $E_0 < E_H$ and open up the modulus to get two conditions,

$$1 > 1 + \tau(E_0 - E_H) \tag{4.16}$$

$$1 > -1 - \tau(E_0 - E_H) \tag{4.17}$$

The two conditions (4.16) and (4.17) imply,

$$0 < \tau < \frac{2}{E_H - E_0} \tag{4.18}$$

Thus, if we knew the highest energy E_H and the lowest (ground state) energy E_0 in the many body spectrum, we can set τ to its maximal value of $2/(E_H - E_0)$. But since we do not know E_H and E_0 we try to arrive at an approximate estimate τ_{approx}.

We can roughly estimate τ_{approx} using some knowledge of the model under consideration. In reference to the Hubbard model on the square lattice we obtain a crude estimate for the largest eigenvalue E_H, by considering the largest diagonal element obtained by maximizing the number of doubly occupied pairs,

$$E_H \approx \text{diag}_{\text{max}} = U\text{min}\,(n_u, n_d) \tag{4.19}$$

To estimate the ground state energy E_0, we simply calculate the Hartree Fock energy.

Practically however, the value of τ we used in our simulations is much smaller than the upper bound derived above (for the case of deterministic projection). We scaled the upper bound on τ by a factor κ that we empirically found to be in the range of 0.1 to 0.5 (depending on the system and the choice of moves etc.).

4.3 .5 Monte Carlo Moves

We have already discussed the walker dynamics in section 4.3 .1 and classified the moves as "diagonal" and "off diagonal" based on the terms they correspond to in the application of the projector (see equation (4.7)). The diagonal move is straightforward to perform, it involves a simple rescaling of walker weights and needs no further discussion.

Recall the off diagonal moves correspond to the terms $-\sum_j \tau H_{ij} C_j(t)$ that occur in equation (4.7). In principle, for a given walker associated with configuration j, one may create walkers on *all* the states i that are "connected" to it via the Hamiltonian (i.e. $H_{ij} \neq 0$). However, this is computationally infeasible (it is equivalent to performing exact projection) as it will lead to a rapidly growing number of walkers, and we will quickly run out of resources to handle them. Instead, one only "samples" the action of the off diagonal term, by probabilistically carrying out this action.

Before proceeding with this discussion, we remark on an aspect common to

the "moves" we discuss here. We divide large walker weights into smaller ones before performing the move. For example, a walker with weight 5.5 will be split into 5 walkers of weight 1.1 and for each one of these walkers an off-diagonal move will be performed independently. (If the weight of the walker is less than 1 then the walker weight remains the way it is). The advantage of doing this splitting (or "branching" [17]) is that it reduces the statistical fluctuations introduced in the spawning process. The above mentioned process is unbiased: it does not affect the quantum mechanical averages being evaluated, but changes only the *efficiency* (the magnitude of the statistical errors) of the stochastic projection.

There is some ingenuity involved in how one might perform the off diagonal move. Every "walker move" from j to i can be thought of consisting of two parts: The first one of these is the "proposal step", where configuration i is proposed with a certain probability $p(j \rightarrow i)$. The second part is the "acceptance step" (which is *not* the Metropolis accept-reject). We require that the total probability $p(j \rightarrow i)\mathcal{A}(j \rightarrow i)$ for the parent walker at j spawning a child walker on i is,

$$p(j \rightarrow i)\mathcal{A}(j \rightarrow i) = |\tau H_{ij}| \tag{4.20}$$

The acceptance probability $\mathcal{A}(j \rightarrow i)$ and the weight of the parent walker are used to determine the weight of the child walker

$$w_{\text{child}} = \mathcal{A}(j \rightarrow i) \times w_{\text{parent}} \times \text{sign}(-\tau H_{ij}) \tag{4.21}$$

There are two distinct "off diagonal moves" in our code which differ in their choice of $p(j \rightarrow i)$. The first of these is called the "uniform move". The idea is to spawn a progeny walker on state i which is "connected to" the parent walker living on state j. To do so, one makes a list of all possible connections to the

state j. This list is not made explicitly: the terms in the Hamiltonian directly tell us rules for moving electrons which give us a way of calculating the total number of connections. It is possible that the terms in the Hamiltonian when acting on state j will lead to unphysical states (such as two electrons of the same spin on the same site or orbital forbidden by the Pauli exclusion principle) and/or states which have a zero Hamiltonian matrix element for a non-trivial reason. All of these possibilities are included in the "list of possibilities" when making the "uniform move", which (often) makes it easy to exactly calculate the "Number of possibilities". The proposal probability $p(j \rightarrow i)$ for any i is set "uniformly" to exactly 1/Number of possibilities.

The second choice of move is the "heat bath move" and relies on explicitly constructing the list of all connections i to state j and computing the projector matrix elements $-\tau H_{ij}$. Once this list has been constructed, walkers may be spawned on one or more states i by this method. If one walker is spawned, the proposal probability for choosing a state i to spawn to is,

$$p(j \rightarrow i) = \frac{|\tau H_{ij}|}{\sum_k |\tau H_{kj}|} \tag{4.22}$$

This walker gets the sign of $-\tau H_{ij}$ and a total weight of $w_{\text{parent}} \sum_k |\tau H_{kj}|$.

It is not always easy to choose between performing one move type over the other, as each have their advantages and disadvantages. The "uniform move", unlike the "heat bath" move, does not require the generation of the list of "connections" and associated computation of all the matrix elements, making it (relatively) computationally cheap. However, by design, the uniform moves choose "unimportant states" as frequently as "important ones" to spawn on, thereby effectively slowing down the projection process. Since there can be large fluctuations of walker weights by spawning on few states, practically it also means one

may need a much smaller time step τ than what one would consider "optimal" based on the estimate of $2/(E_H - E_0)$.

4.3 .6 Join Operation

After the progeny walkers have been spawned, it is likely that the new list (or "generation") of walkers is longer than desired (the objective is to keep the walker population roughly constant) and consists of walkers with "small weights". An *unbiased* way of reducing the size of this list is to "join walkers" with small weights [16].

To be explicit, we scan the list of walkers and if their weights exceed a certain threshold w_{min} they do not participate in the "join operation" (a common choice for w_{min} was 0.5). The walkers which have weight smaller than this cutoff are grouped into clusters whose combined weight is equal to or just exceeds w_{min}. This "grouping" of walkers may be done by sequentially scanning the list of walkers. To give a concrete example consider $w_{min} = 0.5$ and consider a walker list having weights 1.2, 4.0, -0.1, 0.25, -3.5, 0.3, 0.46, -0.4, 0.12. The walkers with weights 1.2, 4.0 and -3.5 do not participate in the join operation. The walkers with weight -0.1 and -0.4 form one group of walkers and the walkers with weights 0.25, 0.30 and 0.46,0.12 form two other groups.

In each group, the combined absolute weight of the group is given to *only one* walker preserving the sign of the walker. Thus in group 1 the walker with weight -0.1 gets the full weight of -0.5 with $1/5$ probability, the -0.4 weight walker gets the full weight of -0.5 with probability $4/5$.

4.4 Full Configuration Interaction - Quantum Monte Carlo (FCIQMC)

The main ingredients of projector Monte Carlo have been discussed in the preceding section. There is often scope for improvements in the efficiency of algorithms in terms of storage, speed of computation of matrix elements and good choices of proposal probabilities for moves. However, all these improvements do no great service to ameliorating the 'sign problem'.

Two ingredients that are believed to be crucial to ameliorating the sign problem in QMC form the subject of the papers by Alavi and coworkers [3, 4]. The purpose of this exposition is also to provide more context for understanding our SQMC method.

4.4 .1 Walker annihilation

Alavi et al. [3] proposed working in the space of "determinants" (i.e. in the second quantized notation). Note that working in an "antisymmetrized basis" *does not eliminate* the sign problem, but might have some advantages [18] in promoting "walker coincidences", in comparison to the case where individual electrons have labels (i.e. first quantization) [9].

The main problem with the projector QMC procedure described in section 4.3 is that there are walkers of two signs. To appreciate why this is a "problem", we follow the ideas presented in a recent paper by Spencer et al. [19].

Split the projector into a part that comprises only of non negative matrix

[9] For our purposes, it is not crucial whether the particles are fermionic or spins (or even bosons). As long as the projector (written in the basis of our choice) has off diagonal negative elements, there is a sign problem.

elements P_+ and another that comprises of P_- [10]. Thus we may write the full projector P as,

$$P = P_+ - P_- \tag{4.23}$$

Positive walkers at time $(n+1)\tau$ are created from walkers at time $n\tau$ that have positive (negative) matrix elements and positive (negative) walker weights and negative walkers are created from at time $n\tau$ that have negative (positive) matrix elements and positive (negative) walker weights. Thus the equations satisfied by the the positive and negative walker populations, represented by vectors $\mathbf{w}_+$ (all positive real numbers) and $\mathbf{w}_-$ (all negative real numbers), in the large time limit, are,

$$\mathbf{w}_+ = P_+\mathbf{w}_+ - P_-\mathbf{w}_- \tag{4.24a}$$

$$\mathbf{w}_- = P_+\mathbf{w}_- - P_-\mathbf{w}_+ \tag{4.24b}$$

One can define the total weight of the walkers $\mathbf{w} = \mathbf{w}_+ + \mathbf{w}_-$ and the total *absolute* weight of the walkers $\mathbf{n} = \mathbf{w}_+ - \mathbf{w}_-$ and recast equations (4.24a) and (4.24b) into the form,

$$\mathbf{w} = (P_+ - P_-)\mathbf{w} \tag{4.25a}$$

$$\mathbf{n} = (P_+ + P_-)\mathbf{n} \tag{4.25b}$$

Thus we see that there are effectively two equations at play in the walker dynamics. It is equation (4.25a), whose eigenvalue and eigenvector we desire in our simulation, but there is equation (4.25b) we have to deal with as well. Since the dominant eigenvalue of $P_+ + P_-$ is larger than the dominant eigenvalue of $P_- - P_-$, we will see that if allowed to run freely, the projector Monte Carlo algorithm will give a vanishingly small signal for $\mathbf{w}$ in comparison to $\mathbf{n}$ (i.e. the absolute weight of the walkers will be far greater than their combined signed

[10] P_- is the part of the projector that creates the "sign problem"

weight). Thus the problem of finding the fermionic ground state is hard (unless P_- is exactly zero i.e. no sign problem).

The ingredient that can be introduced here is to perform "annihilation" (or "cancellation") of walkers of opposite weights [20] to enhance the desired signal w. In short, to use projector QMC for systems with a sign problem, it is important to introduce a coupling between the positive and negative walker weights (maybe even in a slightly "biased way") to *favor cancellations*.

FCIQMC aims to achieve a "reasonable rate of cancellations" by adding or subtracting walker weights at every time step. In order to have a sufficiently large rate of "walker coincidences" one needs to make sure that their number is "large". The "large walker" limit which could go into millions or in some cases of billions of walkers or much larger depending on the size of the Hilbert space in question and the severity of the sign problem. This is in stark contrast to sign problem free calculations where a few hundred to few thousand walkers are enough for the purpose of simulation.

4.4 .2 The initiator approximation

The main problem with FCIQMC is the requirement of very large number of walkers to achieve a high rate of walker cancellations. To ameliorate this problem Cleland et al. [4] introduced the "initiator approximation" which we presently discuss.

Though the initiator approximation can come in various forms, its main essence is motivated by the following: Walkers which have "very small" weights

and whose signs are not coherent with the sign of the larger weight walkers (which are assumed to faithfully represent their signs of the true wavefunction), may spawn progeny which in turn have the 'wrong sign' weights. It is these walkers that may play an instrumental role in the propagation of "noise" and ideally we would like to suppress their role in the projection process.

One may thus modify the walker dynamics and deny progeny to be spawned from the walkers with "small weights". The "preferred walkers" or "initiators" are those walkers which have developed enough weight (or walker population), beyond some user defined cutoff (known as "initiator threshold"). The list of "initiators" is not fixed, it may be quite dynamic: states which were once initiators in the past may not be so in the future and vice versa. One may also broaden the definition of "initiators" to include certain "preferred states" to be "permanent initiators" based on some user specified criterion (for example the Hartree Fock determinant never loses its initiator status).

Clearly this idea is *biased*, i.e. it introduces a systematic error in the projection process and apriori it is not clear what the severity of this approximation really is. However, one must appreciate that in the limit of large walker population all determinants in the space will have enough amplitude to be able to spawn (every state is an "initiator"), so the approximation becomes exact in this limit. Another limit where the initiator approximation becomes exact is when the initiator threshold goes to 0 (though we are plagued by the sign problem in this limit and are back to FCIQMC).

The main aim of the "initiator approximation" is thus to bring down the walker population participating in the projection process to a manageable number in comparison to the original version of FCIQMC [3]. However, the walker

population must be large enough such that the systematic error ("initiator bias") is brought down to levels at or below the magnitude of statistical errors in the energy.

Even though the approximation becomes "exact" in the infinite population limit, we observed that (in practice) the *bias* is not eliminated in a monotone fashion on increasing the size of the walker population [11]. There appears to be no rigorous justification for why the approach to the infinite walker limit must be "smooth".

[11] The "initiator bias" is quite system specific. For example, for the chemistry systems the initiator approximation is found to work quite well but for the Hubbard systems there is a large dependence of the initiator bias and has found to even depend on the choice of time step τ.

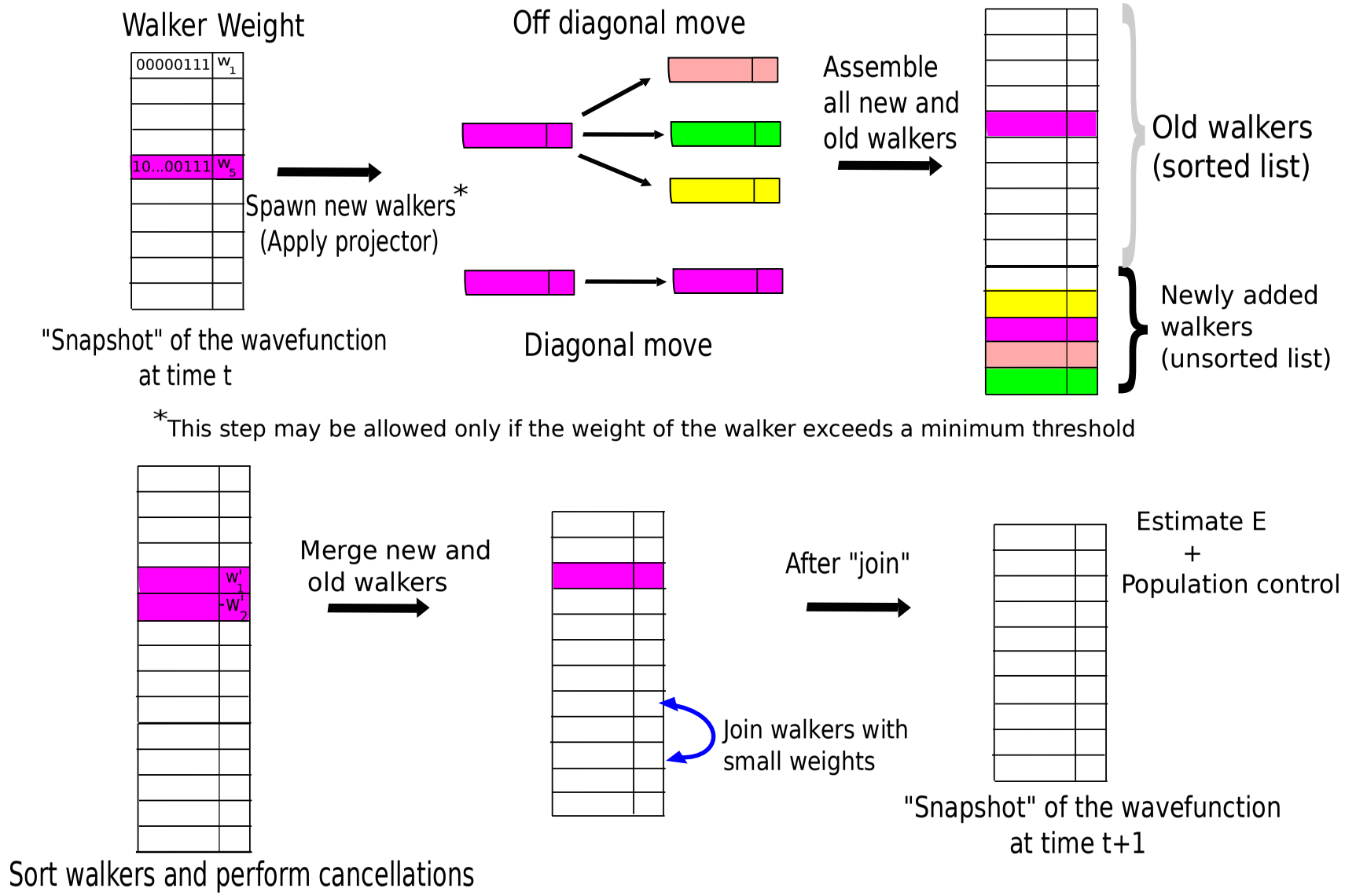

Figure 4.1: Summary of the steps involved in the FCIQMC algorithm.

4.5 Semistochastic QMC

We proposed a semi-stochastic improvement to FCIQMC, in which we perform the projection onto the ground state deterministically in a relatively small "important" space and stochastically everywhere else. In this section I will provide the details of the projection process, keeping in mind the general ingredients for Projector (Green's function) Monte Carlo and the recent FCIQMC development.

4.5 .1 Generation of the trial wavefunction and deterministic space

The first ingredient necessary for SQMC is to decide *before* the QMC run, the division of the Hilbert space into "important" and "unimportant" states. What is "important" and what is "unimportant" is arbitrary, but it is reasonable to assume that only "good choices" for this division are desired and ultimately useful. The projector will be applied deterministically for states within the "important subspace" and hence it is more apt to call it the "deterministic subspace". We will show when discussing our results, that the choice of deterministic space (associated with the projector) and the trial wavefunction (used for mixed energy measurement) can greatly enhance the *efficiency* of SQMC calculations over conventional FCIQMC calculations.

A simple choice for performing the "division of the Hilbert space" may be to allow states that are certain (small) number of steps away from the Hartree Fock state (i.e. look at the excitation levels of the state with respect to Hartree

Fock) to form the "deterministic subspace". However, instead of resorting to such heuristics, it is desirable to have an automated way of performing this selection without any assumptions about the system under consideration. This is what we finally adopted, to generate the results for this Chapter.

SQMC also incorporates the idea of working with a trial wavefunction Ψ_T beyond just a single determinant wavefunction. (In FCIQMC [3, 4], only a single state (the HF determinant) was used to compute the mixed energy). We emphasize, that improving $|\psi_T\rangle$ has its advantages because its quality can reduce fluctuations and bias in the mixed estimate of the dominant eigenvalue. This reduction can be achieved with almost no additional computational cost by storing nonzero $\sum_{j\in\mathcal{T}} H_{ij}t_j$ terms.

Here we briefly describe an algorithm that automates the creation of the "deterministic" space and the trial wavefunction based on some parameters input by the user. In particular, the user *predecides* the desired sizes of the spaces and provides a "guide" for how these spaces must be created. There might be different guidelines the user provides for the two spaces; however in practice we found that one set of guiding rules was adequate to generate both.

The principle behind the creation of these spaces is to use a few powers of the projector followed by a weight based truncation of the obtained states and diagonalization in the space of the retained states. To be concrete, our algorithm is,

Step 1 Begin with the Hartree Fock state(s) and generate all states "connected" to it via one application of the Hamiltonian to it. Call them the "retained states".

Step 2 Diagonalize the Hamiltonian in the basis of "retained states" (at the first iteration retain the Hartree Fock determinant + its connections) and obtain the lowest energy eigenvector in this space. For convenience, sort this vector by weight of each state (in descending order of absolute magnitude).

Step 3 The user (as part of the "truncation guidelines") will prespecify how many of the obtained states are to be retained and how many of these retained states are to be deemed as "initiators". For example, if the user says 5 initiators and 12 states (in total) are to be retained, then the states with the 5 largest weights become the "initiators" and the next 7 states following them become the "non initiators". The rest of the states are completely discarded. If one (or more) states have nearly the same weight as the least important state kept in the "retained space", we ensure we select them as well, even if that means going over any user specified threshold. With respect to the example above, the 13^{th} and 14^{th} state might have the same weight as the 12^{th} one in which case we include them in our list of "retained states".

Step 4 Treat the initiators as the "reference" and generate all connections (via another application of the Hamiltonian) to this reference. Note that the "non initiators" are not involved in this stage.

Step 5 Consider the union of the newly generated states and all the previously retained states (initiators and non initiators) and repeat Steps 2-4 for a number of times pre-specified by the user.

Step 6 At the last application of the Hamiltonian, there is no requirement to divide the lowest energy eigenvector into initiators and non initiators.

If the trial wavefunction is desired, one may take the lowest energy eigen-

vector generated at the end of Step 6 as the trial wavefunction Ψ_T. If the deterministic space is desired, one may take all the states generated at the end of Step 6 and form the projector in that space and store it sparsely. An important point to note here is that, we can only consider a "deterministic space" that is small enough such that the projection matrix in this space can be (sparsely) stored (in addition to storage of non zero energy numerators $\sum_{j\in\mathcal{T}} H_{ij}t_j$) without worrying about computer memory constraints.

4.5 .2 Applying the projector

Now we describe how the projector is "applied" to a set of walkers in the SQMC method. For this purpose, the reader may want to refer to the section 4.3 to put things in perspective.

Let $\mathcal{D}$ be the set of indices of vector components treated deterministically, and let $\mathcal{S}$ be the set of those treated stochastically, where $\mathcal{D} \cup \mathcal{S} = \{1, \ldots, N\}$, $\mathcal{D} \cap \mathcal{S} = \emptyset$, and $|\mathcal{D}| \ll N$. Accordingly, P is the sum of a deterministic block $P^{\mathcal{D}}$, and a stochastic complement $P^{\mathcal{S}}$,

$$P = P^{\mathcal{D}} + P^{\mathcal{S}}, \tag{4.26}$$

where

$$P_{ij}^{\mathcal{D}} = \begin{cases} P_{ij}, & \text{if } i,j \in \mathcal{D}, \\ 0 & \text{otherwise.} \end{cases} \tag{4.27}$$

Note, that if the deterministic space is the entire space, then there is no sign problem or statistical noise. Consequently, we can expect that using a deterministic subspace that is not the entire space will reduce the sign problem and statistical noise.

We now discuss how the action of the projector P is stochastically implemented to get the walker weights from time t to time $t+\tau$, with an emphasis on highlighting the differences with respect to purely stochastic projection.

1. To account for the off-diagonal elements in $P^{\mathcal{S}}$, for each walker on $|j\rangle$, a move to $|i\rangle \neq |j\rangle$ is made with probability $p(j \to i)$. A single walker on $|j\rangle$ contributes
$$\begin{cases} 0, & i,j \in \mathcal{D} \\ \dfrac{P_{ij}}{p(j \to i)} \dfrac{w_j^{(t)}}{n_j^{(t)}} & \text{otherwise} \end{cases} \tag{4.28}$$
to the signed walker weight on $|i\rangle$. The choice of $p(j \to i)$ determines the probability that particular off-diagonal moves are made (see section 4.3 .5).

2. The diagonal elements are rescaled for $|j\rangle \in \mathcal{S}$ as is mentioned in section 4.3 .1.

3. Deterministic evolution is performed with $P^{\mathcal{D}}$ (stored sparsely in memory) i.e. this part of the projector is applied exactly. The contribution to the signed weight on $|i\rangle$, with $|j\rangle \in \mathcal{D}$, is
$$\sum_{j \in \mathcal{D}} P_{ij}^{\mathcal{D}} w_i^{(t)}. \tag{4.29}$$

4. Finally, for each $|i\rangle$, all signed walker weights generated on $|i\rangle$ are summed.

5. Walkers living on states in the deterministic space never lose their initiator status i.e. they are always allowed to spawn children walkers independent of their weight. Other walkers are treated as initiators or non-initiators based on their weight. In the conventional initiator approach, a state must have a minimum absolute weight w in order to contribute an off-diagonal

move. In our modification of this approach, $w = cm^p$, where m is the number of moves the walker has made since its last visit to the deterministic space and c and p are constants, chosen to be 1 for the applications in this Chapter.

6. Once the new "generation" of walkers has been obtained, the join operation is performed. However, states which are in $\mathcal{D}$ do not participate in the join irrespective of their weights.

After sufficiently many (stochastic) multiplications by P, contributions from subdominant eigenvectors die out on average and the walkers are said to be "equilibrated". The way we detect equilibration is by checking the stability (relative constancy) of three quantities:

1. The weight on the most dominant state (say the Hartree Fock state) deemed to be a "permanent initiator".
2. The total population of walkers (absolute sum of walker weights)
3. The mixed energy

In order to speed up equilibration, we also choose a larger time step than what is finally used when measuring the energy.

At the end of the equilibration process, we reset our estimators for calculating the projected energy and start afresh [12]. To see how to calculate the running average for the mixed estimator for the energy, see section 4.3 .2.

[12]Note that at this point, the walker population is not affected, only the computation of averages is restarted

4.6 SQMC Simulations of the Hubbard Model

Given the introduction to SQMC, we now apply it to the Hubbard Hamiltonian and benchmark our results against previous QMC approaches. To do so, we first write down the Hubbard Hamiltonian in momentum space and discuss how the Monte Carlo moves were carried out.

4.6 .1 Hubbard Hamiltonian in momentum space

Consider the Hubbard Hamiltonian,

$$H_{\text{Hubbard}} = -t \sum_{\langle i,j \rangle, \sigma} c^{\dagger}_{i,\sigma} c_{j,\sigma} + U \sum_{i} n_{i,\uparrow} n_{i,\downarrow} \tag{4.30}$$

defined on the 2D square lattice with periodic boundary conditions in both directions. We can re-express (4.30) in the plane wave basis by Fourier transforming the electron creation - annihilation operators as follows,

$$c^{\dagger}_{\mathbf{r},\sigma} = \frac{1}{\sqrt{N}} \sum_{\mathbf{k}} e^{i\mathbf{k}\cdot\mathbf{r}} c^{\dagger}_{\mathbf{k},\sigma} \tag{4.31}$$

$$c_{\mathbf{r},\sigma} = \frac{1}{\sqrt{N}} \sum_{\mathbf{k}} e^{-i\mathbf{k}\cdot\mathbf{r}} c_{\mathbf{k},\sigma} \tag{4.32}$$

where N is the total number of sites in the system. $\mathbf{k}$ refers to the single particle momenta which are given by $(k_x, k_y) = (\frac{m\pi}{L_x}, \frac{n\pi}{L_y})$, where m, n are even integers. The momentum in each direction is in the range $(-\pi, \pi]$.

Consider the hopping part of the Hamiltonian. Substituting the above relations we get,

$$H_{\text{hop}} = -\frac{t}{N} \sum_{\langle i,j \rangle} \sum_{\mathbf{k},\mathbf{k}',\sigma} e^{i\mathbf{k}\cdot\mathbf{r}_i} e^{-i\mathbf{k}'\cdot\mathbf{r}_j} c^{\dagger}_{\mathbf{k},\sigma} c_{\mathbf{k}',\sigma} \tag{4.33}$$

which (for a translationally invariant lattice) may be recast into the form,

$$H_{\text{hop}} = -2t \sum_{\mathbf{k},\sigma} \left(\cos(k_x a) + \cos(k_y a)\right) c^{\dagger}_{\mathbf{k},\sigma} c_{\mathbf{k},\sigma} \tag{4.34}$$

For convenience of notation we define,

$$\epsilon(\mathbf{k}) \equiv -2t \left(\cos(k_x a) + \cos(k_y a)\right) \tag{4.35}$$

The hopping part of the Hamiltonian is now diagonal in momentum space. So this part of the Hamiltonian leads only to "diagonal moves". The Hamiltonian matrix element for a configuration of electrons in momentum space $|\{k_\uparrow\}\{k_\downarrow\}\rangle$ is,

$$\langle \{k_\uparrow\}\{k_\downarrow\} | H | \{k_\uparrow\}\{k_\downarrow\}\rangle = \sum_{k_\uparrow \in occupied} \epsilon(\mathbf{k}) + \sum_{k_\downarrow \in occupied} \epsilon(\mathbf{k}) \tag{4.36}$$

(We will soon see that there is a diagonal contribution from the interaction energy part of the Hamiltonian as well, but it is constant).

Now consider the interaction energy term of the Hubbard Hamiltonian. Plugging in the Fourier transformed electron creation-destruction operators we get,

$$\begin{aligned} H_U &= \frac{U}{(\sqrt{N})^4} \sum_i \sum_{k,k',q,q'} e^{i\mathbf{k}\cdot\mathbf{r}_i} e^{-i\mathbf{k}'\cdot\mathbf{r}_i} e^{i\mathbf{q}\cdot\mathbf{r}_i} e^{-i\mathbf{q}'\cdot\mathbf{r}_i} c^{\dagger}_{\mathbf{k},\uparrow} c_{\mathbf{k}',\uparrow} c^{\dagger}_{\mathbf{q},\downarrow} c_{\mathbf{q}',\downarrow} && \text{(4.37a)} \\ &= \frac{U}{N^2} \sum_{k,k',q,q'} \sum_i e^{i\mathbf{r_i}\cdot(\mathbf{k}-\mathbf{k}'+\mathbf{q}-\mathbf{q}')} c^{\dagger}_{\mathbf{k},\uparrow} c_{\mathbf{k}',\uparrow} c^{\dagger}_{\mathbf{q},\downarrow} c_{\mathbf{q}',\downarrow} && \text{(4.37b)} \end{aligned}$$

and using the identity $\sum_i e^{i\mathbf{r_i}\cdot(\mathbf{k}-\mathbf{k}'+\mathbf{q}-\mathbf{q}')} = N\delta_{\mathbf{k},\mathbf{k}'-\mathbf{q}+\mathbf{q}'}$ and $c_{\mathbf{k}',\uparrow} c^{\dagger}_{\mathbf{q},\downarrow} = c^{\dagger}_{\mathbf{q},\downarrow} c_{\mathbf{k}',\uparrow}$ we get,

$$H_U = \frac{U}{N} \sum_{k',q,q'} c^{\dagger}_{\mathbf{k}'-\mathbf{q}+\mathbf{q}',\uparrow} c^{\dagger}_{\mathbf{q},\downarrow} c_{\mathbf{k}',\uparrow} c_{\mathbf{q}',\downarrow} \tag{4.37c}$$

To give it a more illuminating form we could use the variable $\mathbf{Q} = \mathbf{q} - \mathbf{q}'$ giving us,

$$H_U = \frac{U}{N} \sum_{k',q',\mathbf{Q}} c^{\dagger}_{\mathbf{k}'-\mathbf{Q},\uparrow} c^{\dagger}_{\mathbf{q}'+\mathbf{Q},\downarrow} c_{\mathbf{k}',\uparrow} c_{\mathbf{q}',\downarrow} \tag{4.38}$$

At this point we note that the term corresponding to $\mathbf{Q} = 0$ is simply a constant (so it could be dropped or simply added to the diagonal without changing any of the physics. For a fair comparison with the real space case we could just add this constant right at the end of the calculation.) i.e.,

$$\frac{U}{N}\sum_{k',q'} c^{\dagger}_{\mathbf{k}',\uparrow}c^{\dagger}_{\mathbf{q}',\downarrow}c_{\mathbf{k}',\uparrow}c_{\mathbf{q}',\downarrow} = \frac{U}{N}\sum_{\mathbf{k}'} c^{\dagger}_{\mathbf{k}',\uparrow}c_{\mathbf{k}',\uparrow}\sum_{\mathbf{q}'} c^{\dagger}_{\mathbf{q}',\downarrow}c_{\mathbf{q}',\downarrow} \tag{4.39a}$$

$$= \frac{U}{N}N_{\uparrow}N_{\downarrow} \tag{4.39b}$$

Thus the off diagonal matrix elements are computed (algorithmically) as follows,

1. If there is exactly one electron in a different location in the up bra and up ket determinants and exactly one in the down bra and down ket determinants, then the matrix element is possibly non zero. Else return a zero matrix element.
2. If Step 1 does not yield a zero matrix element, see if the difference of momenta in the up bra and up ket is exactly equal to negative of the momentum difference in the down bra and down ket. If yes, the matrix element is $\pm U/N$ (with the sign coming from the anticommutation relations of electron operators).‘

To find the list of connected (via the Hamiltonian) determinants for a given configuration, we choose an electron in the up configuration and one in the down configuration. For each such pair of electrons, add momentum $\mathbf{Q}$ to the chosen up electron and momentum $-\mathbf{Q}$ to the down chosen electron. If no such final momenta exist or the final momenta are not allowed (by Pauli's exclusion principle) no new determinant is constructed for that $\mathbf{Q}$. Perform the calculation for all $\mathbf{Q}$, each $\mathbf{Q}$ giving a connected determinant.

We use exact diagonalization studies and other guides to select the correct momentum sector to work in. One must note that the Hamiltonian conserves momentum so the Monte Carlo moves ensure we stay in the same momentum sector as the starting state.

For the purpose of this Chapter we restrict ourselves to closed shell systems that have total momentum $\mathbf{K} = (0,0)$. (Other systems with $n_\uparrow = n_\downarrow$ and that have a known non-degenerate ground state can be argued to have a total momentum of (0,0). This follows from the fact that the Hamiltonian is time reversal symmetric i.e. under the transformation $t \to -t$, we must have $\uparrow \to \downarrow$, $\downarrow \to \uparrow$ and $\mathbf{K} \to -\mathbf{K}$. Hence the ground state momentum must be $(0,0)$.)

4.6 .2 Moves in momentum space

Given a up and down determinant in momentum space we select a random up electron having momentum $\mathbf{k}$ and random down electron having momentum $\mathbf{q}$. Then we choose another (empty) up electron momentum to scatter to (say $\mathbf{k}'$). This information yields the vector $\mathbf{Q} = \mathbf{k}' - \mathbf{k}$. Hence we can compute the new down momentum to scatter to $\mathbf{q}' = \mathbf{q} - \mathbf{Q}$. If there is no $\downarrow$ electron with momentum $\mathbf{q}'$, we compute the proposal probability

$$\text{proposal probability} = \frac{1}{n_\uparrow} \times \frac{1}{n_\downarrow} \times \frac{1}{N - n_\uparrow} \tag{4.40}$$

else we necessarily reject this move i.e. we do not spawn any walkers.

The reason we did not fully explore "heat bath moves" for this model is that the number of connections to a state (is approximately) $n_u n_d (N - \min(n_u, n_d))$ which scales poorly with system size.

4.6 .3 Results and Discussion

We now discuss the results obtained from our SQMC simulations. For various sizes of the deterministic space, we demonstrate the improvements of SQMC over the real weight version of FCIQMC defined by a deterministic space which includes only the Hartree-Fock determinant.

The systems we have focused on for this presentation correspond to fillings which correspond to "closed shells". We have performed "uniform moves" throughout and have not explored "heat bath moves" since they are in general computationally quite expensive because of the poor scaling of the connectivity of the Hubbard Hamiltonian in momentum space (see section 4.3 .5).

To show the gain in efficiency of SQMC we computed the relative efficiency, *i.e.*, the efficiency normalized by that of the stochastic method ($|\mathcal{D}| = 1$), with $|\mathcal{T}| = 1$,

$$\begin{aligned} \text{Relative efficiency} &\equiv \frac{\text{Efficiency of SQMC simulation}}{\text{Efficiency of SQMC simulation with } \mathcal{T}=1 \ \mathcal{D}=1} \\ &= \frac{\left(\text{Error}^2 \times \text{Time}\right)_{\mathcal{T}=1,\mathcal{D}=1}}{\left(\text{Error}^2 \times \text{Time}\right)_{\mathcal{T},\mathcal{D}}} \end{aligned} \tag{4.41}$$

Fig. 4.2 shows the relative efficiency of SQMC *vs.* the size of the deterministic space for the 8×8 square lattice Hubbard model with periodic boundaries, $U/t = 4$ and at a filling of 10 electrons (5 $\uparrow$ and 5 $\downarrow$). The orders of magnitude increases in efficiency demonstrate the benefits not only of SQMC but also of improving the trial wave function. The gain of just using the largest deterministic space is a factor of 22, while the benefit of just using the largest trial wave function is a factor of 42. Both together yield a factor of about 900 as seen in the plot, but the two gains are not always multiplicative.

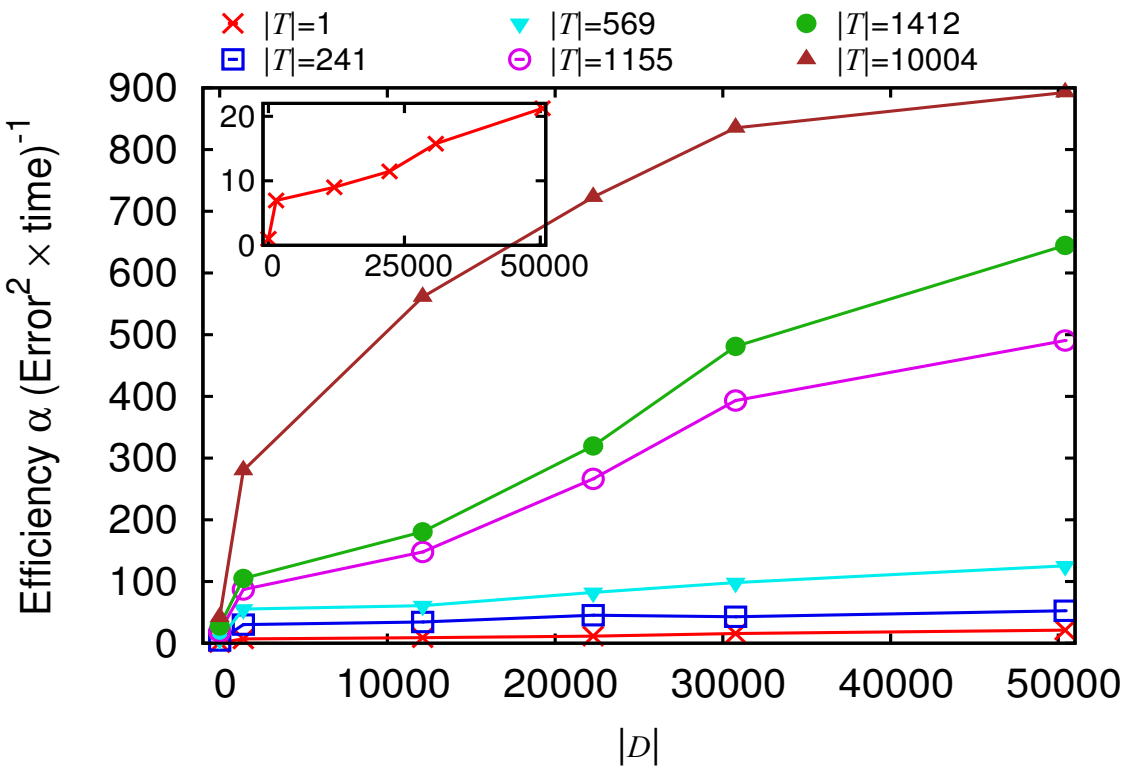

Figure 4.2: Relative efficiency of SQMC *vs.* dimension $|\mathcal{D}|$ of the deterministic space for the simple-square 8×8 Hubbard model with periodic boundaries, $U/t = 4$ and 10 electrons. Results are shown for trial wave functions of increasing size. The inset shows the $|\mathcal{T}| = 1$ curve on an expanded scale. For this system, $N \approx 10^{12}$.

While the statistical error is important, we would like to see how well the SQMC method is able to reduce the systematic error due to the "initiator approximation" (see section 4.4 .2). This we discovered, is quite system specific and depends on the choice of the trial wavefunction. In some cases, however, SQMC is not only much more efficient than the stochastic method, but also the initiator bias is *significantly* reduced.

For example, consider Fig. 4.3 which shows the biased estimates of the energy as obtained by both the SQMC and stochastic method *vs.* the average number of occupied determinants for the 8×8 Hubbard model with $U/t = 1$ and 50 electrons. SQMC appears to have essentially no bias, even with few walk-

ers. This is an advantage, as a larger average number of occupied determinants (corresponding to using a larger walker population) proportionately increases the time required for the SQMC calculation.

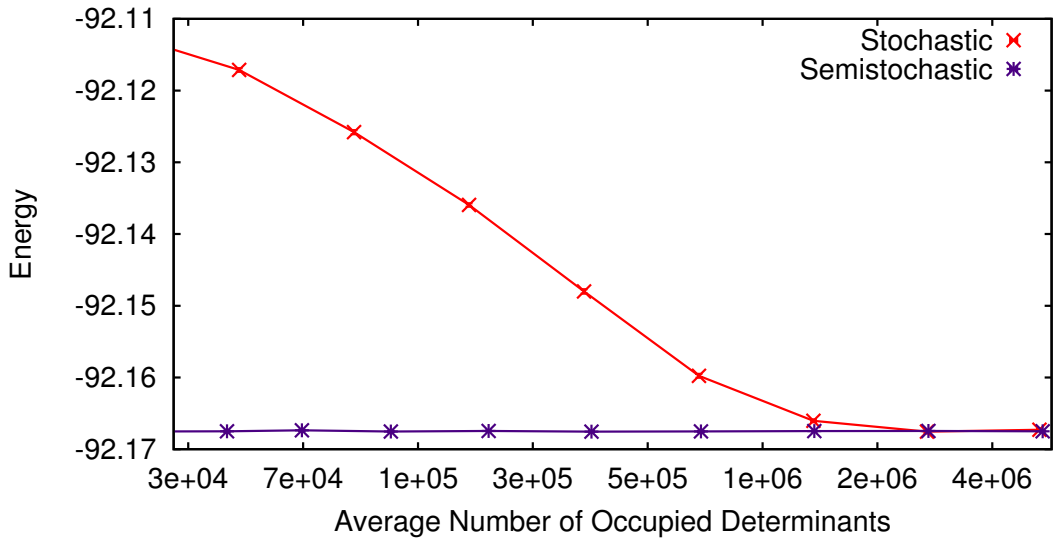

Figure 4.3: Energy of SQMC and the stochastic method *vs.* the average number of occupied determinants for the simple-square 8×8 Hubbard model with $U/t = 1$ and 50 electrons.

But the "initiator bias" is *not always* reduced with SQMC. For example, let us consider Figure 4.4 which shows the energy of the 8×8 Hubbard model at $U/t = 4$ and with a filling of 10 electrons using the SQMC method and the corresponding purely stochastic version. We observe that the two methods are consistent with each other in the "large walker" limit (which for this system seems to be around the one million mark). Also, for very small populations, the SQMC bias (with respect to the large walker limit) seems to be smaller than the corresponding FCIQMC method, but there is not much to choose between the methods beyond the 5000 walker mark.

The above examples also suggest that the size of the Hilbert space *alone* is not responsible for the potential gains that SQMC may or may not give. SQMC

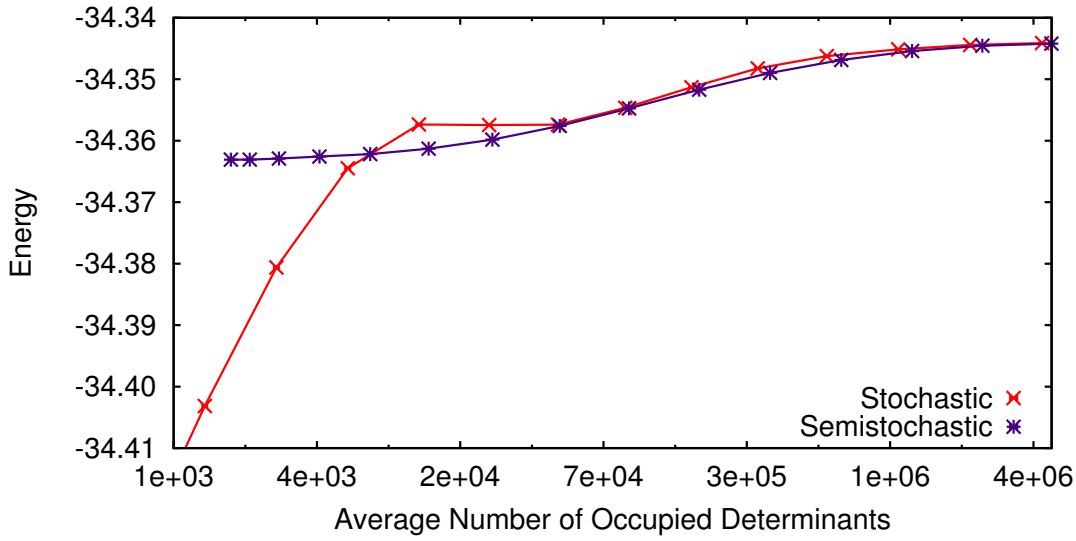

Figure 4.4: Energy of SQMC and the stochastic method *vs.* the average number of occupied determinants for the simple-square 8×8 Hubbard model with $U/t = 4$ and 10 electrons. The trial wave function for each of these calculations is the Hartree-Fock determinant. The deterministic space reference state for each SQMC calculation is the Hartree Fock determinant, yielding a deterministic space of 1412 determinants. For this system, $N \approx 10^{12}$.

is a profitable venture when the underlying wavefunction has a structure which has relatively small number of important states and the rest are relatively unimportant. Such a division of the Hilbert space does not depend only on the size, but also on the choice of basis employed and the amount of correlation present in the system.

Finally, we discuss our results for the Hubbard model for the 8x8 model with 26 electrons at $U/t = 4$, a challenging problem for SQMC. In Figure 4.5, we compare our results to other existing techniques, namely the Fixed Node Green's Function Monte Carlo (FN-GFMC) [15], Auxiliary Field Quantum Monte Carlo [21] and Constrained Path Monte Carlo [22].

First, we observe that the SQMC energies are significantly lower than the corresponding (variational) FN-GFMC result, obtained by choosing an opti-

mized Gutzwiller-Hartree Fock wavefunction (see for example Chapter 3). The AFQMC results have no systematic errors but their statistical error bars are large (0.1 t or so) because of the presence of a sign problem for this system. Meanwhile, the CPMC results are sign problem free but are known to be non variational (and biased).

However, recent unpublished results by Zhang [23], using a (variational) "released node" method show that the CPMC value shown in Figure 4.5 is probably quite accurate. This would mean that that even though SQMC energies are

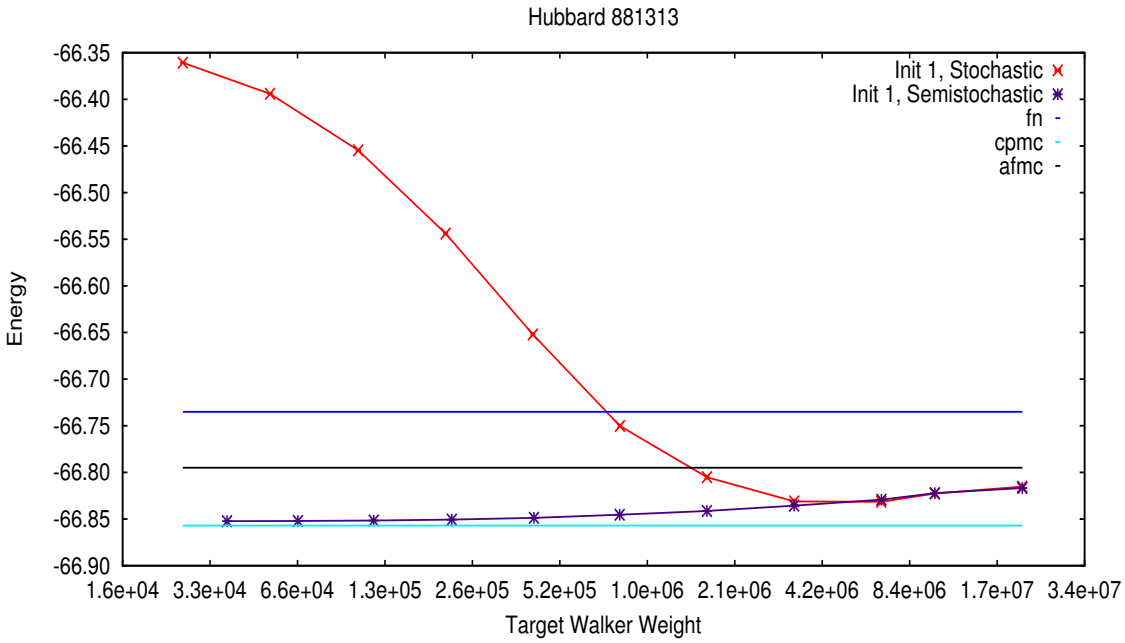

Figure 4.5: The energy of the 8x8 Hubbard model with 26 electrons, compared to other Quantum Monte Carlo methods.

quite competitive with existing techniques for this system (and come with small statistical errors), its systematic errors are somewhat uncontrolled and possibly even non-monotone. This is evidenced by the fact that the SQMC energy is close to the CPMC value at small walker populations and *increases* at larger populations. This means that the value for the energy must decrease again at some *even larger* walker population not accessible in our current implementation. This is

perhaps the most worrying feature about the "initiator approximation", a feature which we did not see for quantum chemical systems.

As mentioned previously, SQMC is limited by the size of the deterministic space that can be stored. In an effort to go to larger walker populations and larger sizes of the deterministic space, we implemented the symmetries of the Hubbard Hamiltonian on a square lattice into our SQMC code (for details see Appendix 4.A). Even though this gives only a (linear) reduction in the size of the space by a factor of 16, it can be the crucial difference between being able to store the projector (in computer memory) versus not being able to do so.

Figure 4.6 shows energies for the 8×8 Hubbard model with 26 electrons at $U/t = 4$, and serves as a benchmark for testing our implementation of symmetries. For both methods shown here, we have taken $\mathcal{T} = 1$ which corresponds to the HF determinant (note that the HF determinant is invariant under symmetry operations for closed shells). Also, the same deterministic space was chosen: the symmetry-adapted Hilbert space has (roughly) a factor of 16 smaller size than the space without symmetries imposed.

We observe that the projected energy *vs* walker population curve with the use of symmetry is essentially a rescaled version of the curve obtained without the use of symmetry. Thus, one could in principle go to roughly 16 times larger walker populations and deterministic spaces with this implementation. More work in this direction is in progress.

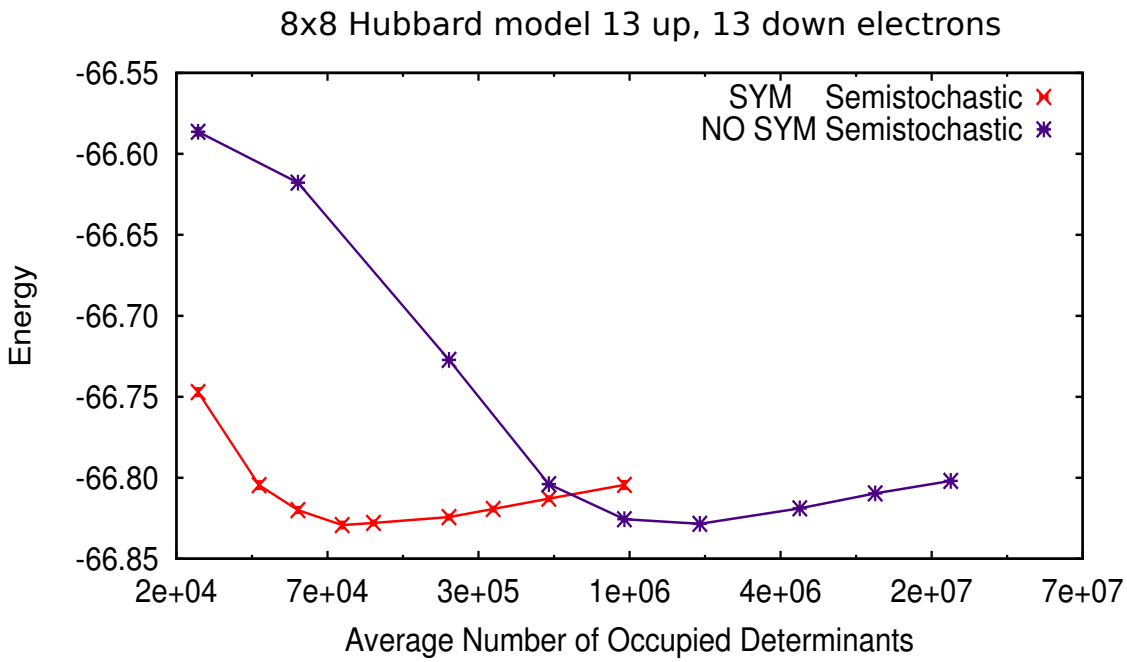

Figure 4.6: The use of symmetries of the square lattice reduces the size of the space and hence the number of walkers needed for FCIQMC.

4.A Incorporating spatial and time-reversal symmetries

This section elaborates upon our implementation of spatial and time symmetries of the Hubbard model in the SQMC code. For this purpose, we first discuss all the symmetries of the square lattice Hubbard model. Then we introduce the concept of a "representative state" (needed to represent a symmetry-adapted state) and how to compute the Hamiltonian in the basis of symmetry-adapted states.

The SQMC code is written in a general way, such that it is relatively easy to add a new model system into the program. To understand what needs to be added, we must realize that the routines specific to a model Hamiltonian are,

1. Computation of the Hamiltonian matrix element in a specified basis.

2. Spawning of walkers from a given occupied state i (having a non zero number of walkers on it) onto a new state (j) which is connected to it via the Hamiltonian (i.e. $H_{ij} \neq 0$).
3. Trial wavefunction for computing the projected energy (mixed estimator).

While the Hubbard model in momentum space has already been discussed in section 4.6 , we will elaborate on our implementation for "symmetric version" of the computation of the Hamiltonian.

4.A .1 Spatial and time symmetries of the square lattice

Since we have considered the square lattice Hubbard model, we have spatial symmetries we can incorporate in our basis. By working in momentum space (and a particular momentum sector), we have already accounted for translational symmetry thereby reducing the $\begin{pmatrix} N_{\text{sites}} \\ n_\uparrow \end{pmatrix} \times \begin{pmatrix} N_{\text{sites}} \\ n_\downarrow \end{pmatrix}$ Hilbert space by (roughly) a factor of N_{sites}.

We use the four fold symmetry of the square lattice (rigid rotation of the $x-y$ axes in the 2D plane by 0, 90, 180, 270 degrees) denoted by the group C_4. Mathematically these operations can be summarized as,

Operation (g)	Transformation
I	$k_x, k_y \rightarrow k_x, k_y$
C_1	$k_x, k_y \rightarrow k_y, -k_x$
C_2	$k_x, k_y \rightarrow -k_x, -k_y$
C_3	$k_x, k_y \rightarrow -k_y, k_x$

Table 4.1: Transformations for group C_4

We also consider the symmetry under reflection along the $k_x = -k_y$ diagonal, which we denote as the "parity" of the wavefunction,

Operation (g)	Transformation
I	$k_x, k_y \rightarrow k_x, k_y$
P	$k_x, k_y \rightarrow -k_y, -k_x$

Table 4.2: Transformations for the inversion group

The combination of the four-fold operations and inversion, correspond to 8 spatial operations: the group collectively being called D_8.

In the case of $n_\uparrow = n_\downarrow$, we also utilize the time reversal symmetry of the spin part of the wavefunction, shown below,

Operation (g)	Transformation
I	$\lvert\{k_\uparrow\}, \{k_\downarrow\}\rangle \rightarrow \lvert\{k_\uparrow\}, \{k_\downarrow\}\rangle$
Z	$\lvert\{k_\uparrow\}, \{k_\downarrow\}\rangle \rightarrow \lvert\{k_\downarrow\}, \{k_\uparrow\}\rangle$

Table 4.3: Transformations for time reversal

All space and time operations acting on a state give a list of 16 (not necessarily distinct) states. Thus, we expect a Hilbert space size reduction by *approximately* a factor of 16. (We say *approximate* because there could be *repetitions* in the list of 16 states. A trivial example is the closed shell Hartree Fock configuration which is invariant under spatial rotation and reflection and also under time reversal.)

In our code, we have implemented the symmetry for closed shell systems, the spatial symmetries being described by the A_1 representation of D_8 (this can be easily generalized if the symmetry of the ground state is known for other fillings). The character table of this group is known (all characters equal 1), but one has to careful to account for the additional phase introduced because of the

anticommutation relations of fermion operators (see Appendix 4.A .3).

To incorporate the time reversal symmetry, the user simply provides the values of z, the eigenvalue of the time reversal operator. For closed shells (with equal number of up and down electrons), the Hartree Fock state has a non zero amplitude in the ground state wavefunction, based on which we conclude that the ground state wavefunction has $z = 1$.

4.A .2 Symmetry-adapted States and Representatives

To understand how symmetries are implemented we need to understand the concept of a "representative" state.

Let us say we have a state, call it s. A symmetry operation (a group element denoted by g) acting on s gives a state s'. Among the list of all s' (each obtained by a different element g of the group), we can choose any one of the states to act as a "representative" for all others, since we are guaranteed that the contributions of the states related by symmetry differ only by a constant factor of $\chi(g)$, the character of the group (in a given irreducible representation). In practice, we adopt a convention that the "representative" is the state which has the smallest integer representation of the "up determinant". If two or more states in the list of all s' have the same (lowest integer) value of the "up determinant", one goes on to compare their "down determinants" and takes the smallest of these.

Note that the list of s' could have multiple instances of s occurring in it (from different group operations) with phases (characters) that may add up or cancel in the symmetry-adapted state.

4.A .3 Accounting for the correct fermion sign when mapping indices

We now present a subtlety in the calculation of the character $\chi(g)$ when dealing with fermions. For this purpose we consider electrons of one spin type (the generalization to the case of two determinants is straightforward). Consider electronic configurations as shown in Fig.(4.7). The states are given as,

$$|\psi_1\rangle = c_1^\dagger c_2^\dagger c_3^\dagger |vac\rangle \tag{4.42}$$

$$|\psi_2\rangle = c_1^\dagger c_2^\dagger c_5^\dagger |vac\rangle \tag{4.43}$$

Under the operation C_1 (rotation by 90 degrees), one needs to perform the transformations,

$$1 \to 1' \quad 2 \to 3' \quad 3 \to 4' \quad 4 \to 5' \quad 5 \to 2' \tag{4.44}$$

Thus the new states under transformation are,

$$c_1^\dagger c_2^\dagger c_3^\dagger |vac\rangle \to c_{1'}^\dagger c_{3'}^\dagger c_{4'}^\dagger |vac\rangle \tag{4.45}$$

$$c_1^\dagger c_2^\dagger c_5^\dagger |vac\rangle \to c_{1'}^\dagger c_{3'}^\dagger c_{2'}^\dagger |vac\rangle = -c_{1'}^\dagger c_{2'}^\dagger c_{3'}^\dagger |vac\rangle \tag{4.46}$$

Note that for $|\psi_1\rangle$ the spatial indices after transformation are already *normal ordered*. However the indices in $|\psi_2\rangle$ are not normal ordered and hence there is an extra minus sign that comes in when the rearrangement of operators is performed.

4.A .4 Hamiltonian in the symmetry-adapted basis

Following the paper by De Raedt and Frick [24], we now show how to evaluate the "symmetrized" Hamiltonian matrix element in terms of the unsym-

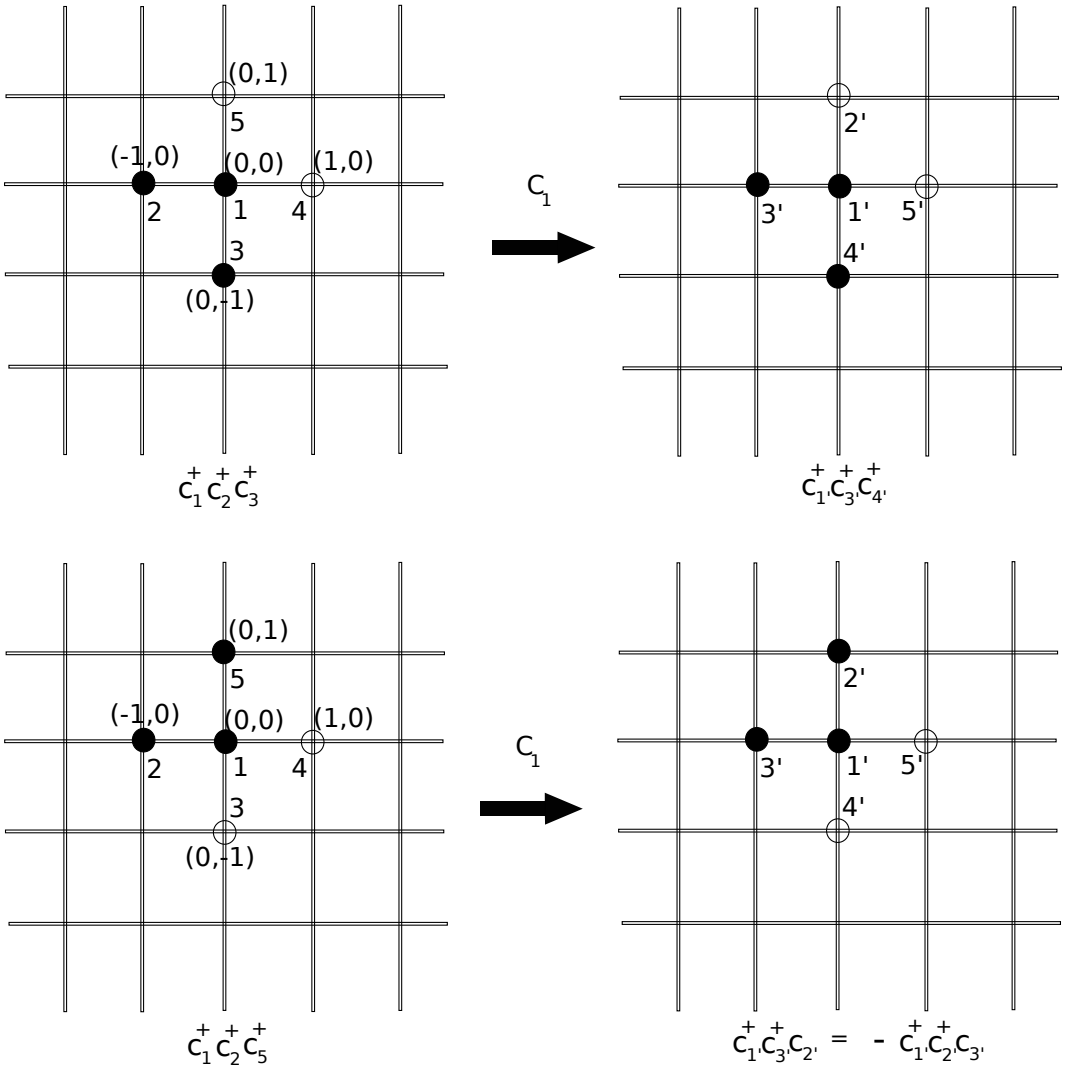

Figure 4.7: Accounting for the fermion sign when mapping indices. In the top configuration, the spatial rotation (here in momentum space) retains the normal ordering of the sites (or in general "orbitals"). In the lower configuration, under the very same rotation, one needs to normal order, resulting in an extra minus sign.

metrized Hamiltonian matrix element. The Hamiltonian possesses all the symmetries that we're imposing (of course!) and thus commutes with the group operations.

Some definitions and notations are now in order. r and s will be used to refer to unsymmetrized states (in particular, the "representatives") and $\tilde{r}$ and $\tilde{s}$ will be used to refer to the respective symmetry-adapted states constructed from r and s. To be explicit,

$$|\tilde{r}\rangle = \frac{1}{\mathcal{N}_r} \sum_R O_R \ \chi(R)|r\rangle \tag{4.47a}$$

$$|\tilde{s}\rangle = \frac{1}{\mathcal{N}_s} \sum_S O_S \ \chi(S)|s\rangle \tag{4.47b}$$

where O_R and O_S refer to the operators of the symmetry group. $\mathcal{N}_r$ and $\mathcal{N}_s$ are appropriate normalization factors that ensure that $|\tilde{r}\rangle$ and $\tilde{s}\rangle$ are normalized.

Computing $\langle\tilde{s}|H|\tilde{r}\rangle$ by inserting expressions from equations (4.47a) and (4.47b) we get,

$$\langle\tilde{s}|H|\tilde{r}\rangle = \frac{1}{\mathcal{N}_r\mathcal{N}_s} \sum_{R,S} \chi(S)^*\chi(R)\langle s|O_S^\dagger H O_R|r\rangle \tag{4.48}$$

Using $[H, O_R] = 0$ and defining $O_T^\dagger = O_S^\dagger O_R$ (i.e. $O_S = O_R O_T$) we get,

$$\langle\tilde{s}|H|\tilde{r}\rangle = \frac{1}{\mathcal{N}_r\mathcal{N}_s} \sum_T \sum_R \chi(RT)^*\chi(R)\langle s|O_T^\dagger H|r\rangle \tag{4.49}$$

Finally we perform the sum $\chi(RT)^*\chi(R)$ over the R operations and define $g(T)$ to be,

$$g(T) \equiv \sum_R \chi(RT)^*\chi(R) \tag{4.50}$$

Thus we have,

$$\langle\tilde{s}|H|\tilde{r}\rangle = \frac{1}{\mathcal{N}_r\mathcal{N}_s} \sum_T g(T)\langle s|O_T^\dagger H|r\rangle \tag{4.51}$$

Equation (4.49) tells us that we can simply use the (unsymmetrized) Hamiltonian acting on the representative r and the known values of $\chi(R)$ to compute the symmetrized Hamiltonian matrix element.

From equations (4.50) and (4.51), we observe that the number of computations of the unsymmetrized Hamiltonian H needed is a maximum of the size of the group (and not its square!). For example, for the square lattice Hubbard model (with equal number of $n_\uparrow = n_\downarrow$ to enable use of time reversal), the maximum number of computations of the unsymmetrized Hamiltonian required is 16, not 256 as one would have naively assumed.

BIBLIOGRAPHY

[1] W. M. C. Foulkes, L. Mitas, R. J. Needs, and G. Rajagopal, Rev. Mod. Phys. **73**, 33 (2001).

[2] *Quantum Monte Carlo Methods in Physics and Chemistry*, *NATO ASI Ser. C 525*, edited by M. P. Nightingale and C. J. Umrigar (Kluwer, Dordrecht, 1999).

[3] G. H. Booth, A. J. W. Thom, and A. Alavi, J. Chem. Phys. **131**, 054106 (2009).

[4] D. Cleland, G. H. Booth, and A. Alavi, J. Chem. Phys. **132**, 041103 (2010).

[5] G. H. Booth and A. Alavi, J. Chem. Phys. **132**, 174104 (2010).

[6] G. H. Booth, D. Cleland, A. J. W. Thom, and A. Alavi, J. Chem. Phys. **135**, 084104 (2011).

[7] J. Shepherd, G. Booth, A. Grüneis, and A. Alavi, Phys. Rev. B **85**, 081103(R) (2012).

[8] G. Booth, Ph.D. thesis, Clare College, University of Cambridge (2010). unpublished.

[9] Y. Ohtsuka and S. Nagase, Chemical Physics Letters **463**, 431 (2008).

[10] Y. Ohtsuka and S. Nagase, Chemical Physics Letters **485**, 367 (2010).

[11] Y. Ohtsuka and S. Nagase, Theoretical Chemistry Accounts **130**, 501 (2011).

[12] F. R. Petruzielo, A. A. Holmes, H. J. Changlani, M. P. Nightingale, C. J. Umrigar, arXiv:1207.6138, accepted for publication in *Physical Review Letters* (2012).

[13] R. Blankenbecler and R. L. Sugar, Phys. Rev. D **27**, 1304 (1983).

[14] N. Trivedi and D. M. Ceperley, Phys. Rev. B **40**, 2737 (1989); N. Trivedi and D. M. Ceperley, Phys. Rev. B **41**, 4552 (1990).

[15] H. J. M. van Bemmel, D. F. B. ten Haaf, W. van Saarloos, J. M. J. van Leeuwen, and G. An, Phys. Rev. Lett. **72**, 2442 (1994); D. F. B. ten Haaf,

H. J. M. van Bemmel, J. M. J. van Leeuwen, and W. van Saarloos, Phys. Rev. B **51**, 13039 (1995).

[16] C. J. Umrigar, M. P. Nightingale, and K. J. Runge, J. Chem. Phys. **99**, 2865 (1993).

[17] R. Assaraf, M. Caffarel, and A. Khelif, Phys. Rev. E **61**, 4566 (2000).

[18] M. H. Kolodrubetz, J. S. Spencer, B. K. Clark, W. M. C. Foulkes, arXiv:1209.3044.

[19] J. S. Spencer, N. S. Blunt, and W. M. Foulkes, The Journal of Chemical Physics **136**, 054110 (2012).

[20] D. M. Arnow, M. H. Kalos, M. A. Lee, and K. E. Schmidt, The Journal of Chemical Physics **77**, 5562 (1982).

[21] N. Furukawa and M. Imada, Journal of the Physical Society of Japan **61**, 3331 (1992).

[22] S. Zhang, J. Carlson, and J. E. Gubernatis, Phys. Rev. B **55**, 7464 (1997).

[23] S. Zhang, private communication.

[24] H. D. Raedt and M. Frick, Physics Reports **231**, 107 (1993).

CHAPTER 5

CONCLUDING REMARKS AND OUTLOOK

In the preceding chapters, I have outlined my efforts in search of a numerical method that can deal with strongly correlated systems.

The first effort involved the generalization of the Jastrow wavefunction to beyond just a pair form - the resulting wavefunction being christened "Correlator Product States"(CPS) [1] (see Chapter 3) or extended Jastrow wavefunctions. Other authors in the literature have named these wavefunctions Entangled Plaquette States (EPS) [2] or Complete Graph Tensor Network States (CGTN) [3].

We have demonstrated in this thesis, that correlators of increasing size can provide accurate energies of the 2D Heisenberg model and the spinless fermion model in one dimension. Some preliminary calculations for frustrated spin systems (here the $J_1 - J_2$ model) also look promising. With the use of a Slater determinant, CPS can also be used for spinless fermions and the spinfull fermion Hubbard model in two dimensions.

After the publication of our paper [1], other studies have also been carried out with CPS wavefunctions. Assam et al. [4] have used these wavefunctions to perform calculations on spin models such as the transverse field Ising model and the Heisenberg antiferromagnet on a square lattice. Clark et al. [5] have used these wavefunctions to study the possibility of a spin liquid on the $J_1 - J_2$ model on the honeycomb lattice; a direction that was also taken by Mezzacapo and Boninsegni [6]. Mezzacapo et al. have also used CPS to explore the $J_1 - J_2$ model on the triangular lattice [7]. Neuscamman and Chan [8] have used the CPS wavefunction to study the 30 site molecular magnet corresponding to

$Mo_{72}Fe_{30}$ which is described by a $s = 5/2$ Heisenberg model on a icosidodecahedron, which seems to be competitive with recent DMRG calculations [9].

The importance of a good wavefunction for accurate Variational and Projector Monte Carlo calculations cannot be emphasized enough. Thus, even though CPS have been found to be good approximation for some model systems, one must ask the question: What kind of correlations does the CPS *not* capture? As I have already pointed out, the CPS could not be directly applied to fermions in two dimensions and had to be used in conjunction with a determinant.

The second effort involved an exploration of the performance of the recently proposed Full Configuration Interaction - Quantum Monte Carlo [10] method for the Hubbard model. This work led us to a semistochastic formulation of Projector Monte Carlo (SQMC) [11] (see Chapter 4) which improves the efficiency of FCIQMC. SQMC is capable of reducing the statistical fluctuations and the bias (systematic error) introduced by the "initiator" approximation of FCIQMC. With respect to the Hubbard model on a square lattice, low fillings or low U/t are ideally conducive for this method, because of the presence of a "importance hierarchy" of configurations.

However, in order to describe the Hubbard model in the "physically interesting" regimes (fillings around 0.8 and $U/t \sim 4 - 10$), it appears that some idea is still missing. Since the FCIQMC and SQMC algorithms scale unfavorably with system size, studying higher than quarter filling at $U/t = 4$ on a 8x8 lattice (in the momentum space basis) appears to be a challenge (at least on a single core). This is because even a few hundred million walkers could not eliminate the *systematic* error (bias) introduced from the initiator approximation. There are ongoing efforts in the Umrigar group to study and reduce this bias in a sys-

tematic way.

Some other technical improvements are also called for. The first of these directions is to parallelize the FCIQMC/SQMC code to be able to go the very large (billions) walker limit. This is a significant (and almost essential) step forward. One must note that unlike other QMC methods, there is considerable amount of inter processor communication involved in FCIQMC/SQMC, as one has to perform cancellations of walker weights at every time step and walkers from one computer node can spawn new walkers that belong to another computer node.

Another direction, which we have not adequately explored and which has not been presented in this thesis, is to use *importance sampling* with good guiding wavefunctions. For this purpose one could potentially use the CPS wavefunctions (with a Slater determinant) or with Pfaffian [12] or symmetry-projected Hartree-Fock-Bogoliubov wavefunctions [13].

Yet another direction, which I am very interested in, is the search for an "optimal" many-body basis which can concentrate the weight of the wavefunction on a relatively small number of states. In this thesis we only explored the momentum space basis, but one would ideally like to "adjust" the choice of basis depending on U/t and filling. One idea for obtaining an "optimal basis" is to perform local basis transformations of the occupation number kets, much in the spirit of renormalization group approaches. Though there is a loss of sparsity of the Hamiltonian under such a transformation, one might be able to retain more "important states" this way, thereby improving the accuracy of SQMC calculations.

BIBLIOGRAPHY

[1] H. J. Changlani, J. M. Kinder, C. J. Umrigar, and G. K.-L. Chan, Phys. Rev. B **80**, 245116 (2009).

[2] F. Mezzacapo, N. Schuch, M. Boninsegni, and J. I. Cirac, New J. Phys. **11**, 083026 (2009), the ansatz considered here has the same form as the CPS.

[3] K. H. Marti *et al.*, New Journal of Physics **12**, 103008 (2010).

[4] S. Al-Assam, S. R. Clark, C. J. Foot, and D. Jaksch, Phys. Rev. B **84**, 205108 (2011).

[5] B. K. Clark, D. A. Abanin, and S. L. Sondhi, Phys. Rev. Lett. **107**, 087204 (2011).

[6] F. Mezzacapo and M. Boninsegni, Phys. Rev. B **85**, 060402 (2012).

[7] F. Mezzacapo and J. I. Cirac, New Journal of Physics **12**, 103039 (2010).

[8] E. Neuscamman and G. K.-L. Chan, Phys. Rev. B **86**, 064402 (2012).

[9] J. Ummethum, J. Schnack, and A. M. Läuchli, Journal of Magnetism and Magnetic Materials **327**, 103 (2013).

[10] G. H. Booth, A. J. W. Thom, and A. Alavi, J. Chem. Phys. **131**, 054106 (2009).

[11] F. R. Petruzielo, A. A. Holmes, H. J. Changlani, M. P. Nightingale, C. J. Umrigar, arXiv:1207.6138, accepted for publication in *Physical Review Letters* (2012).

[12] E. Neuscamman, C. J. Umrigar, and G. K.-L. Chan, Phys. Rev. B **85**, 045103 (2012).

[13] G. E. Scuseria *et al.*, The Journal of Chemical Physics **135**, 124108 (2011).

Part II

Randomly diluted antiferromagnet at percolation

CHAPTER 6

HEISENBERG ANTIFERROMAGNET: LOW ENERGY SPECTRUM AND EVEN/ODD SUBLATTICE IMBALANCE

6.1 Introduction

This part of the thesis details my investigations of the low energy spectrum of a Heisenberg antiferromagnet diluted with non magnetic impurities. There are two major motivations for this study: one experimental and the other theoretical, which I describe below.

From the point of view of the cuprates, (which we encountered in Chapter 1), in 2002, Vajk et al. [1] were able to dope the copper-oxygen planes of La_2CuO_4 with non magnetic impurities (distributed randomly) to the desired concentration of diluents [1]. The magnetic copper atoms were replaced with non magnetic zinc or magnesium thereby disrupting the antiferromagnetic long range order known to exist in the clean material. Neutron diffraction was used to study the magnetic ordering in these planes for different doping concentrations.

Their studies revealed that long range antiferromagnetic order persisted even at a "critical concentration" (the technical term being the 'percolation threshold') of dopants at which point the largest connected cluster of copper atoms could be considered "weakly connected" (or "finitely ramified"[2]). We emphasize that at the percolation threshold, a macroscopically large connected cluster exists, doping it a bit more will lead to small isolated clusters.

[1] Earlier experiments [2, 3, 4] had been able to create samples only with a small amount of dilution.

[2] A finitely ramified cluster is one which can be broken into segments by cutting a finite number of bonds.

One might naively *assume* that such a "weakly connected" percolation cluster is quite 1-D like and hence *cannot* support long range antiferromagnetic order (at least for a Hamiltonian that is local) [3]. Thus their finding is quite remarkable and was difficult to argue convincingly at a theoretical level.

To put things in historical perspective, the above mentioned experiment [1] itself was motivated by previous theoretical investigations of *quantum* systems [4] on percolation clusters (see examples such as Sachdev et al. [6], Chernyshev et al. [7], Chen and Castro-Neto [8], Sandvik [9], Senthil and Sachdev [10] and references therein). In particular, the work of Chen and Castro-Neto [8] had argued that antiferromagnetic long range order is destroyed in La_2CuO_4 at a doping concentration smaller than that needed to achieve the percolation threshold.

This experiment led to independent numerical studies of the randomly diluted Heisenberg model on the square lattice by Sandvik [11] and Vajk and Greven [12] using (sign problem free) Quantum Monte Carlo, both of which confirmed that simulations could replicate the findings of the experiment. From an analytical view point, Bray-Ali et al. [13] have provided a framework within spin wave theory for understanding the existence of long range order on a percolation cluster, but it is not clear if their results carry through for the spin 1/2 case (where quantum fluctuations can be large). Thus (we believe that) only a limited understanding exists of *how* long range order survives the onslaught of dilution to the percolation threshold.

The other motivation for pursuing this line of research arises from an investigation into the low energy spectrum of the unfrustrated Heisenberg antiferro-

[3] The Heisenberg model has no long range order in one dimension at zero temperature.

[4] There is a long history of studies of *classical* spin systems on percolation clusters which we will not address in this thesis. The interested reader may refer to the book by Stauffer and Aharony [5].

magnet on percolation clusters. It had been argued by Vojta and Schmalian [14] that even though randomly diluted antiferromagnets have the geometry of non-uniform fractal objects, their low energy excitations are described by the same model that describes uniform systems - the so called "quantum rotor" model [15]. To be specific, it was suggested that the lowest energy gap, for a randomly diluted antiferromagnet (at percolation) on a finite cluster with N sites, would scale with system size as $1/N$. This finite size scaling had also been suggested by QMC studies of Yu et al. [16], but their method of estimation of this gap was indirect and relied on an assumption about the divergence of the correlation length with decreasing temperature [5]. This finding was directly challenged by numerical studies by Wang and Sandvik [17, 18]; who could conclusively (at least numerically) show that the gap (estimated variationally) *did not* scale as $1/N$. We attempt to understand the origin of this new energy scale through our investigations.

The two motivations ("why is there long range order in the ground state?" and "what are the low energy excitations?") are not independent of one another. Our philosophy is that an understanding of the ground state of this system may be achieved by trying to understand the relationship it shares with the *excited states* in the low energy spectrum. In particular, the central question this part of the thesis aims to address is: what are the effective low energy degrees of freedom which are responsible for the propagation of long range antiferromagnetic order? And how can these degrees of freedom be detected in numerical many-body calculations? Even though the system that motivates these questions is quite specific, the ideas that arise from them (we believe) are quite general.

[5] Yu et al. [16] measured the finite temperature scaling of the correlation length using the functional form $\zeta \sim T^{-1/z}$ which is not necessarily true in general situations, where z is the dynamic exponent.

We appreciated [6] that existing many-body techniques were limited in their scope for yielding information about excited states of strongly correlated spin systems in greater than one dimension. (One reason for this problem is that *loops* in the lattice create the exponentially hard problem of growing number of uncontracted indices when using Tensor Network States as was seen in Chapter 2.) Thus, instead of trying to address the problem of simulating a randomly diluted antiferromagnet on a *square lattice*, we asked the equivalent questions on a randomly diluted (coordination 3) *Bethe lattice* (see an illustration of these lattices in Fig. 6.1). The advantage of having this 'loop-less' lattice was that we could study ground and excited states with an existing numerical technique, the Density Matrix Renormalization Group (which we are somewhat familiar with based on the exposition in Chapter 2), after it had been suitably modified to be applied to generic tree graphs.

We would like to emphasize that even though the square and Bethe lattices are (obviously) very distinct, when diluted to the "percolation threshold" the resultant clusters are statistically similar[7]. From here on, we will not try to connect our results to the case of the square lattice; rather we will use the intuition gained by considering the Bethe lattice to develop our understanding of the problem at large.

In order to understand the research presented in this part of the thesis, there are some concepts that we alluded to above and other pertinent concepts that exist in the literature that need to be explained. In the remainder of the Chapter, I will attempt to fill in these gaps and further motivate the specific questions we

[6] Historically, the order of development of this project was slightly different. We began investigating the Bethe lattice percolation problem with Exact Diagonalization before we realized the added benefit that the lattice was well suited for DMRG

[7] For example, the *spectral dimension*, related to the graph's connectivity, is 1.27 on the square lattice and 4/3 on the Bethe lattice at their percolation threshold.

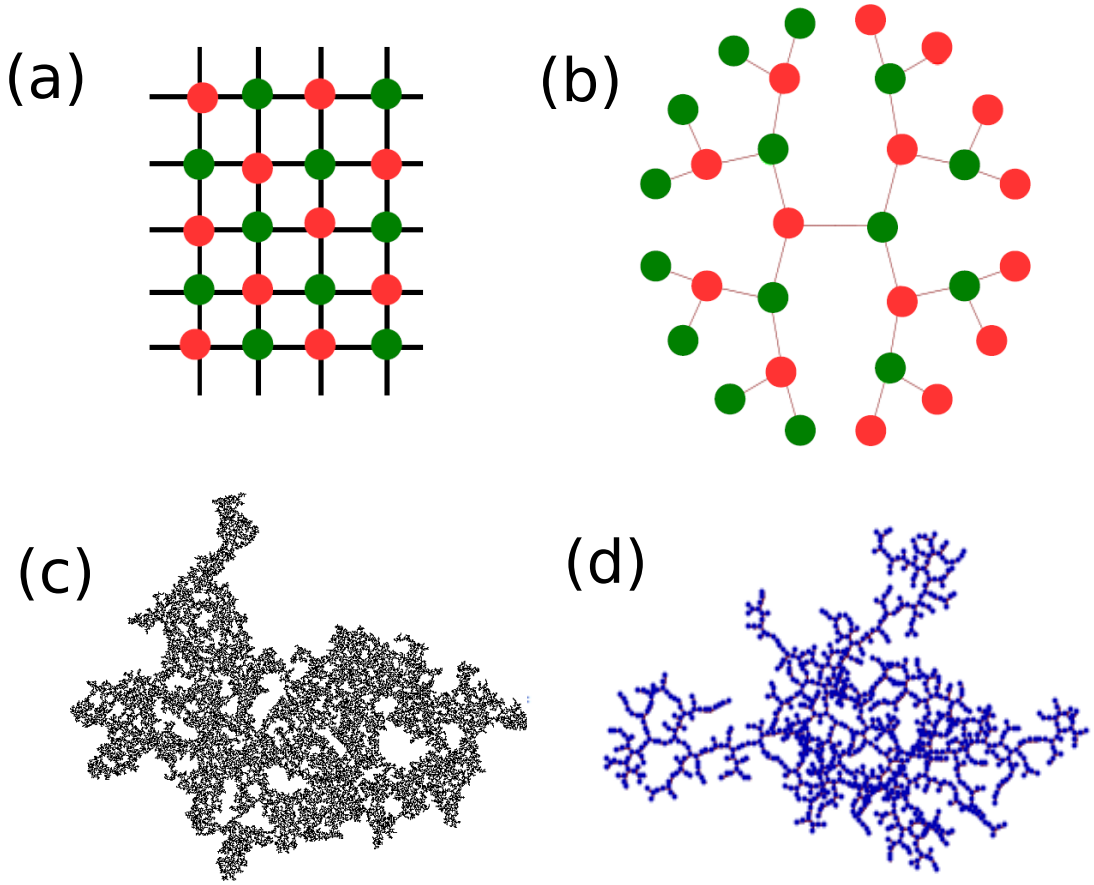

Figure 6.1: The square and Bethe Lattice are shown in Figure (a) and (b) respectively. (c) and (d) show clusters obtained by randomly diluting the square and Bethe lattice respectively (at their percolation threshold). The picture of the diluted square lattice (shown in (c)) was taken from [19]. The picture of a diluted Bethe lattice (shown in (d)) was generated by the author in Mathematica. Figure (d) might appear slightly misleading because it shows some 'crossings' which appear as loops (an artifact of the graph embedding algorithm); when there are absolutely none.

are trying to address.

To begin with, I will give a brief overview of the model used for describing quenched disorder ("percolation clusters") in the Copper oxygen planes. Then, I will motivate a puzzle about the "anomalous" finite-size scaling of the lowest energy gap on a randomly diluted antiferromagnet, much in contrast to its clean (uniform) counterpart. To understand this, I will summarize briefly the "tower of states" seen in low energy spectra of clean, unfrustrated antiferromagnets. In order to appreciate the main geometrical difference between the clean and diluted systems, I will introduce the concept of global and local even/odd sublattice imbalance. It will turn out that even/odd sublattice imbalance can significantly affect the nature of the low energy spectrum of a clean system. The importance of the concept is highlighted by the fact that we carried out a systematic numerical study of this effect by considering the antiferromagnet on a regular Cayley tree in Chapter 8. I will finally conclude by giving an outline of what is to come in the Chapters following this one.

6.2 Percolation Theory

To understand the role of quenched disorder in an antiferromagnet theoretically, we need to have a mathematical model for describing the disorder. Since the non magnetic Zn or Mg impurities randomly (see Fig. 6.2) replaced the magnetic Cu atoms in the experiment [1], the disorder is *not correlated*. Also note that the Hamiltonian involves only a nearest neighbor interaction, which allows us to model this system as a 'percolation cluster'.

For this purpose, we describe what we mean by 'percolation' (for an in-

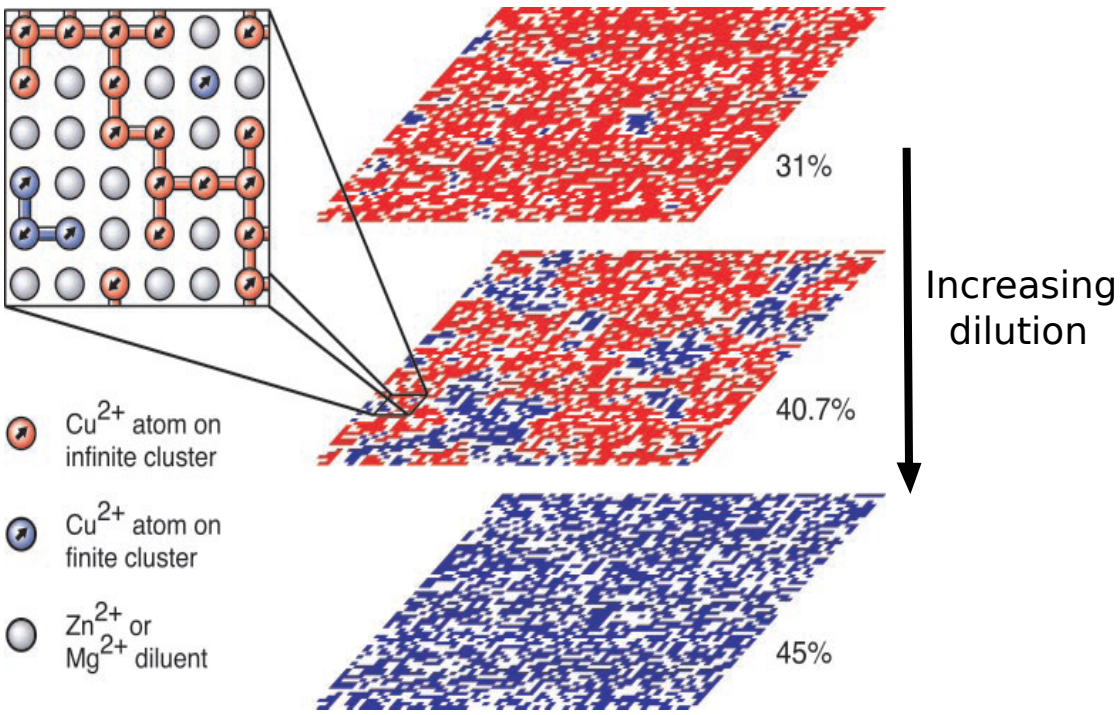

Figure 6.2: Experimental realization of an antiferromagnet at and away from the percolation threshold. The Copper atoms are randomly replaced by non magnetic Zn or Mg. The largest connected cluster has been shown in red and the smaller connected clusters have been shown in blue. The white regions indicate the Zn or Mg ions. This picture has been taken from Vajk et al. [1]

troduction to percolation theory one may refer to the books by Stauffer and Aharony [5] and an introductory article by Christensen [20]). To do so succinctly, we use an illustration (Fig. 6.3(a) and (b)) showing 'percolation' on a underlying Bethe lattice network. Think of starting off from a "active root" node and forming a link with a nearest neighbor with probability p (indicated by dark bonds in Fig. 6.3(b)). If successful, the new site is considered "active" and can carry on the process of making new links (each with probability p). (See for example Figure 6.3(b) which shows a cluster after two growth steps). Thus, percolation can be thought of as a dynamic process where one builds a "percolation cluster" by probabilistically adding bonds to existing active sites. Once no new links form, the process of cluster formation is complete.

As we increase p, we expect to see, on average, clusters of increasing size (N). One can mathematically argue that there is a network (lattice) dependent "critical probability" (or the 'percolation threshold' referred to as p_c), at which an infinite cluster first appears. Said another way, the average cluster size $\langle N \rangle$ obeys,

$$\begin{aligned} \langle N \rangle &\rightarrow \text{finite} \quad p < p_c \\ \langle N \rangle &\rightarrow \infty \qquad p \geq p_c \end{aligned} \tag{6.1}$$

To illustrate this point we show a plot in Figure 6.3(c) for the $z = 3$ Bethe lattice. We do observe the purely geometrical phase transition, one that occurs without any reference to any underlying microscopics (or Hamiltonian) [8].

Our introduction to percolation was specific to the Bethe Lattice where we 'grew clusters' by 'adding sites/bonds' to one site. This growth process can actually be shown to be exactly equivalent to starting from a clean system and removing bonds (bond percolation) or sites (site percolation) with probability 1-p. It is 'site percolation' which is relevant for the experiment by Vajk et al. [1].

For the coordination z Bethe Lattice, bond and site percolation are equivalent and the percolation threshold p_c can be shown [20] to be exactly,

$$p_c = \frac{1}{z-1} \tag{6.2}$$

Since we are working with the coordination 3 Bethe Lattice we will always consider $p_c = 1/2$.

Percolation provides a test bed for investigating the competition between geometrical disorder and quantum mechanics. To elucidate this point, note that

[8] Apart from the application we discuss in this thesis, some areas where percolation theory has been used include studies of forest fires [21], disease spreading, flow of fluids through porous media and electrical conductivity in mixtures of metals and insulators.

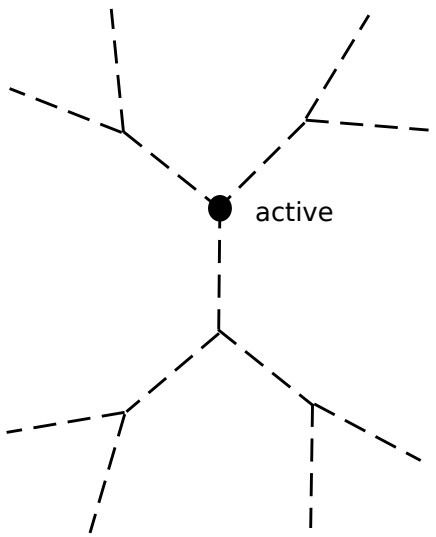

(a) Initial configuration

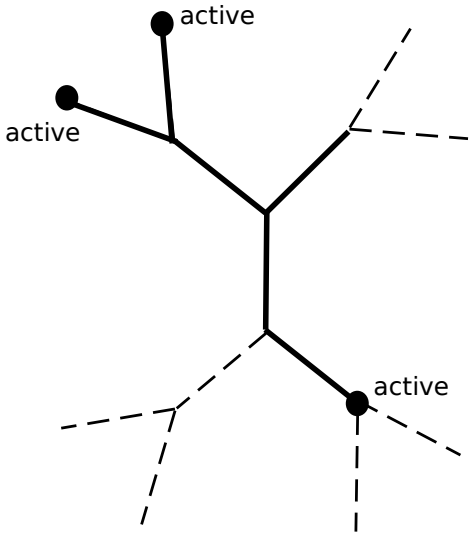

(b) Percolation cluster after two growth steps

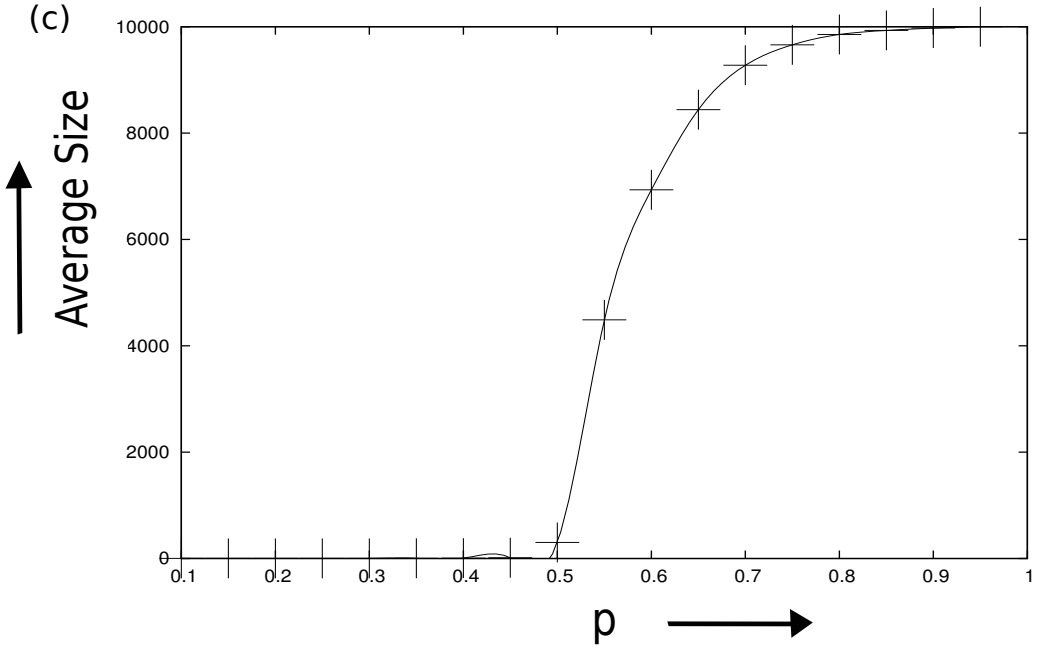

Figure 6.3: (a) and (b) Schematic of percolation on the $z = 3$ Bethe lattice. In (a) we begin with exactly one active site. In (b) we show a percolation cluster after two growth steps. The dark bonds are percolated. (c) The average cluster size vs p shows that the observed percolation threshold on the $z = 3$ Bethe lattice is close to $p = 0.5$, consistent with the theoretical value (see equation (6.2)) of p_c

if p is small, the clusters are small and there is no way in which antiferromagnetic long range antiferromagnetic order can propagate. If p is large (close to one), the clusters resemble the underlying (clean) lattice and so it is quantum fluctuations which determine if the system has long range order. Right at the percolation threshold, it is not obvious in which way the scales will be tipped (and why), making it an interesting regime of parameter space to study.

6.3 Rotor Model and "Tower" of States

In order to understand what the low energy spectrum of a randomly diluted antiferromagnet looks like, we must try to understand what its clean counterpart is.

The square lattice (nearest neighbor) antiferromagnet is unfrustrated because the lattice is bipartite [9]. The ground state of the (nearest neighbor) Heisenberg model has Néel order and one could quantitatively establish this by defining a Néel vector pointing in some definite direction in space. However, for a finite uniform system (which has equal number of sites on the two sublattices), one always gets a singlet ground state ($S = 0$) [22]. This means that there is no real preferred orientation in spin space this system would like to choose to align its Néel vector.

In his seminal paper, Anderson [23] reconciled the apparent paradox that one can have Néel order consistent with a $S = 0$ ground state (for equal number

[9] A bipartite lattice is one in which the entire lattice can be split into two sublattices, A and B such that there are connections between a site in A and a site in B, but no $A - A$ or $B - B$ connections. The Bethe lattice is bipartite and so is the honeycomb lattice, but the triangular lattice is not.

of sites on both sublattices). His idea was that the Néel state is a superposition of practically degenerate states. He argued that the Néel vector surely would precess according to the laws of quantum mechanics, but the rate would be so slow that one can think of it as 'practically' stationary. In short, the Néel state is a result of 'symmetry breaking' (ubiquitous in condensed matter physics!).

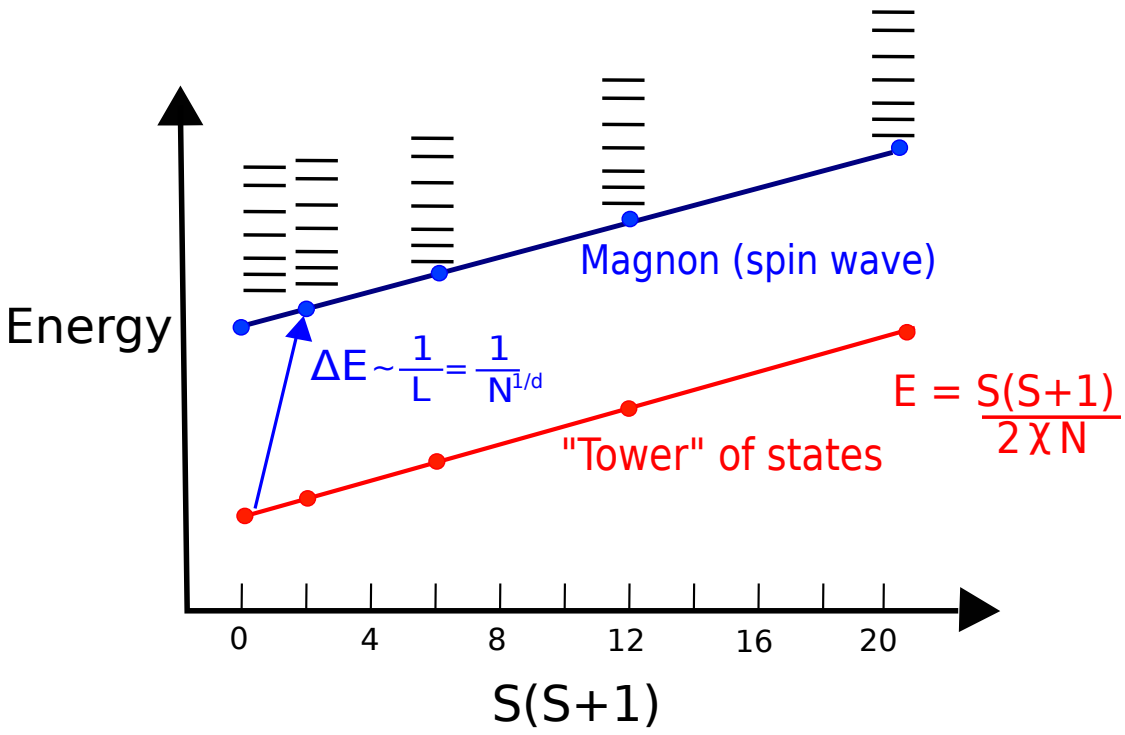

Figure 6.4: Typical low energy spectrum of an unfrustrated antiferromagnet showing the "tower" of states.

This idea has been put in a more concrete form by various authors. The states that are supposed to be 'practically degenerate', are not truly degenerate in a finite system and show up as definite spin (S) states in an exact diagonalization calculation of the Heisenberg Hamiltonian (as they must, because the Heisenberg model is rotationally symmetric). Neuberger and Ziman [24] and Gross, Sánchez-Velasco and Siggia [25] were one of the first ones to explicitly write down the form of the low energy Hamiltonian.

The idea involved is as follows: since the Néel vector can be thought of as a combined spin object precessing very slowly about some axis, it can be mapped to a model for a rigid rotor [15]. In classical mechanics, the energy E of this rigid rotor (rotating about some axis) is given by,

$$E = \frac{L^2}{2I} \tag{6.3}$$

where L is its angular momentum and I is its moment of inertia about its axis of rotation.

Analogously for the "quantum rotor", the Hamiltonian is,

$$\hat{H}_{\text{low}} = \frac{\hat{S}^2}{2I} \tag{6.4}$$

where S is its (spin) angular momentum and I is its moment of inertia about its axis of rotation. For a uniform system I is extensive by which we mean,

$$I = \chi N \tag{6.5}$$

where χ is the magnetic susceptibility and N is the total number of sites. Thus, the eigenenergies of H_{low} are given by (see also Fig. 6.4),

$$E = \frac{S(S+1)}{2\chi N} \tag{6.6}$$

In her work, Lhuillier [26] has also referred to the eigenstates of the rotor Hamiltonian as the 'Quasi Degenerate Joint States' (QDJS)[10]. For the purpose of the rest of this thesis, we will adopt one common terminology and simply call these states the "tower of states".

[10]The term "quasi degenerate states" will used by us in this thesis not only to refer to states which are almost degenerate due to symmetry breaking, but also for other reasons.

6.4 Global and Local Imbalance

We now turn to a concept that plays an important role in Chapters 8 and 9.

Consider two finite clusters shown in Figure 6.5. For sake of comparison we have also plotted the low energy spectrum of these clusters. For both clusters, the number of even (red, sublattice A) sites is equal to the number of odd (green, sublattice B) sites. Thus, the clusters have no "global even/odd sublattice imbalance" i.e. the number of sites on the A sublattice, n_A, exactly equals the number of sites on the B sublattice, n_B. Following a theorem of Lieb and Mattis [22] for bipartite lattices, the ground state has spin S given by,

$$S = \frac{|n_A - n_B|}{2} \tag{6.7}$$

Thus a "(globally) balanced cluster" has a singlet ($S = 0$) ground state. Since $E(S)$ for the unfrustrated antiferromagnet is guaranteed to be monotonic [27], the first excited state is a triplet ($S = 1$).

When considering only a smaller part of the cluster in Fig. 6.5(b), one observes that the count of even and odd sublattice sites is not the same. Thus there is a "local imbalance" of even/odd sites. This local imbalance is ultimately responsible for some spins being left "uncovered by dimers" or "dangling" (as has also been indicated in Fig. 6.5(b)).

As mentioned previously, our study is motivated by the numerical observations of Wang and Sandvik [17, 18]. For square lattice percolation clusters at the critical percolation threshold p_c, they observed the presence of an energy scale smaller than the $1/N$ rotor energy scale. They attributed this energy scale to the formation of long range singlets by 'dangling spins'.

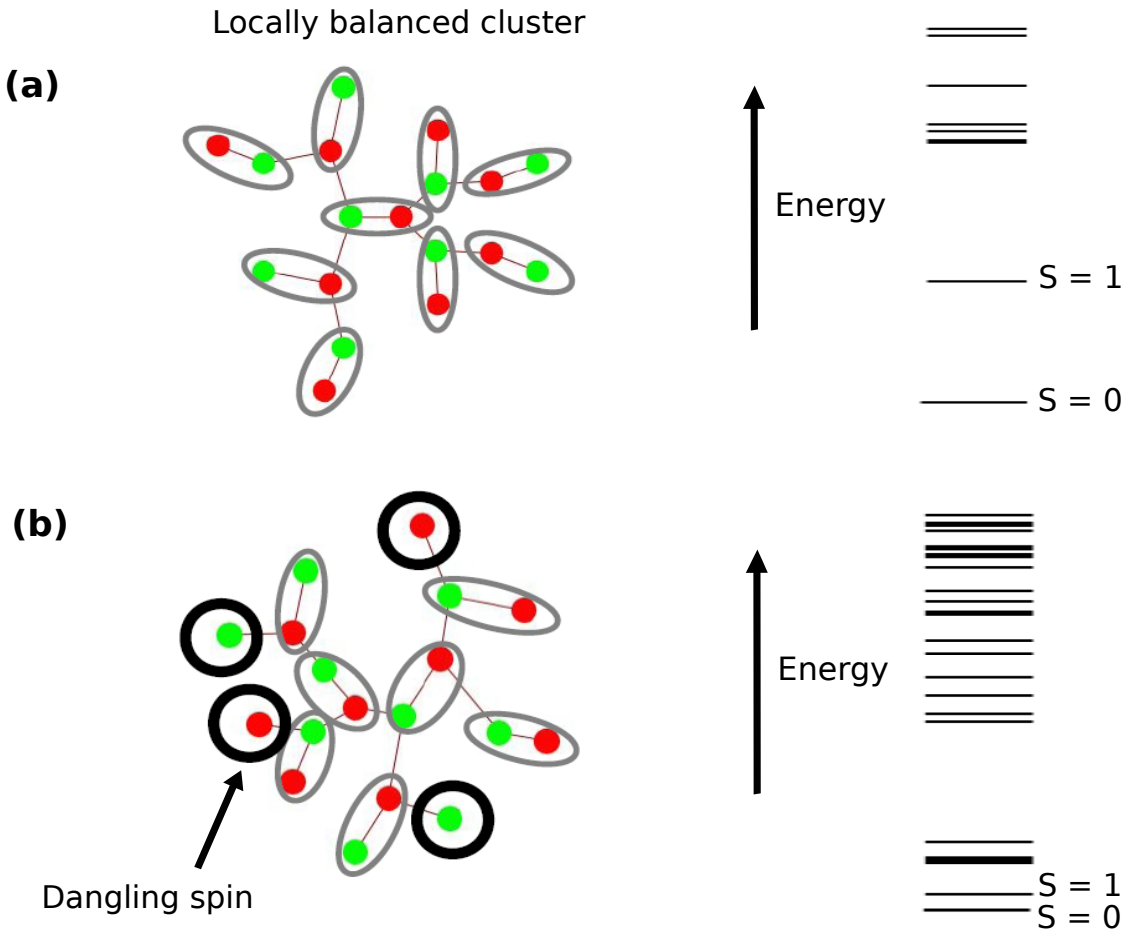

Figure 6.5: Two balanced clusters (a) without and (b) with local even/odd sublattice imbalance and their corresponding low energy spectra.

Thus, our main focus in this thesis is to further explore *why* the spectra of the clusters of the type shown in Fig. 6.5 are *qualitatively* different and to highlight the dependence of the nature and number of low energy states on the number of dangling degrees of freedom.

6.5 Outline of Part II of this thesis

The remainder of Part II is divided as follows.

In Chapter 7, we give an overview of our implementation of the DMRG algorithm applied to generic trees. This is the chief numerical technique used for Chapters 8 and 9.

In Chapter 8, to highlight the relationship between even/odd sublattice imbalance and the low energy spectrum, we present our paper [28] on the general properties of the ground state and excited states of *regular* Cayley trees (Bethe lattice). We use a variational ansatz given by the single mode approximation [29], in conjunction with an argument from first order perturbation theory, to explain the finite size scaling of the spin gap. We also corroborate our observations of the ground state properties, by the use of the Schwinger Boson mean field theory (SBMFT) [30] (the lead author in the last part being Shivam Ghosh).

Finally, in Chapter 9, we present our paper [31] on the Heisenberg antiferromagnet on the Bethe lattice at the percolation threshold. Our focus is on understanding how the "dangling spins" collectively act as "emergent" spin 1/2 objects and to demonstrate the numerical diagnostics we used to detect these degrees of freedom.

BIBLIOGRAPHY

[1] O. P. Vajk *et al.*, Science **295**, 1691 (2002).

[2] M. Hücker *et al.*, Phys. Rev. B **59**, R725 (1999).

[3] M. Corti *et al.*, Phys. Rev. B **52**, 4226 (1995).

[4] B. Keimer *et al.*, Phys. Rev. B **46**, 14034 (1992).

[5] D. Stauffer and A. Aharony, *Introduction to Percolation Theory* (Taylor and Francis, New York, 1992).

[6] S. Sachdev, C. Buragohain, and M. Vojta, Science **286**, 2479 (1999).

[7] A. L. Chernyshev, Y. C. Chen, and A. H. Castro Neto, Phys. Rev. Lett. **87**, 067209 (2001).

[8] Y.-C. Chen and A. H. Castro Neto, Phys. Rev. B **61**, R3772 (2000).

[9] A. W. Sandvik, Phys. Rev. B **66**, 024418 (2002).

[10] T. Senthil and S. Sachdev, Phys. Rev. Lett. **77**, 5292 (1996).

[11] A. W. Sandvik, Phys. Rev. Lett. **89**, 177201 (2002).

[12] O. P. Vajk and M. Greven, Phys. Rev. Lett. **89**, 177202 (2002).

[13] N. Bray-Ali, J. E. Moore, T. Senthil, and A. Vishwanath, Phys. Rev. B **73**, 064417 (2006).

[14] T. Vojta and J. Schmalian, Phys. Rev. Lett. **95**, 237206 (2005).

[15] Subir Sachdev, *Quantum Phase Transitions*, Cambridge University Press, 1999.

[16] R. Yu, T. Roscilde, and S. Haas, Phys. Rev. Lett. **94**, 197204 (2005).

[17] L. Wang and A. W. Sandvik, Phys. Rev. Lett. **97**, 117204 (2006).

[18] L. Wang and A. W. Sandvik, Phys. Rev. B **81**, 054417 (2010).

[19] D.Tiggemann, http://da.nieltiggemann.de/science/percolation/index.html.

[20] K. Christensen, MIT Lecture notes, http://www.mit.edu/ levitov/ 8.334/notes/percol_notes.pdf .

[21] J. Millington, R. Romero-Calcerrada, J. Wainwright, and G. Perry, Journal of Artificial Societies and Social Simulation **11**, 4 (2008).

[22] W. Marshall, Proc. Roy. soc. London A 232, 48 (1955); E. H. Lieb and D. Mattis, J. of Math. Phys. 3, 749(1962); M.B. Hastings, Phys. Rev. B 69, 104431 (2004).

[23] P. W. Anderson, Phys. Rev. **86**, 694 (1952).

[24] H. Neuberger and T. Ziman, Phys. Rev. B **39**, 2608 (1989).

[25] M. Gross, E. Sánchez-Velasco, and E. Siggia, Phys. Rev. B **39**, 2484 (1989).

[26] C. Lhuillier arXiv:cond-mat/0502464v1 (unpublished).

[27] A.Auerbach, *Interacting electrons and Quantum Magnetism*, Springer-Verlag, 1994.

[28] H. J. Changlani, S. Ghosh, C. L. Henley and A.M. Läuchli, arXiv:1208.1773.

[29] R.P. Feynman, *Statistical Mechanics* (Benjamin, New York, 1972).

[30] A. Auerbach and D. P. Arovas, Phys. Rev. Lett. **61**, 617 (1988).

[31] H. J. Changlani, S. Ghosh, S. Pujari and C. L. Henley, arXiv:1210.4621.

CHAPTER 7

DENSITY MATRIX RENORMALIZATION GROUP ON GENERIC TREES

This Chapter is a significant expansion of Section III of the paper [1] under peer review in Physical Review B.

7.1 Introduction

The Density Matrix Renormalization Group (DMRG) is a powerful numerical technique for studying many-body systems. It was developed by White [2] for one dimensional systems to remedy the problems associated with the Numerical Renormalization Group (NRG) [3]. I gave a brief outline of the idea involved in Chapter 2. The reader interested in a general review of the method and its applications may refer to the article by Schollwöck [4].

My method of presentation of the DMRG in this Chapter is slightly unconventional. Instead of going the regular route of explaining DMRG for 1D systems, I will immediately delve into a discussion focused on looking at a generic "tree". A tree is a lattice without loops, a feature it has in common with the 1D lattice[1]. For the purpose of illustration, I have decided to demonstrate this method for a regular Cayley tree or Bethe lattice, a lattice we introduced in Chapter 6. However, we will keep in mind that all the steps directly carry over even when the tree is not regular.

The objective of this Chapter is to highlight some of the details of the workings of the algorithm, and give the reader a sense of the 'nuts and bolts' for

[1] A 1D lattice is also a special case of a tree

how a DMRG code works. I will also discuss the measurements that go beyond ones which involve ground state expectation values. I would like to highlight through this Chapter, that even though DMRG was primarily invented to obtain ground states of many body systems, it is not too difficult to obtain (some) excited states as well. In particular, the matrix elements of operators that connect the ground state to excited states can reveal very useful insights into the low energy physics, and so it is important to understand how they are measured in the DMRG. Some of these matrix elements *cannot* be computed with other algorithms (it appears), such as Quantum Monte Carlo and so there is an advantage to using DMRG in these situations [2].

There was another outcome of my "tree implementation" of DMRG. With minor modifications, I adapted my code to the case of the Husimi Cactus, a lattice of corner sharing triangles, the center of each triangle being a vertex on the Cayley tree/ Bethe Lattice. I am not aware of any published work on the DMRG algorithm for the Husimi Cactus.

In order to get a perspective for what has been done with the "tree implementation" of DMRG in the past, we briefly review the literature. The earliest works in this regard were by Otsuka [5] and Friedman [6] who realized that the DMRG is applicable to the Cayley tree and they used it to study the quantum spin 1/2 XXZ and Heisenberg models respectively. Their algorithms 'built up' the lattice in a hierarchical way [3], and their methods applied only to *regular* trees. In the same spirit, Lepetit et al. [7] considered the fermionic Hubbard model at half filling on the Cayley tree with DMRG. More recently, Kumar et al. [8] have revisited the problem of a spin 1/2 Heisenberg antiferromagnet on a regular

[2]The advantage of QMC over DMRG is that the former scales more favorably than the latter with system size

[3]The idea of 'building' a lattice will become clearer a little later in the Chapter.

Cayley tree and improved upon the scaling of previous DMRG algorithms, by considering an efficient way to hierarchically build the lattice [4].

In comparison to all the above, our implementation has focused our efforts in a direction that enabled us to study the properties of *any* finite tree (and not necessarily regular ones). This was eventually essential in understanding percolation clusters (discussed in Chapter 9).

Before we proceed with a discussion of the algorithm, we spell out the notation we have used in this Chapter. d is the number of degrees of freedom per site. For example, $d = 2$ for a spin 1/2 Hamiltonian. z is the coordination number of a site (Although most of our discussion is based on uniform z, a generalization to site dependent z is straightforward). M will be used to denote the number of retained states on a local cluster of sites (or "block of sites"). N_s refers to the total number of sites on the tree.

7.2 Purpose of the DMRG calculation

Our objective is to simulate the nearest neighbor spin 1/2 Heisenberg Hamiltonian H defined on a generic tree graph,

$$H = J \sum_{\langle i,j \rangle} \mathbf{S}_i \cdot \mathbf{S}_j \tag{7.1}$$

where $\mathbf{S}_i$ refers to a spin 1/2 operator on site i of the tree graph. The notation $\langle i, j \rangle$ indicates sites i and j are nearest neighbors. Our task is to obtain the low energy spectrum and expectation values of certain one and two site operators (computed in the low energy subspace).

[4] The work done by Kumar et al. [8] is very closely related to the work presented in this Chapter, but the objectives of the research and the interpretation of the results are different.

Some useful definitions are now in order. We define the "root" site of the tree to be the central most site (or "focal point") of the tree. One can define a sense of directionality on a tree: the direction from the boundaries to the root is referred to as "inwards", the direction from the root to the boundaries is referred to as "outwards". This allows us to define the terminology "parent site" and "daughter sites". A site i is said to have "parent" relationship to a "daughter site" j, if i lies on the path connecting j to the root of the tree.

Our method of approach for the DMRG will be to construct, for *every* site in the system, a description of the low energy wavefunctions in terms of the spin half degree on the site and the basis states on the z blocks surrounding it. To carry out this process, we will require the construction of basis transformations that relate the basis spanned by the site degree of freedom (denoted by $|s\rangle$) and the states of $z-1$ blocks (call them $|\beta_i\rangle$) corresponding to the (immediate) daughters attached directly to the site, to the basis spanned by their combination ($|\alpha\rangle$). Mathematically, this relation may be written as,

$$|\alpha\rangle = \sum_{\beta_1,\beta_2...\beta_z-1,s} C^{\alpha}_{\beta_1,\beta_2...\beta_{z-1},s}|\beta_1\rangle|\beta_2\rangle...|\beta_{z-1}\rangle|s\rangle \tag{7.2}$$

where $C^{\alpha}_{\beta_1,\beta_2...\beta_{z-1},s}$ represents the coefficients of expansion of the state $|\alpha\rangle$ in terms of $|\beta_1\rangle|\beta_2\rangle...|\beta_{z-1}\rangle|s\rangle$. The construction of $C^{\alpha}_{\beta_1,\beta_2...\beta_{z-1},s}$ will be explained later in the Chapter.

7.3 Initialization of the DMRG

Consider a segment of a tree located at its boundary and having three sites labelled 1,2,3 (see top of Figure 7.1). We disconnect this segment from the rest of the system and consider only the Heisenberg Hamiltonian defined for these

sites (which we denote as $H_{1,2,3}$). We begin by being naive about "truncating" the local Hilbert space of the segment i.e. we adhere to the idea of retaining the M lowest energy states [5] of $H_{1,2,3}$.

At the end of this calculation, we record the matrix elements of $\langle\alpha|\mathbf{S_1}|\alpha'\rangle$ (i.e. $\langle\alpha|S_1^+|\alpha'\rangle$, $\langle\alpha|S_1^-|\alpha'\rangle$, $\langle\alpha|S_1^z|\alpha'\rangle$), keeping in mind that this information will be used for the subsequent calculation as we go "inwards" towards the root (center) of the tree. A strategic thing to do here is *not* to store $\mathbf{S_1}$ as a $M \times M$ matrix; instead use the fact that operator $\hat{S}_1^+$ can connect only states with S_z that differ by 1 and the operator $\hat{S}_z$ is diagonal in this basis. Simply said, we take advantage of the fact that the M retained states can be grouped according to their total S_z value.

Let us now explicitly show how the subsequent step of 'building up' the lattice works. Consider now two segments or blocks (see bottom of Figure 7.1), having sites (1,2,3) and (4,5,6), which had (previously) been treated independently (i.e. assuming the two segments were totally in isolation). Armed with the information of the spin operators stored on blocks (1,2,3) and (4,5,6), we can calculate the full Hamiltonian (H_{1-7}) for this system,

$$H_{1-7} \equiv H_{1,2,3} + H_{4,5,6} + \mathbf{S_1} \cdot \mathbf{S_7} + \mathbf{S_4} \cdot \mathbf{S_7} \tag{7.3}$$

where $H_{1,2,3}$ and $H_{4,5,6}$ refer to the Hamiltonian of blocks corresponding to sites 1,2,3 and 4,5,6 respectively.

To see how the matrix elements of the full Hamiltonian (H_{1-7}) are computed, consider,

$$H_{IJ} \equiv \langle\alpha'\beta's_7'|H_{1-7}|\alpha\beta s_7\rangle \tag{7.4}$$

[5] One must make sure to adjust M appropriately to include all degenerate multiplets to maintain the $SU(2)$ symmetry of the Hamiltonian and corresponding wavefunctions.

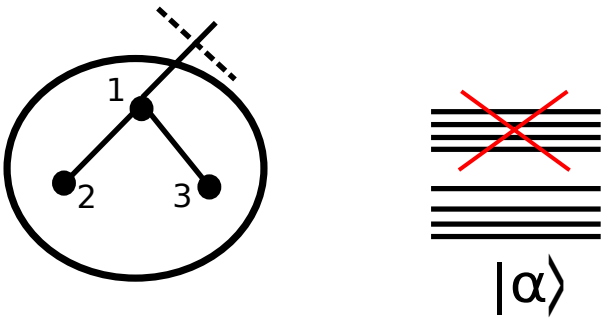

Step 1a : Retain only the M (here 4) lowest energy states α on the "block" made of sites 1,2,3

Step 1b : Store the matrix elements such as $\langle\alpha'|\mathbf{S}_i|\alpha\rangle$

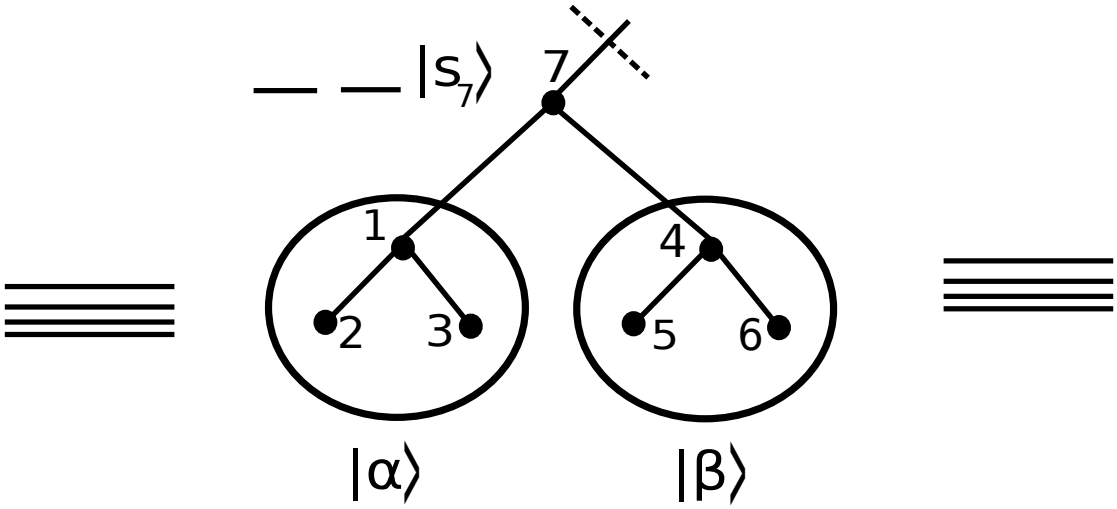

Step 2 : Use information from previous blocks to solve for new system comprising sites 1 through 7

Figure 7.1: Demonstration of "energy based" renormalization steps on a tree lattice in the absence of an environment.

where I refers to the compact index $\alpha'\beta's'_7$ and J refers to the compact index $\alpha\beta s_7$.

Substituting equation (7.3) in equation (7.4) and using the fact that (α, α'), (β, β') and (s, s') are defined on the blocks (1,2,3), (4,5,6) and (7) respectively we get,

$$\begin{aligned} H_{IJ} &= \delta_{\beta,\beta'}\delta_{s_7,s'_7}\langle\alpha'|H_{1,2,3}|\alpha\rangle + \delta_{\alpha,\alpha'}\delta_{s_7,s'_7}\langle\beta'|H_{4,5,6}|\beta\rangle \\ &\quad +\delta_{\beta,\beta'}\langle\alpha'|\mathbf{S_1}|\alpha\rangle\cdot\langle s'_7|\mathbf{S_7}|s_7\rangle + \delta_{\alpha,\alpha'}\langle\beta'|\mathbf{S_4}|\beta\rangle\cdot\langle s'_7|\mathbf{S_7}|s_7\rangle \end{aligned} \tag{7.5}$$

where $\delta_{a,b}$ refers to the Kronecker delta function.

Note that the stored Hamiltonians $\langle\alpha'|H_{1,2,3}|\alpha\rangle$, $\langle\beta'|H_{4,5,6}|\beta\rangle$ and spin matrix elements $\langle\alpha'|\mathbf{S_1}|\alpha\rangle$ and $\langle\beta'|\mathbf{S_4}|\beta\rangle$ are used to to compute the matrix elements of H_{1-7}. (In case the Heisenberg Hamiltonian had next to nearest neighbor interactions, one would *also* need $\langle\alpha'|\mathbf{S_2}|\alpha\rangle$, $\langle\alpha'|\mathbf{S_3}|\alpha\rangle$, $\langle\beta'|\mathbf{S_5}|\beta\rangle$ and $\langle\beta'|\mathbf{S_6}|\beta\rangle$.)

This combined system (comprising of sites 1 through 7) has a basis size of dM^2. We use an iterative diagonalization scheme (such as Lanczos [9], also see 2.A) to obtain *only* the M lowest eigenenergies and corresponding eigenvectors. Note that the eigenvectors (call them $|\gamma\rangle$) are linear combinations of $|\alpha\beta s_7\rangle$, i.e.

$$|\gamma\rangle = \sum_{\alpha,\beta,s_7} C^{\gamma}_{\alpha\beta s_7}|\alpha\rangle|\beta\rangle|s_7\rangle \tag{7.6}$$

so the matrix element $\langle\gamma'|\mathbf{S_7}|\gamma\rangle$ can be computed as,

$$\langle\gamma'|\mathbf{S_7}|\gamma\rangle = \sum_{\alpha,\beta,s_7,s'_7} C^{\gamma}_{\alpha\beta s_7}C^{\gamma'}_{\alpha\beta s'_7}\langle s'_7|\mathbf{S_7}|\mathbf{s_7}\rangle \tag{7.7}$$

At this point we may decide to store operators other than $\langle\gamma'|\mathbf{S_7}|\gamma\rangle$ as well. For example $\langle\gamma'|\mathbf{S_1}|\gamma\rangle$ can be computed as,

$$\langle\gamma'|\mathbf{S_1}|\gamma\rangle = \sum_{\alpha,\alpha',\beta,s_7} C^{\gamma}_{\alpha\ \beta\ s_7}C^{\gamma'}_{\alpha'\ \beta\ s_7}\langle\alpha'|\mathbf{S_1}|\alpha\rangle \tag{7.8}$$

We emphasize that since the Heisenberg Hamiltonian considered for this exposition is a nearest neighbor one, we do not need any operator other than $\langle\gamma'|\mathbf{S_7}|\gamma\rangle$ to carry on the next step of 'adding a site' [6].

One can thus keep performing the process of blocking inwards i.e. towards the root of the tree [7], storing the required amount of information needed to progress to the next stage. This process is carried on till all the "blocking processes meet" at the center of the tree. At the end of the initialization calculation, one has a crude description of the full Hamiltonian on a tree in terms of the "root" degree of freedom surrounded by z blocks (see for example Figure 7.2 which shows a sample system with $z = 3$).

We have already been provided the wisdom (in the literature, see for example [10]) that the manner in which we performed the Hilbert space truncation of a block is *not* accurate. This is because at every stage, we totally ignored the influence of other parts of the cluster (the "environment") on the truncation criterion for the Hilbert space basis on the block. Despite this missing (and crucial) ingredient, the description of the low energy wavefunctions generated (via a sequence of "renormalization" transformations) is a reasonable *starting point* and can be systematically improved.

While the end result of our calculations are expected to be independent of this initialization, a good choice for the starting guess wavefunction can greatly accelerate the rate at which we converge to the final result. In particular, we modify our criterion for retaining states on a block when targeting an excited state (say in a high S_z sector). During the initialization we introduce a "fake" uniform magnetic field in the Hamiltonian to favor retention of states that de-

[6] 'Adding a site' may be used interchangeably with 'building the lattice'.
[7] The "blocking processes" occur independently at various parts of the tree.

scribe the high energy wavefunction.

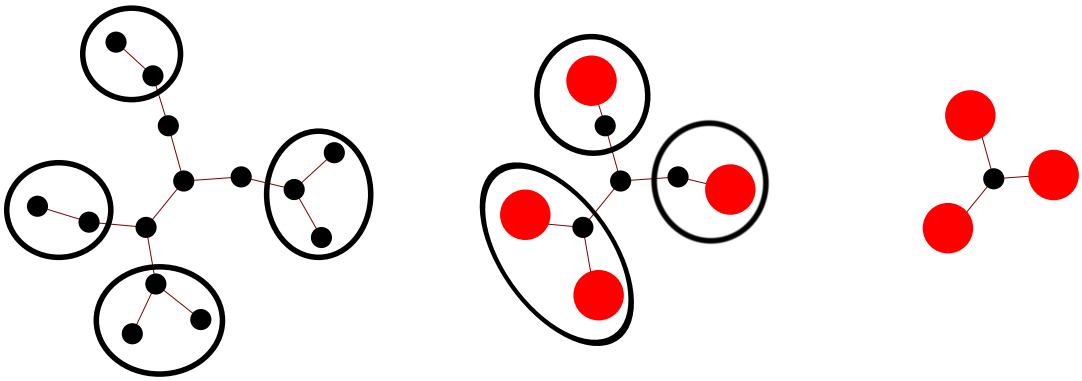

Figure 7.2: Initialization step of the DMRG involving multiple independent renormalization procedures on the tree utilizing energy based truncation. The “army continues to march in” from all sides till one reaches the geometrically central point (often called the “focal point" or “root”). Here we show all stages for a given tree. The red dots represent renormalized blocks.

7.4 Density matrix based truncation

We will now consider how every "iteration" in the DMRG is carried out to systematically approach the ground (or excited) state(s) of the system. For this purpose, we require a description of the full Hamiltonian in terms of a "site" degree of freedom (here $(\uparrow, \downarrow)$) and the basis spanned by the M^z states retained on the z blocks surrounding it.

At every iteration we use the Lanczos algorithm [9] to solve for the lowest energy eigenvector of the *entire* system (also referred to as the "superblock" or "universe") [8]. Treating one of the blocks as the "environment" and the remaining $z-1$ blocks and the "site" collectively as the “system”, we obtain the reduced

[8] Recall the method for generating the Hamiltonian matrix elements from equations (7.4) and (7.5) for the case where two blocks were connected to one site. It is straightforward to generalize this idea of Hamiltonian computation to the case of one site and z blocks.

density matrix (RDM) of the system from the ground state of the superblock by computing;

$$\rho \equiv \mathrm{Tr}_{\mathrm{env}} \left(|\Psi_{\mathrm{GS}} \rangle \langle \Psi_{\mathrm{GS}}| \right) \tag{7.9}$$

To be explicit about what this operation entails, consider $z = 3$ blocks having (not necessarily complete) basis states $|\alpha_1\rangle, |\alpha_2\rangle, |\alpha_3\rangle$ surrounding the site with physical degrees of freedom s. Treating block 3 (with basis states $|\alpha_3\rangle$) as the environment we define,

$$|\Psi_{GS}\rangle \equiv \sum_{\alpha_1,\alpha_2,\alpha_3,s} \psi^{\alpha_1,\alpha_2,\alpha_3,s} |\alpha_1\rangle|\alpha_2\rangle|\alpha_3\rangle|s\rangle \tag{7.10}$$

Treating α_1, α_2, s (α_1', α_2', s') as a compact index A (A'), we have,

$$\rho^{A,A'} = \sum_{\alpha_3} \psi^{\alpha_1,\alpha_2,\alpha_3,s} \psi^{\alpha_1',\alpha_2',\alpha_3,s'} \tag{7.11}$$

Note that the density matrix is a $dM^{z-1} \times dM^{z-1}$ matrix and is matrix-block diagonal since it is composed of sectors with definite total S_z.

During each iteration of the DMRG, each block surrounding the "site" takes its turn being the "environment" while the other blocks together with the "site" act as the "new system" (see for example Figure 7.3). (There is arbitrariness here in the order of choosing a block as an "environment". Empirically we observed this order of performing RG steps is not very crucial to the final result.)

The reduced density matrix of the site plus the $z - 1$ "systems" is computed and its eigenvectors with the largest M eigenvalues are retained. The matrix elements of the spin operator of the "site" are recorded in this basis. In fact, all the subtleties of saving the spin operators (or possibly more operators on a block of sites) apply directly from section 7.3 of this Chapter. The *only* thing that has changed is the density matrix based truncation instead of an energy based truncation.

In addition to the ground state density matrix, we have also targeted higher excited states, by performing a state averaging of the reduced density matrix,

$$\rho^{avg} \equiv \frac{\sum_i w_i \mathrm{Tr}_{\mathrm{env}} \left(|\psi_{\mathrm{i}} \rangle \langle \psi_{\mathrm{i}}| \right)}{\sum_i w_i} \tag{7.12}$$

where w_i is the positive weight given to the density matrix formed from state $|\psi_i\rangle$. In most cases, we simply used $w_i = 1$ for all states we targeted [9]. An advantage of "state averaging" is that it often helps us to prevent (or get us out of) solutions which are local (but not global) minima. The reduced density matrix is diagonalized and only M states with the highest eigenvalues (out of the total dM^z states) are kept on the block.

7.5 Sweep algorithm

Once the density matrix based truncations with the root as "site" are completed, the algorithm proceeds to consider a new division of the lattice into "systems" and "environment" by considering a site on the shell one step out from the root. Each of the z sites connected to the original root gets its turn being the "new root".

After all the sites one step out from the root have been treated as the "new root", we consider the sites which are two steps away from the root (or one step away from the previous sites used to divide the system). This "sweeping out" process continues till one reaches the exterior of the cluster.

After reaching the exterior of the cluster, we "sweep in". However, this time (and for all future sweeps) we have an environment present, whose states we

[9] The number of target states is much smaller than M

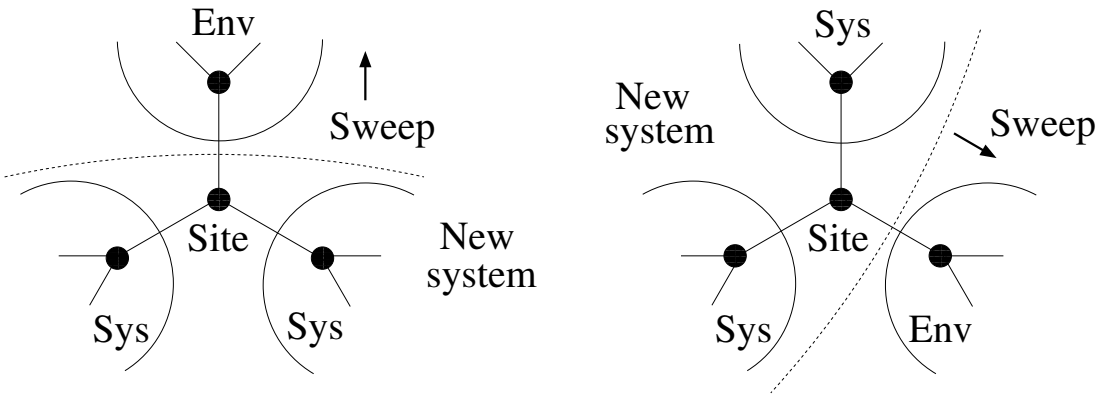

Figure 7.3: Division of the Cayley tree locally into site, system(s) and environment as required by the DMRG. One renormalization step consists of combining the site and system(s) into a new system, retaining the states governed by tracing out the environment degrees of freedom.

trace over to guide the density matrix based truncation process. This in-out-in sweep continues till convergence of the energy is attained. One "complete sweep" is defined to be a "sweep out" (from the root to the boundaries) followed by a "sweep in" (from boundaries to the root) operation.

The scaling of the algorithm (per sweep) can be understood as follows. Each Lanczos diagonalization of the superblock costs $M^z d$ amount of effort and there are N_s such diagonalizations needed, where N_s is the number of sites in the tree. For a highly symmetrical lattice (such as the regular Cayley tree), assuming the desired wavefunction has the full symmetry of the lattice, one can reduce this computational cost to $O(\log_2(N_s)M^z d)$. However this has not been implemented.

The reduced density matrix computed from the eigenvector of the superblock has dimensions $M^{z-1}d \times M^{z-1}d$, which costs $M^{3(z-1)}d^3$ amount of computational effort to diagonalize. However, one must keep in mind that this reduced density matrix has a block diagonal structure owing to the fact that the retained states have definite S_z symmetry, which brings down the cost associated with

this step.

7.6 Computing expectations

The end result of the DMRG calculation is an explicit (yet compact) representation of the wavefunction in terms of the block states with which we can efficiently compute various kinds of correlation functions. Notice that in the DMRG procedure described earlier, there exist *multiple* descriptions of the wavefunction depending on the way one divides or "cuts" the universe (full system) into "systems", "site" and "environment".

We perform "measurements" of expectation value of operators in the desired states, after the sweep algorithm has "converged". Our criterion for convergence is to check whether the energy of the target states is not changing i.e. the obtained state is a fixed point of the sweep procedure. Ideally one would have a good representation of the desired wavefunction(s) for any division of the universe into system and block. In practice, the limitation on M does not guarantee this. Thus we make measurements only for the "cut" that involves the "root" site.

For the purpose of this thesis, we have measured the spin-spin correlation functions $\langle \mathbf{S}_i \cdot \mathbf{S}_j \rangle$ and the matrix elements $\langle l | \, S_i^+ \, | l' \rangle$, where l and l' refer to eigenstates of the Heisenberg Hamiltonian. For Chapter 8 we required the matrix element $\langle 1 | \, S_i^+ \, | 0 \rangle$, where $|0\rangle$ ($|1\rangle$) refers to the ground state singlet (first excited state triplet) and has the labels $|S = 0, S_z = 0\rangle$ ($|S = 1, S_z = 1\rangle$). The matrix element $\langle 1 | \, S_i^+ \, | 0 \rangle$ is computed by targeting the ground and excited state in the same DMRG run, so that both states $|0\rangle$ and $|1\rangle$, have the same block representation.

7.6 .1 Matrix elements involving a single site

To demonstrate the computation of a matrix element involving a single site i, consider $\langle l'|S_i^+|l\rangle$, where $|l'\rangle$ and $|l\rangle$ are two distinct states (wavefunctions) and the total S_z of state $|l'\rangle$ is one larger than the total S_z of $|l\rangle$. Let us take the root to be site r and connected to $z = 3$ blocks with representations given by the states $|\alpha_1\rangle$,$|\alpha_2\rangle$,$|\alpha_3\rangle$. Let the immediate sites connected to the root be called r_1,r_2,r_3. Also assume that site i belongs to block 1. The setup for this calculation is illustrated in Figure 7.4.

Consider the wavefunctions $|l\rangle$ and $|l'\rangle$ to be described in terms of the block states and the spin degree of freedom on the root i.e.

$$|l\rangle \equiv \sum_{\alpha_1,\alpha_2,\alpha_3,s_r} \psi_l^{\alpha_1,\alpha_2,\alpha_3,s_r} |\alpha_1\rangle|\alpha_2\rangle|\alpha_3\rangle|s_r\rangle \tag{7.13}$$

$$|l'\rangle \equiv \sum_{\alpha_1,\alpha_2,\alpha_3,s_r} \psi_{l'}^{\alpha_1,\alpha_2,\alpha_3,s_r} |\alpha_1\rangle|\alpha_2\rangle|\alpha_3\rangle|s_r\rangle \tag{7.14}$$

where $\psi_{l(l')}^{\alpha_1,\alpha_2,\alpha_3,s}$ are coefficients of the expansion of the wavefunctions $|l\rangle(|l'\rangle)$ in the $|\alpha_1\rangle|\alpha_2\rangle|\alpha_3\rangle|s_r\rangle$ basis.

Thus the desired matrix element is,

$$\langle l'|S_i^+|l\rangle = \sum_{\alpha_1,\alpha_1',\alpha_2,\alpha_3,s_r} \psi_l^{\alpha_1,\alpha_2,\alpha_3,s_r}\ \psi_{l'}^{\alpha_1',\alpha_2,\alpha_3,s_r}\ \langle\alpha_1'|S_i^+|\alpha_1\rangle \tag{7.15}$$

Now it is possible that we did not store $\langle\alpha_1'|S_i^+|\alpha_1\rangle$ previously (or for some reason chose not to store it). However, note that we have stored all the transformation matrices (the 'renormalization group transformations') that tell us how to express the basis states of the 'parent block' in terms of the basis states of the 'daughter blocks'. Thus, one may express $|\alpha\rangle$ in terms of the $|\beta_1\rangle|\beta_2\rangle|s_{r_1}\rangle$

$$|\alpha_1\rangle = \sum_{\beta_1,\beta_2,s_{r_1}} C_{\beta_1,\beta_2,s_{r_1}}^{\alpha_1} |\beta_1\rangle|\beta_2\rangle|s_{r_1}\rangle \tag{7.16}$$

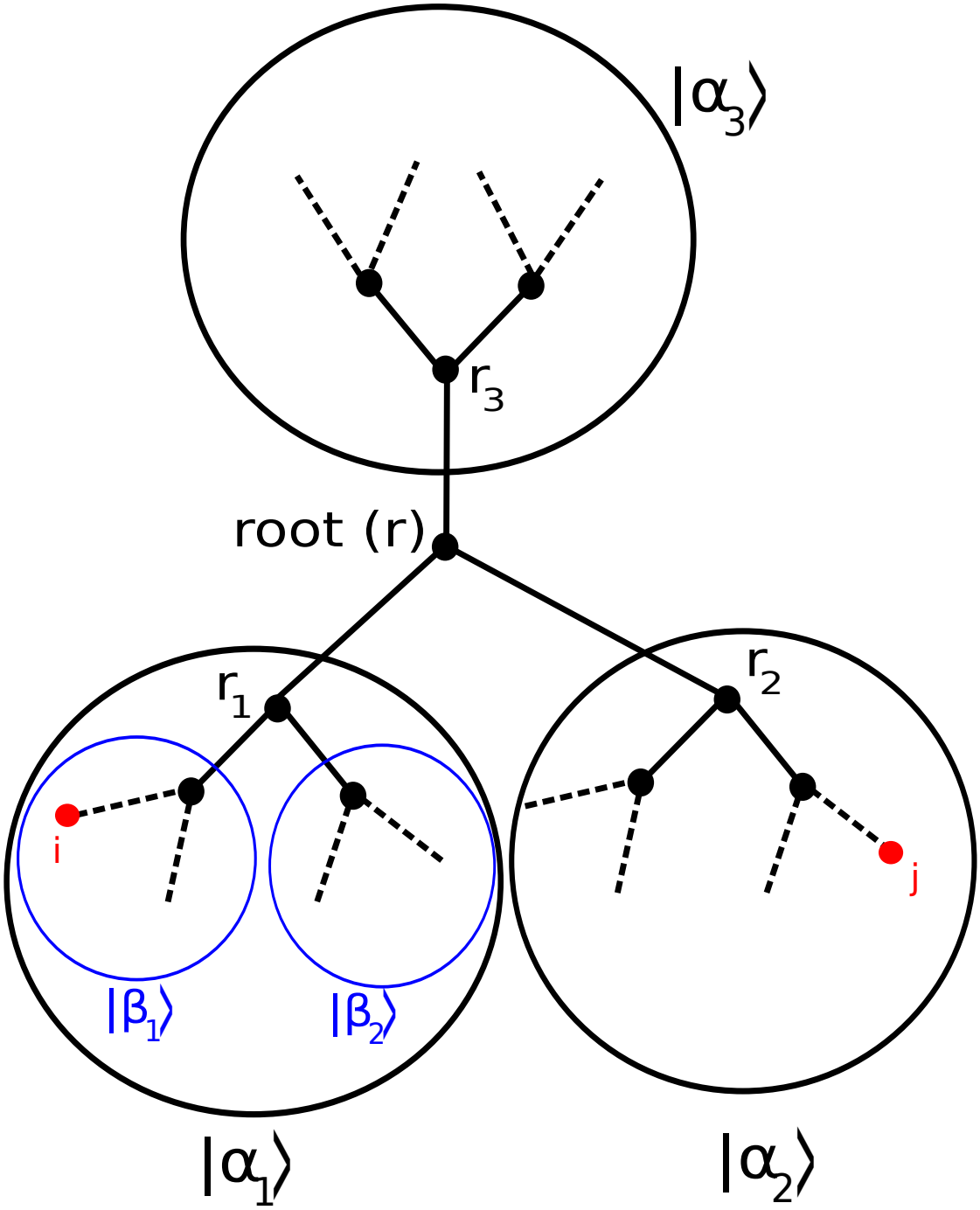

Figure 7.4: Computation of one and two site matrix elements in DMRG on a tree lattice.

Now say i belongs to daughter block 1. We may compute $\langle \alpha_1' | S_i^+ | \alpha_1 \rangle$ as,

$$\langle \alpha_1' | S_i^+ | \alpha_1 \rangle = \sum_{\beta_1, \beta_1', \beta_2, s_{r_1}} C^{\alpha_1'}_{\beta_1', \beta_2, s_{r_1}} C^{\alpha_1}_{\beta_1, \beta_2, s_{r_1}} \langle \beta_1' | S_i^+ | \beta_1 \rangle \tag{7.17}$$

To elaborate the point being made here, we note, that the user may not have even stored $\langle \beta_1' | S_i^+ | \beta_1 \rangle$. The $|\beta_1\rangle$ basis can further be re-expressed in terms of its "daughter basis". The procedure of "going deeper" into the tree may be repeated till one reaches the point where site i is the head of the tree and only the matrix element required is $\langle s_i' | S_i^+ | s_i \rangle$ which is trivial to compute (i.e. simply use the spin 1/2 algebra).

In summary, once the matrix element of S_i^+ is known in some daughter basis one can "work one's way up" to get the desired $\langle \alpha_1' | S_i^+ | \alpha_1 \rangle$. Also note that computationally, calculating $\langle \alpha_1' | S_i^+ | \alpha_1 \rangle$ is a very feasible operation, both from the point of view of storage and time. From the point of view of storage, all we need is a sequence of the matrix elements from $\langle s_i' | S_i^+ | s_i \rangle$ to $\langle \beta_1' | S_i^+ | \beta_1 \rangle$ to arrive at the desired $\langle \alpha_1' | S_i^+ | \alpha_1 \rangle$. Each of these objects is at most a $M \times M$ matrix (its storage being significantly less than M^2 if stored sparsely) which is quite affordable for the M that we deal with. Time wise, we have to perform g computations of matrix elements where g is the "chemical distance" of the site i from the root. Each such computation costs order dM^z operations, z being the coordination number of a site.

7.6 .2 Matrix elements involving two sites

The two site matrix elements are straightforward and essentially use the same idea as the one site matrix elements with minor modifications. Consider,

for the sake of simplicity, the case of computing $\langle l'|S_i^+ S_j^-|l\rangle$ (other correlation functions also follow in a similar fashion) where i belongs to block 1 and j belongs to block 2 as shown in Figure 7.4. Since the $S_i^+ S_j^-$ operator does not change the total S_z, it can only couple l and l' having the same total S_z.

Adhering to the notations described in section 7.6 .1 we obtain,

$$\langle l'|S_i^+ S_j^-|l\rangle = \sum_{\alpha_1,\alpha_1',\alpha_2,\alpha_2',\alpha_3,s_r} \psi_l^{\alpha_1,\alpha_2,\alpha_3,s_r}\ \psi_{l'}^{\alpha_1',\alpha_2',\alpha_3,s_r}\ \langle\alpha_1'|S_i^+|\alpha_1\rangle\langle\alpha_2'|S_j^-|\alpha_2\rangle \quad (7.18)$$

Since one index less is summed over than the one site matrix element case, the computation is order M times more expensive (time-wise) on the whole. As in the one-site case, we need $\langle\alpha_1'|S_i^+|\alpha_1\rangle$ and $\langle\alpha_2'|S_j^-|\alpha_2\rangle$.

The reader may naturally ask, what happens when the two sites are on the same block $|\alpha_1\rangle$? In that case, we treat $S_i^+ S_j^-$ just like the one site operator till a depth at which the sites i and j begin to belong to two different daughter blocks. Beyond this depth we require the one site matrix elements of site i and site j in their individual daughter blocks.

7.6 .3 Entanglement spectrum

We also study the eigenvalues of the reduced density matrix (for a particular division of the lattice), collectively known as the "entanglement spectrum" [11, 12]. These turn out to be a very useful probe of the low energy degrees of freedom (as we will see in section 8.4 .3). This needs no extra effort in the DMRG, since these eigenvalues are computed anyway as part of the truncation process.

7.7 Parameters and benchmarks

All calculations reported here are for the $z = 3$ case and $M \leq 160$. For all systems considered here we get reasonable convergence of the energy within 20 sweeps (see for example Figure 7.5). To benchmark our calculations we have also compared our results with Exact Diagonalization data where possible.

We tested our code for three different geometries of the Cayley tree - the bond centered, site centered and Fibonacci trees, which will be formally discussed in Chapter 8. For the present discussion, it is not crucial to understand the differences between the trees, this section will just showcase some of our trial calculations. One can see from Table 7.1 that the convergence of the energy (in the S_z sector corresponding to the spin S_0 of the ground state) and the spin gap (defined to be $E(S_0 + 1) - E(S_0)$) is rapid as a function of the number of retained states on a block (M) for the site centered and Fibonacci trees. However, for the bond centered tree (Table 7.2), the convergence with M is comparatively slower. Based on our data, we conclude that while larger M calculations are certainly desirable, the present calculations are sufficiently accurate to make quantitative estimates in Chapter 8.

M	$N_s = 190$		$N_s = 176$	
	E_{GS}	Δ	E_{GS}	Δ
20	-74.54049387	0.9397293	-76.46983049	0.08834668
60	-74.54054021	0.9397198	-76.47071767	0.08725531
100	-74.54054022	0.9397198	-76.47072851	0.08725207

Table 7.1: Energy (E_{GS}) and Spin gap (Δ) for the 190 site site-centered and 176 site Fibonacci lattices for various values of M.

As we can see from these benchmarks (and based on our experience), the

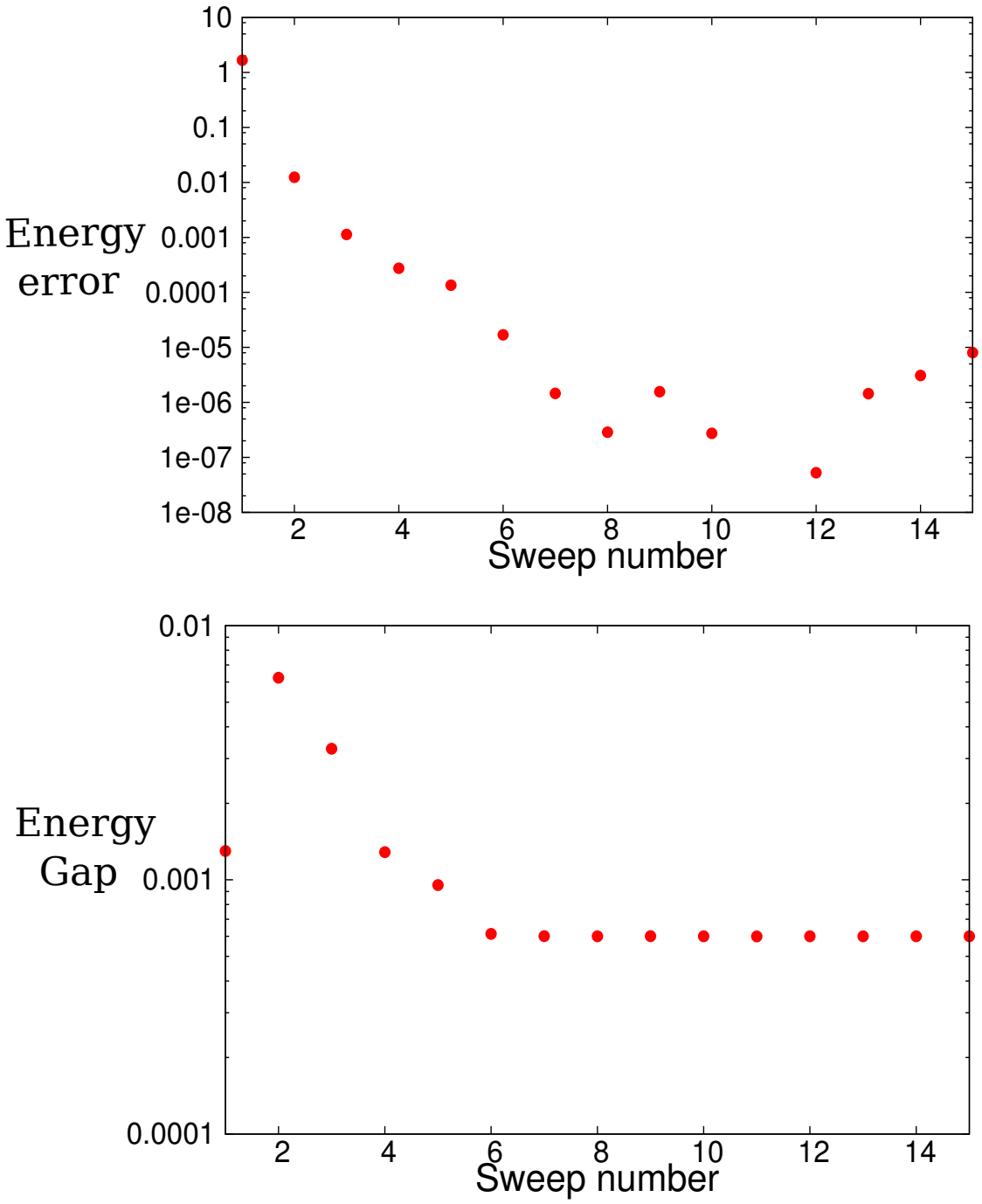

Figure 7.5: As a representative example to demonstrate convergence of the ground state energy and the spin gap, we consider a 126 site bond centered tree and fixed $M = 140$. The error in the ground state energy is calculated with respect to the lowest energy encountered in the sweeps. The lowest energy was encountered in sweep 11 which is why the energy error for that point is absent. Even though the energy appears to increase after sweep 11, we note that the error is well within the accuracy of the Lanczos diagonalization of the superblock Hamiltonian.

M	E_{GS}	Δ	$\langle 1 \vert s_c^+ \vert 0 \rangle$	$\langle 1 \vert s_b^+ \vert 0 \rangle$
60	-49.3405119	3.4×10^{-4}	0.310	0.370
80	-49.3412938	5.7×10^{-4}	0.300	0.344
100	-49.3415002	6.0×10^{-4}	0.280	0.337
120	-49.3415347	6.0×10^{-4}	0.279	0.335
140	-49.3415521	6.0×10^{-4}	0.278	0.335

Table 7.2: Energy (E_{GS}), Spin gap (Δ) and s^+ matrix elements for the central (c) and boundary (b) sites for the 126 site bond-centered for various values of M.$|0\rangle$ and $|1\rangle$ refer to the lowest singlet and triplet respectively.

number of states M per block needed to describe properties of a state (to a certain numerical precision) depends on not only the number of sites in the cluster N, but also the *nature* of the ground state being described. In more concrete terms, the number of states M directly depends on the amount of (ground state) entanglement entropy. If the entropy is high, M is large; if the ground state is weakly entangled one can perform accurate calculations even with small M. In this Chapter, we will not delve into why the above mentioned trees behave differently, we reserve that discussion for Chapter 8.

BIBLIOGRAPHY

[1] H. J. Changlani, S. Ghosh, C. L. Henley and A.M. Läuchli, arXiv:1208.1773.

[2] S. R. White, Phys. Rev. Lett. **69**, 2863 (1992).

[3] K. G. Wilson, Rev. Mod. Phys. **47**, 773 (1975).

[4] U. Schollwöck, Rev. Mod. Phys. **77**, 259 (2005).

[5] H. Otsuka, Phys. Rev. B **53**, 14004 (1996).

[6] B. Friedman, Journal of Physics: Condensed Matter **9**, 9021 (1997).

[7] M.-B. Lepetit, M. Cousy, and G.M. Pastor, Eur. Phys. J. B **13**, 421 (2000).

[8] M. Kumar, S. Ramasesha, and Z. G. Soos, Phys. Rev. B **85**, 134415 (2012).

[9] *Templates for the Solution of Algebraic Eigenvalue Problems: a Practical Guide* Z.Bai, J. Demmel, J. Dongarra, A. Ruhe, and H. van der Vorst, Society for Industrial and Applied Mathematics (2000).

[10] S. R. White and R. M. Noack, Phys. Rev. Lett. **68**, 3487 (1992).

[11] P. Calabrese and A. Lefevre, Phys. Rev. A **78**, 032329 (2008).

[12] H. Li and F. D. M. Haldane, Phys. Rev. Lett. **101**, 010504 (2008).

CHAPTER 8

HEISENBERG ANTIFERROMAGNET ON CAYLEY TREES

This Chapter is a reproduction (with minor presentational changes for the purpose of this thesis) of Sections I-VIII (except Section III) of the paper [1] under peer review in Physical Review B. This paper may also be accessed online at the address http://arxiv.org/pdf/1208.1773v1.pdf . Section III of this paper has already been discussed as Chapter 7 of this thesis, which details the working of the DMRG algorithm as applied to generic tree graphs. The author acknowledges Shivam Ghosh as the lead on the Schwinger Boson calculations presented in Section 8.5 of this Chapter.

8.1 Motivation for considering the Cayley Tree

Quantum antiferromagnetism for unfrustrated systems has been one of the most extensively researched subjects in condensed matter physics. One of the simplest models in this family, the nearest neighbor spin $\frac{1}{2}$ Heisenberg antiferromagnet on the square lattice, has been studied extensively: analytically with spin wave [2, 3, 4] and Schwinger Boson approaches [5, 6, 7, 8, 9] and numerically with Quantum Monte Carlo [10] (which has no "sign problem" for bipartite lattices). That said, effects from physical imperfections such as the presence of open edges [11, 12] and static non magnetic impurities [13] are less well understood and hence are areas of active research. Random dilution, for example, has been found to affect the low energy spectrum drastically, as has been demonstrated in recent numerical studies by Wang and Sandvik [14, 15]. They showed that the singlet-triplet energy gap on finite clusters, at the percolation threshold, is much smaller than that expected from the conventional Anderson

tower of states (or “quantum rotor” states) [16, 17, 18, 19, 20]. This was in disagreement with a previous theoretical result [21].

Wang and Sandvik attributed the mechanism of the creation of this low energy scale to the presence of regions of "local sublattice imbalance", arising out of areas in the cluster where the number of opposite sublattice sites were unequal. In their picture, geometric constraints of a diluted square lattice forbid spins from pairing up with their neighbors into dimers, leaving some of them unpaired or "dangling" [14]. They believe these emergent spins to be the effective low energy degrees of freedom.

By considering the undiluted nearest neighbor Heisenberg model on the Cayley tree (or Bethe lattice) (shown in Figure 8.1) we have been able to systematically investigate the effect of sublattice imbalance on the low energy spectrum. In particular, we contend that the effect of sublattice imbalance is to create a "tower of states", lower than the Anderson tower of states. Aided by numerical calculations, we propose a framework for understanding this relationship. We also find that Schwinger Boson Mean Field theory [8] is a good description of the many body ground state and can reproduce many of its features quantitatively.

Previous studies of this model by Otsuka [22] and Friedman [23] focused primarily on ground state properties and excited states were not considered in these studies. More recently Kumar et al. [24] have significantly extended this analysis to both the spin-1/2 and spin-1 Heisenberg model. We use all these studies as useful benchmarks for our own numerical calculations.

The Cayley tree is a lattice without loops, with all sites (except those on the

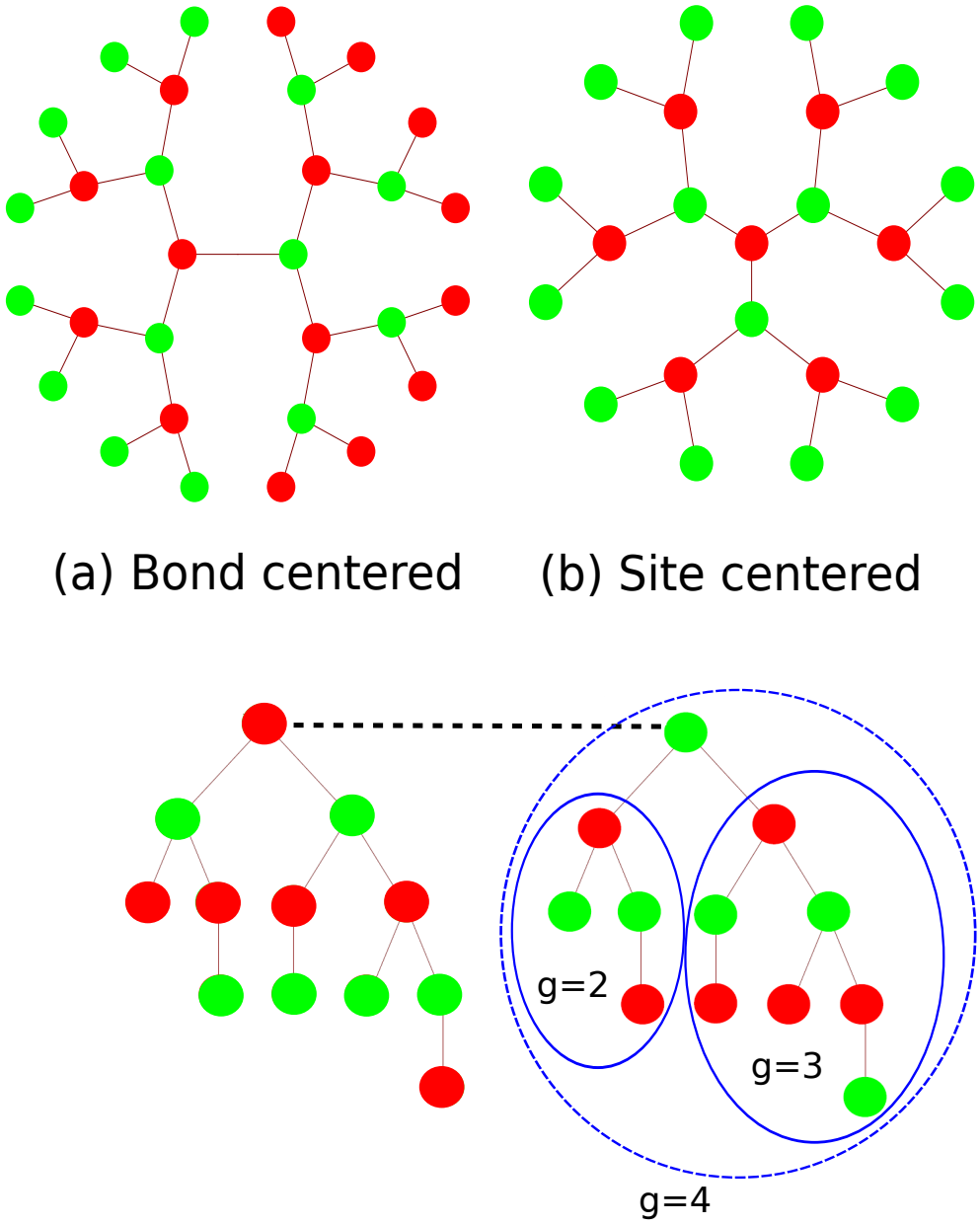

Figure 8.1: (Color online) (a) The bond-centered Cayley tree. (b) The site-centered Cayley tree. In both cases all sites, other than those on the boundary, have coordination 3. (c) The "Fibonacci Cayley tree" is constructed hierarchically and has some coordination 2 sites. The figure shows a generation 4 cluster generated by connecting the roots (head sites) of the generation 2 and generation 3 trees to a common site (the root of the generation 4 tree). To have a globally balanced cluster we introduced a bond connecting the root of the generation 4 tree with the root of its mirror image. All clusters in (a),(b),(c) are bipartite (the dark (red) and light (green) colors show the two sublattices) and have no loops.

boundary) having a coordination z. The number of sites on the boundary is asymptotically the same as the number of sites in the bulk [1]. This is a pathology of the Cayley tree, in contrast to lattices in Euclidean space. As a consequence, different ways of approaching the thermodynamic limit may give different results in any problem based on the Cayley tree. In particular, when we use three different limiting sequences of finite clusters (see sec. 8.2), we find qualitatively different limiting behaviors; a central thrust of the Chapter is to explain why. But it is generally possible in Cayley tree problems to define a "bulk" limit if, rather than averaging expectations over the entire cluster, one evaluates them only within a cluster of some fixed size which is kept at the center while the boundaries get farther and farther away [2].

From a theorist perspective, the Cayley tree achieves many simplifications which makes exact solutions possible. For example, the Bose Hubbard model on this lattice has been recently solved by Semerijan, Tarzia and Zamponi [26]. It has also been used as a tool to study the Brinkman-Rice transition for the Hubbard model [27]. It has also found applications in the treatment of the quantum impurity problem which is at the heart of Dynamical Mean Field Theory (DMFT) [28]. There has also been interest in the study of dendrimers [29, 30, 31], but it does not appear that a spin model has been realized on such a topology experimentally.

The complete absence of loops makes this lattice conducive for the Density Matrix Renormalization Group (DMRG) algorithm [32]. With the DMRG

[1] We will later modify this definition of the Cayley tree to also include the Fibonacci-Cayley tree.

[2] In the literature, the "Bethe lattice" is often used to refer to the thermodynamic limit of the "Cayley tree", where the effect of boundaries is eliminated (see for example Laumann et al. [25] which considers random graphs of fixed connectivity). For the purpose of this work, the presence of open boundaries will play an important role in the low energy physics and so we will simply use the term "Cayley tree" from now on.

method we have an explicit (yet compact) representation of ground and excited state many body wavefunctions which gives us lots of information to understand the low energy properties of these systems. In particular, reduced density matrices can be used as tools to understand properties of these states [33].

The remainder of this Chapter is divided as follows. In section 8.2 we introduce the model and lattices being investigated and define a measure of sublattice imbalance associated with them. In section 8.3 , we discuss the properties of the ground and excited states of these trees. In section 8.4 , we use a variational ansatz given by the single mode approximation, in conjunction with an argument from first order perturbation theory, to explain the finite size scaling of the spin gap. Finally, in section 8.5 , we corroborate our observations of the ground state properties, by the use of the Schwinger Boson mean field theory (SBMFT).

8.2 The Model

We consider the nearest neighbor antiferromagnetic spin 1/2 Heisenberg model with uniform coupling J,

$$H = J \sum_{\langle i,j \rangle} \mathbf{S}_i \cdot \mathbf{S}_j \tag{8.1}$$

In this Chapter, we use spin rotational symmetry of the Hamiltonian (8.1), to label many body states by $|S, S_z\rangle$, where S refers to the spin of the state and S_z is its z component. On a bipartite lattice (with sublattices A and B), like the Cayley tree, with n_A sites in sublattice A and n_B sites in sublattice B, it is rigorously known [34] that the ground state of the Heisenberg Hamiltonian has a net spin $S = \left|\frac{n_A - n_B}{2}\right|$.

The first kind of tree we consider is the "bond-centered" Cayley tree of the form depicted in Figure 8.1(a). The number of sites N_s for such a cluster is related to the "generation" g by,

$$N_s(g) = 2^{g+1} - 2 \tag{8.2}$$

Since the bond centered clusters have no "global imbalance" i.e. $n_A = n_B$, the ground state is a singlet (and the monotonicity of the energy with spin S implies that the first excited state is a triplet).

As mentioned before, the notion of "local sublattice imbalance" will be crucial in understanding the low energy physics. For the bond centered cluster, we define a measure of imbalance (which we refer to as I_b from here on) by dividing the cluster at the central bond into two equal parts. We count the excess of one sublattice over the other in one half of the cluster and multiply by 1/2 for spin 1/2. It can be easily shown that $I_b(g)$ is related to the generation g as,

$$I_b(g) = \frac{2^g \pm 1}{6} \tag{8.3}$$

where $+(-)$ is for g odd(even).

Figure 8.1(b) shows the more usual way of defining a Cayley tree and which we refer to as "site-centered". The number of sites is related to the generation g by,

$$N_s(g) = 3\,(2^g - 1) + 1 \tag{8.4}$$

Unlike the bond centered cluster, a global sublattice imbalance exists here which leads to a ground state spin of $S_0 \equiv 2^{g-1}$. We measure the imbalance $I_s(g)$ in any of the three symmetrical arms of the site centered Cayley tree. As before, we measure the excess sites of one sublattice over the other (in one arm) and

multiply by 1/2. This definition is particularly convenient as it gives us $I_s(g) = I_b(g)$ for all g.

A recent publication on the study of the Heisenberg model on the Cayley tree by Kumar, Ramasesha and Soos [24] considers the site-centered clusters. We confirm their results for the site-centered case, but interestingly find that the bond-centered cluster has significantly different ground and excited state properties. We will provide some brief comparisons in section 8.3 to illustrate this point.

How is the situation different if there is no imbalance locally? To address this, we introduce the "Fibonacci Cayley tree", an example of which is shown in Figure 8.1(c). The recipe for generating this lattice is to make generation $g+1$ by attaching the roots (head sites) of the generation g and $g-1$ trees to a common site (which becomes the root/head of the new tree). Figure 8.1(c) shows how the $g = 2$ and $g = 3$ tree are combined to get the $g = 4$ tree.

If we label the number of odd/even sublattice sites by A_g and B_g, then (counting the root as even), we get,

$$A_{g+1} = 1 + B_g + B_{g-1} \tag{8.5a}$$

$$B_{g+1} = A_g + A_{g-1} \tag{8.5b}$$

The total number of sites N_s at generation $g+1$ is,

$$\begin{aligned} N_s(g+1) &= A_{g+1} + B_{g+1} \\ &= 1 + B_g + B_{g-1} + A_g + A_{g-1} \\ &= 1 + N_s(g) + N_s(g-1) \end{aligned} \tag{8.6}$$

Observe that $N_s(g)$ satisfies the Fibonacci recursion, that is, $N_s(g) = F_{g+1} - 1$, where F_g is the g-th Fibonacci number. The size of this lattice grows as τ^g where

τ is the golden ratio $\tau = (1+\sqrt{5})/2 \sim 1.618$. Also, every third generation is unbalanced by one and every other generation is both globally and locally balanced. Table 8.1 lists out the sizes of the Fibonacci-Cayley clusters along with the number of sites in each sublattice, for up to $g = 11$ generations.

Generation (g)	No. of A sites A_g	No. of B sites B_g	Total no. of sites $N_s(g)$
0	1	0	1
1	1	1	2
2	2	2	4
3	4	3	7
4	6	6	12
5	10	10	20
6	17	16	33
7	27	27	54
8	44	44	88
9	72	71	143
10	116	116	232
11	188	188	376

Table 8.1: Number of sites in Fibonacci-Cayley trees shown up to 11 generations. A_g and B_g indicate the number of A and B sublattice sites respectively.

In order to have a balanced cluster at *every* generation, we combine two identical generation g Fibonacci constructions (as in equation (8.6)), by introducing a bond connecting their roots, as is illustrated in Figure 8.1(c).

8.3 Ground And Excited States

Using the DMRG algorithm presented in Chapter 7, we calculate the ground state energy and spin gap and point out the differences between the bond and site centered clusters. To highlight the role of local imbalance, we also compare the excited states of the bond-centered and Fibonacci trees, both of which are

globally balanced.

8.3 .1 Ground State Energy, Spin-spin correlations and Spin Gap

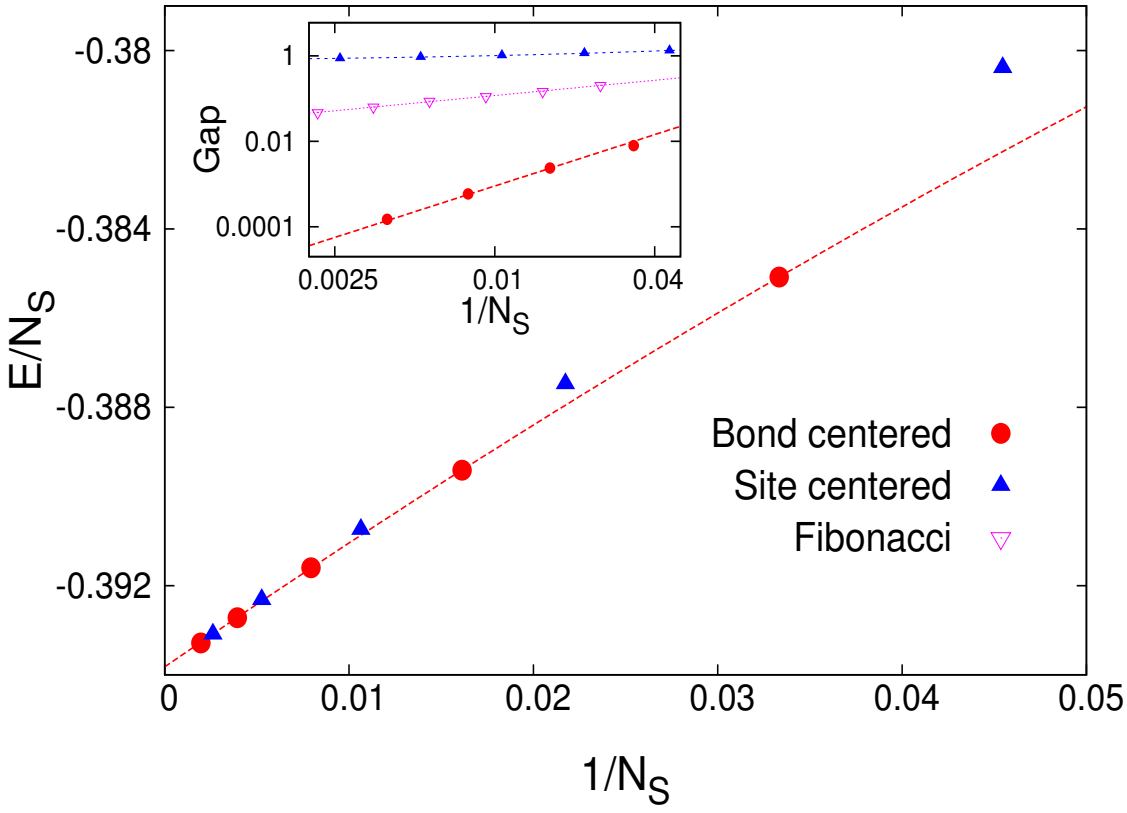

Figure 8.2: Ground state energy per site for the bond centered and site centered Cayley trees for various lattice sizes. The Fibonacci Cayley tree energies are out of the scale considered. A fit to the bond centered results given by Eq.(8.8) has been shown. Inset: Finite size scaling of the energy gap Δ plotted on a log-log scale. The bond-centered and Fibonacci clusters appear gapless in the infinite lattice limit, with a finite size scaling exponent of $\alpha \approx 2$ and $\alpha \approx 0.6$. However, the site-centered clusters have a finite Δ in the infinite lattice limit in concordance with the results of Ref. [24]. The lines shown are fits to the DMRG data using equations (8.9, 8.10).

We consider the bond-centered, site-centered and Fibonacci clusters and compute the ground state energy and the spin gap Δ defined as,

$$\Delta = E_{GS}(S_0 + 1) - E_{GS}(S_0) \tag{8.7}$$

where S_0 is the spin of the ground state.

In order to compute the energy per site in the infinite lattice limit e_0 we fit E_{GS}/N_s to the functional form,

$$\frac{E_{GS}}{N_s} = e_o + \frac{a}{N_s} + \frac{b}{N_s^2} \tag{8.8}$$

For the bond and site-centered clusters we get $e_0 = -0.393855(2)$ and $e_0 = -0.393854(2)$ respectively both of which are consistent within error bars of extrapolation and with the value of $e_0 = -0.39385$ reported by Ref. [24] for site-centered clusters.

In comparison, as Table 8.2 shows, the energy per site of the Fibonacci tree is significantly lower than either of the bond or site centered trees. This is achieved by the formation of very strong nearest neighbor dimers (especially on the boundary, as the degree of dimerization dies down as one proceeds inwards). The degree of boundary dimerization is more limited in the site and bond centered trees.

Despite the dissimilarities between the three lattices, the "bulk limit" of the estimated energy per bond, based on taking an average of nearest neighbor $\langle \mathbf{S}_i \cdot \mathbf{S}_j \rangle$ over the innermost bonds, is roughly identical for all three kinds of Cayley tree, about $-0.35J$.

We now turn to a discussion of the spin gap. The site-centered cluster has a spin gap in the infinite lattice limit, which we obtained by fitting to,

$$\Delta = \Delta_\infty + \frac{c}{N_s^\alpha} \tag{8.9}$$

and found Δ_∞ to be 0.731(4) and $\alpha \sim 0.5$.

The bond-centered and Fibonacci clusters appear to be gapless in the infi-

Cluster	e_0	a	b	Δ
Bond centered	$-0.393855(2)$	0.292(1)	$-1.05(4)$	$\sim N_s^{-2}$
Site centered	$-0.393854(1)$	0.291(1)	+0.099(3)	0.73 + $2.86/N_s^{0.5}$
Fibonacci	$-0.435433(1)$	0.167(1)	$-0.42(4)$	$\sim N_s^{-0.6}$

Table 8.2: Ground state energy per site e_0, finite size scaling parameters for the ground state energy a, b (from Eq.(8.8)) and spin gap Δ (from equations(8.9,8.10) for the bond-centered, site-centered and Fibonacci clusters.

nite lattice limit, based on simulations of cluster sizes up to 254 and 464 sites respectively. We computed the finite size scaling of this gap using,

$$\Delta \sim N_s^{-\alpha} \tag{8.10}$$

Empirically, the value of $\alpha \sim 0.6$ for Fibonacci and $\alpha \sim 2$ for the bond centered clusters matches rather well with our data (see inset of Fig. 8.2).

Denoting the ground state as $|0\rangle$, we also compute the ground state connected correlation function defined here as,

$$G_{ij} \equiv \langle 0 | \mathbf{S}_i \cdot \mathbf{S}_j | 0 \rangle - \langle 0 | S_i^z | 0 \rangle \langle 0 | S_j^z | 0 \rangle \tag{8.11}$$

For the bond-centered and Fibonacci clusters, $\langle 0 | S_i^z | 0 \rangle = 0$ for all i, and hence we have,

$$G_{ij} = \langle 0 | \mathbf{S}_i \cdot \mathbf{S}_j | 0 \rangle \tag{8.12}$$

Figure 8.3 shows sample correlation functions on the bond-centered and Fibonacci trees and Figure 8.4 shows some sample correlation functions on the site-centered tree. The marked difference in the behavior of the spin gap and the

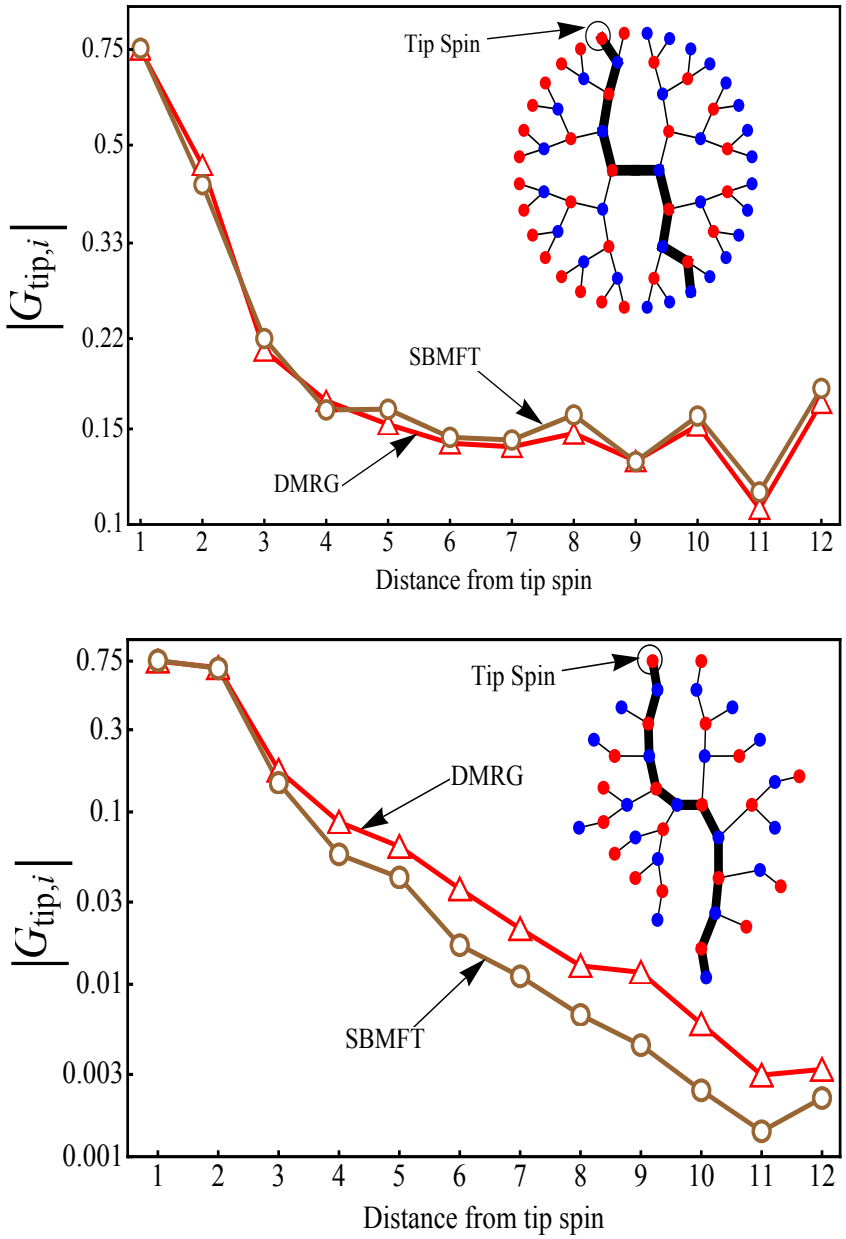

Figure 8.3: (Color online) Ground state spin-spin correlations $G_{a,i}$, as in equation (8.11), for the bond centered and Fibonacci Cayley trees. The reference spin a is the tip spin and is held fixed while the other spin i is take at distance a along the highlighted path. DMRG results are compared with numerical solutions of Schwinger Boson mean field theory (SBMFT) from Section 8.5 . Above: Bond-centered tree with $N_s = 126$ sites. The SBMFT corrrelations shown have been scaled up by an overall factor of 1.8 to take into account corrections beyond mean field (in the broken symmetry phase). The DMRG and SBMFT results show good agreement, asymptoting to a constant. Below: Fibonacci tree with $N_s = 40$ sites. For the "quantum disordered" phase, the SBMFT correlations were scaled up by an overall factor of $3/2$ (For details see section 8.5 .2). Correlations appear to be decaying exponentially with distance.

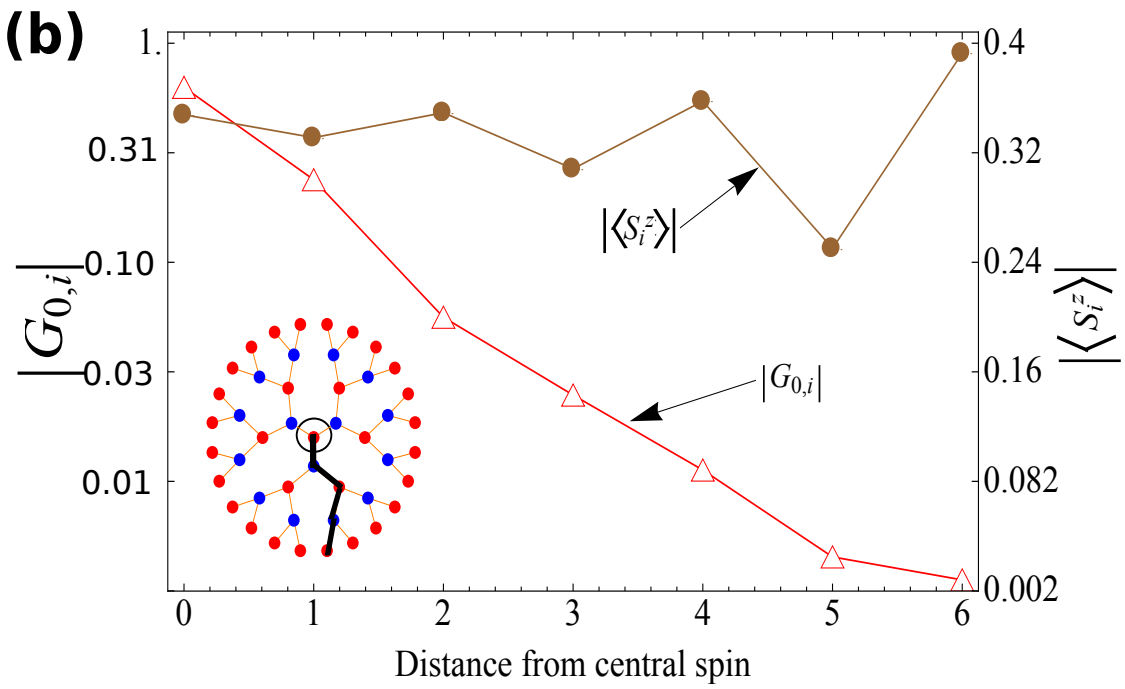

Figure 8.4: (Color online) Ground state spin-spin correlations $G_{a,i}$, as in equation (8.11), for the site-centered tree. The reference spin a is held fixed (here at the central most site) while the other spin i is take at distance a along the highlighted path. The data shown is for the cluster with $N_s = 190$ sites, in the maximum S_z member of the ground state multiplet ($S_z = S_0$). The magnetization $|\langle S_i^z \rangle|$ is also shown, as a function of distance from the center. Even though the connected correlation function decays to zero exponentially fast, the long range order is encoded in the fact that that the magnetization is non zero.

spin correlations between the site- and bond-centered clusters can be attributed to a different manifestation on the two type of clusters of the spontaneous spin symmetry breaking occurring in the thermodynamic limit. First, the behavior of the spin correlations can be understood in the following way: on the site centered clusters, the system has an extensive total spin $S = 2^{g-1}$ in the ground state. By choosing a particular state out of this large multiplet it is possible to orient the Néel vector at no energy cost in this finite size system. In particular if one considers the $S^z = S$ state of the multiplet, the local $\langle S_i^z \rangle$ expectation values will reflect the ordering pattern directly. This situation is somewhat analogous to ferrimagnetic systems. In the case of the bond-centered clusters we have a

unique $S = 0$ ground state, which forbids finite $\langle S_i^z \rangle$ expectation values on a finite system, and the long-range order then has to be coded in the correlation functions leveling off to a finite value at long distances.

8.3 .2 Low energy Tower of States

For the balanced Heisenberg antiferromagnet ($n_A = n_B$ with a singlet ground state) on a regular unfrustrated lattice (e.g. square in 2D or cubic in 3D), with number of sites N_s, it has been noted and argued [19, 20] that the low energy Hamiltonian can be described by a rigid rotor model,

$$H_{rot} = \frac{\mathbf{S}^2}{2I} = \frac{S(S+1)}{2I} \tag{8.13}$$

where **S** it the total angular momentum (spin), and

$$I \cong \chi N_s \tag{8.14}$$

where χ is the susceptibility of **S** to a field coupling to it. Thus, we have a sequence of multiplets, popularly referred to as the "Anderson Tower of States", which become degenerate in the limit $N_s \to \infty$ thus making $SU(2)$ symmetry breaking possible in this limit.

To see if this behavior is found on the Cayley tree, we computed the ground state energy in every S_z sector. This may be identified with the multiplet energy $E(S)$, since $E(S)$ is monotonic in S and $S \geq S_z$.

For the bond centered clusters, a tower of states exists, but an anomalous one. In Fig. 8.5 we observe that in the bond-centered case, the $E(S)$ curve consists of *two* linear pieces, joined at a critical spin S^* which depends on the cluster

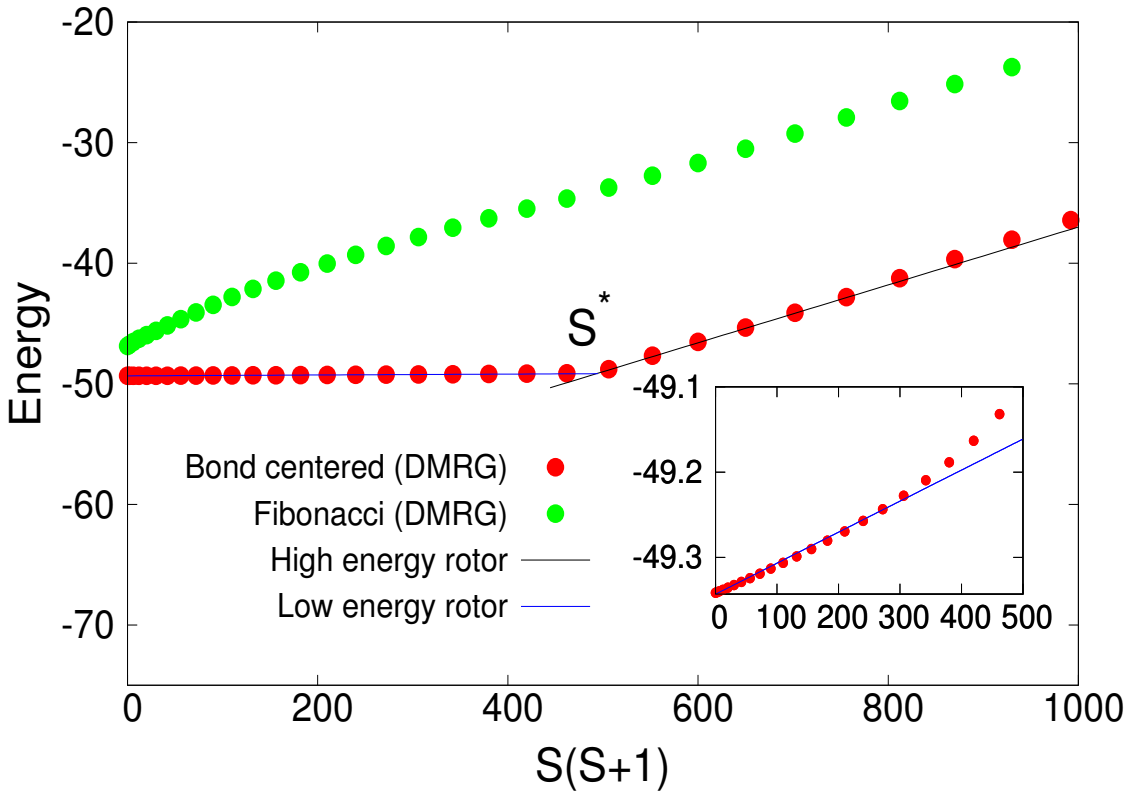

Figure 8.5: Lowest energy level in every S_z sector for the 108 Fibonacci and the 126 site bond-centered Cayley tree. The range of S from 0 to S^* has been magnified and shown in the inset for the 126 site cluster. It shows a tower of states with a much larger moment of inertia than expected from the Anderson tower. This is seen as a sharp kink like feature at S^*. In contrast, for the Fibonacci tree, the transition from the low to high S behavior is less well defined.

size. In effect, the system has two moments of inertia, $I_{\rm low}$ for $S < S^*$ and the (much smaller) $I_{\rm high}$ for $S > S^*$. Fig. 8.6 plots the size dependence of these moments of inertia, showing that $I_{\rm low} \sim N_s^2$ while $I_{\rm high} \sim N_s$; it will be our task in Sec. 8.4 .3, to explain this difference. We also observe that

$$S^* = 2I_b \tag{8.15}$$

where I_b is the sublattice imbalance on one half of the bond-centered cluster as defined in equation (8.3).

For the Fibonacci tree, we do not find a clear distinction between the two

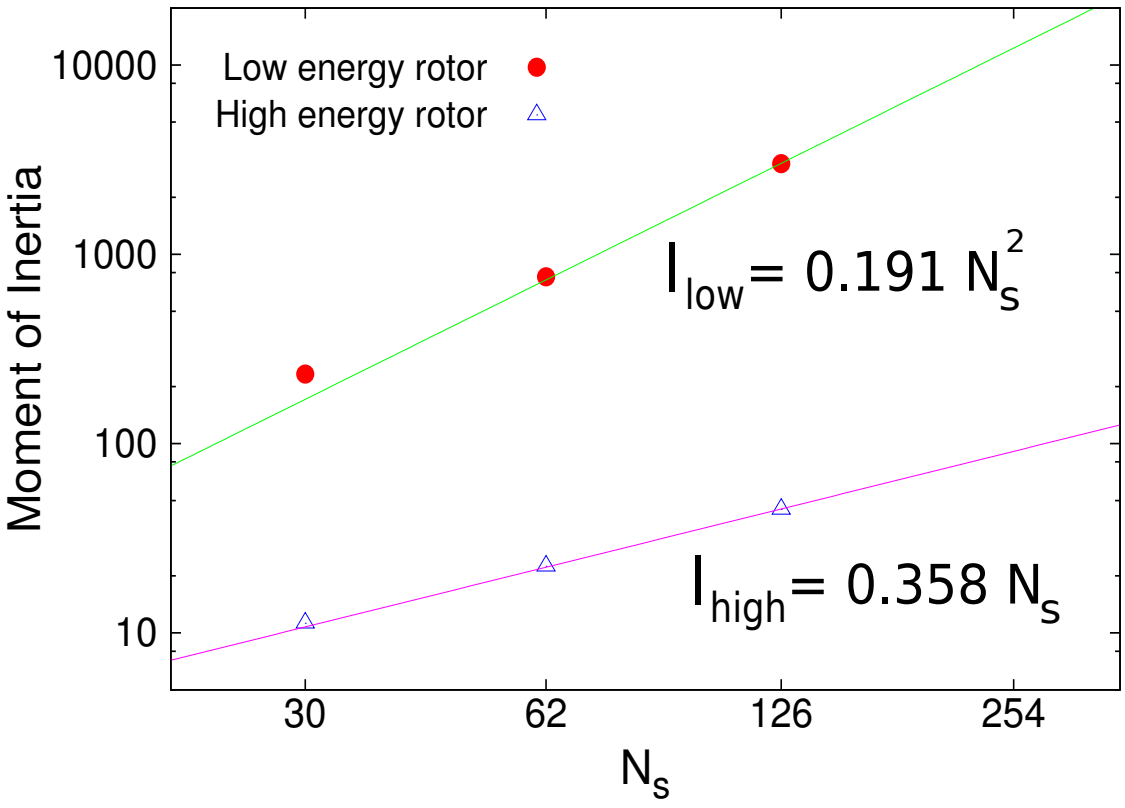

Figure 8.6: Moment of inertia of the low ($I_{\rm low}$) and high energy ($I_{\rm high}$) rotors as a function of lattice size (N_s) for the bond centered tree of various sizes as shown on a log-log plot.

linear pieces as seen in Fig. 8.5. The scaling of the energy gaps ($E(S+1)-E(S)$) changes from $N_s^{-0.6}$ for small S, to the $1/N_s$ Anderson scaling for large S.

In contrast with the gapless spectrum of the bond-centered and Fibonacci clusters, the site-centered case has a finite spin gap (see Table 8.2) in the infinite lattice limit.

A complementary probe of the low energy physics is the magnetization (m) (see Fig. 8.7) defined as,

$$m = \frac{1}{N_s}\sum_i \langle S_i^z \rangle_{GS} \tag{8.16}$$

as a function of a uniform applied magnetic field h. For the bond-centered clusters, we observe a rapid increase in magnetization for small h and it seems the

saturation magnetization is about $m^* \sim 1/6$ (i.e. $m^*/m_{\rm sat} \sim 1/3$). Beyond this rapid rise of the magnetization at small field, the magnetization curve displays a surprisingly rich structure, with several plateau-like features at intermediate magnetization, linked by more susceptible parts of the magnetization curve. We note that the first plateau at m^* seems to have a similar extent in magnetic field as for the site-centered clusters studied in Ref. [24]. The detailed characterization of the magnetization curve as $N_s \to \infty$ appears to be an interesting problem for future studies.

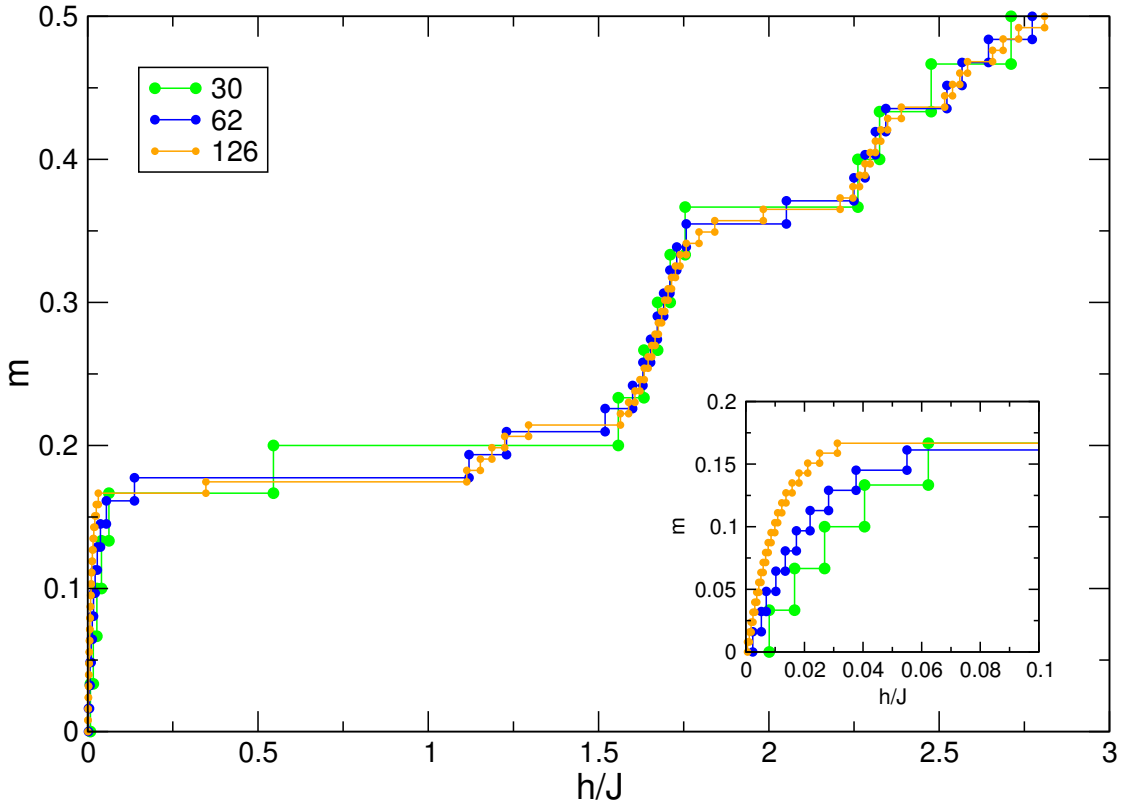

Figure 8.7: Magnetization curves for bond-centered Cayley trees of various sizes obtained using DMRG. Inset: The rapid rise of the magnetization with application of a small magnetic field indicates a susceptibility diverging with system size.

In Fig. 8.8, we also show the magnetization curves for sites on various shells of the 62-site bond-centered Cayley tree. For small S_z (or equivalently small

magnetic fields), we infer that while the boundary spins are most susceptible, the spins in the interior also have a comparably high susceptibility, which decreases as we go inwards.

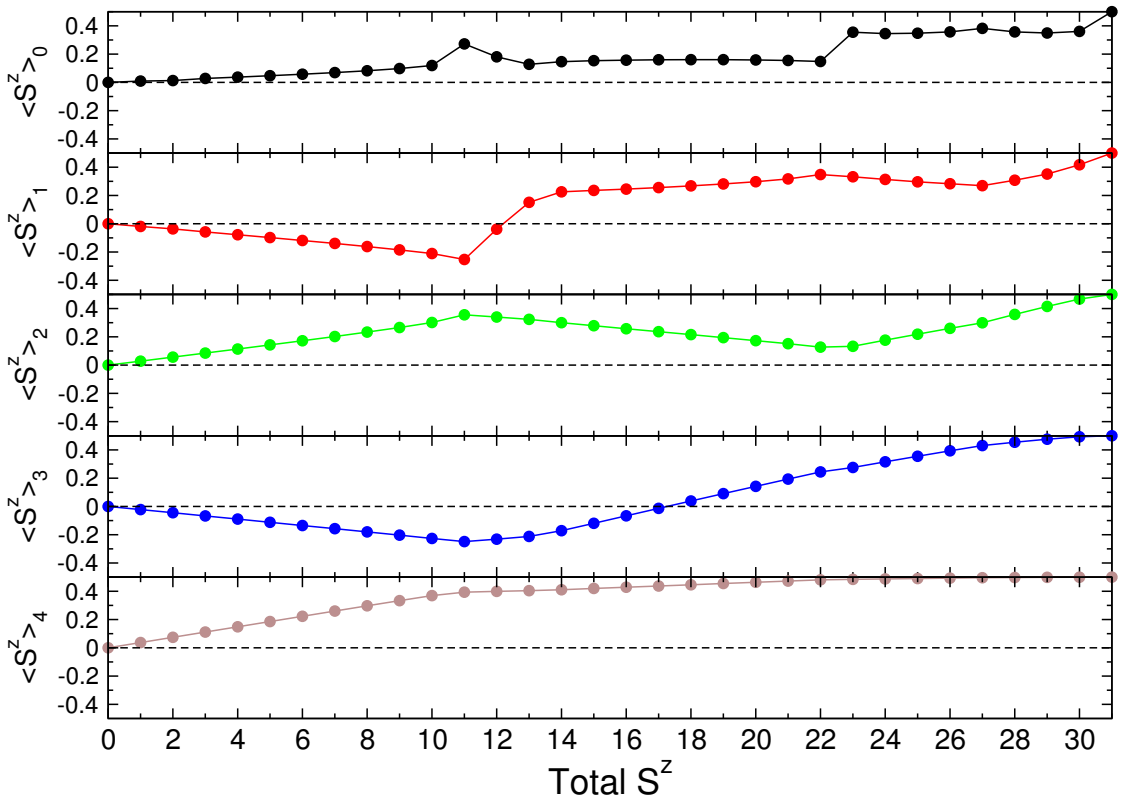

Figure 8.8: Magnetization curves for sites on various shells of the 62 site bond-centered Cayley tree. The subscript refers to the shell on which the site is present, that is, 0 refers to the central two sites and the 4 refers to the boundary.

8.4 Single Mode Approximation for the excited state

How do we understand the origin of the "anomalous" states in the low energy spectrum for the bond-centered tree? In order to address this question, we study the nature of the triplet excited state and its relation to the ground state using the single mode approximation [35](SMA for short). Assuming the

knowledge of the ground state wavefunction $|0\rangle$ (analytically or from a numerical method), the SMA ansatz for the trial state $|1'\rangle \equiv |S=1, S_z=1\rangle$ state is given by,

$$|1'\rangle = \frac{1}{\mathcal{N}_{1'}} \sum_{j=1}^{N_s} u_j S_j^+ |0\rangle \tag{8.17}$$

where u_j are variational parameters and $\mathcal{N}_{1'}$ is a normalization factor given by,

$$\mathcal{N}_{1'} \equiv \sqrt{\sum_{k,l} u_k^* u_l \left\langle 0 \left| S_k^- S_l^+ \right| 0 \right\rangle} \tag{8.18}$$

Using the spin symmetry of the Hamiltonian (and hence its eigenfunctions) and the fact that the ground state has $S_z = 0$, the normalization factor $\mathcal{N}_{1'}$ (8.18) can be written as,

$$\mathcal{N}_{1'} = \sqrt{\sum_{k,l} \frac{2}{3} u_k u_l G_{kl}} \tag{8.19}$$

where G_{kl} is the spin-spin correlation function previously defined in Eq.(8.12).

For a singlet ground state, observe that, there is a gauge degree of freedom in the choice of the SMA wavefunction (8.17), an arbitrary constant shift u, i.e.,

$$\sum_i u_i S_i^+ |0\rangle = \sum_i (u_i + u) S_i^+ |0\rangle \tag{8.20}$$

since for a ground state with total spin $S = 0$,

$$u \sum_i S_i^+ |0\rangle = u S_{tot}^+ |0\rangle = 0 \tag{8.21}$$

It can also be shown [3] that the normalization $\mathcal{N}_{1'}$ in Eq.(8.19) is invariant under the transformation $u_i \to u_i + u$.

[3] The expression $\sum_{k,l} u_k u_l G_{kl}$ is invariant under the transformation $u_i \to u_i + u$ though it is not manifestly evident at first glance. One can prove this, by using two results specific to a singlet state. First, $\sum_{ij} G_{ij} = S(S+1)$ which equals zero for a singlet state. Second, $\sum_{ij} u_j G_{ij} = \sum_j \left\langle S_z^{tot} s_j^z \right\rangle$ which equals zero for a state with $S_z^{tot} = 0$.

For a given trial state ψ_T which is a function of some parameters u_j, the variational principle guarantees that,

$$E_T \equiv \frac{\langle \psi_T(\{u_j\}) | H | \psi_T(\{u_j\}) \rangle}{\langle \psi_T(\{u_j\}) | \psi_T(\{u_j\}) \rangle} \tag{8.22}$$

where E_0 refers to the energy of the lowest lying state with the same symmetry as the trial wavefunction. The best wavefunction is obtained by optimization of the parameters u_j by minimizing the variational energy E_T. Note that within the SMA formalism, the ground state (and hence the ground state energy) is assumed, which implies that the SMA spin gap is also a variational estimate for the true spin gap.

Here we will show that the SMA does turn out to be a very good ansatz for the bond-centered tree based on the close to 100 % overlap of the SMA wavefunction with the wavefunction from DMRG. Our procedure does not require explicit knowledge of the wavefunction, rather only certain matrix elements and correlation functions are necessary. We will derive our intuition from numerical calculations and construct coefficients u_j (occurring in Eq.(8.17)) to obtain a variational state with a gap that goes to 0 faster than $1/N_s$. The aim of this section is thus to understand the operator that creates the triplet wavefunction from the ground state singlet. This in turn will tell us how the spins collectively act, which will be used to understand the existence of an "anomalous" energy scale.

A similar SMA calculation was performed by Laumann et al. [36], who considered AKLT models on the Cayley tree, where the analytical form of the correlation functions is known. Instead, we use the values of $\langle 1 | S_i^+ | 0 \rangle$ and G_{ij} from our DMRG calculations as inputs for our analysis. In addition, we make no assumptions about the variational parameters $\{u_j\}$.

8.4 .1 Obtaining the SMA coefficients from maximization of overlap with the true wavefunction

The overlap of an approximate wavefunction with the exact one can serve as a good measure of its quality. Thus we consider the overlap of the SMA wavefunction with the true triplet state $|1\rangle \equiv |S = 1, S_z = 1\rangle$ i.e.,

$$\begin{aligned} O &\equiv \langle 1 \, | 1' \rangle \\ &= \frac{\sum_j u_j f_j}{\sqrt{\sum_{k,l} \frac{2}{3} u_k u_l G_{kl}}} \end{aligned} \tag{8.23}$$

and try to maximize it. We have defined f_i to be,

$$f_i \equiv \left\langle 1 \left| S_j^+ \right| 0 \right\rangle \tag{8.24}$$

We christen f_i as the "flippability" of a spin. This is motivated from its very definition: the more easily flipped spins have a larger contribution to the formation of the first excited triplet.

We now present a method to obtain the optimal parameters u_j to construct $|1'\rangle$. To meet the requirements of a high overlap of the SMA wavefunction $|1'\rangle$ with the exact many body triplet $|1\rangle$, subject to the constraint that it is normalized, we devise a cost function C_{SMA} defined as,

$$C_{SMA} = -\sum_j u_j f_j + \lambda \left(\mathcal{N}_{1'}^2 - 1 \right) \tag{8.25}$$

where we have introduced λ as a Lagrange multiplier. Taking $\{u_j\}$ as our variational parameters, and setting the derivatives of C_{SMA} to 0, we get,

$$\frac{\partial C_{SMA}}{\partial u_i} = -f_i + \frac{4}{3}\lambda \sum_{l \neq i} u_l G_{il} + \lambda u_i = 0 \tag{8.26}$$

Thus we get the set of equations (one equation for each i) ,

$$f_i = \frac{4}{3}\lambda \sum_j G_{ij} u_j \tag{8.27}$$

To explicitly obtain a state $|1'\rangle$ which has a high overlap with $|1\rangle$, we solve the above linear equations for u_i numerically. Note that the matrix G always has exactly one zero eigenvalue because of the gauge degree of freedom (8.20). Hence we cannot simply invert G to obtain u_i: instead, we directly solve the linear system of equations (8.27) using dgesv in LAPACK.

A natural choice of gauge for the parameters $\{u_j\}$ is to satisfy,

$$\sum_i u_i = 0 \tag{8.28}$$

Our observation from the numerical solution of equation (8.27) for the bond-centered Cayley tree is that $u_i > 0$ for i on one side of the central bond and $u_i < 0$ on the other side. We have also plotted the amplitudes of the optimal SMA coefficients for the 30, 62 and 126 site balanced Cayley trees in Fig. 8.9.

8.4 .2 Comparison of various SMA wavefunctions

We now try to understand the qualitative nature of the SMA solution from the perspective of minimizing the triplet energy. We consider various functional forms for u_i and numerically compute their overlap with the exact triplet and compare SMA gap estimates.

For the nearest neighbor Heisenberg model, the SMA gap is given by (for a derivation refer to Appendix 8.A),

$$\Delta_{SMA} = \frac{-\sum_{\langle k,l\rangle} (u_k - u_l)^2 G_{kl}}{2\sum_{ij} u_i u_j G_{ij}} \tag{8.29}$$

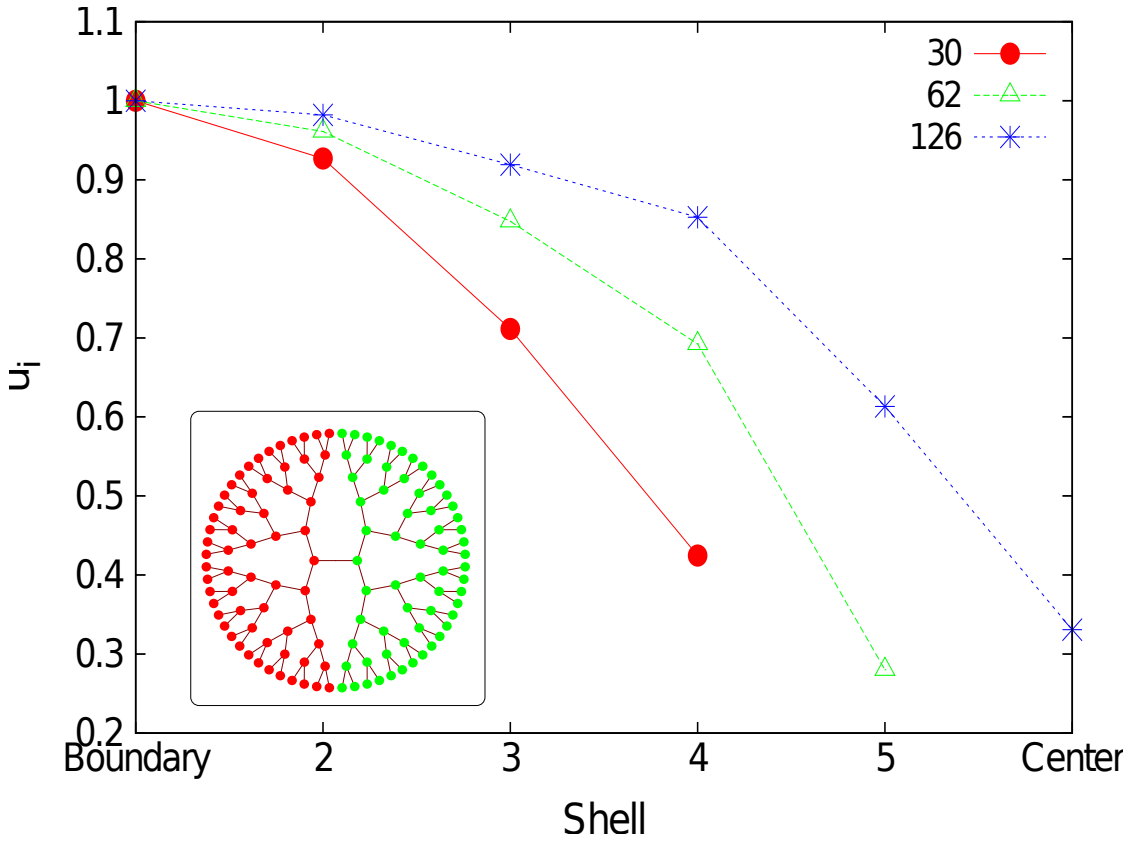

Figure 8.9: (Color online) Amplitude of the SMA coefficients u_i for various shells (normalized with respect to amplitude on the boundary) for the $N_s = 30$,62 and 126 site bond-centered lattices. Inset: The sign structure of u_i is the same as equation (8.30). Dark (red) and light (green) indicates negative and positive u_i respectively.

Observe that the numerator (containing terms depending on $u_k - u_l$) and the denominator (being proportional to $\mathcal{N}_{1'}^2$), and thus Δ_{SMA} are invariant under the transformation $u_i \to u_i + u$.

To minimize the SMA gap, one would like to minimize the numerator and maximize the denominator of equation (8.29) (note both the numerator and denominator are positive). To minimize the numerator, we can try to keep $u_k \approx u_l$

for as many bonds as possible, and hence consider the "left-right" ansatz,

$$u_i = \begin{cases} +1 & i \in \text{left of central bond} \\ -1 & i \in \text{right of central bond} \end{cases}$$

which is consistent with the gauge condition (8.28). This sign structure is in concordance with the numerical solution of equations (8.27) for the bond centered Cayley tree.

Note that this is quite contrary to the "staggered pattern", one obtains by solving equations (8.27) for the square lattice. The staggered pattern is defined as,

$$u_i = \begin{cases} +1 & i \in \text{even sublattice} \\ -1 & i \in \text{odd sublattice} \end{cases}$$

The staggered pattern is an energetically expensive solution for the bond-centered Cayley tree. Even though it maximizes the denominator making it $O(N_s^2)$, the numerator is also large i.e. $O(N_s)$. Thus the SMA gap scales only as $O(1/N_s)$

Table 8.3 verifies the arguments presented above by explicitly listing out the SMA gap and overlap with the exact wavefunction for the various choices of u_i we have considered here. Our inference is that the optimal and the “left-right” ansatz are qualitatively similar and yield a much smaller SMA gap than the "staggered" ansatz.

The SMA calculations suggest that all the spins are involved in the construction of the first excited state from the ground state. The u_i corresponding to the central spins is roughly a third as large in the "optimal solution" and exactly as large as the u_i of the boundary spins in the "left-right" ansatz. The point to note here is that in either case the contribution of the spins in the interior is not small.

This suggests that the antiferromagnetic bonds between successive shells do a reasonable job of locking spins together (within each half of the bond centered tree), resulting in an emergent degree of freedom which is what we call a "giant spin". This interpretation will be established next in section 8.4 .3.

Table 8.3: SMA gap and wavefunction overlap with excited state from DMRG for various functional forms of u_i

lattice Size	Ansatz	SMA Gap	Overlap
30	Optimal	0.0135	0.998
	Left-Right	0.0341	0.993
	Staggered	0.2680	0.912
62	Optimal	0.0039	0.999
	Left-Right	0.0116	0.997
	Staggered	0.1612	0.946
126	Optimal	0.0010	≈ 1
	Left-Right	0.0028	≈ 1
	Staggered	0.0905	0.975

8.4 .3 The "Giant Spins" Picture

As we inferred previously, there are indications that strong antiferromagnetic correlations force all spins in one half of the bond-centered cluster to act collectively as a single magnetic moment. We make this understanding more concrete in the present section.

We divide the bond-centered Cayley tree into two equal halves at the central

bond. Using the ground state, we compute the reduced density matrix ρ_{RDM} (see Eq. (7.9)) of one of the halves and diagonalize it. The corresponding eigenvalues are arranged by total S_z and the resultant plot (see Figure 8.10) is the "entanglement spectrum". The calculation of the entanglement spectrum needs no extra effort in the DMRG procedure we outlined in Chapter 7. Appropriate cuts are also chosen for the site-centered and Fibonacci trees as shown in Figure 8.11 and Figure 8.12 respectively.

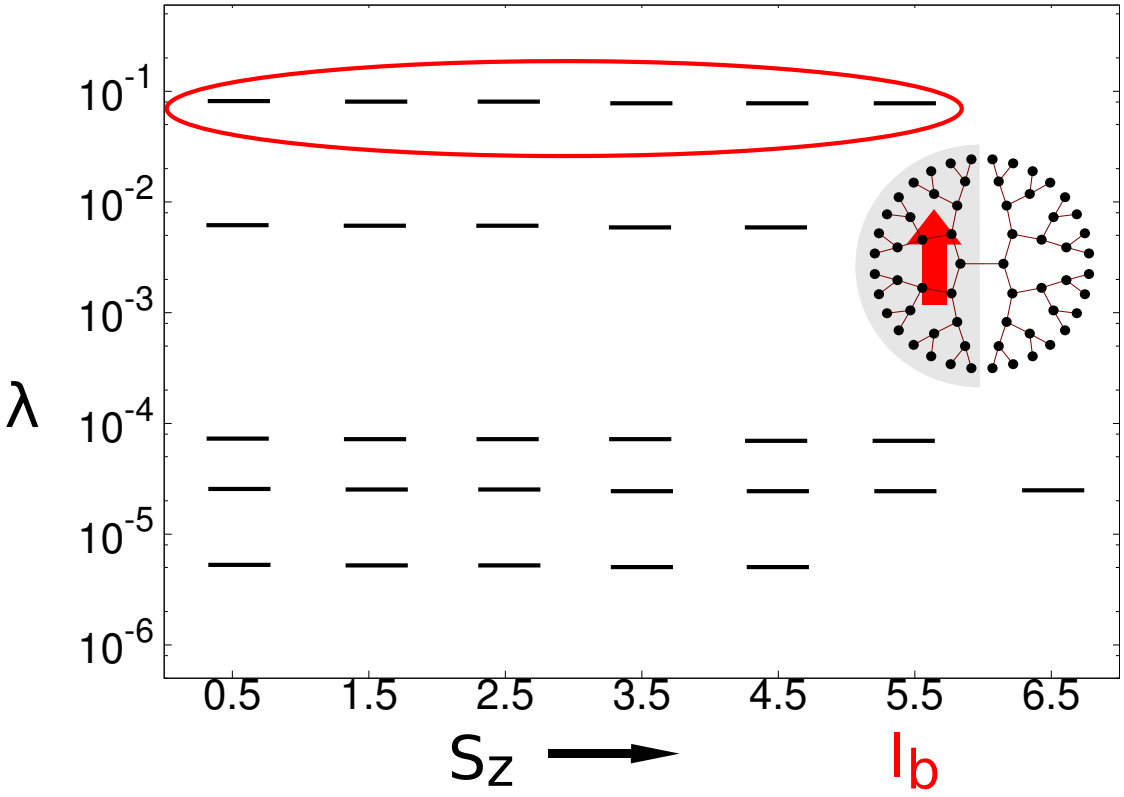

Figure 8.10: (Color online) The entanglement spectrum for the bond-centered tree as shown in the inset. λ refers to the eigenvalue of the reduced density matrix of the shaded area. The ground state for the bond-centered tree is a singlet and only the $S_z > 0$ sectors are shown. I_b denotes the "imbalance" metric defined in the introduction (refer to Eq.(8.3)). The largest degenerate eigenvalues of the reduced density matrix indicate a multiplet whose spin length exactly equals the imbalance I_b.

The entanglement spectrum shows a copy of the largest eigenvalue in every

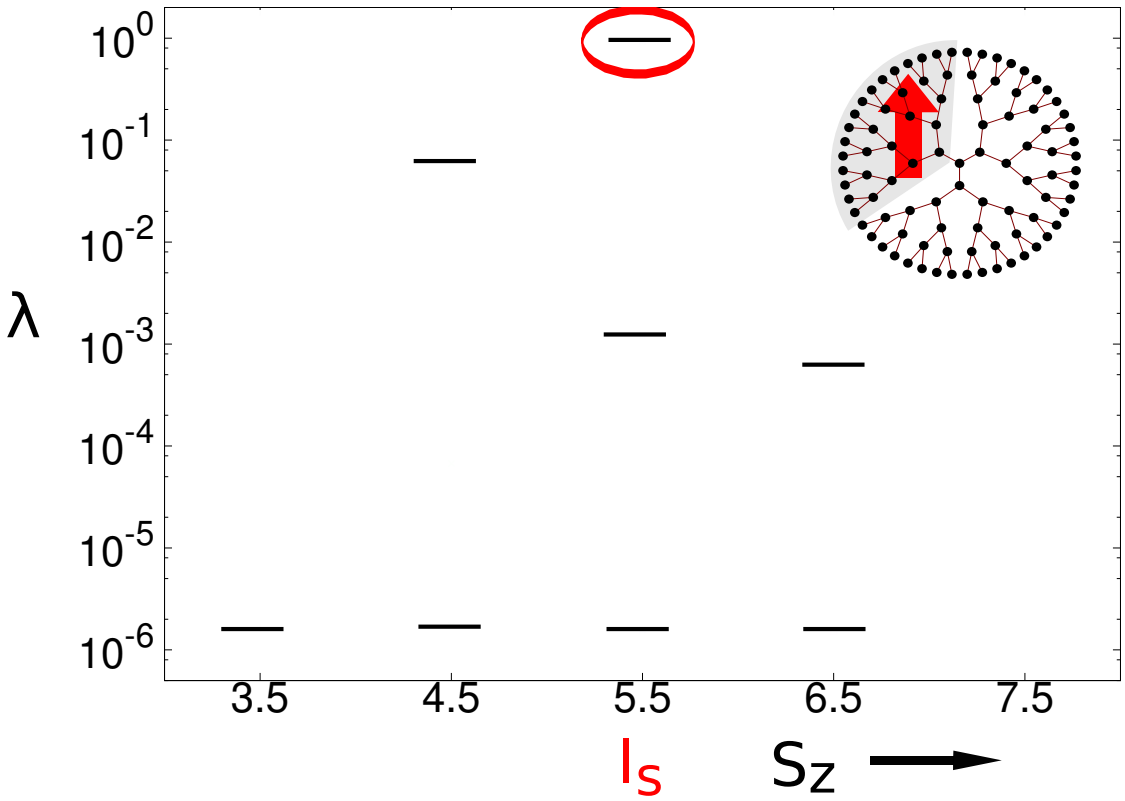

Figure 8.11: (Color online) The entanglement spectrum for the site-centered tree as shown in the inset. λ refers to the eigenvalue of the reduced density matrix of the shaded area. For the site-centered cluster we chose to work with the maximal S_z sector (which is the S_z=16 for the 94 site cluster). I_s denotes the "imbalance" metric defined in the introduction (refer to Eq.(8.3)). The density matrix has largest weight in a state whose spin is I_s.

S_z sector ranging from $-I_b$ to $+I_b$, where I_b is the net sublattice imbalance and is given by $(2^g \pm 1)/6$ as mentioned in equation (8.3). This indicates the presence of a "giant spin" of spin length I_b whose multiplet is given by the eigenvectors corresponding to these large eigenvalues. Given this picture, we explain the existence of the "anomalous" scale of energies.

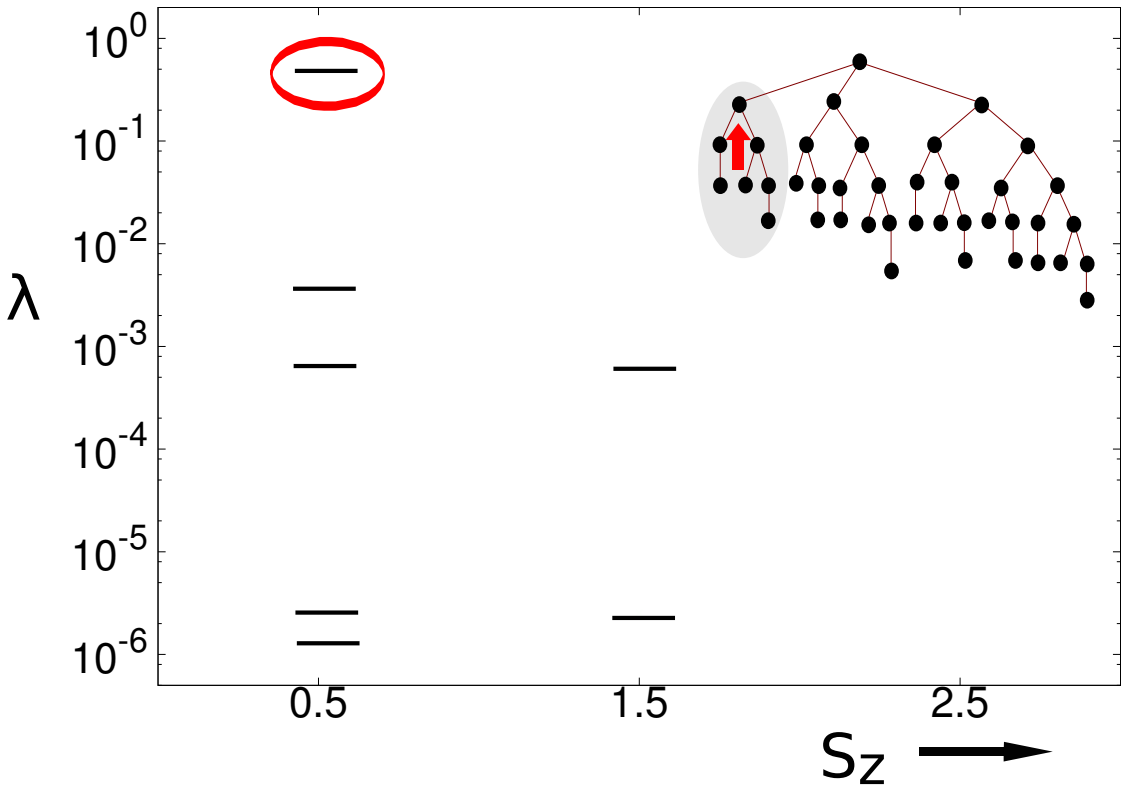

Figure 8.12: (Color online) The entanglement spectrum for the Fibonacci tree as shown in the inset. λ refers to the eigenvalue of the reduced density matrix of the shaded area. The ground state for the Fibonacci clusters is a singlet and only the $S_z > 0$ sectors are shown. For the Fibonacci case, a spin 1/2 state has the largest weight in the density matrix.

Bond-centered tree

The Heisenberg Hamiltonian on the bond centered Cayley tree may be rewritten as,

$$H = H_{\text{left}} + H_{\text{right}} + J\mathbf{S}_0 \cdot \mathbf{S}_1 \tag{8.30}$$

where 0 and 1 refer to the central two sites of the bond-centered tree (as has been schematically represented in Fig. 8.13).

We treat the term corresponding to the central bond $J\mathbf{S}_0 \cdot \mathbf{S}_1$ as a perturbation within degenerate first order perturbation theory. The many body ground state

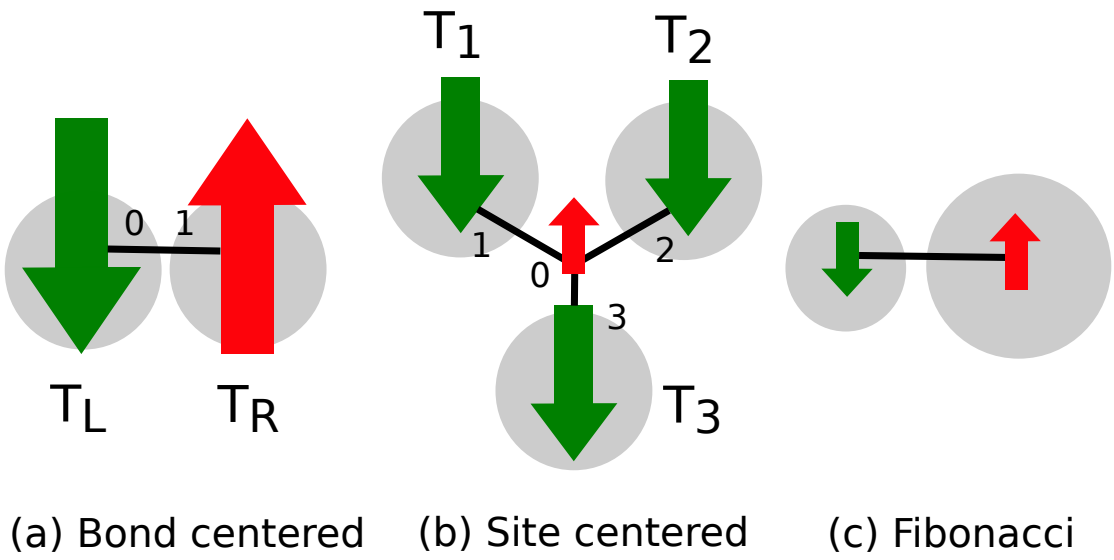

Figure 8.13: (Color online) Schematic of the "giant spins", which are the low-energy degrees of freedom for the bond and site centered clusters (and absent for the Fibonacci tree). The numbering of sites shown here is used for the purpose of explaining our arguments in the text.

on each half is a degenerate multiplet of spin I_b. Since all spins on the left and right contribute in a definite proportion to the "giant spin" operators $\mathbf{T}_L$ and $\mathbf{T}_R$, one can re-express the expectation values of the $J\mathbf{S}_0 \cdot \mathbf{S}_1$ in terms of $\mathbf{T}_L$ and $\mathbf{T}_R$. Note that expectation values of the term $J\mathbf{S}_0 \cdot \mathbf{S}_1$ are computed in the product basis of the two systems given by $|T_L, T_L^z\rangle \otimes |T_R, T_R^z\rangle$.

If all the spins in one half of the cluster had equal participation in their collective multiplet, then,

$$\left\langle T_L, T_L^z \left| \mathbf{S}_o \right| T_L T_L^{\prime z} \right\rangle = - \left\langle T_L, T_L^z \left| \mathbf{S}_e \right| T_L T_L^{\prime z} \right\rangle \tag{8.31}$$

where e (o) refers to *any* even(odd) sublattice site in the same half of the bond centered cluster. Therefore, if one were to create the equally weighted spin operator $\mathbf{T_L} = \sum_{i \in \text{left}} \mathbf{S}_i$ and consider its matrix elements one would get,

$$\langle \mathbf{T_L} \rangle = \pm 2 I_b \langle \mathbf{S}_0 \rangle \tag{8.32}$$

where 0 refers to the central site in one half of the bond centered cluster. The sign depends on whether the central site and the boundary sites are on the same (+) or opposite (−) sublattices.

What happens when the spins are not equally participating in the multiplet? The simplifying assumption we make here is that within the projected low energy subspace, each individual spin half operator at lattice site i, $\mathbf{S}_i$, is proportional to the operator $\mathbf{T}_L/I_b$. Using the fact that $I_b \sim N_s$, this relation can be expressed as,

$$\mathbf{S}_0 = \frac{\gamma_b}{N_s}\mathbf{T}_L \tag{8.33}$$

where the constant γ_b has been used to denote the proportionality factor. A similar relation exists for $\mathbf{S}_1$ and $\mathbf{T}_R$. From equation (8.33) it follows that,

$$J\left\langle \mathbf{S}_0 \cdot \mathbf{S}_1 \right\rangle = \frac{J\gamma_b^2}{N_s^2}\left\langle \mathbf{T}_L \cdot \mathbf{T}_R \right\rangle \tag{8.34}$$

The Hamiltonian $\mathbf{T}_L \cdot \mathbf{T}_R$ is diagonalized by coupling the left and right "giant spins" into a spin for the whole system i.e. $\mathbf{T} = \mathbf{T}_L + \mathbf{T}_R$, whose eigenstates are given by $|T, T^z\rangle$.

$$\left\langle \mathbf{T}_L \cdot \mathbf{T}_R \right\rangle_{|T,T^z\rangle} = \frac{1}{2}\left\langle \mathbf{T}^2 - \mathbf{T}_L^2 - \mathbf{T}_R^2 \right\rangle \tag{8.35a}$$

$$= \frac{1}{2}T(T+1) - I_b(I_b+1) \tag{8.35b}$$

where T varies from $0, 1....., 2I_b$. Note that T_L and T_R are constant and equal to I_b. The term $I_b(I_b+1)$ is a harmless constant energy shift to all states. Thus, the energy spectrum (up to a overall shift) as a function of T is simply,

$$E(T) = \frac{J\gamma_b^2}{2N_s^2}\,T(T+1) \tag{8.36}$$

This is exactly the Hamiltonian of a quantum rotor with a "anomalous" moment of inertia scaling as N_s^2. This simple picture, hence, rather remarkably explains

our numerical observations in section 8.3 of this Chapter. We find γ_b to be ~ 3.24 from fits to our numerical data based on Fig. 8.6.

Note that though the giant spins are interacting via a weak bond, the fact that they are paired up in a singlet ground state makes the state highly entangled. In comparison, as we shall soon see, the ground state of the site-centered tree (in the $S_z = S_0$ sector) is closer to a product state of the giant spins and hence has a lower degree of entanglement. (This also explains why the convergence of DMRG calculations is more rapid with the number of states M for the site-centered case as compared to the bond-centered case.)

Site-centered tree

Let us now perform essentially the same analysis for the site centered Cayley tree to further shed light on (and validate) the "giant spins" picture. Rewriting the Heisenberg Hamiltonian as,

$$H = H_1 + H_2 + H_3 + J\mathbf{S}_0 \cdot (\mathbf{S}_1 + \mathbf{S}_2 + \mathbf{S}_3) \tag{8.37}$$

where 0 refers to the central site and 1,2,3 refer to the sites connected to it (as has been schematically represented in Fig. 8.13).

As before, make the substitution of $\mathbf{S}_1$,$\mathbf{S}_2$,$\mathbf{S}_3$ in terms of the giant spins $\mathbf{T}_1$,$\mathbf{T}_2$,$\mathbf{T}_3$ each of which has spin length I_s. Then couple the three giant spins into a bigger giant spin $\mathbf{T}$. The Hamiltonian now reads as,

$$H = H_1 + H_2 + H_3 + \frac{J\gamma_s}{N_s}\mathbf{S}_0 \cdot \mathbf{T} \tag{8.38}$$

where γ_s is a constant and $\mathbf{T} = \mathbf{T}_1 + \mathbf{T}_2 + \mathbf{T}_3$. Note that the angular momentum coupling rules predict that the value of T are in the range from 0,1... to $3I_s$.

Let us now couple the giant spin $\mathbf{T}$ to the spin $1/2$ degree of freedom at the center of the cluster. The energy (in units of $J\gamma_s/N_s$ and up to a constant of $-\frac{3}{4}$) for the $S = 3I_s + \frac{1}{2}$ and $3I_s - \frac{1}{2}$ states is given by,

$$E_{3I_s}^{3I_s+\frac{1}{2}} = \left(3I_s + \frac{1}{2}\right)\left(3I_s + \frac{3}{2}\right) - 3I_s\left(3I_s + 1\right) \tag{8.39a}$$

$$E_{3I_s}^{3I_s-\frac{1}{2}} = \left(3I_s - \frac{1}{2}\right)\left(3I_s + \frac{1}{2}\right) - 3I_s\left(3I_s + 1\right) \tag{8.39b}$$

where the superscript indicates the global value of the spin S and the subscript is used to indicate the T value it was made of. Similarly we have,

$$E_{3I_s-1}^{3I_s-\frac{1}{2}} = \left(3I_s - \frac{1}{2}\right)\left(3I_s + \frac{1}{2}\right) - 3I_s\left(3I_s - 1\right) \tag{8.40a}$$

$$E_{3I_s-1}^{3I_s-\frac{3}{2}} = \left(3I_s - \frac{3}{2}\right)\left(3I_s - \frac{1}{2}\right) - 3I_s\left(3I_s - 1\right) \tag{8.40b}$$

Simplifying equations and incorporating the constant of $-\frac{3}{4}$ we get,

$$E_{3I_s}^{3I_s+\frac{1}{2}} = 3I_s \tag{8.41a}$$

$$E_{3I_s}^{3I_s-\frac{1}{2}} = -3I_s - 1 \tag{8.41b}$$

$$E_{3I_s-1}^{3I_s-\frac{1}{2}} = 3I_s - 1 \tag{8.41c}$$

$$E_{3I_s-1}^{3I_s-\frac{3}{2}} = -3I_s \tag{8.41d}$$

Observe that $E_{3I_s}^{3I_s-\frac{1}{2}}$ is the lowest energy. This is in concordance with the Lieb-Mattis theorem [34] i.e. the ground state has total spin $S_0 = 3I_s - \frac{1}{2}$. The energy gap (now in absolute units) of the S_0 to $S_0 + 1$ transition is given by,

$$\Delta\left(S_0 \to S_0 + 1\right) = \frac{J\gamma_s}{N_s}\left(6I_s + 1\right) \tag{8.42}$$

Since I_s is approximately $N_s/18$ for large N_s we get a gap of,

$$\Delta\left(S_0 \to S_0 + 1\right) \approx \frac{J\gamma_s}{3} \tag{8.43}$$

This is consistent with our numerical observation that the gap is finite in the large N_s limit. Since the measured gap is $\sim 0.73J$ we infer that γ must be ~ 2.19.

We give further credibility to our giant spin interpretation by testing the prediction of the gap for the S_0 to $S_0 - 1$ transition. This transition turns out to be gapless in the large N_s limit,

$$\Delta\left(S_0 \rightarrow S_0 - 1\right) \approx \frac{J\gamma_s}{N_s} \tag{8.44}$$

which is consistent with our DMRG calculations as shown in Figure 8.14. The measured γ_s from the fit of the DMRG data to $\Delta = J\gamma_s/N_s$ is found to be ~ 2.19 consistent with the estimate from equation (8.43), serving as another check of the theory.

Fibonacci Cayley tree

The entanglement spectrum of the Fibonacci Cayley tree (see Fig. 8.12) indicates the creation of a spin 1/2 degree of freedom as opposed to the "giant spins" encountered previously. The cut shown in Fig. 8.12 shows a region having an imbalance of one, which is the maximum possible for any cut.

We believe the lowest energy excitation of this system involves a breaking of a dimer and creation of two unpaired spins. Since the bonds in the interior have a decreasing dimerization strength, the energy required to create this excitation is expected to be vanishingly small in the infinite lattice limit. This is seen in the spin gap in Table 8.2, but an explanation of the observed numerical exponent is a subject of further investigation and beyond the scope of this Chapter.

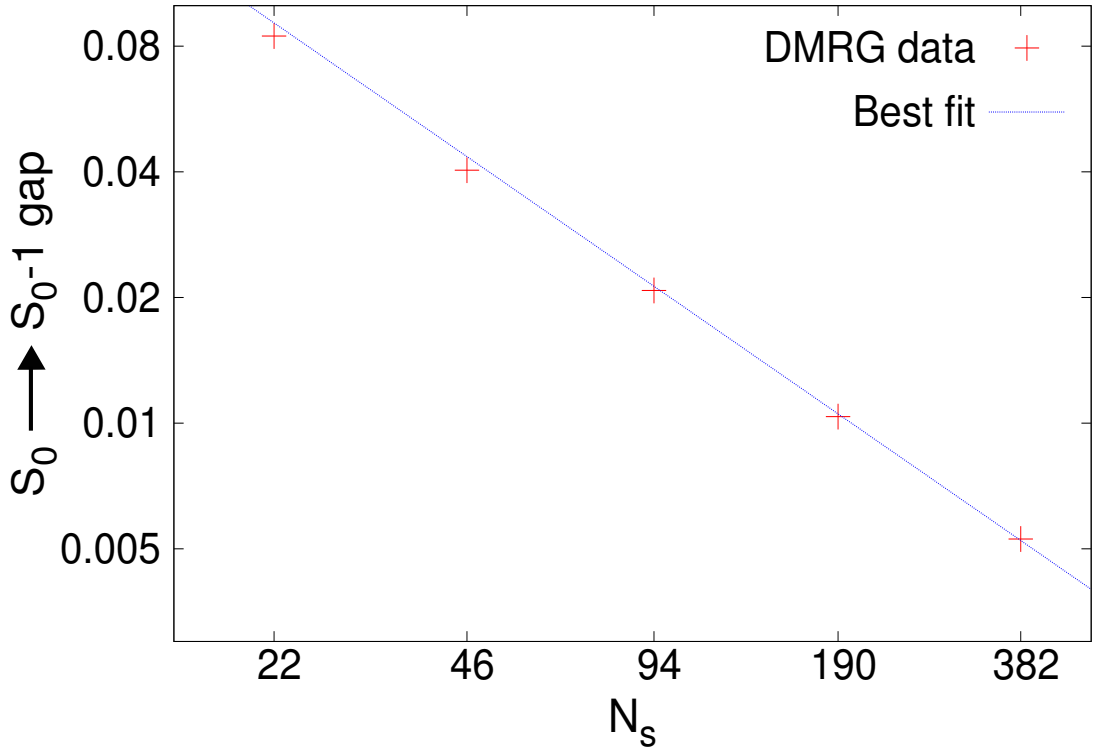

Figure 8.14: (Color online) For the site centered clusters, the scaling of the S_0 to $S_0 - 1$ energy gap serves as one of the test beds for the "giant spins" picture presented in the text. Here we see a reasonable agreement of the DMRG data with the predicted scaling of $1/N_s$

8.5 Schwinger Boson Mean Field Theory For Singlet Ground states

Can we understand the presence or absence of long range order on these trees at the mean field level? For this we appeal to the Schwinger Boson Mean Field Theory [8] which is capable of describing quantum disordered and ordered states within the same framework [7, 37]. In this section[4] we will see that this theory is a good description of the singlet ground states of the bond centered and Fibonacci trees. This section also serves to expand the domain

[4]The lead work on this section was carried out by Shivam Ghosh.

of application of the Schwinger Boson formalism to situations where multiple parameters need to be optimized simultaneously [38] (such as non uniform systems or systems with very few symmetries).

8.5 .1 Notation and formal set-up

The $SU(N)$ Heisenberg Hamiltonian is expressed in terms of Schwinger Bosons by defining a bond operator,

$$\mathcal{A}_{ij} = \sum_{m=1}^{N} b_{im} b_{jm} \tag{8.45}$$

where each Schwinger boson operator b_{im} carries two labels, i or j for site indices and m for flavor index. The physical Heisenberg model Eq.(8.1) corresponds to $N = 2$. The procedure is to decouple the quartic bosonic Hamiltonian into a one-body mean field Hamiltonian by doing an expansion in $1/N$. Solving the mean field Hamiltonian and putting in $N = 2$ allows us to compare the SBMFT results with DMRG calculations.

The $SU(N)$ Hamiltonian in terms of Schwinger bosons is,

$$\mathcal{H}_{\text{Heisenberg}} = -\frac{J}{N} \sum_{\langle ij \rangle} \left(\mathcal{A}_{ij}^{\dagger} \mathcal{A}_{ij} - 2S^2 \right) \tag{8.46}$$

The mapping of the spin Hamiltonian to Schwinger bosons is exact if we meet the condition site by site,

$$\sum_{m=1}^{N} b_{im}^{\dagger} b_{im} = NS \tag{8.47}$$

which ensures that the Hilbert space of the bosons is restricted by the spin size S (and the corresponding $|S, S_z\rangle$ states). However, we will impose this constraint only on the expectation $b_{im}^{\dagger} b_{im} \rightarrow \langle b_{im}^{\dagger} b_{im} \rangle_{MF}$. As a result of not satisfying

Eq.(8.47) exactly, the mean field energy E_{MF} and correlations differ from exact results (DMRG calculations) by overall scale factors [8, 39].

The decoupled mean field Hamiltonian $\mathcal{H}_{MF}$ is expressed in terms of the following variational parameters: a set of bond variables Q_{ij} for every bond i, j, Lagrange multipliers λ_i which impose Eq.(8.47) and a condensate field $\beta_i = \delta_{1,m}\langle b_{im}\rangle/\sqrt{N}$ which develops a non-zero value in a phase with LRO [37]. $\mathcal{H}_{MF}$ is then given by [9],

$$\begin{aligned}\mathcal{H}_{MF} &= \sum_{i=1}^{N_s}\lambda_i\left(\sum_{m=1}^{N} b_{im}^\dagger b_{im} - NS\right) + \frac{N}{J}\sum_{\langle ij\rangle}|Q_{ij}|^2 \\ &+ \sum_{i<j}\left(Q_{ij}\mathcal{A}_{ij}^\dagger + Q_{ij}^*\mathcal{A}_{ij}\right) \\ &+ \frac{1}{\sqrt{N}}\sum_{i=1}^{N_s}\left(\phi_i^* b_{i1} + \phi_i b_{i1}^\dagger\right) \end{aligned} \tag{8.48}$$

The field ϕ_i couples linearly to Schwinger bosons and is conjugate to $\delta_{1,m}\langle b_{im}^\dagger\rangle$. As a result of this parameterization, the lowest spinon frequency mode ω_0 of the $m = 1$ flavor develops a macroscopic occupation of Schwinger bosons on Bose condensation. At the mean field level the different boson flavors decouple and the part of the mean field Hamiltonian quadratic in bosonic operators $b_{im}, b_{im}^\dagger$ ($m = 2, ..., N$) can be expressed as $N-1$ copies of a quadratic Hamiltonian $\mathcal{H}_{MF}^m$. $\mathcal{H}_{MF}^m$ is given by,

$$\mathcal{H}_{MF}^m = \sum_{i=1}^{N_s}\lambda_i b_{im}^\dagger b_{im} + \sum_{i<j}\left(Q_{ij}b_{im}^\dagger b_{jm}^\dagger + \text{h.c.}\right) \tag{8.49}$$

Integrating out the bosonic fields then gives us a set of single-spinon frequency modes and the total mean field energy E_{MF}. Since we do not have the luxury of momentum space, we adopt a real space Bogoliubov diagonalization procedure [40]. Since $\mathcal{H}_{MF}^m$ is block diagonal in the flavor basis (the Hamiltonian is the same for all $N-1$ flavors) we can now drop the flavor index m and

express it as

$$\mathcal{H}^m_{MF} = \frac{1}{2}\begin{pmatrix} \mathbf{b}^\dagger & \mathbf{b} \end{pmatrix}\begin{pmatrix} \mathbf{\Lambda} & \boldsymbol{Q} \\ \boldsymbol{Q} & \mathbf{\Lambda} \end{pmatrix}\begin{pmatrix} \mathbf{b} \\ \mathbf{b}^\dagger \end{pmatrix} \tag{8.50}$$

where $m \neq 1$, $\mathbf{b} = (b_1, b_2, ..., b_{N_s})$ and $\mathbf{\Lambda}$ and $\boldsymbol{Q}$ are $N_s \times N_s$ matrices given by $\mathbf{\Lambda}_{ij} = \lambda_i \delta_{ij}$ and $\boldsymbol{Q}_{ij} = Q_{ij}$ for nearest neighbor sites i, j. $\mathcal{H}^m_{MF}$ can now be diagonalized by introducing Bogoliubov transformation matrices, $\mathbf{U}$ and $\mathbf{V}$ defined as follows,

$$\begin{pmatrix} \mathbf{b} \\ \mathbf{b}^\dagger \end{pmatrix} = \begin{pmatrix} \mathbf{U} & \mathbf{V} \\ \mathbf{V}^* & \mathbf{U}^* \end{pmatrix}\begin{pmatrix} \boldsymbol{\alpha} \\ \boldsymbol{\alpha}^\dagger \end{pmatrix} \tag{8.51}$$

where $\boldsymbol{\alpha} = (\alpha_1, \alpha_2, ..., \alpha_{N_s})$ is a vector of Bogoliubov quasiparticle annihilation operators. Each quasiparticle creation (annihilation) operator $\alpha^\dagger_\mu$ (α_μ) creates (destroys) a bosonic quasiparticle in the single particle mode μ, where μ goes from 1 to N_s. The transformation (8.51) allows us to switch to the Bogoliubov quasiparticle basis where $\mathcal{H}^m_{MF}$ becomes,

$$\mathcal{H}^m_{MF} = \sum_{\mu=1}^{N_s} \omega_\mu \left(\alpha^\dagger_\mu \alpha_\mu + \frac{1}{2}\right) \tag{8.52}$$

We can now perform a Legendre transformation to replace the field ϕ_i by β_i, allowing us to express E_{MF} as,

$$\frac{E_{MF}}{N} = \sum_{\mu=1}^{N_s} \frac{1}{2}\omega_{\mu_i} + \frac{1}{J}\sum_{i>j} |Q_{ij}|^2 - \left(S + \frac{1}{2}\right)\sum_{i=1}^{N_s} \lambda_i + E_{cond} \tag{8.53}$$

and E_{cond} is given by,

$$E_{cond} = \sum_{i=1}^{N_s} \lambda_i |\beta_i|^2 + \sum_{i<j} \left(Q_{ij}\beta^*_i \beta^*_j + \text{h.c.}\right) \tag{8.54}$$

We now consider the case of $N = 2$. The variational parameters $\{\lambda_i\}, \{Q_{ij}\}$ and $\{\beta_i\}$ are determined by minimizing E_{MF} with respect to each of them giving the

following constraints,

$$\frac{\partial E_{MF}}{\partial \lambda_i} = 0 \Rightarrow |\beta_i|^2 + \langle b_{i2}^\dagger b_{i2} \rangle = S \tag{8.55a}$$

$$\frac{\partial E_{MF}}{\partial Q_{ij}} = 0 \Rightarrow \beta_i^* \beta_j^* + \frac{\langle \mathcal{A}_{ij} \rangle}{N} + \frac{1}{J} Q_{ij} = 0 \tag{8.55b}$$

$$\frac{\partial E_{MF}}{\partial \beta_i} = 0 \Rightarrow \lambda_i \beta_i^* + \sum_{j \text{ n.n.} i} Q_{ij}^* \beta_j^* = 0 \tag{8.55c}$$

One of the obvious considerations of applying this theory to such a non-uniform lattice is the large number of variational parameters which, in general, scale with the system size N_s. However, due to the symmetries of the Cayley tree the number of independent parameters are reduced to order g (the generation of the tree). The task then is to find an optimal set of parameters $\{\lambda_i^*, Q_{ij}^*, \beta_i^*\}$ which satisfy the constraints in (8.55a), (8.55b) and (8.55c). This is done numerically and is discussed in section 8.5 .3. The resulting optimal $E_{MF}(\lambda_i^*, Q_{ij}^*, \beta_i^*)$ can be related to the physical Heisenberg energy via,

$$E_{\text{Heisenberg}} = 2E_{MF} + \sum_{\langle ij \rangle} JS^2 \tag{8.56}$$

A note on the β_i minimization constraint (8.55c): a trivial solution of this equation is to choose $\beta_i = 0$ for all sites. This is the quantum disordered phase. A non zero value of β_i signals condensation of Schwinger bosons and long range order.

For finite uniform systems there is no spontaneous symmetry breaking and correspondingly no condensation of bosons [41]. Introduction of the condensate field β_i is analogous to applying a staggered field in the system that couples to the staggered magnetization. This breaks the degeneracy of the single particle energies corresponding to the two boson flavors (for $N = 2$). The condensate fraction begins to build up in the flavor mode with the lowest frequency.

The algorithm tries to initially find a self-consistent mean field solution by varying only the set of λ_i and Q_{ij}. However, if we cannot satisfy the constraints in equations (8.55a, 8.55b) (with $\beta_i = 0$), we resort to adding the condensate field β_i, as an additional set of variational parameters. While we cannot completely rule out the possibility of a solution with $\beta_i = 0$, we believe that the appearance of a condensate is *physical*.

8.5 .2 Correlation functions

Here we compute correlation functions that enter into the self consistency equations (8.55a, 8.55b, 8.55c). The boson density of a given flavor at site i is given by (suppressing the flavor index),

$$\begin{aligned}
\langle b_i^\dagger b_i \rangle &= \sum_{p,q=1}^{N_s} \langle \left(\mathbf{U}_{ip}^* \boldsymbol{\alpha}_p^\dagger + \mathbf{V}_{ip}^* \boldsymbol{\alpha}_p \right) \left(\mathbf{U}_{iq} \boldsymbol{\alpha}_q + \mathbf{V}_{iq} \boldsymbol{\alpha}_q^\dagger \right) \rangle \\
&= \sum_{p,q=1}^{N_s} \mathbf{V}_{ip}^* \mathbf{V}_{iq} \langle \boldsymbol{\alpha}_p \boldsymbol{\alpha}_q^\dagger \rangle \\
&= \left(\mathbf{V}^* \mathbf{V}^T \right)_{ii} \qquad (8.57)
\end{aligned}$$

The indices p, q run over all single particle modes and we made use of $\langle \boldsymbol{\alpha}_p \boldsymbol{\alpha}_q^\dagger \rangle = \delta_{p,q}$ which follows since the SBMFT many body ground state is the vacuum of Bogoliubov quasiparticles. Similarly,

$$\langle b_i b_j \rangle = \left(\mathbf{U} \mathbf{V}^T \right)_{ij} \qquad (8.58)$$

Spin correlation functions G_{ij} can be computed in a similar fashion. The only complication arises in the $SU(2)$ broken symmetry phase where, due to loss of spin rotational invariance, we need to compute the $\langle S_i^z S_j^z \rangle$ correlations. This involves evaluating a quartic expectation which we decouple into a series of

two point functions using Wick's theorem. For simplicity of notation we define the following combinations of $\mathbf{U}$ and $\mathbf{V}$ matrices,

$$\begin{aligned} \tilde{\mathbf{Q}} &\equiv \mathbf{U}\mathbf{V}^T \\ \tilde{\mathbf{U}} &\equiv \mathbf{U}\mathbf{U}^\dagger \\ \tilde{\mathbf{V}} &\equiv \mathbf{V}\mathbf{V}^T \end{aligned} \tag{8.59}$$

Spin correlations in the Quantum disordered and the broken symmetry LRO phase are then given by,

$$(G_{ij})_{Q.dis.} = \begin{cases} -\frac{3}{2}\tilde{\mathbf{Q}}^\dagger_{ij}\tilde{\mathbf{Q}}_{ij} \\ \text{for } i \in A, j \in B \\ \\ \frac{3}{2}\tilde{\mathbf{V}}_{ij}\tilde{\mathbf{U}}_{ij} \\ \text{for } (i,j) \in A \text{ or } B \end{cases} \tag{8.60a}$$

$$(G_{ij})_{LRO} = \begin{cases} -N\beta_i\beta_j\tilde{\mathbf{Q}}_{ij} - \frac{1}{4}\tilde{\mathbf{Q}}^\dagger_{ij}\tilde{\mathbf{Q}}_{ij} \\ \text{for } i \in A, j \in B \\ \\ \frac{1}{2}N\beta_i\beta_j\left(\tilde{\mathbf{U}} + \tilde{\mathbf{V}}\right)_{ij} + \frac{1}{4}\tilde{\mathbf{V}}_{ij}\tilde{\mathbf{U}}_{ij} \\ \text{for } (i,j) \in A \text{ or } B \end{cases} \tag{8.60b}$$

In the quantum disordered phase SBMFT overestimates G_{ij} by an overall scale factor [8] of $3/2$. We normalize the SBMFT correlation function by this factor to take into account the $1/N$ fluctuation effects for $N = 2$. Similarly, in the phase with LRO we find that we need to scale up G_{ij} by a factor of 1.8 to make it agree quantitatively with DMRG results. Similar overall scale factors have been

reported previously [39]. These overall scale factors can be suppressed by using Gutzwiller projected mean field wavefunctions [42], which is feasible only for small system sizes. Such projected wavefunctions have also been shown to give energies in agreement with exact results [42, 39].

8.5 .3 Numerical Implementation

Using the symmetry of the bond-centered Cayley tree, we reduce the number of variational mean field parameters. A first simplification results from the fact that all sites within a given shell on the lattice are equivalent and are therefore assigned the same λ_i and β_i. Similarly, all bonds connecting two successive shells are equivalent and have the same Q_{ij}. For the Fibonacci cluster there are fewer exact symmetries (only reflection about the central bond) compared to the Cayley tree and therefore a larger number of variational parameters are required.

We use the Nelder Mead simplex optimizer from the GSL library to minimize the following weighted combined cost function which aims to reduce (8.53) subject to the constraints (8.55a), (8.55b) and (8.55c). Since each of these constraint equations are obtained by minimizing (8.53) with respect to the variational parameters λ_i, Q_{ij} and β_i, enforcing the constraints will minimize E_{MF}.

$$C\left(\{\lambda_i\},\{Q_{ij}\},\{\beta_i\}\right) = \mu_0 C_\lambda + \mu_1 C_Q + \mu_2 C_\beta \tag{8.61}$$

where $\{\mu_0, \mu_1, \mu_2\}$ are relative weights of terms in the cost function and the costs

are given by,

$$C_\lambda = \sum_{i=1}^{N_s} \left(\left(|\beta_i|^2 + \langle b_{i2}^\dagger b_{i2} \rangle \right) - S \right)^2 \tag{8.62a}$$

$$C_Q = \sum_{i<j} \left(\beta_i \beta_j + \frac{1}{N} \langle \mathcal{A}_{ij} \rangle + \frac{1}{J} Q_{ij} \right)^2 \tag{8.62b}$$

$$C_\beta = \sum_{i=1}^{N_s} \left(\lambda_i \beta_i^* + \sum_{j \ \text{n.n.}_i} Q_{ij}^* \beta_j^* \right)^2 \tag{8.62c}$$

In practice, to minimize the weighted cost function (8.61), tolerance values for the C_β and C_λ are set at 10^{-8} and 10^{-14} respectively and the Q_{ij} are solved for self-consistently. A good initial guess for the Q_{ij} is a pattern that favors dimerization as suggested by results from Exact Diagonalization for small clusters. A good rule of thumb for the bond centered cluster is to begin by dimerizing (assigning a high value of Q_{ij}) the outermost bond and to create a pattern, moving inwards, of alternating bond strengths.

For cases requiring a larger number of variational parameters (like in the case of the Fibonacci cluster) it helps to guide the Nelder Mead optimization using a "relaxation" algorithm. The algorithm starts with an initial guess for the Q_{ij} and allows the optimizer to find an optimal set of λ_i. If the tolerance level for C_λ is not met, the Q_{ij} are allowed to relax: i.e. the best set of λ_i is taken as initial guess in an optimization where the Q_{ij} are now taken to be the variational parameters. Thus, by alternating in the choice of variational parameters between λ_i and the Q_{ij} for each optimization cycle we converge to the desired tolerance limit.

The stability of the obtained mean field solution was checked by adding small random perturbations to the optimal mean field parameters. In the quantum disordered phase, the saddle point was checked to correspond to a maxi-

mum in λ_i and a minimum in the Q_{ij}.

Every optimization cycle scales as $\sim N_s^3\tau$, where τ is the total time for functional evaluation taken by the optimizer to converge to a solution. A typical optimization time for the N_s=126 cluster is about 20 minutes on a personal workstation (2.7 GHz Intel Core i7).

8.5 .4 Results

The landscape of the cost function (8.61) in parameter space has many local minima with very similar mean field energies (differing by 1% or less). As a result, we get a zoo of physically plausible mean field solutions, all of which satisfy (8.55a) and have comparable E_{MF}. To choose the optimal solution from amongst those, we look at the β_i minimization constraint (8.55c) and hand pick the one which has the lowest C_β. In other words, the chosen solution has the lowest spinon frequency ω_0.

The mean field energy and correlation functions for the bond-centered Cayley trees suffer from significant finite size effects. As a result, for the finite systems considered above, the lowest spinon frequency is always gapped $\omega_0 \neq 0$ in spite of a very low $\beta_{cost}(\sim 10^{-8})$. However, with increasing system size, ω_0 lowers and spinons begin to condense in this lowest frequency mode. Fig. 8.15 shows a finite size fit to the lowest spinon mode. Spinon condensation and a very small ω_0 suggest long range order in the thermodynamic limit.

Since condensation of spinons signals long range order, sites with a higher condensate fraction have a greater participation in establishing Néel order on

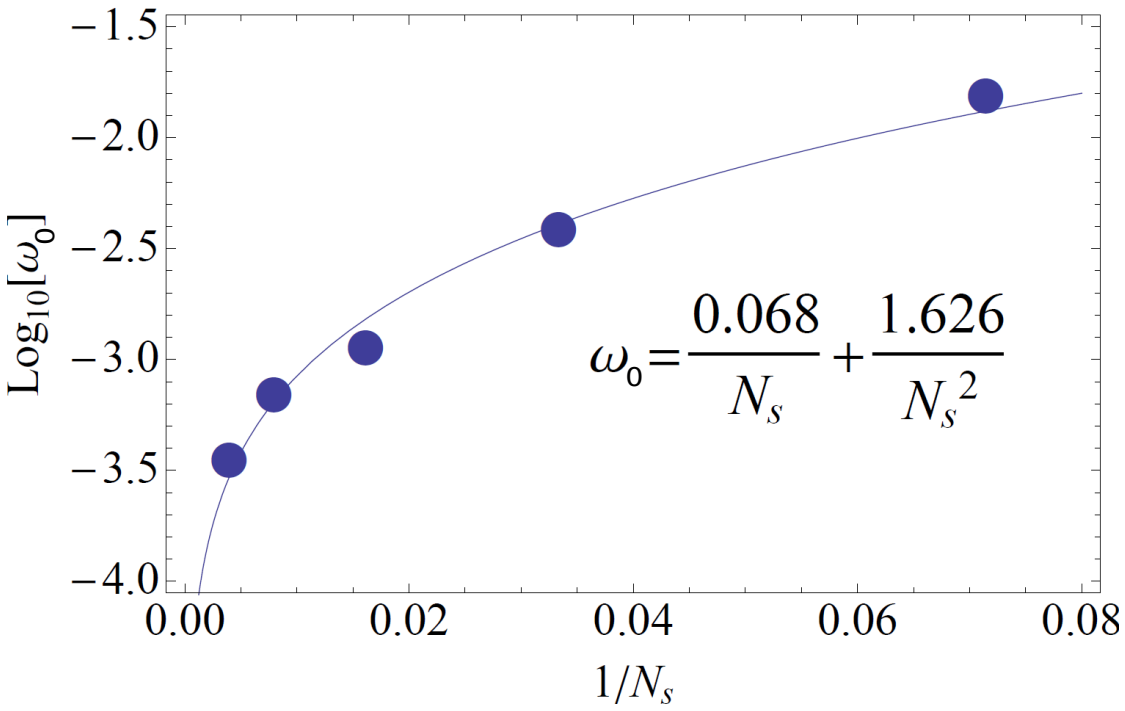

Figure 8.15: (Color online) The lowest spinon frequency appears to go to 0 as $1/N_s$. This signals appearance of long range order within the Schwinger Boson Theory.

the cluster. By mapping out the condensate fraction on different radial shells in Fig. 8.16(b) we notice the strong correspondence between sites with large condensate densities and those with a high "flippability" as in Eq.(8.24).

Our results can be put in perspective with respect to a heuristic for computing the number of "dangling spins" proposed by Wang and Sandvik [14, 15] in the context of percolation clusters on the square lattice. We “dimerize" the lattice maximally as shown in Fig. 8.16(a) and the spins that remain are called "dangling". These are the representative spins participating as the low energy degrees of freedom. (Note that the choice of maximal dimer covering is not unique but the number of uncovered spins is the same in all such coverings)

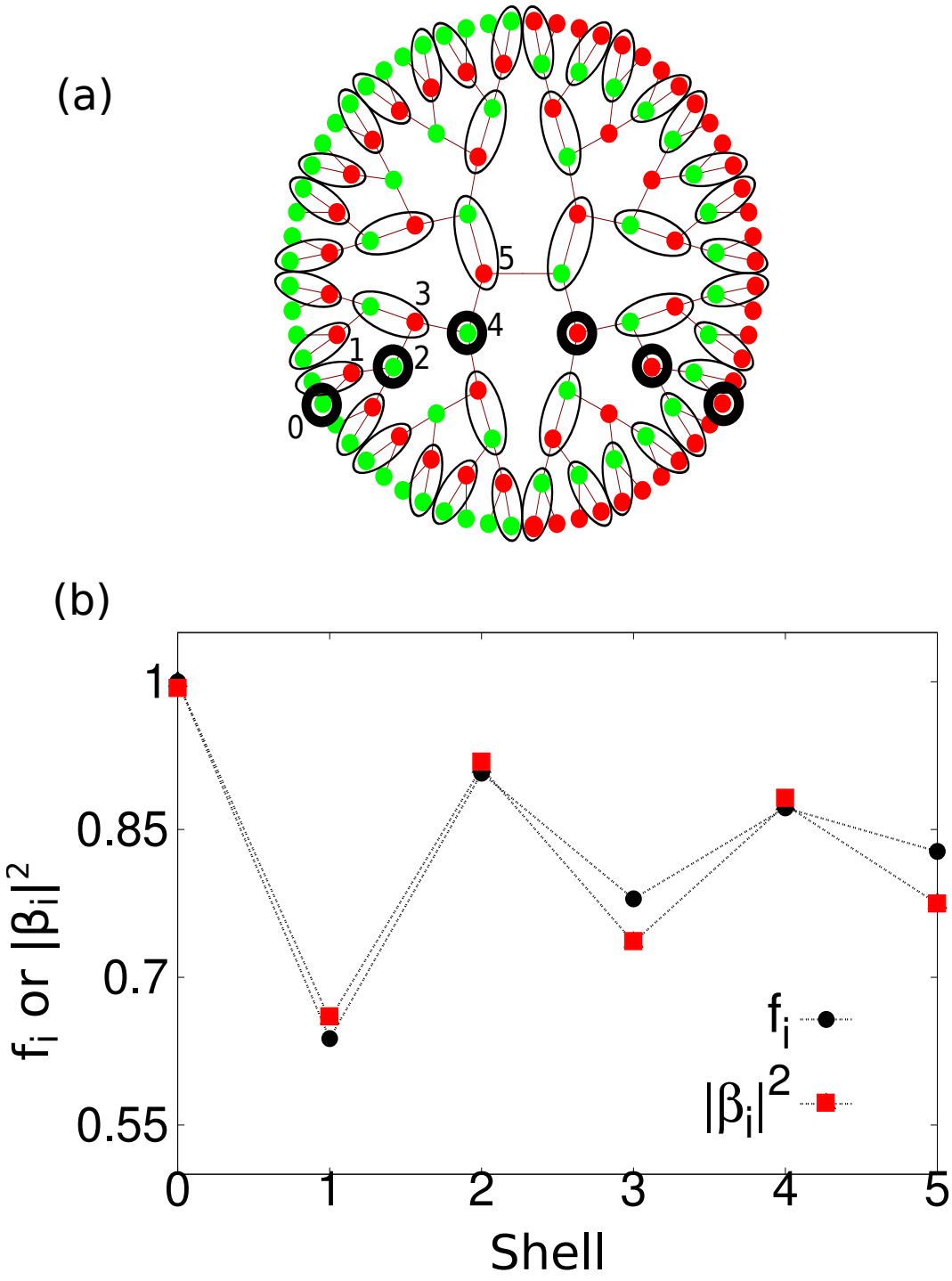

Figure 8.16: (Color online) (a): Heuristic for computing the number of "dangling spins" as proposed by Wang and Sandvik. (b): The "flippability" as in Eq.(8.24) computed from DMRG and the condensate fraction $|\beta_i|^2$ computed from SBMFT on every shell of the bond centered Cayley tree. Both quantities are qualitatively consistent with each other and confirm the "dangling" spin heuristic shown above.

8.6 Conclusion

In this Chapter, we have explored the relationship between sublattice imbalance and nature of the low energy spectrum of the bond-centered, site-centered and Fibonacci Cayley trees.

For the bond-centered Cayley tree, we find that the spin gap scales with size as $1/N_s^{\alpha}$ where α was found to be ≈ 2. We discover an entire tower of states (Fig. 8.5) with a much larger moment of inertia (Fig. 8.6) than the Anderson Tower of States. This low energy scale persists up to a spin value of $S^* = 2I_b$, where I_b refers to a measure of the imbalance (or the number of "unpaired spins") on the bond centered tree (as in Eq.(8.3)).

To highlight the role of sublattice imbalance, we introduced the Fibonacci Cayley tree in sec. 8.2 , which does not have any locally unpaired spins. We found it lacks the low lying states characteristic of the bond-centered tree (see Fig. 8.5). Instead, the spin gap vanishes as $\approx 1/N_s^{0.6}$. However, both trees have similar susceptibilities ($\sim N_s$) at sufficiently large magnetic fields. This is because the strength of the dimerization is relatively weak at sufficiently high energy scales (comparable to J), allowing all spins to lock together, leading to an extensive susceptibility.

For the site centered tree, our results are in good agreement with a recent study [24]. We report a finite spin gap of $\Delta = 0.731(4)$ in the infinite lattice limit and a ground state energy of $e_0 = -0.393854(1)$.

Our results can be explained within a unifying framework of individual spins coupling together to form collective spin degrees of freedom which we re-

fer to as "giant spins". The idea for coupling big sublattice spins is well known [17] in the context of regular lattices. However, we emphasize that the "giant spins" are created by coupling all spins (both even and odd sublattice spins) in regions with large local sublattice imbalances. For the bond- and site-centered lattices, we find that all lattice sites have a (nearly) uniform participation in the "giant spins". This picture is developed in section 8.4 using the single mode approximation for the excited state and by observing the entanglement spectrum.

In a broader context, our study aims to understand the nature of unpaired spins coupling in a strongly dimerized background. Such spins, termed as "dangling spins", have been predicted from numerical simulations [14, 15] for systems with quenched random dilution. Thus, a natural extension of our study is to consider such dangling spins on percolation clusters where we expect that they couple hierarchically to form emergent giant spins at different length scales. This is the subject of our paper [43].

In this Chapter, we have explored several techniques to develop our understanding. To begin with, we obtain accurate many-body wavefunctions and their expectations using an implementation of the Density Matrix Renormalization Group (DMRG) procedure (described in Chapter 7) that works for generic trees. In general, this procedure is expected to be well suited to hierarchical lattices and those with few or no loops, such as the Husimi cactus [44, 45], a lattice of corner sharing triangles (whose centers form the vertices of a Cayley tree) and which is locally like the kagome lattice.

To have an understanding at the mean field level, we adapted Schwinger Boson Mean Field Theory (SBMFT) to a larger number of variational parameters than considered previously [42, 39, 46]. We were able to study spin correla-

tions of the bond-centered and Fibonacci trees (singlet ground states). Rather remarkably, the theory is quite accurate *quantitatively* in predicting ground state spin-spin correlation functions (see Fig. 8.3), up to overall multiplicative scale factors (as discussed in section 8.5). The recipe outlined in section 8.5 can be used to navigate through the zoo of feasible mean field solutions by giving relative weights to the constraint equations (8.62a, 8.62b, 8.62c).

We believe that most applications of SBMFT have focused on quantum disordered phases [47, 48], but the broken symmetry phase has received less attention. The setup can also be generalized to handle frustrated spin systems without the need to have an ansatz for the mean field fluxes or the decoupling parameters [47]. This might lead to novel spin liquid ground states with new kinds of broken symmetries [38].

After our work was completed, we came across recent results by G.Misguich [38], who has done an extensive numerical study of SBMFT formalism for spatially inhomogeneous states, mostly concentrating on gapped systems. However, his study differs from ours in that we include the condensate field as a variational parameter. It will be interesting to apply our formalism to further investigate his proposed set of ground states.

8.A Derivation of the SMA gap equation for the Heisenberg Model

In section 8.4 , we introduced the single mode approximation (SMA) for the excited state in terms of the ground state,

$$|1'\rangle = \sum_i u_i S_i^+ |0\rangle \tag{8.63}$$

where $|0\rangle$ is the singlet ground state and $|1'\rangle$ is the approximate triplet excited state. i refers to a site index. In this Appendix, we will derive an expression for the SMA energy gap Δ_{SMA} in terms of the ground state correlations and the parameters u_i.

The expression for the gap between the ground and first excited state is,

$$\Delta = \frac{\langle 1' | H | 1' \rangle}{\langle 1' | 1' \rangle} - E_0 \tag{8.64}$$

where E_0 is the ground state energy. Plugging in the expression for $|1'\rangle$ from equation (8.63) we have,

$$\begin{aligned}
\Delta_{SMA} &= \frac{\left\langle 0 \left| \sum_{ij} u_i u_j S_j^- H S_i^+ \right| 0 \right\rangle}{\left\langle 0 \left| \sum_{ij} u_i u_j S_j^- S_i^+ \right| 0 \right\rangle} - E_0 && \text{(8.65a)} \\
&= \frac{\sum_{ij} u_i u_j \left\langle S_j^- \left[H, S_i^+ \right] \right\rangle}{\sum_{ij} u_i u_j \left\langle S_j^- S_i^+ \right\rangle} + \frac{\sum_{ij} u_i u_j \left\langle S_j^- S_i^+ H \right\rangle}{\sum_{ij} u_i u_j \left\langle S_j^- S_i^+ \right\rangle} - E_0 && \text{(8.65b)} \\
&= \frac{\sum_{ij} u_i u_j \left\langle S_j^- \left[H, S_i^+ \right] \right\rangle}{2 \sum_{ij} u_i u_j \left\langle S_j^z S_i^z \right\rangle} && \text{(8.65c)}
\end{aligned}$$

Next, consider the nearest neighbor Heisenberg Hamiltonian,

$$H = \frac{J}{2} \sum_{\langle k,l \rangle} \left(S_k^z S_l^z + \frac{1}{2} \left(S_k^+ S_l^- + S_k^- S_l^+ \right) \right) \tag{8.66}$$

where $\langle k, l \rangle$ refer to nearest neighbor pairs. We have included a factor of $1/2$ outside to compensate for counting each nearest neighbor term twice.

We now calculate $[H, S_i^+]$ occurring in Eq.(8.65c). To do so, we calculate $\left[\mathbf{S}_k \cdot \mathbf{S}_l, S_i^+\right]$ as,

$$\begin{aligned}\left[\mathbf{S}_k \cdot \mathbf{S}_l, S_i^+\right] &= S_k^z \left[S_l^z, S_i^+\right] + S_l^z \left[S_k^z, S_i^+\right] \\ &\quad + \frac{1}{2}\left(S_k^+ \left[S_l^-, S_i^+\right] + \left[S_k^-, S_i^+\right] S_l^+\right) \qquad (8.67a) \\ &= \delta_{il} S_k^z S_l^+ + \delta_{ik} S_l^z S_k^+ - \delta_{il} S_k^+ S_l^z - \delta_{ik} S_k^z S_l^+ \qquad (8.67b)\end{aligned}$$

The numerator of Eq.(8.65c) involves the term $\left\langle S_j^- \left[H, S_i^+\right]\right\rangle$. Hence we now consider the action of the S_j^- operator on the simplified expression for $\left[\mathbf{S}_k \cdot \mathbf{S}_l, S_i^+\right]$ in Eq.(8.67b).

Consider only the terms that have $j = k$ or $j = l$ (since $k = l$ terms do not occur in the Hamiltonian we do not have to worry about the possibility $j = k = l$). In addition, time reversal symmetry of the ground state wavefunction (equivalent to simply asserting the $S_z \to -S_z$ symmetry of the ground state) ensures that if both $j \neq k$ and $j \neq l$ then the three point correlation function is exactly 0. This latter point is rather subtle and so we expand on this in Appendix 8.B .

Thus the expression for $S_j^- \left[\mathbf{S}_k \cdot \mathbf{S}_l, S_i^+\right]$ (after retaining only the $j = k$ and $j = l$ terms) is,

$$\begin{aligned}S_j^- \left[\mathbf{S}_k \cdot \mathbf{S}_l, S_i^+\right] = &-\delta_{ik}\delta_{jl}\left(\frac{1}{2} - S_l^z\right) S_k^z - \delta_{ik}\delta_{jk}\frac{S_k^- S_l^+}{2} \\ &-\delta_{il}\delta_{jk}\left(\frac{1}{2} - S_k^z\right) S_l^z - \delta_{il}\delta_{jl}\frac{S_l^- S_k^+}{2} \\ &+\delta_{jk}\delta_{il}\frac{S_k^- S_l^+}{2} + \delta_{jl}\delta_{il}\left(\frac{1}{2} - S_l^z\right) S_k^z \\ &+\delta_{jk}\delta_{ik}\left(\frac{1}{2} - S_k^z\right) S_l^z + \frac{1}{2} S_k^+ S_l^- \delta_{ik}\delta_{jl} \qquad (8.68)\end{aligned}$$

Inserting (8.68), in the expression for the SMA gap (8.65c) for the Heisenberg

Hamiltonian and utilizing $\langle S_i^z \rangle = 0$ for all i, we obtain,

$$\Delta_{SMA} = -\frac{\sum_{\langle k,l \rangle} (u_k - u_l)^2 \langle S_k^z S_l^z \rangle}{2 \sum_{ij} u_i u_j \langle S_i^z S_j^z \rangle} \tag{8.69}$$

8.B Why is $\langle \psi | S_j^- S_k^+ S_l^z | \psi \rangle = 0$ for distinct j, k, l ?

To derive the SMA gap equation in Appendix 8.A , we used,

$$\langle \psi | S_j^- S_k^+ S_l^z | \psi \rangle = 0 \tag{8.70}$$

for distinct site indices j, k, l. In this Appendix, we will prove this statement for *any* wavefunction which is invariant under time reversal.

Consider three distinct spins i, j, k. Express the wavefunction in the basis spanned by the three spins at sites j, k, l and the rest of the spins (collectively termed as "environment" e),

$$|\psi\rangle = \sum_{s'_j s'_k s'_l} \sum_e w_e^{s'_j s'_k s'_l} |s'_j s'_k s'_l\rangle \otimes |e\rangle \tag{8.71}$$

Since this wavefunction is an eigenstate of the Heisenberg model (with no external magnetic fields), it follows that under time reversal (denoted by operator T) we have,

$$\psi \to z\psi \tag{8.72}$$

where z is ± 1.

This implies that the coefficients in the wavefunction satisfy the relation,

$$w_e^{s'_j s'_k s'_l} = z w_{-e}^{-s'_j - s'_k - s'_l} \tag{8.73}$$

The action of the operator $S_j^- S_k^+ S_l^z$ on $|\psi\rangle$ from Eq.(8.71) yields,

$$S_j^- S_k^+ S_l^z \, |\psi\rangle = \sum_{s_l'} \sum_{e} w_e^{\uparrow\downarrow s_l'} S_l' \, |\downarrow\uparrow s_l'\rangle \otimes |e\rangle \tag{8.74}$$

Now acting Eq.(8.74) with $\langle\psi|$ from the left and using the orthogonality of the basis we get,

$$\begin{aligned} \langle\psi| \, S_j^- S_k^+ S_l^z \, |\psi\rangle &= \sum_{s_l'} \sum_{e} w_e^{\downarrow\uparrow s_l'} w_e^{\uparrow\downarrow s_l'} S_l' & (8.75) \\ &= \frac{1}{2} \sum_{e_-} w_{e_-}^{\downarrow\uparrow\uparrow} w_{e_-}^{\uparrow\downarrow\uparrow} - \frac{1}{2} \sum_{e_+} w_{e_+}^{\downarrow\uparrow\downarrow} w_{e_+}^{\uparrow\downarrow\downarrow} & (8.76) \end{aligned}$$

where $e_+(e_-)$ reflects the fact that the environment carries a net S_z of $+(-)\frac{1}{2}$ since the wavefunction consists of $S_{tot}^z = 0$ terms only. Under inversion of all spins in e_+ we get e_-. With this in mind, consider the second sum on the right. Using the time reversal symmetry of the wavefunction i.e. $w_{e_+}^{\downarrow\uparrow\downarrow} = z w_{e_-}^{\uparrow\downarrow\uparrow}$ and $w_{e_+}^{\uparrow\downarrow\downarrow} = z w_{e_-}^{\downarrow\uparrow\uparrow}$ (as seen from Eq.(8.73)), in Eq.(8.76) we get,

$$\begin{aligned} \langle\psi| \, S_j^- S_k^+ S_l^z \, |\psi\rangle &= \frac{1}{2} \sum_{e_-} w_{e_-}^{\downarrow\uparrow\uparrow} w_{e_-}^{\uparrow\downarrow\uparrow} - \frac{1}{2} z^2 \sum_{e_-} w_{e_-}^{\downarrow\uparrow\uparrow} w_{e_-}^{\uparrow\downarrow\uparrow} & (8.77) \\ &= 0 & (8.78) \end{aligned}$$

where we have used $z^2 = 1$.

8.C Schwinger Boson Mean Field Theory Calculations

As mentioned in section 8.5 , optimization of multiple parameters occurring in the Schwinger Boson theory for non uniform systems was quite a challenging task. Hence, for the interested reader, we report the exact values of the parameters obtained from our calculations, so that they may be able to reproduce our results.

The optimal mean field parameters are tabulated in Table 8.4 for different lattice sizes. In each column (from top to down) the parameters label inner to outermost most bonds/sites. The Q_{ij} alternate in strength across successive bonds consistent with the location of unpaired spins. Similar alternation in the condensate field β_i indicates the variation in the density of dangling spins across shells.

The ground state energy from SBMFT for the 126 site cluster was found to be $\approx -0.533J$. This is lower than the DMRG estimate $-0.39385J$. This can be attributed to the well known fact [41, 46] about the non variational nature of SBMFT energies. This is because of not satisfying the constraints in Eq.(8.47) exactly.

N_s	bond $\langle i,j \rangle$	$-Q^*_{ij}$	λ^*_i	β^*_i
14	0 1	0.672	1.639	0
	1 2	0.539	2.318	0
	2 3	0.676	0.523	0
30	0 1	0.561	1.921	0
	1 2	0.633	1.487	0
	2 3	0.543	2.345	0
	3 4	0.673	0.536	0
62	0 1	0.646	1.720	0
	1 2	0.570	1.975	0
	2 3	0.630	1.514	0
	3 4	0.551	2.345	0
	4 5	0.680	0.544	0
126	0 1	0.568	1.893	0.430
	1 2	0.622	1.656	0.445
	2 3	0.579	2.026	0.392
	3 4	0.622	1.497	0.420
	4 5	0.550	2.320	0.353
	5 6	0.677	0.546	0.443
254	0 1	0.631	1.669	0.495
	1 2	0.560	1.986	0.454
	2 3	0.622	1.537	0.504
	3 4	0.571	1.965	0.455
	4 5	0.622	1.495	0.497
	5 6	0.550	2.263	0.449
	6 7	0.671	0.563	0.560

Table 8.4: Optimal SBMFT parameters for bond centered clusters of various sizes

BIBLIOGRAPHY

[1] H. J. Changlani, S. Ghosh, C. L. Henley and A.M. Läuchli, arXiv:1208.1773.

[2] M. Takahashi, Phys. Rev. Lett. **58**, 168 (1987).

[3] J. E. Hirsch and S. Tang, Phys. Rev. B **39**, 2887 (1989).

[4] E. Manousakis, Rev. Mod. Phys. **63**, 1 (1991).

[5] A. Chubukov, Phys. Rev. B **44**, 12318 (1991).

[6] A. V. Chubukov, S. Sachdev, and J. Ye, Phys. Rev. B **49**, 11919 (1994).

[7] S. Sarker, C. Jayaprakash, H. R. Krishnamurthy, and M. Ma, Phys. Rev. B **40**, 5028 (1989).

[8] A. Auerbach and D. P. Arovas, Phys. Rev. Lett. **61**, 617 (1988).

[9] A.Auerbach, D.P.Arovas, arXiv:0809.4836v2 (unpublished).

[10] N. Trivedi and D. M. Ceperley, Phys. Rev. B **41**, 4552 (1990).

[11] K. H. Höglund and A. W. Sandvik, Phys. Rev. B **79**, 020405 (2009).

[12] M. A. Metlitski and S. Sachdev, Phys. Rev. B **78**, 174410 (2008).

[13] A. L. Chernyshev, Y. C. Chen, and A. H. Castro Neto, Phys. Rev. Lett. **87**, 067209 (2001).

[14] L. Wang and A. W. Sandvik, Phys. Rev. Lett. **97**, 117204 (2006).

[15] L. Wang and A. W. Sandvik, Phys. Rev. B **81**, 054417 (2010).

[16] P. W. Anderson, Phys. Rev. **86**, 694 (1952).

[17] C. Lhuillier arXiv:cond-mat/0502464v1 (unpublished).

[18] Subir Sachdev, *Quantum Phase Transitions*, Cambridge University Press, 1999.

[19] H. Neuberger and T. Ziman, Phys. Rev. B **39**, 2608 (1989).

[20] M. Gross, E. Sánchez-Velasco, and E. Siggia, Phys. Rev. B **39**, 2484 (1989).

[21] T. Vojta and J. Schmalian, Phys. Rev. Lett. **95**, 237206 (2005).

[22] H. Otsuka, Phys. Rev. B **53**, 14004 (1996).

[23] B. Friedman, Journal of Physics: Condensed Matter **9**, 9021 (1997).

[24] M. Kumar, S. Ramasesha, and Z. G. Soos, Phys. Rev. B **85**, 134415 (2012).

[25] C. R. Laumann, S. A. Parameswaran, and S. L. Sondhi, Phys. Rev. B **80**, 144415 (2009).

[26] G. Semerjian, M. Tarzia, and F. Zamponi, Phys. Rev. B **80**, 014524 (2009).

[27] W. F. Brinkman and T. M. Rice, Phys. Rev. B **2**, 4302 (1970).

[28] A. Georges, G. Kotliar, W. Krauth, and M. J. Rozenberg, Rev. Mod. Phys. **68**, 13 (1996).

[29] M. A. Martin-Delgado, J. Rodriguez-Laguna, and G. Sierra, Phys. Rev. B **65**, 155116 (2002).

[30] D. Astruc, E. Boisselier, and C. Ornelas, Chemical Reviews **110**, 1857 (2010), pMID: 20356105.

[31] M. Takahata *et al.*, International Journal of Quantum Chemistry **105**, 615 (2005).

[32] S. R. White, Phys. Rev. Lett. **69**, 2863 (1992).

[33] W. Münder *et al.*, New Journal of Physics **12**, 075027 (2010).

[34] W. Marshall, Proc. Roy. soc. London A 232, 48 (1955); E. H. Lieb and D. Mattis, J. of Math. Phys. 3, 749(1962); M.B. Hastings, Phys. Rev. B 69, 104431 (2004).

[35] R.P. Feynman, *Statistical Mechanics* (Benjamin, New York, 1972).

[36] C. R. Laumann, S. A. Parameswaran, S. L. Sondhi, and F. Zamponi, Phys. Rev. B **81**, 174204 (2010).

[37] S. Sachdev, Phys. Rev. B **45**, 12377 (1992).

[38] G. Misguich, arXiv:1207.4058v1(2012).

[39] L. Messio, O. Cépas, and C. Lhuillier, Phys. Rev. B **81**, 064428 (2010).

[40] See for example: E.R. Mucciolo, A.H. Castro Neto, Claudio Chamon, Phys. Rev. B69, 214424 (2004).

[41] A.Auerbach, *Interacting electrons and Quantum Magnetism*, Springer-Verlag, 1994.

[42] T. Tay and O. I. Motrunich, Phys. Rev. B **84**, 020404 (2011).

[43] H. J. Changlani, S. Ghosh, S. Pujari and C. L. Henley, arXiv:1210.4621.

[44] P. Chandra and B. Doucot, Journal of Physics A: Mathematical and General **27**, 1541 (1994).

[45] H.J. Changlani, R. Lamberty, C.L. Henley (in preparation).

[46] L. Messio, B. Bernu, and C. Lhuillier, Phys. Rev. Lett. **108**, 207204 (2012).

[47] X.-G. Wen, Phys. Rev. B **65**, 165113 (2002).

[48] F. Wang, Phys. Rev. B **82**, 024419 (2010).

CHAPTER 9

EMERGENT SPINS ON A BETHE LATTICE AT PERCOLATION

The text of this Chapter is a reproduction (with minor presentational changes for this thesis) of the paper written on the same subject in 2012 [1]. This paper may also be accessed online at http://arxiv.org/pdf/1210.4621v1.pdf . I acknowledge the combined efforts that were involved in this project with Shivam Ghosh and Sumiran Pujari.

9.1 Introduction

Quantum spins on percolation clusters [2] provide an ideal testbed for studying the interplay between geometrical disorder and quantum fluctuations. The Hamiltonian for these problems is

$$\mathcal{H} = \sum_{\langle ij \rangle} J \mathbf{S}_i \cdot \mathbf{S}_j \tag{9.1}$$

where $\mathbf{S_i}$ are Pauli spin $1/2$ operators and the sum runs over nearest-neighbor occupied sites, and $J > 0$. Theoretical [3, 4] and experimental [5] studies of quantum spins on diluted square lattices have focused on the question of whether long range order survives up to the classical percolation threshold p_c. A numerical study [6] seems to have settled this question and found long range order to be robust to quantum fluctuations, surviving all the way up to p_c.

The excitations are less straightforward. For uniform lattices with number of sites N, the lowest energy scale *consistent with Néel order breaking a continuous symmetry* is $\sim JN^{-1}$, corresponding to a "tower" of states: mixtures of symmetry-broken states that become degenerate in the thermodynamic

limit [7, 8, 9]. However, a Quantum Monte Carlo study by Wang and Sandvik [10, 11] discovered a somewhat "anomalous" finite size scaling of the spin gap Δ_{low}: $\Delta_{low} \approx N^{-2}$ (for clusters with a singlet ground state) or $\Delta_{low} \approx N^{-1.5}$ (for generic clusters, most with a non-singlet ground state). A strong correspondence was shown [10, 11] between these low lying states and places on the cluster where there is a local imbalance between the number of even and odd sites. It was conjectured that, in each such place, a spin degree emerges which is effectively decoupled from the antiferromagnetic order and hence was called a "dangling spin."

The goal of this Chapter is to characterize the dangling-spin degrees of freedom numerically, relating their nature to the local geometry of the cluster, and to explain the observed low energy spectrum in terms of mediated interactions between dangling spins. Our Hamiltonian is (9.1) on clusters obtained by randomly diluting the Bethe Lattice of coordination 3 at its percolation threshold, $p_c = 1/2$ (see examples of small clusters in Fig. 9.1). The lack of loops in the Bethe lattice is conducive for using the Density Matrix Renormalization Group (DMRG) algorithm [12], as adapted to generic tree graphs, to obtain ground and (some) excited states [13].

In the rest of this Chapter, we first show that a typical percolation cluster's spectrum has a clearly separated low energy component, with a multiplicity consistent with the expected number of weakly coupled spin-1/2 (sometimes spin-1) dangling spins. We next show that each dangling spin is somewhat delocalized over a few sites: on the one hand, we model it as an unpaired spin in a dimerized background to predict the dangling spin's nature from the local geometry; on the other hand, by processing spin expectations we obtain

the explicit "localized state wavefunction" for each dangling spin. Finally, for each cluster we construct the effective Hamiltonian of the emergent dangling spins, consisting of *pairwise*, unfrustrated exchange interactions decaying exponentially with separation, mediated by the background of almost dimerized spins on the balanced parts of the cluster; this accurately reproduces the details of that cluster's low-energy spectrum.

9.2 Exact correspondence between dangling spins and low energy spectrum

We carried out DMRG calculations for several hundred balanced clusters (i.e. having equal number of even and odd sublattice sites) [1] for sizes up to $N = 100$, targeting multiple excited states in the low energy spectrum. Since the number of low energy states was found to increase rapidly with an increase in the number of dangling spins, we restricted our analysis to the case of four dangling spins [2]. For analyses where only the ground state properties were of interest or where only the lowest energy gap Δ_{low} was required, larger clusters ($N = 200$), with an *arbitrary* number of dangling spins, were also studied.

In a typical percolation cluster, we observed a distinct set of low-lying energy levels we shall call "quasi-degenerate" (QD) [14] since (we claim) they would be exactly degenerate in the limit that the dangling spins are fully decoupled from the rest of the sites. The QD states are separated from the continuum of

[1] Balanced clusters necessarily have a singlet ground state.

[2] When only a count of the number of low energy states was desired, we looked at the approximate energies obtained at the end of the initialization step of the DMRG (as described in 7). This allowed us to probe clusters with six dangling spins.

higher energy Quantum Rotor and spin wave states by a finite size gap we call Δ (specifically defined as the difference between the mean of QD levels and the lowest non-QD level). The set of QD states are identified by looking at the difference in energies of consecutive states up to the Quantum rotor excitation and finding the pair of states with the largest gap. The lower energy state in this pair and all states below that make up the QD spectrum [3]. The energy scale characterizing the spread of the QD states, $\sigma_{\rm QD}$, is defined to be the standard deviation of the QD energies from their mean value. The ratio $r = \sigma_{\rm QD}/\Delta$ was found to be small (for example $r \sim 0.17 \pm 0.1$ for $N = 50$ and see Figure 9.2), justifying our notion of a separation of scales.

9.3 Exact correspondence between dangling spins and low energy spectrum

Figure 9.1 also shows a striking correspondence between the number of low lying QD states, $\mathcal{N}_{\rm QD}$, and the number of dangling spins n_d on the percolation cluster. We find that $\mathcal{N}_{\rm QD} = 2^{n_{1/2}}3^{n_1}$, where $n_{1/2}$ and n_1 are integers and $n_{1/2} + 2n_1 = n_d$. Our interpretation of this multiplicity is that $2n_1$ of the dangling spins pair up so as to form a spin-1, while the others remain as spin-half degrees of freedom. There is thus a one-to-one correspondence between the low-energy (QD) eigenstates and the Hilbert space of the posited emergent spins. We used an algorithm (to be described in the next section) that relies only on the cluster geometry to objectively predict the numbers $n_{1/2}$ and n_1 for each cluster, and

[3] Interactions between dangling spins separated by different length scales creates an entire hierarchy of energy levels. Some of these might even be higher than the first Quantum Rotor excitation. However, there will always be a set of low lying states arising from splittings between the most distant spins on the cluster. We label these states as 'QD' spectrum for computing *r*.

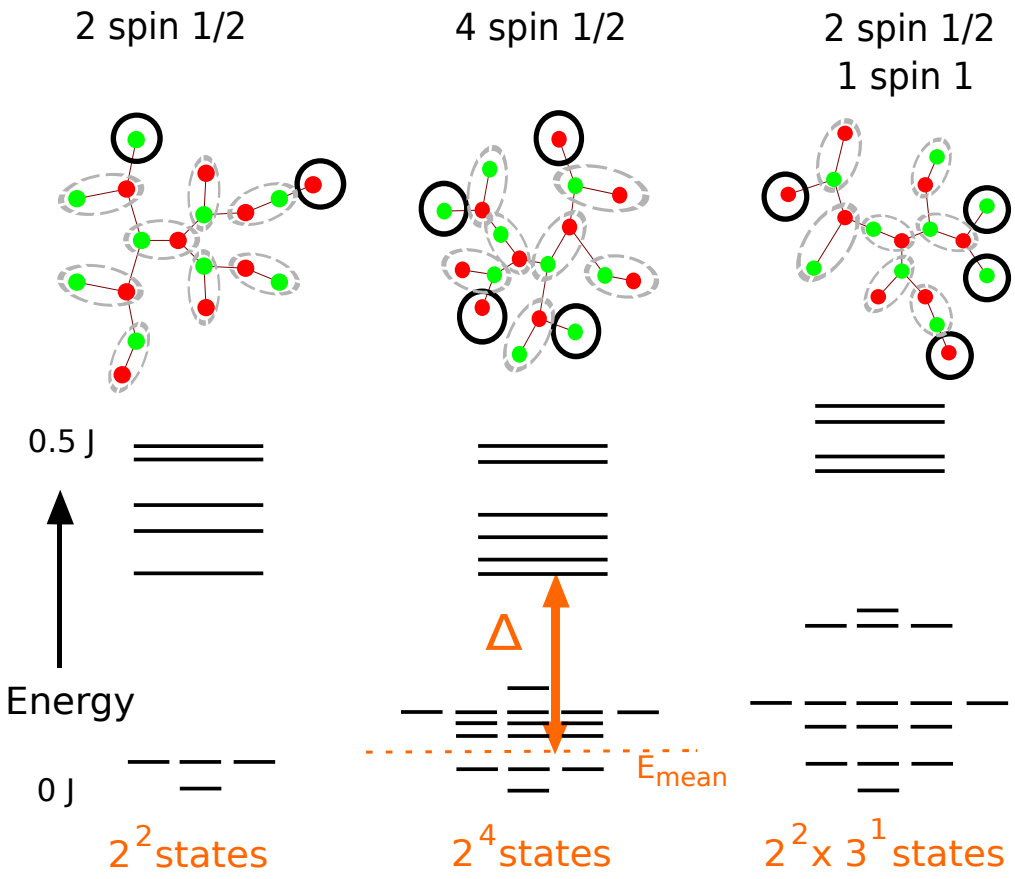

Figure 9.1: (Color online) Three different percolation clusters (all of the same size $N = 18$) are shown with their corresponding low energy spectra. The 'red' and 'green' circles indicate even and odd sites. The broken dashed lines show dimer coverings which serve as a heuristic to locate the "dangling spins". Dangling spins in each cluster have been circled with thick black lines. Low energy spectra for each of the clusters show low lying quasi degenerate (QD) states separated from the continuum by an energy scale Δ. $\sigma_{\rm QD}$ (not shown) is a measure of the spread of energies in the QD space.

verified that their predicted relationship with $\mathcal{N}_{\rm QD}$ was satisfied in every cluster.

We also directly measured the lowest singlet-triplet gaps Δ_{low} for an ensemble of balanced clusters. Its typical value scales as $N^{-1.9\pm0.1}$, which appears remarkably similar to the scaling previously seen on square lattice percolation clusters [10, 11].

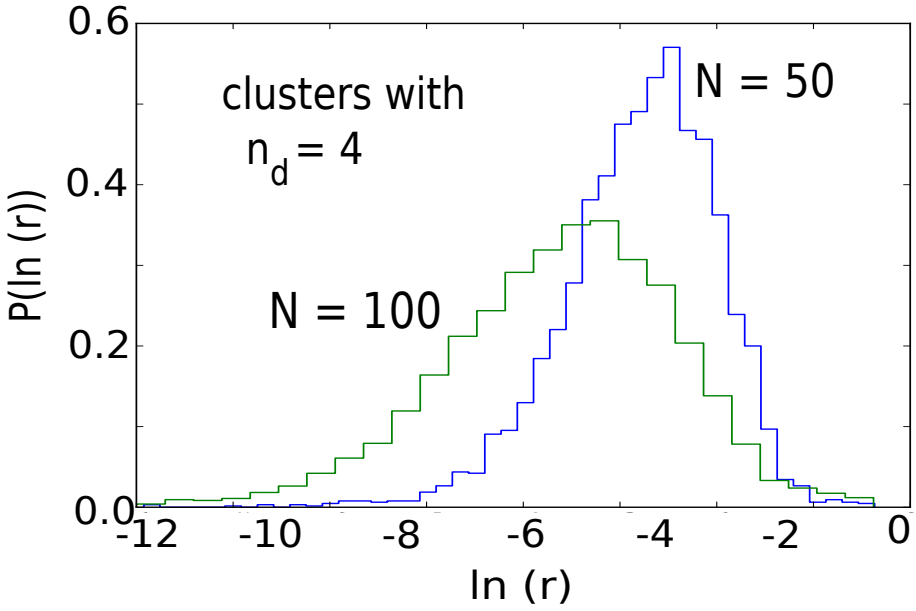

Figure 9.2: (Color online) Ratio (r) of the spread of the quasi degenerate (QD) energies (denoted by $\sigma_{\rm QD}$) to the QD gap (Δ) for an ensemble of percolation clusters for sizes $N = 50$ and $N = 100$ having four dangling spins $n_d = 4$.

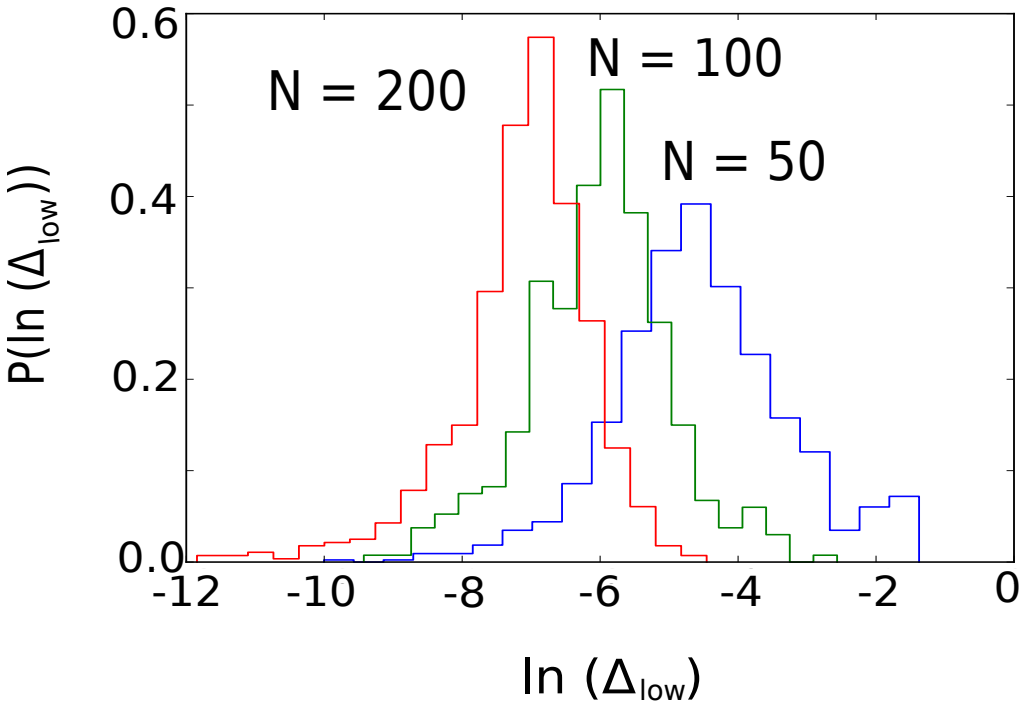

Figure 9.3: (Color online) Distribution of the lowest energy gaps (singlet-triplet) for an ensemble of percolation clusters of sizes $N = 50, 100, 200$.

9.4 Locating Dangling degrees of freedom in real space

Having established the presence of emergent spin-half and spin-one degrees of freedom, we now develop two complementary ways of looking at them.

The first is within the framework of a quantum monomer-dimer model. We imagine that the wavefunction is a product of valence bonds in which the N spins are paired (dimerized) into singlets to the maximum extent possible (optimal configuration). Even when even and odd sites are balanced *globally*, there remain some uncovered sites, i.e. monomers, due to *local* imbalances. These are spin-1/2 degrees of freedom and (within this picture) represent the dangling spins. There are multiple ways to optimally place the monomers; the actual wavefunction is imagined to be a superposition of these ways.

Our geometric algorithm, based on the valence bond framework, finds one element from the set of optimal dimerizations of the cluster and then attempts to find other elements of the set by locally replacing monomers with adjacent dimers. In spirit, this is a "greedy" algorithm which tries to place dimers wherever possible (to obtain an optimal dimerization pattern), working from the outer sites inwards on the cluster.

Given any cluster, there are two operations which cut it down to a smaller cluster or clusters, such that all optimal dimerizations on the smaller cluster(s) are in 1-to-1 correspondence with *some* of dimerizations on the larger one. The first operation is that, wherever two sites have coordination 1 or 2, we can remove both (given the dimerization on the smaller cluster, just insert another dimer to get the dimerization on the larger one). The second operation is that, wherever we find a pair of adjacent sites with respective coordinations 3 and 1

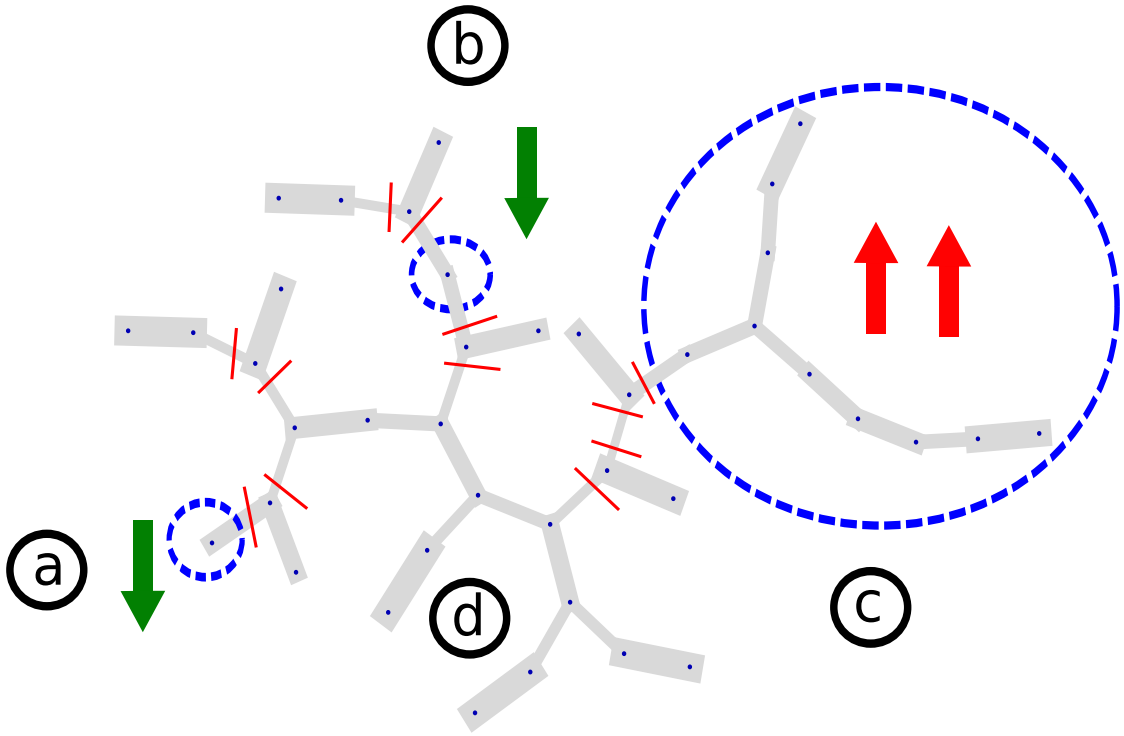

Figure 9.4: (Color online):Typical geometrical motifs in Cayley tree percolation clusters, as related to monomer/dimer construction. We disconnect the cluster into "spans", shown by (blue) dashed circles, at the "prong" bonds, as indicated by the (red) cut lines. The thickness of the (grey) bonds is directly proportional to $\langle \mathbf{S}_i \cdot \mathbf{S}_j \rangle$.

(a "prong"), we can always place a dimer on that pair, which fragments the rest into two subclusters (Fig.9.4); a very common special case is the fork, at which we can arbitrarily choose either side to be the "prong". These two operations can be used recursively till only isolated sites remain, each corresponding to one monomer in the original cluster. Furthermore, any other optimal dimerization is accessible from the special one we constructed, by repeatedly exchanging a monomer with an adjacent dimer.

A monomer can thus "hop" to sites on the lattice via such local monomer-dimer rearrangements as shown in Fig.9.5(c). Our rule-of-thumb is that two monomers (of the same sublattice) form a spin-1 if and only if they can ap-

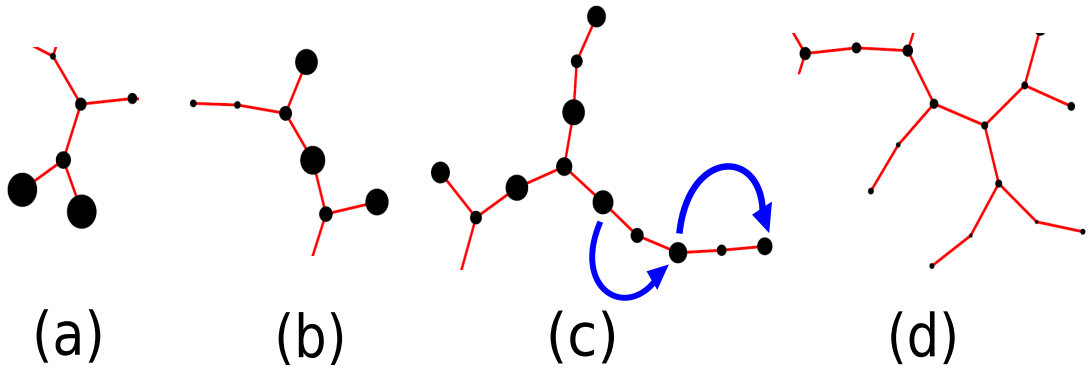

Figure 9.5: (Color online): Spatial profiles associated with "dangling spins", shown on the subclusters marked (a)-(d) of the same cluster shown in Fig. 9.4. The area of the black circles is proportional to ω_{ii} given by Eq. (9.4). (a) shows a "fork" (b) shows a site surrounded by two "hairs" (c) shows a subcluster where two monomers on the same sublattice are present forming an effective spin-1. The (blue) arrows indicate the monomer is free to hop around (delocalize) within the subcluster. (d) shows a region where the spins are "inert" (largely dimerized) and do not participate in the low energy physics.

proach to the minimal separation of two steps [4]. We check this possibility by enumerating all dimerizations accessible from the one generated by our algorithm.

Fig. 9.4 also shows some typical geometrical motifs seen in an ensemble of percolation clusters. In Fig. 9.4(a), a spin-half dangling spin is localized at the tip of the fork. The arms of the fork have a strong dimerization and prevent the localized monomer from hopping to other sites in the cluster. Fig. 9.4(b) shows another type of spin-half degree of freedom, which is trapped in the interval between (or on) two "prongs". Fig. 9.4(c) is an example of an emergent spin-one excitation. For comparison, we also show in Fig. 9.4(d) a region of strong dimerization with no dangling spins.

[4]This prescription for predicting spin ones was found to be invalid for ∼3% clusters with $n_d = 4$. For these clusters, two monomers at lattice spacings greater than two, were found to behave as a spin one in the low energy spectrum. A more stringent criterion for forming a spin one is to have the relative spacing between the spin one monomers to be much smaller than the typical separation of the spin one pair from other spins on the cluster.

Our second way to capture the spatial nature of a dangling spin degree of freedom starts from the idea that it could be adiabatically connected to an uncoupled spin, analogous to the Landau quasiparticle that is adiabatically connected to a free electron. Thus, our program is to label each emergent spin-1/2 degree of freedom by a "quasi spin" operator $\mathbf{T}_\alpha$, where the index α labels each region on the cluster with a local spin imbalance. The $\mathbf{T}_\alpha$'s are idealized as having a spin-half algebra. The actual "quasi spin" excitation is a composite object involving multi-spin excitations, localized on a few sites.

Our assumption is that the quasi-spin quantum numbers are sufficient to label all the QD states; furthermore, we expect the action of any spin operator $\mathbf{S}_i$, when restricted to the QD states, practically reduces to a linear combination of $\mathbf{T}_\alpha$'s acting on the quasi spins. Specifically, let $\hat{P}_{\rm QD}$ be the projection operator onto the QD subspace. Let $\mathbf{S}_{i,\rm QD} \equiv \hat{P}_{\rm QD}\mathbf{S}_i\hat{P}_{\rm QD}$ Then,

$$\mathbf{S}_{i,\rm QD} \cong \sum_\alpha u_i^{(\alpha)}\mathbf{T}_\alpha \tag{9.2}$$

where each mode $u_i^{(\alpha)}$ has most of its weight on sites within the region α and is expected to decay rapidly outside [15].

Two operators $\hat{P}, \hat{Q}$ are said to be *orthogonal* when their Frobenius inner product $\left(\hat{P}, \hat{Q}\right)_F \equiv \mathrm{Tr}\left(\hat{P}^\dagger\hat{Q}\right)$ is exactly zero. In this sense, the $\mathbf{T}_\alpha$ operators are orthogonal to each other. Since each $\mathbf{T}_\alpha$ is a quasi-spin $1/2$ operator its inner product with itself is $1/2$ (for each spin component).

In light of Eq.(9.2), we can also construct a good approximation $\widetilde{\mathbf{T}}_\alpha$ to each operator $\mathbf{T}_\alpha$, by choosing any representative site i in the dangling region α and normalizing the restriction of its spin operator to the QD states:

$$\widetilde{\mathbf{T}}_\alpha \equiv \frac{\mathbf{S}_{i,\rm QD}}{\sqrt{2}||\mathbf{S}_{i,\rm QD}||} \tag{9.3}$$

where $||\hat{O}|| \equiv (\hat{O}, \hat{O})_F^{1/2}$ is the norm of any operator $\hat{O}$. Note that the $\widetilde{\mathbf{T}}_\alpha$'s are *not* orthogonal to each other. A procedure to construct the $\mathbf{T}_\alpha$'s from the $\widetilde{\mathbf{T}}_\alpha$'s will be discussed in the next section.

Given the proposed relationship of the bare spins to the quasi spins, we discuss two related but independent measurements to recover the mode vectors $u_i^{(\alpha)}$ from numerically evaluated expectations. For all the measurements proposed here, it was sufficient to record (within DMRG) all matrix elements of the form $\langle l'|S_i^+|l\rangle$ and energies E_l for eigenstates l, l' in the QD subspace.

First, we consider the operator overlap ω_{ij} between two spins *i* and *j* on the lattice, defined to be,

$$\omega_{ij} \equiv \left(S_{i,\mathrm{QD}}^+, S_{j,\mathrm{QD}}^+\right)_F \tag{9.4}$$

We substitute our ansatz (9.2) into (9.4) and use the operator orthogonality of the $\mathbf{T}_\alpha$'s, to get $\omega_{ij} = \sum_\alpha u_i^{(\alpha)} u_j^{(\alpha)}$. If we consider a site *i* to be well within a dangling region α (i.e. $u_i^{(\alpha)}$ is relatively large) then the amplitude on the remaining sites *j* (but far away from other dangling regions) is approximately $u_i^{(\alpha)} u_j^{(\alpha)}$. Thus, the relative amplitudes of the mode vector can be recovered by this method.

Our second measurement involves computation of the inter-site spin susceptibility matrix,

$$\chi_{ij} = \int_0^\infty \langle \hat{S}_i^z(\tau) \hat{S}_j^z(0)\rangle_{GS} d\tau = \sum_n \frac{\langle 0|\hat{S}_i^z|n\rangle\langle n|\hat{S}_j^z|0\rangle}{E_n - E_0} \tag{9.5}$$

where τ is imaginary time, $|0\rangle$ denotes the ground state and E_n is the energy of an excited state $|n\rangle$ [16]. The χ_{ij} matrix is a generalization of the χ_{ii} measurement proposed in Ref. [10, 11].

Though the sum runs over all excited states, it can be well approximated by taking only the states in the QD subspace. Then χ_{ij} can also be expressed in

terms of the mode profiles $u_i^{(\alpha)}$,

$$\chi_{ij} = \sum_{\alpha\beta} u_i^{(\alpha)} u_j^{(\beta)} X_{\alpha\beta}; \qquad X_{\alpha\beta} \equiv \sum_{n\in \mathrm{QD}} \frac{\langle 0|\mathbf{T}_\alpha^z|n\rangle\langle n|\mathbf{T}_\beta^z|0\rangle}{E_n - E_0} \tag{9.6}$$

Consider site $i(j)$ in dangling region α (β). From equation (9.6) it follows that $\chi_{ij} \approx u_i^{(\alpha)} u_j^{(\beta)} X_{\alpha\beta}$, where the last factor is *independent* of sites i, j (so long as we stay within those regions). Within this approximation, the susceptibility matrix breaks up into blocks of rank 1 from which we can immediately pull out the $u_i^{(\alpha)}$ and $u_j^{(\beta)}$ modes.

9.5 Effective Hamiltonian in the Quasi degenerate subspace

According to our ansatz (9.2), there is a one-to-one correspondence between the QD Hilbert space and the Hilbert space of a set of abstract "quasi spin" operators $\mathbf{T}_\alpha$. (For simplicity, assume they all have spin 1/2.) The latter are labeled using an Ising basis $|\phi_t\rangle$, where t stands for the quantum numbers $\{t_1^z, t_2^z, ...t_{n_d}^z\}$, with $t_\alpha = \pm 1/2$. We want to find the unitary matrix $\mathbf{M}$ of coefficients expressing the QD states $|l\rangle$ (in eigenenergy basis) in terms of the quasi-spin basis, $|l\rangle = \sum_t M_{lt}|\phi_t\rangle$.

Using $\widetilde{\mathbf{T}}_\alpha$ from (9.3), we define $\hat{Q}_\alpha^{\pm 1/2} \equiv (\frac{1}{2} \pm \widetilde{\mathbf{T}}_\alpha^z)$, which is *almost* a projection operator, and let

$$|\widetilde{\phi}_t\rangle \propto \prod_{\alpha=1}^{n_d} \hat{Q}_\alpha^{t_\alpha}|n\rangle \tag{9.7}$$

where $|n\rangle$ could be any QD state (that is not annihilated by the operator prefactors) and $|\widetilde{\phi}_t\rangle$ is normalized. Finally, define a matrix $\underline{\Omega}$ by $\Omega_{tt'} \equiv \langle\widetilde{\phi}_t|\widetilde{\phi}_{t'}\rangle$ – which is *almost* the identity matrix – and construct the orthonormal quasi spin basis of

the QD states as

$$|\phi_t\rangle \equiv \sum_{t'} (\underline{\Omega}^{-1/2})_{tt'} |\widetilde{\phi}_{t'}\rangle. \tag{9.8}$$

The quasi spin operators $\mathbf{T}_\alpha$ are then defined so as to have the appropriate matrix elements in this basis.

Now consider the effective low energy Hamiltonian written in terms of the many body eigenstates $|l\rangle$,

$$\mathcal{H}_{\text{eff}} \equiv \sum_{l \in \text{QD}} E_l |l\rangle\langle l| = \sum_{tt'} h_{tt'} |\phi_t\rangle\langle\phi_{t'}|, \tag{9.9}$$

where E_l is the eigenenergy of QD state $|l\rangle$, and the matrix elements $h_{tt'}$ can be calculated since we know the transformation between the bases $\{|l\rangle\}$ and $\{|\phi_t\rangle\}$. Every term $|\phi_t\rangle\langle\phi_{t'}|$ can be uniquely expressed as a polynomial in the spin operators $\{T^z_\alpha\}$ and $\{T^\pm_\alpha\}$.

The effective Hamiltonian (9.9) then takes the new form of,

$$\mathcal{H}_{\text{eff}} \equiv \sum_{\mu,\nu} J_{\mu\nu} \mathbf{T}_\mu \cdot \mathbf{T}_\nu + \text{multi spin terms}; \tag{9.10}$$

(The two-spin terms must have this Heisenberg form due to the exact rotational symmetry retained by the QD states.)

Although the magnitude of $J_{\mu\nu}$ depends on the detailed geometry of the cluster along the path connecting dangling regions μ and ν, roughly speaking it decays with distance (using as metric the number of steps within the Bethe lattice, the so-called "chemical" distance). This is quantified by the scatter plots in Fig. 9.6, for an ensemble limited to clusters of equal size $N = 100$ each having two dangling spin-1/2 spins ($n_d = n_{1/2} = 2$) [5].

[5] We observed a weak dependence of the coupling (for a given "effective distance") on the size of the cluster. A more detailed analysis will be carried out elsewhere.

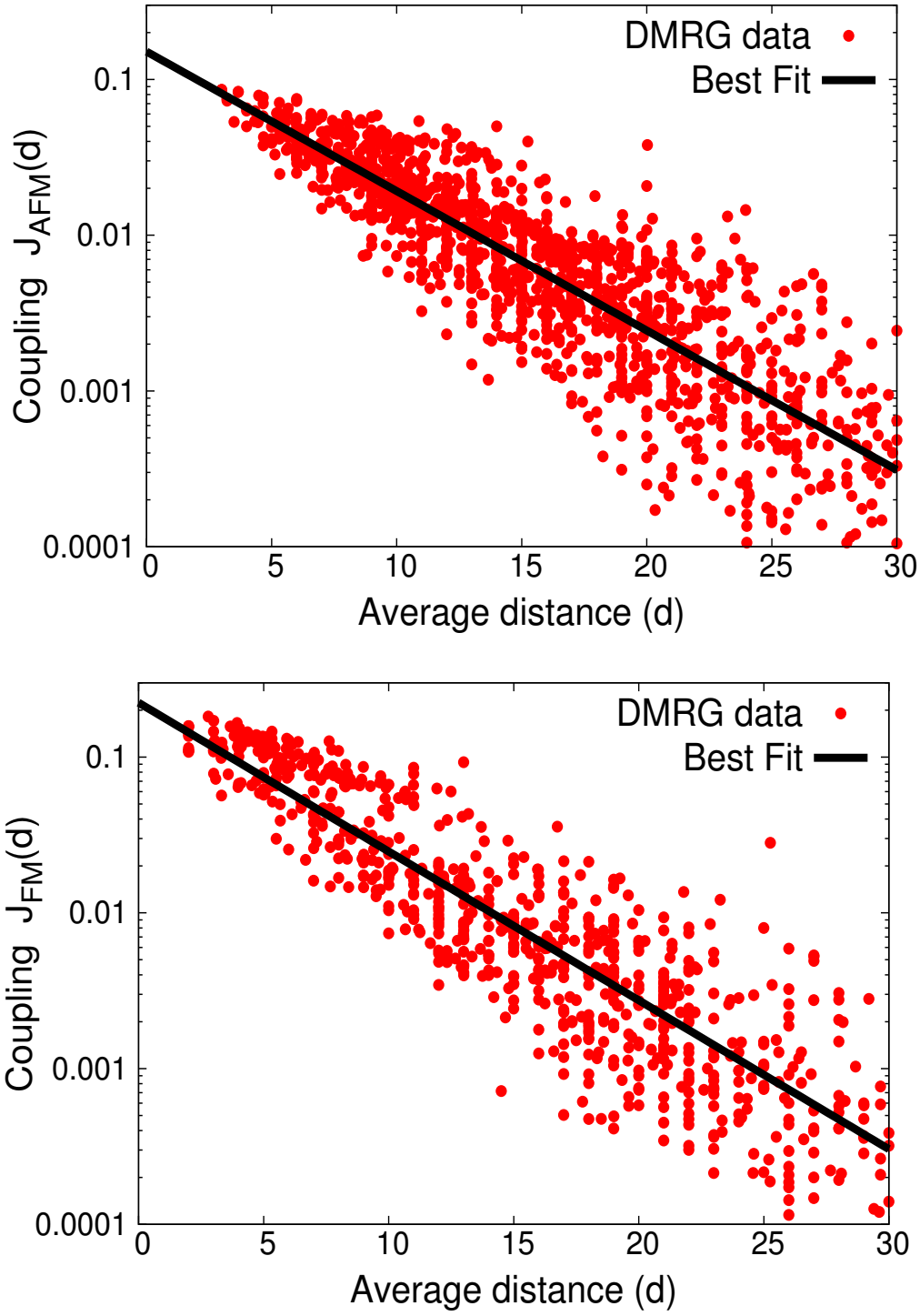

Figure 9.6: (Color online) Effective couplings J_{12} between two dangling spins as a function of their effective separation obtained from clusters having exactly two dangling spins. (a) dangling spins on opposite sublattices (antiferromagnetic coupling) (b) on same sublattice (ferromagnetic coupling).

Since each dangling region is in general spread out over multiple sites, we must define an "effective distance" between two of them:

$$\bar{d}_{\mu\nu} \equiv \sum_{ij} |u_i^{(\mu)}|^2 |u_j^{(\nu)}|^2 d_{ij} \tag{9.11}$$

where d_{ij} is the distance between sites i and j belonging to dangling regions μ and ν, and the amplitudes $u_i^{(\alpha)}$ for mode α are normalized. Figure 9.6 shows that indeed $J_{\mu\nu} \approx J_0 e^{-\bar{d}_{\mu\nu}/\xi}$, where $(J_0, \xi) \approx (+0.15, 4.85)$ for an even/odd pair of dangling spins, which are *always* antiferromagnetically coupled, or $(-0.22, 4.55)$ for a pair on the same sublattice. In the *ferromagnetic* case, choosing to fit only to clusters which do not form a spin-1 gives parameter values closer to the *antiferromagnetic* case.

We considered another ensemble of clusters with $N = 50$ having four dangling spins ($n_d = 4$) and obtained the effective Hamiltonian using the same prescription. We found that the non-pair terms typically account for a weight of at most 5% (using the Frobenius norm) in the Hamiltonian (9.10), confirming that the effective Hamiltonian is well approximated by pairwise Heisenberg exchange (at least in the limit of dilute monomer concentration).

9.6 Conclusion

We addressed the excitations of the spin 1/2 Heisenberg antiferromagnet on Bethe lattice percolation clusters. The emergent low energy degrees of freedom were found to be composite "dangling spin" excitations arising wherever there is a local imbalance between the even and odd sublattices [10, 11]. (The same kind of imbalance was shown to determine the low energy spectra of *regular*

Cayley trees in Chapter 8). We classified dangling spins based on the local cluster geometry and described an algorithm to predict their locations on clusters of arbitrary size.

Each of these emergent degrees of freedom is associated with a profile ($u_i^{(\alpha)}$ in the text) that plays the role of a "spinon wavepacket wavefunction" [17]; the degree of localization of the dangling spins could, in future work, be quantified using metrics (e.g. localization lengths) borrowed from Anderson localization. We did not, however, address the fundamental reason why a dangling spin degree of freedom decouples from the cluster, an effectively zero-energy excitation; that will be addressed in a subsequent publication [15].

The dangling spins interact via an effective low energy Hamiltonian, consisting of unfrustrated Heisenberg couplings that decay (roughly) exponentially with separation. If we adopt the fitted dependences in Figure 9.6 as our *definition* of our Hamiltonian, it should be possible to understand the low-energy states for arbitrary clusters that are much too large for the DMRG (involving thousands of sites), but will be tractable using the strong disorder renormalization group method [18](also see a connection of our work to this reference in Appendix 9.A), and thus finally explain the scaling of the spin gap Δ_{low} with cluster size that was found in Refs. [10, 11]. It would be interesting to see if the finite size scaling is *exactly* N^{-2} and if so, whether it is universal.

Finally, how does long range magnetic order survive in the scenario of dangling spins mediating interactions across strongly dimerized inert regions? We observed that spin correlations had an exponential decay across dimers but revived in regions on the cluster where a dangling spin was located. This suggests that in the thermodynamic limit, locally unbalanced regions are crucial for the

propagation of magnetic order on percolation clusters.

9.A Connection to past work

Our work on diluted antiferromagnets has a connection to the work done by Bhatt and Lee [18] in the early 1980's with *important* differences. I would like to briefly point this out.

Bhatt and Lee [18] were motivated to model doped semiconductors (such as phosphorus in silicon) at sufficiently low donor concentrations that retained the non-metallic nature of the material. They were interested in studying the magnetic ordering caused by the antiferromagnetic exchange coupling J between localized donor electrons (which they modelled as spin $1/2$ degrees of freedom) at temperatures much smaller than J. The donor electrons were distributed randomly on a three dimensional lattice and the Hamiltonian was taken to be,

$$\mathcal{H} = \sum_{i,j} J(\mathbf{r_i} - \mathbf{r_j}) \mathbf{S_i} \cdot \mathbf{S_j} \tag{9.12}$$

where the form of the antiferromagnetic coupling between the spins was *assumed* to be $J(\mathbf{r_i} - \mathbf{r_j}) = \exp(|\mathbf{r_i} - \mathbf{r_j}|/\zeta)$. Since all the couplings have the same sign, it leads to *frustration* in the model, which can prevent ordering down to the lowest temperatures and this was the central result of their paper.

In contrast, the effective Hamiltonian we derived in the randomly diluted antiferromagnet was shown to have *unfrustrated* couplings (since the underlying model is unfrustrated, the effective model is too). Thus even though our *derived* functional form of the Hamiltonian looks like the form *assumed* by Bhatt and Lee, the physics of our problem is expected to be quite different from theirs.

BIBLIOGRAPHY

[1] H. J. Changlani, S. Ghosh, S. Pujari and C. L. Henley, arXiv:1210.4621.

[2] D. Stauffer and A. Aharony, *Introduction to Percolation Theory* (Taylor and Francis, New York, 1992).

[3] Y.-C. Chen and A. H. Castro Neto, Phys. Rev. B **61**, R3772 (2000).

[4] N. Bray-Ali, J. E. Moore, T. Senthil, and A. Vishwanath, Phys. Rev. B **73**, 064417 (2006).

[5] O. P. Vajk *et al.*, Science **295**, 1691 (2002).

[6] A. W. Sandvik, Phys. Rev. Lett. **89**, 177201 (2002).

[7] P. W. Anderson, Phys. Rev. **86**, 694 (1952).

[8] H. Neuberger and T. Ziman, Phys. Rev. B **39**, 2608 (1989).

[9] M. Gross, E. Sánchez-Velasco, and E. Siggia, Phys. Rev. B **39**, 2484 (1989).

[10] L. Wang and A. W. Sandvik, Phys. Rev. Lett. **97**, 117204 (2006).

[11] L. Wang and A. W. Sandvik, Phys. Rev. B **81**, 054417 (2010).

[12] S. R. White, Phys. Rev. Lett. **69**, 2863 (1992).

[13] H. J. Changlani, S. Ghosh, C. L. Henley and A.M. Läuchli, arXiv:1208.1773.

[14] C. Lhuillier arXiv:cond-mat/0502464v1 (unpublished).

[15] S. Ghosh, H. J. Changlani and C. L. Henley (unpublished).

[16] The χ_{ij} matrix is a generalization of the χ_{ii} measurement proposed in Ref. [10, 11].

[17] Y. Tang and A. W. Sandvik, Phys. Rev. Lett. **107**, 157201 (2011).

[18] R. N. Bhatt and P. A. Lee, Phys. Rev. Lett. **48**, 344 (1982).

CHAPTER 10

CONCLUDING REMARKS AND OUTLOOK

There are various future directions one can take based on the ideas presented in Part II of this thesis. The first is related to the application of the DMRG technique for a graph that resembles the kagome lattice. The second direction suggests possibilities for "cheaper scaling" methods to tackle large (thousands of sites) percolation clusters using the information obtained in this thesis (which was derived by studying small clusters).

10.1 Adapting the DMRG to the Husimi cactus lattice

The DMRG method has been conventionally used for one dimensional systems and for 2D systems which have "small" widths compared to their lengths (note however that strips of width 12 lattice spacings can now be simulated with state-of-the-art codes [1]). In this thesis, we have explored a complementary application of DMRG: we have considered tree lattices whose hierarchical and loop-less structure is very conducive for the algorithm.

This has led to the application of my DMRG code to a lattice of corner sharing triangles each of whose centers is the vertex of a Bethe lattice. This lattice is known as the "Husimi cactus" and is locally like the kagome lattice (see Figure 10.1). Investigations of antiferromagnets on this frustrated lattice [2, 3] have been primarily motivated by studies on the kagome lattice. Thus we consider it apt to briefly summarize the status of the latter.

The nature of the ground state (along with the explanation of the origin of

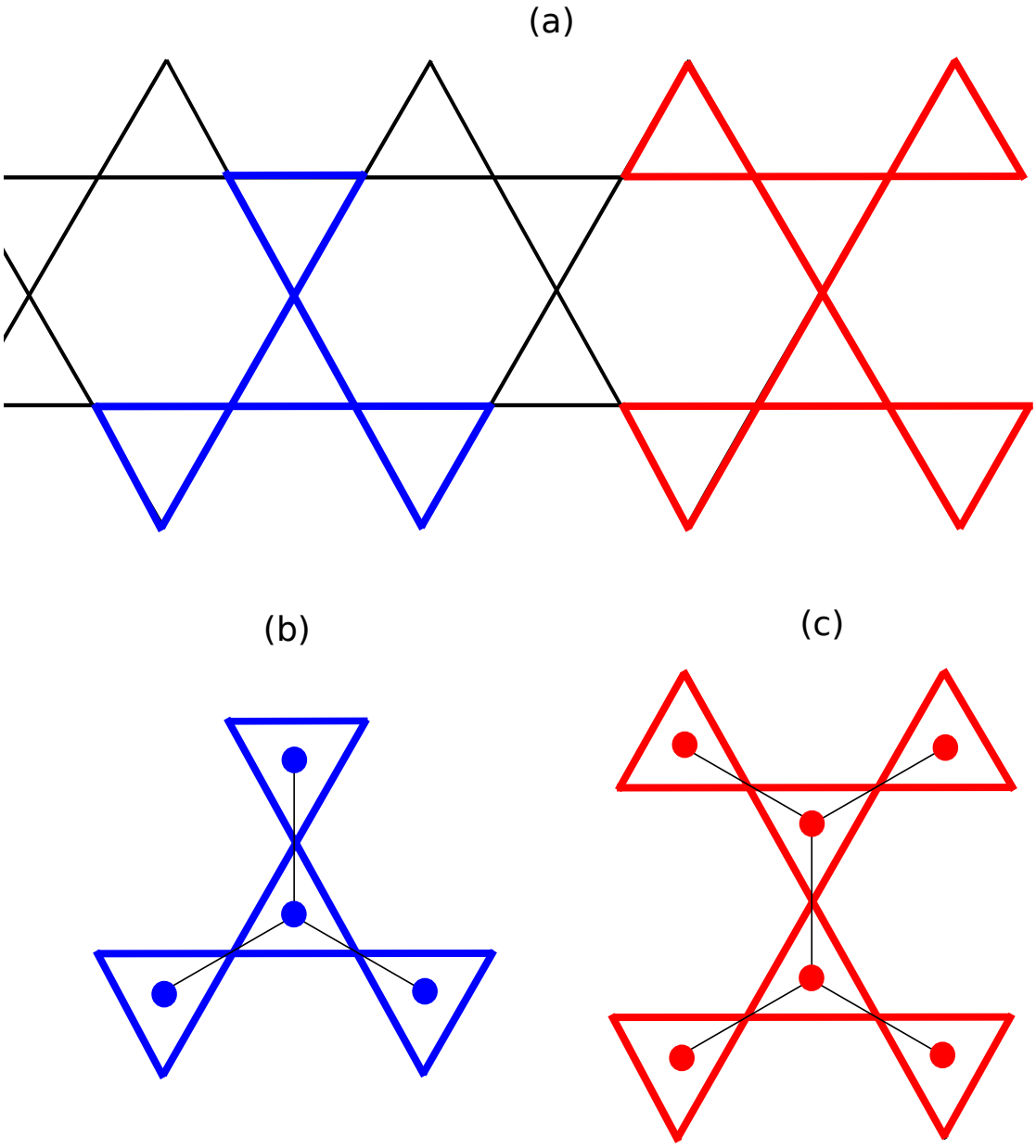

Figure 10.1: (a) Kagome lattice. The Husimi cactus (b),(c) is locally like a kagome lattice but has no loops. (b) is dual to the site-centered and (c) to the bond centered Cayley tree.

the low energy excitations) of the spin 1/2 nearest neighbor antiferromagnetic Heisenberg model on the kagome lattice has been a contentious issue for the last 20 or more years (an idea of the research in this field can be obtained from the papers [4, 5, 6, 7, 8, 9] and the references therein). Recent DMRG calculations by Yan et al. [9] (also by Depenbrock et al. [10]) strongly suggest that the ground state is a gapped spin liquid and its character seems to be of the Z_2 type. This has been recently contested by another study by Iqbal et al. [11] which indicates that the ground state may be a *gapless* U(1) Dirac spin liquid, consistent with an earlier proposal by Ran et al. [7]. To get a sense of how hard a challenge these numerical studies present, we note that all the recently reported competitive energies (per site) are within 1% of each other.

Despite the recent progress in simulations of the spin 1/2 kagome, terribly little is understood about the $s > 1/2$ case. The spin-1 kagome antiferromagnet was the subject of a variational wavefunction study by K. Hida [12]. Some aspects of the spin 3/2 antiferromagnet have been studied with exact diagonalization by Läuchli et al. [13]. Both these studies have dealt with very small system sizes (around 20 sites), and so we believe that a thorough understanding of these systems is far from complete.

We are interested in asking the following question: How does increasing the spin value change the ground state of the kagome lattice Heisenberg antiferromagnet from a spin liquid (for the spin 1/2 case) to a magnetically long range ordered state (as is believed to be the case for large spin). At what spin value does this happen? Recently, a coupled cluster [1] study was carried out by Götze

[1]Coupled cluster theory needs a reference wavefunction into which one can build in correlations. To do so, one uses a finite number of spin operators (correlating a maximum of n spins) in the ansatz. The convergence of the energy and correlation functions to the true result may be slow with n.

et al. [14]; which claims that there is a quantum phase transition on changing the spin value which occurs at around spin 1 or spin 3/2.

Since accurate calculations on the kagome lattice are hard to carry out, our approach is to explore if a similar transition is seen on the "simpler" Husimi cactus lattice. The cactus antiferromagnet is known to have a disordered valence bond state at $S = 1/2$ but a three-sublattice coplanar ordered state in the large S limit [3] and so it might have all the correct ingredients to understand the transition. However, the low energy physics dependent on the presence of loops in the kagome will not be captured in this approach.

10.2 More calculations on disordered systems

In Chapter 9, we presented our DMRG study of the Heisenberg antiferromagnet on finite clusters consisting of up to 200 sites. Improving the implementation of our algorithm will reduce memory and time requirements, but not to an extent that we can simulate thousands of sites. This is because although the DMRG is a very accurate method, its scaling with system size is somewhat unfavorable [2].

For very large clusters, one can thus use a combination of (1) the geometrical heuristics we developed to mark out regions where the "emergent spins" are present and (2) the derived form of the spatial dependence of the couplings, as

[2]The Lanczos diagonalization of the Hamiltonian expressed in terms of the block degrees of freedom costs us M^z amount of work; where M is the number of states retained on a block and z is the coordination number of a site. One such calculation needs to be done for every "cut" of the system as part of the "sweep algorithm" thereby multiplying this cost by the number of sites N. Another point to note is that to achieve a certain accuracy, M itself may need to grow with N (the rate at which it grows is system specific) making very big calculations difficult.

was discussed in Chapter 9. These new "spins" are used to define a unfrustrated Heisenberg model with distance dependent couplings. Since there is a wide spread in the distances between emergent spins (and hence the values of the couplings between them), the new "effective problem" might be conducive to the strong disorder renormalization group (SDRG) method [15, 16]. (I believe that if the SDRG had been directly applied to the bare Heisenberg model, the calculations would have been prone to large systematic errors. This is because the Heisenberg model has just one (bond) energy scale J whereas SDRG works when the distribution of couplings is broad.)

It would be interesting to see if the SDRG procedure yields "giant spins" (arising out of sublattice imbalance) or alternately favors formation of singlets at every stage of the renormalization. The former scenario would hint at the emergence of long range order whereas the latter would suggest a spin disordered state (despite the existence of a geometrically connected cluster). We are also eager to know whether the SDRG can accurately explain the (anomalous) finite size scaling of the singlet-triplet gap seen on percolation clusters (see Chapter 9).

Another direction one could pursue is to investigate if this "anomalous" finite size gap exponent is independent of the dimension of the percolation cluster (as long as the cluster is in greater than one dimension). Since only the ground state energies in the $S_z = 0$ and $S_z = 1$ sectors are required (for balanced clusters), I propose an accurate Quantum Monte Carlo calculation (note there is no sign problem) in each of these spin sectors for ensembles of percolation clusters generated in various dimensions. This study might reveal insights into how the emergent spin objects interact over long distances via the bulk of the cluster.

BIBLIOGRAPHY

[1] E. Stoudenmire and S. R. White, Annual Review of Condensed Matter Physics **3**, 111 (2012).

[2] P. Chandra and B. Doucot, Journal of Physics A: Mathematical and General **27**, 1541 (1994).

[3] B. Doucot and P. Simon, Journal of Physics A: Mathematical and General **31**, 5855 (1998).

[4] J. B. Marston and C. Zeng, Journal of Applied Physics **69**, 5962 (1991).

[5] P. Nikolic and T. Senthil, Phys. Rev. B **68**, 214415 (2003).

[6] R. R. P. Singh and D. A. Huse, Phys. Rev. B **76**, 180407 (2007).

[7] Y. Ran, M. Hermele, P. A. Lee, and X.-G. Wen, Phys. Rev. Lett. **98**, 117205 (2007).

[8] G. Evenbly and G. Vidal, Phys. Rev. Lett. **104**, 187203 (2010).

[9] S. Yan, D. A. Huse, and S. R. White, Science **332**, 1173 (2011).

[10] S. Depenbrock, I. P. McCulloch, and U. Schollwöck, Phys. Rev. Lett. **109**, 067201 (2012).

[11] Y.Iqbal, F. Becca, S. Sorella, D. Poilblanc, arXiv:1209.1858 (2012).

[12] K. Hida, Journal of the Physical Society of Japan **69**, 4003 (2000).

[13] A. Läuchli, S. Dommange, B. Normand, and F. Mila, Phys. Rev. B **76**, 144413 (2007).

[14] O. Götze *et al.*, Phys. Rev. B **84**, 224428 (2011).

[15] S.-k. Ma, C. Dasgupta, and C.-k. Hu, Phys. Rev. Lett. **43**, 1434 (1979).

[16] R. N. Bhatt and P. A. Lee, Phys. Rev. Lett. **48**, 344 (1982).